A (2)

MCR TECHNOLOGY CORPORATION

P.O. Box 10084
Chicago, IL
60610-0084

(312) 326-5007

31 March 1992

PHASE II FINAL REPORT

"High Brightness X-Ray Source for Directed Energy and Holographic Imaging Applications"

Prepared for: Dr. Paul Kepple
Plasma Physics Division
Naval Research Laboratory
Code 4722
4555 Overlook Avenue S.W.
Washington, D.C. 20375-5000

Prepared by: Dr. Armon McPherson, Principal Investigator
and
Dr. Charles K. Rhodes, President
MCR Technology Corporation
P.O. Box 10084
Chicago, IL 60601-0084

Contract #: N00014-89-C-2274

TABLE OF CONTENTS

ABSTRACT

Advances in x-ray imaging technology and x-ray sources are such that a new technology can be brought to commercialization enabling the three-dimensional (3-D) microvisualization of hydrated biological specimens.

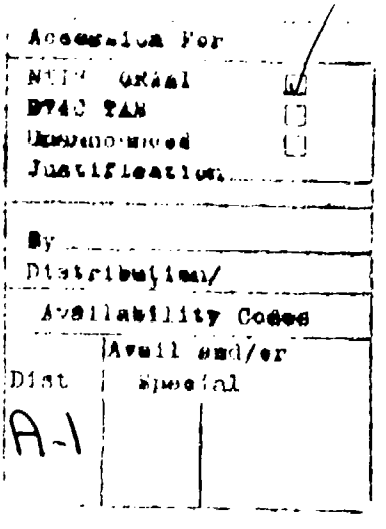

Statement A per telecon
Dr. Paul Kepple NRL/Code 4722
Washington, DC 20375-5000

NWW 4/15/92

I. INTRODUCTION

The Company is engaged in a program whose main goal is the development of a new technology for direct three dimensional (3–D) x–ray holographic imaging. It is believed that this technology will have a wide range of important applications in the defense, medical, and scientific sectors. For example, in the medical area, it is expected that biomedical science will constitute a very active and substantial market. The basis of this view, is represented directly below.

The application of physical technologies for the direct visualization of biological entities has had a long and extremely fruitful history. The invention of the light microscope in the 17th century and the development of the electron microscope shortly before World War II, have obviously been enormously successful scientifically. Equally significantly, these two landmark advances, in addition to revealing radically new physical features of the human environment, have also had a profound and unexpected influence on man's spiritual perception of his world. The light microscope opened up an unseen universe, not only of strange plant and animal life, but also one embodying new shapes and forms, serving to challenge and stimulate the mind. The electron microscope, by greatly enhancing the spatial resolution achievable, led to further seminal findings, such as the first views of viral particles and the complex cytoskeletal structure of cells. As a consequence of the broad biological and medical applications of these two technologies, both now represent valuable basic and widely used tools in biological research and clinical medicine.

Presently, the opportunity exists to take another step in this historical process with the development of a powerful new means of visualization, three–dimensional x–ray microholography.[1] Importantly, unlike electron microscopy, which generally requires stained and desiccated specimens, this new technology will uniquely combine a main feature of the light microscope, the ability to observe

hydrated living matter, with the principal capability of the electron microscope, the power to resolve very small spatial elements, such as those defining the cytoskeletal architecture.

This microholographic technology is composed of two basic and separate components. They are (A) an x–ray laser and (B) an x–ray holographic camera designed specifically for biological specimens. The suitability of x–ray laser technology for this type of imaging arises very naturally, since x–rays (i) can readily penetrate hydrated matter, (ii) intrinsically embody a short spatial scale–length permitting high resolution, and (iii) can attain extraordinarily high exposure rates as a direct consequence of the very high source brightness.

The holographic camera has been sufficiently well developed by the Company that a prototype instrument[2–4] is currently under development. Indeed, since the capability of this technology is quite general, it has been shown by the Company[5] that it is possible to develop a technique of direct imaging for the sequencing and mapping of the human genome based on a modification of this prototype. However, as noted above, the full potential of holography for hydrated specimens, can only be realized when it incorporates a suitable x–ray laser. The resulting 3–D images, on account of the rate of radiation damage, require a source with a brightness that can only be achieved with an x–ray laser. It is important to note that the use of such a laser uniquely provides two important new functions, atomic specificity and "stop–action" imaging. By appropriately selecting the laser wavelength, it is possible to selectively enhance the imaging of a particular atomic species of biological interest such as nitrogen, phosphorus, sulfur, calcium, and potassium, among others. Finally, the exposure time, predicted to be ~ 10^{-13} seconds, is faster than most biological or chemical processes.

Special conditions are required to produce the amplification needed for laser

action at x-ray wavelengths. Amplification in the x-ray region mainly requires prodigious energy deposition rates spatially organized in a high-aspect-ratio volume of material. The fundamental requirement, therefore, reduces to the efficient deposition of energy at very high specific powers in a spatially controlled and nonthermal manner. Canonically, a deposition rate in the 10^{17} – 10^{19} W/cm^3 range is necessary.

To meet this requirement, we have developed an approach that uniquely combines three different components: (1) an energy deposition mechanism based on a highly nonlinear coupling[6,7] to the source of energy used for excitation of the x-ray amplifying medium, (2) a mode of channeled propagation[8–10] capable of guiding both the ultraviolet and x-ray radiation, and (3) a new extremely high brightness ultraviolet pulsed laser technology[11,12] to provide the source of energy for excitation.

It can be seen that these three elements, which appear capable of producing and controlling the most extreme conditions of power density yet realized with laboratory-scale apparatus, fit together in a remarkably congenial way, as outlined in Appendix A. Importantly, the conditions needed to produce the (1) strong nonlinear coupling observed experimentally are exactly (2) those required for channeled propagation and (3) that these conditions can be achieved by present laser technology. The confluence of these three conditions is the key feature of this method for the efficient attainment of the very high-energy-density states of matter needed for x-ray amplification.

This report deals with two central aspects of the developing technology which directly affect the feasibility of commercial application. They are (1) the technology for holographic image reconstruction and (2) the x-ray source technology in particular, the issue associated with the optimum spatial control of the deposition of energy. The effort on both of these questions is aimed principally at reducing

the complexity, cost, and physical scale of the instrumentation needed to serve the targeted applications. Most significantly, the results show indeed that a small laboratory instrument is possible. Full satisfaction of the Statement of Work represented in the Phase II proposal has been accomplished.

II. PHASE II RESEARCH

The Statement of Work for the Phase II effort is presented for reference in Appendix B.

A. DEVELOPMENT OF ALGORITHMS FOR HOLOGRAPHIC IMAGE RECONSTRUCTION

1. 3–D Algorithms

Algorithms suitable for the reconstruction of 3–D images in the x–ray range have been developed and tested by appropriate simulations at visible wavelengths. Appendix C gives a description of the important aspects of this work.

2. Images of Drosophila Embryo

Other subsequent experiments have shown that a properly prepared Drosophila embryo can serve as a very convenient and informative model system for examining the 3–D imaging properties of the microscope. Specifically, since we desire images with (1) high spatial resolution, (2) biological structural specificity, (3) 3–D information, and (4) high contrast, a staining procedure involving silver–enhanced immuno–gold complexes[13] was used. This stain was used to visualize the segmentation of the Drosophila embryo as displayed by using an antibody against the engrailed protein.[14]

A reconstructed image of a Drosophila embryo, at three successive depths, (z), is shown in Fig. (1) taken under dark–field illumination. The study of such images is informing on the operational characteristics of the system such as (1) the sensitivity of the image to the conditions of exposure, (2) the staining procedure, and (3) the numerical procedures used in the reconstruction. These characteristics

represent simulations of their counterparts in the x–ray regime. Of course, the high contrast that can be naturally obtained in the x–ray region will eliminate the need for staining.

Several important aspects of the imaging system are revealed by examining the reconstructions shown in Fig. (1). They are (1) the high contrast shown by the banding, (2) the sharp edges, demonstrating the high spatial resolution, shown most clearly at the edge of the embryo, (3) the absence of speckle, and (4) the 3–D character of the images. The latter point is apparent through examination of the region of invagination toward the bottom right of the embryo.

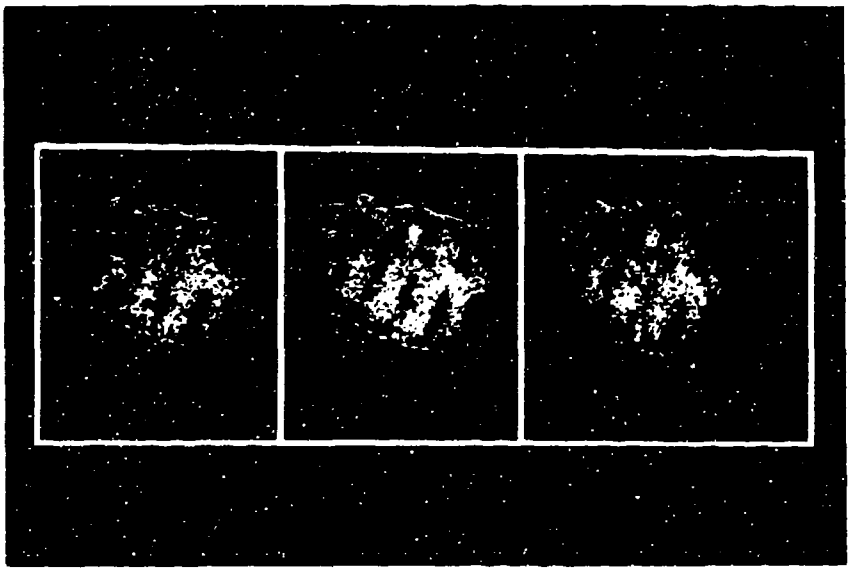

Fig. (1): Reconstructed images of Drosophila embryo stained with silver–enhanced immuno–gold complexes. The image reveals the banded pattern governed by the segmentation genes. The three panels represent reconstructions corresponding to three different depth (z) planes in the specimen. In the left panel, z = +54 μm; in the center panel, z = 0 μm; in the right panel z = –54 μm. The full size of the reconstructed image is ~ 256 μm, as indicated by the black edges at the left and right of the embryo.

B. HOLOGRAPHIC MICROSCOPE

Two basic types of holographic microscopes have been constructed using the Fourier configuration. One version utilizes a glycerol microdrop as the reference wave scatterer. This instrument is described in Appendix D.

A second basic system we have used for the studies conducted with visible radiation is shown in Fig. (2). A convenient configuration is a modification of a Mach–Zehnder (MZ) interferometer geometry. In this configuration have we replaced the spherical reference scatterer with a suitable microscope objective,since, for visible wavelengths, this permits facile and flexible operation. The primary beam of coherent radiation is split into two beams with a beam splitter. Advantage is taken of the inherent polarization of the coherent laser radiation, and a polarizing beam splitter is used. For these studies, the polarization is utilized to control the relative intensity of the two subbeams. In the x–ray case, this relative intensity would be governed by the radius of the spherical reference scatterer One subbeam of the MZ interferometric section of the microscope is used to illuminate the biological specimen, while the other subbeam is brought to a focus by illumination of a compound microscope (CM) objective. Both subbeams are then recombined in a beam–combiner cube and these recombined beams, which form the holographic interference of the specimen, diverge to fill the aperture subtended by the detector (CCD). The fourth direction of the beam combiner is occupied by a CM to permit alignment of the specimen and the reference beam This configuration of the microscope functions as a dark–field microscope and has performed exceptionally well at NA ~ 0.50 with highly scattering biological specimens

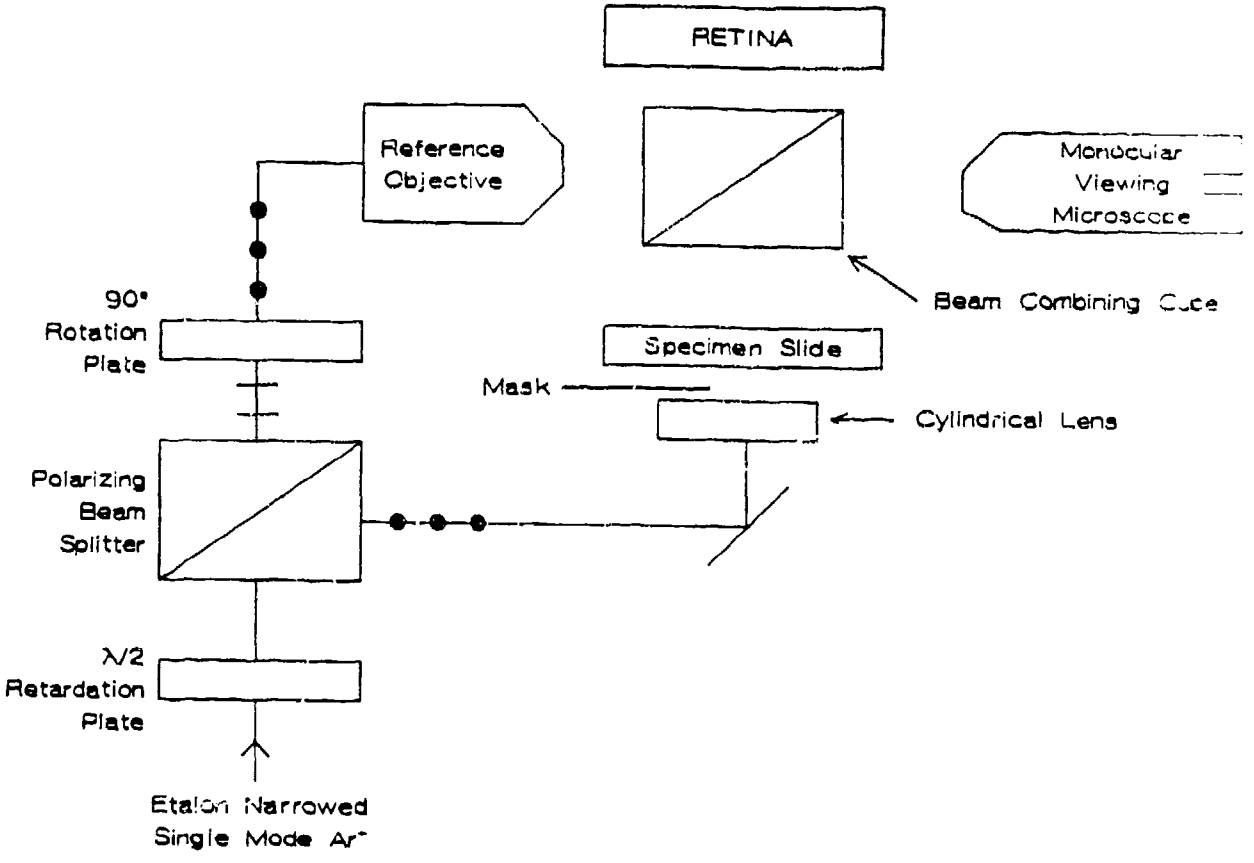

Fig. (2): Schematic of Mach–Zehnder holographic microscope.

A photograph of the existing instrument, which corresponds to the schematic presented in Fig. (2), which was used for the studies at visible wavelengths is given in Fig. (3a). The specific design incorporating the same concepts that has already been built for work at x-ray wavelengths is shown in Fig. (3b). As described in Appendix E, this x-ray camera is sufficiently flexible that it can be used with various sources, such as a free-electron laser.

Studies of the characteristics of operation of this instrument have been performed on several biological materials These include (1) parascaris univalens larva. (2) a fish melanoma histopathology specimen (Xiphophorus maculatus x helleri), (3)

a section through duodenum including a nerve ganglion, and, as noted above, (4) a Drosophila embryo. The latter was used to examine specifically the three–dimensional character of the imaging.

(a)

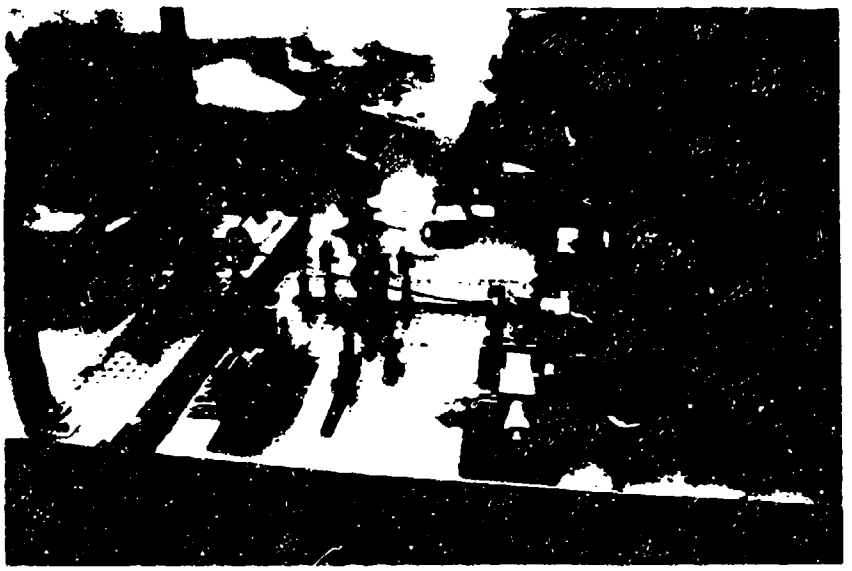

(b)

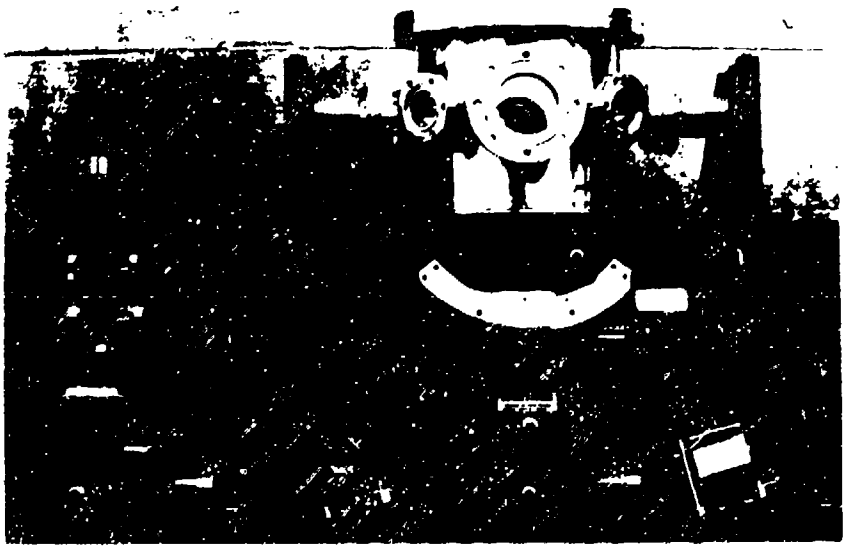

Fig. (3): (a) Photograph of the visible holographic microscope. (b) Photograph of x–ray holographic system.

C. ELECTROMAGNETIC PROPAGATION

As outlined in Section I, the spatial control of the energy deposited for excitation of an x–ray amplifier plays an important role in the fundamental scaling relationship between the required energy, the gain and the wavelength. The critical governing issue, which determines the scaling relationship between the required excitation energy (E) and the amplifier gain (G) of x–ray lasers, is the spatial control of the deposited energy. The information presented in Fig. (4) shows that optimizing the gain (G) per unit energy (E) calls for the guided mode of propagation in order to optimally control the deposition of the energy. Overall, in comparison to traditional forms of excitation, for a fixed x–ray energy output (E_X) and wavelength (λ_X), a reduction of several orders of magnitude in the necessary energy (E) results, as shown in Fig. (5), if this form of confined (channeled) propagation can be achieved. Therefore, if this scaling holds, a relatively small and useful laboratory–scale technology becomes feasible. One joule of energy is seen as sufficient up to a wavelength of several kilovolts (~ 1.6 Å).

At least two types of conditions can lead to the desired confined propagation. They involve (1) the use of guiding structures, such as static waveguides, or (2) propagation that is dynamically confined.[15] Both aspects have been considered.

X-Ray Laser Scaling

Spatial Distribution/Amplifying Volume

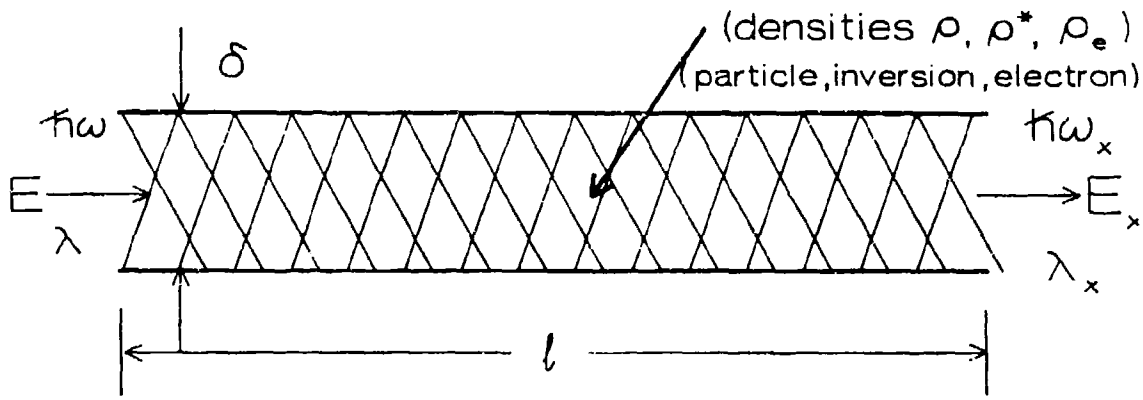

$$E = \frac{\hbar\omega_x \rho^* \delta^2 l}{\eta_x}$$

$$G = \rho^* \sigma_x l$$

Laboratory Scale Technology---

$$\frac{G}{E} = \frac{\eta_x \sigma_x}{\hbar\omega_x \delta^2}$$ ⇨ small δ

$\therefore$ Large l/δ, but $\delta \geq \sqrt{\lambda l}$ free space propagation

Really want to set--

$l >>$ Rayleigh range $l_R \sim \delta^2/\lambda$

$l \sim$ loss length

δ small ρ^* large as possible

$\therefore$ **Guided Mode of Propagation**

Fig. (4): Spatial distribution of energy of excitation (E) for an x-ray ($\hbar\omega_x$) amplifier. Parameters are the same as in Fig. (5) with λ the wavelength of the excitation energy, assumed longitudinally delivered, and with ρ, ρ^*, and ρ_e representing the particle, inversion and electron densities, respectively. The analysis shows that optimization of G/E requires a guided mode of propagation so that high concentrations of power can be organized into high-aspect-ratio spatial volumes.

Energy (E)/Wavelength (λ) Scaling

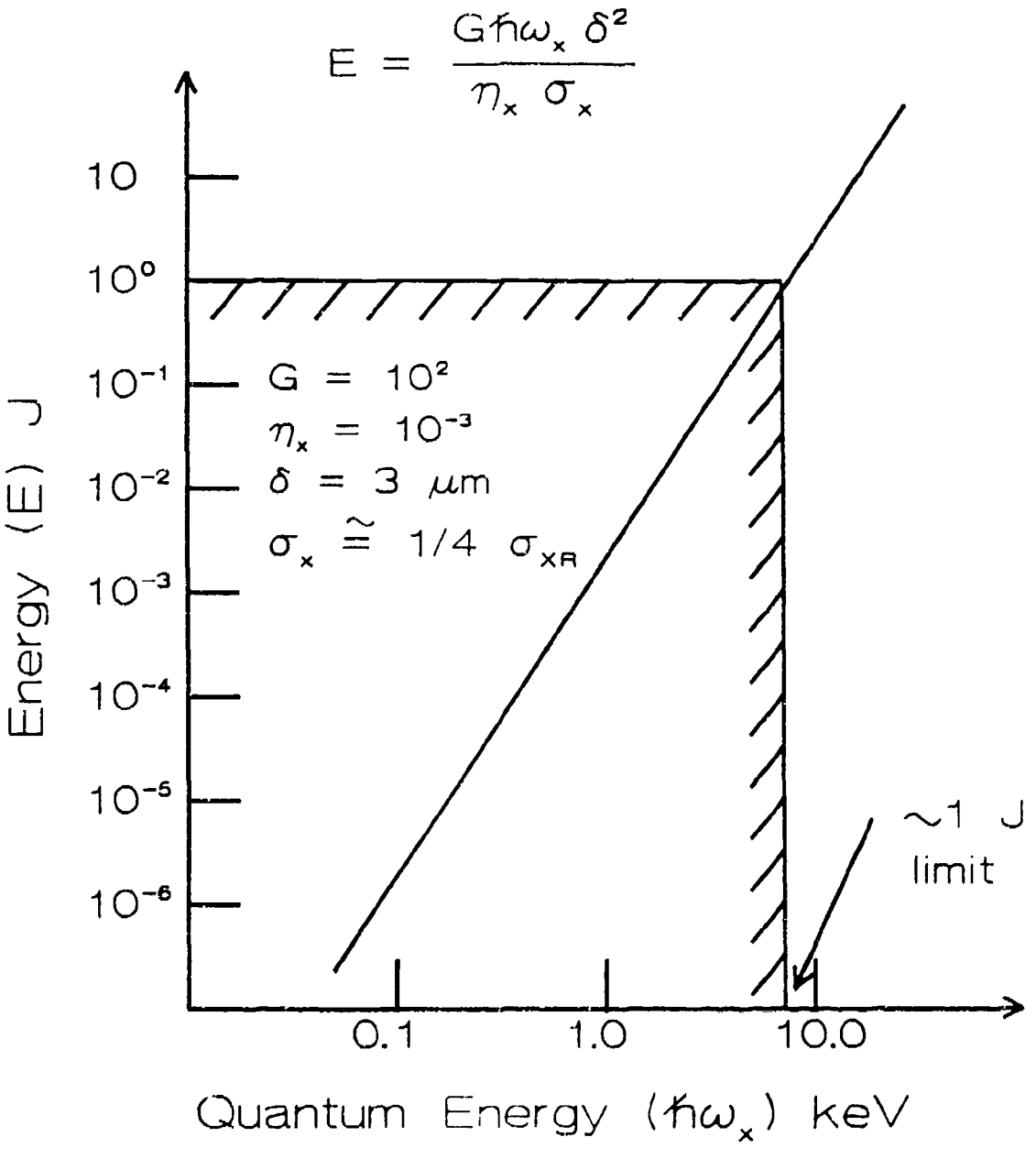

Fig. (5): Scaling relationship between required excitation energy (E) and quantum energy ($\hbar\omega_X$) characteristic of the amplifier. Parameters: total gain exponent G = 100, energy efficiency $\eta_X = 10^{-3}$, channel diameter δ = 3 μm, x-ray ($\hbar\omega_X$) cross section for stimulated emission σ_X, x-ray cross section for stimulated emission for radiatively-broadened transition σ_{XR}.

1. Capillary Guiding Structures

A static guiding structure, assuming that the wave can be properly launched and that the losses are sufficiently low, could potentially serve to provide the desired confined propagation. This possibility was experimentally explored, under subcontract to the Company, by the University of Illinois at Chicago. Basically, it was found that the use of static guiding structures is not feasible for the range of parameters required for x–ray amplification. The report of the subcontractor is given in Appendix F.

2. Dynamical Guiding of Electromagnetic Propagation

Theoretical work[8,16–19] indicates that dynamical guiding of very intense pulsed radiation may be possible under conditions suitable for x–ray amplification. The essential aspects of this theoretical work are given in Appendix A and Appendices (G – I).

Significantly, experimental evidence now exists, as described in Appendix J, that demonstrates for the formation of such a mode of propagation. Specifically, the experimental studies have examined a new relativistic regime of high–intensity short–pulse propagation in plasmas which indicates the development of a stable mode of spatially confined (channeled) propagation. For an electron density of ~ 1.35×10^{21} cm^{-3} and a power of ~ 3×10^{11} W, the results indicated a channel radius < 1 μm and a peak intensity ~ 10^{19} W/cm^2. Comparison of these findings with a dynamical theory yield agreement for both the longitudinal structure and the radial extent of the propagation observed.

The most important outcome of these findings is that it enables the scaling relationship shown in Fig. (5). The existence of this mode of propagation makes possible a small laboratory–scale x–ray laser technology that can serve a multitude of applications including the important biomedical ones of interest to the Company.

III. CONCLUSIONS

The implications of developments achieved under the support of this work for general applications to x–ray imaging and the microcharacterization of condensed matter are extremely important and propitious. In terms of the x–ray source, they are (1) that a properly controlled energy deposition rate, sufficient for the production of stimulated x–ray sources up to a few kilovolts in quantum energy, can now be achieved with an excitation energy of ~ 1 J, (2) that an x–ray output energy of ~ 1 mJ per pulse is achievable with laboratory–scale technology, and (3) that an x–ray beam diameter (~ 2 – 3 μm) arises as a natural consequence of the physics. These parameters represent an exceptionally high peak brightness figure that permits a new and completely unexplored range of physical measurements to be made. Indeed, a high–brightness source of this nature is ideal for the microimaging of condensed matter. In particular, an x–ray source with these parameters is perfectly matched to the requirements for holographic imaging of biological materials[1–3,21] in terms of all its relevant properties, specifically, wavelength (10 – 40 Å), pulse energy (~ 1 mJ), pulse length (~ 10^{-13} s), beam diameter (~ 2 – 3 μm), and divergence (~ 1 mrad). Finally, the 3–D camera technology matched to this source is available

IV. REFERENCES

1. J. C. Solem and G. C. Baldwin, "Microholography of Living Organisms", Science 218, 229 (1982).

2. W. S. Haddad, D. Cullen, K. Boyer and C. K. Rhodes, "Design for a Fourier Transform Holographic Microscope", X-Ray Microscopy II, edited by D. Sayre, M. Howells, J. Kirz, and H. Rarback (Springer-Verlag, Berlin, 1988) p. 284-287.

3 W. S. Haddad, J. C. Solem, D. Cullen, K. Boyer, and C. K. Rhodes, "A Description of the Theory and Apparatus for Digital Reconstruction of Fourier Transform Holograms", in Electronics Imaging '87, Advanced Printing of Paper Summaries, Vol. II (Institute for Graphic Communication, Inc., Boston, 1987) pp.. 683-688.

4. W. S. Haddad, D. Cullen, J. C. Solem, J. W. Longworth, A. McPherson, K. Boyer, and C. K. Rhodes, "Fourier Transform Holographic Microscope", manuscript submitted to Applied Optics.

5. W. Haddad, K. Boyer, R. M. Moriarty, J. C. Solem, and C. K. Rhodes, "Genome Sequencing by Direct Imaging X-Ray Color Holography", Proceedings of the Workshop on X-Ray Microimaging for the Life Sciences, May 24-26, 1989 (Lawrence Berkeley Laboratory, Berkeley, CA, 1989) LBL Report No. 27660, p. 81-84.

6. K. Boyer, H. Jara, T. S. Luk, I. A. McIntyre, A. McPherson, R. Rosman, and C. K. Rhodes, "Limiting Cross Sections for Multiphoton Coupling", Revue Phys. Appl. 22, 1793 (1987).

7. C. K. Rhodes, "Multiphoton Ionization of Atoms", Science 229, 1345 (1985).

8. J. C. Solem, T. S. Luk, K. Boyer, and C. K. Rhodes, "Prospects for X-Ray Amplification with Charge-Displacement Self Channeling", IEEE J. Quantum Electron. QE-25, 2423 (1989).

9. A. B. Borisov, A. V. Borovskiy, O. B. Shiryaev, V. V. Korobkin, A. M. Prokhorov J. C. Solem, T. S. Luk, K. Boyer, and C. K. Rhodes, "Relativistic and Charge-Displacement Self-Channeling of Intense Ultrashort Laser Pulses in Plasmas", submitted to Physical Review A, accepted 9 January 1992.

10. A. B. Borisov, A. V. Borovskiy, V. V. Korobkin, A. M. Prokhorov, O. B Shiryaev, X. M. Shi, T. S. Luk, A. McPherson, J. C. Solem, K. Boyer, and C K. Rhodes, "Observation of Relativistic/Charge-Displacement Self-Channeling of Intense Subpicosecond Ultraviolet (248 nm) Radiation in Plasmas", submitted to Phys. Rev. Lett., 12 November 1991.

11. A. P. Schwarzenbach, T. S. Luk, I. A. McIntyre, U. Johann, A. McPherson, K Boyer, and C. K. Rhodes, "Subpicosecond KrF*-Excimer-Laser Source", Opt Lett. 11, 499 (1986).

12. T. S. Luk, A. McPherson, G. Gibson, K. Boyer, and C. K. Rhodes, "Ultrahigh Intensity KrF* Laser System", Opt. Lett. 14, 1113 (1989).

13. G. Danscher and J. Norguard, "Light Microscope Visualization of Colloidal Gold on Resin Embedded Tissue", J. Histochem. Cytochem. 31, 1394–1398 (1983).

14. B. Alberts, D. Bray, J. Lewis, M. Raff, K. Roberts and J. D. Watson, Molecular Biology of the Cell, Second Edition (Garland Publishing, Inc., New York, 1989(p. 928.

15. K. Boyer, A. B. Borisov, A. V. Borovskiy, O. B. Shiryaev, D. A. Tate, B. E. Bouma, X. Shi, A. McPherson, T. S. Luk, and C. K. Rhodes, "Methods of Concentration of Power in Materials for X–Ray Amplification", Appl. Optics, in press.

16. P. Sprangle, E. Esaray, and A. Ting, "Nonlinear Theory of Intense Laser Plasma Interactions", Phys. Rev. Lett. 64, 2011 (1990).

17. A. B. Borisov, A. V. Borovskiy, V. V. Korobkin, A. M. Prokhorov, C. K. Rhodes, and O. B. Shiryaev, "Stabilization of Relativistic Self–Focusing of Intense Subpicosecond Ultraviolet Pulses in Plasmas", Phys. Rev. Lett. 65, 1753 (1990).

18. A. B. Borisov, A. V. Borovskiy, O. B. Shiryaev, V. V. Korobkin, A. M. Prokhorov, J. C. Solem, T. S. Luk, K. Boyer, and C. K. Rhodes, "Relativistic and Charge–Displacement Self–Channeling of Intense Ultrashort Laser Pulses in Plasmas", Phys. Rev. A, in press.

19. A. B. Borisov, A. V. Borovskiy, V. V. Korobkin, A. M. Prokhorov, O. B. Shiryaev, X. M. Shi, T. S. Luk, A. McPherson, J. C. Solem, K. Boyer, and C. K. Rhodes, "Observation of Relativistic/Charge–Displacement Self–Channeling of Intense Subpicosecond Ultraviolet (248 nm) Radiation in Plasmas", Phys. Rev. Lett., submitted.

20. W. S. Haddad, D. Cullen, J. C. Solem, K. Boyer, and C. K. Rhodes, "X–Ray Fourier–Transform Holographic Microscope", in Short Wavelength Coherent Radiation: Generation and Applications, Vol. 2, R. W. Falcone and J. Kirz, eds. (Optical Society of America, Washington, D.C., 1988) pp. 284–289.

APPENDIX A

Reprinted from the

OSA Proceedings on

Short Wavelength Coherent Radiation: Generation and Applications

Volume 2

Charge-Displacement Self-Channeling as a Method for Energy Concentration

K. Boyer, T. S. Luk, J. C. Solem, and C. K. Rhodes

Laboratory for Atomic, Molecular, and Radiation Physics, Department of Physics
University of Illinois at Chicago, P.O. Box 4348, Chicago, Illinois 60680

Proceedings of the OSA Topical Meeting
on Short Wavelength Coherent Radiation:
Generation and Applications
September 26-29, 1988, North Falmouth, Cape Cod, MA

Charge-Displacement Self-Channeling as a Method for Energy Concentration

K. Boyer, T. S. Luk, J. C. Solem,† and C. K. Rhodes

Laboratory for Atomic, Molecular, and Radiation Physics, Department of Physics
University of Illinois at Chicago, P.O. Box 4348, Chicago, Illinois 60680

Abstract

The concentration of energy arising from charge–displacement self–channeling is discussed. Since high energy deposition rates are expected to arise from multiphoton coupling and the channel can also serve as an effective waveguide for secondary radiation, such circumstances are ideal for generating coherent short wavelength radiation.

Channeled Propagation

Amplification in the x–ray region requires prodigious energy deposition rates [1] spatially organized in a high–aspect–ratio volume of material. The fundamental question, therefore, centers on the controlled deposition of energy at high specific powers. We show that the use of extremely intense (10^{19} – 10^{22} W/cm^2) short pulse (~ 100 fs) radiation may be able to produce both the necessary deposition rates and spatial control by combining (1) the energy deposition [2,3] arising from high–order multiphoton processes with (2) a new mode of channeled propagation involving a charge–displacement mechanism. A significant point that will emerge is that the conditions needed for the strong multiphoton coupling are identical to those found required for the confined propagation.

It appears [4–6] that a fundamentally new regime of electromagnetic propagation will develop in plasmas for subpicosecond radiation of sufficient intensity. In the high intensity case of interest, in which processes generating ionization dominate the coupling, multiphoton ionization is expected to produce a substantial reduction of both the linear and nonlinear refractive indices of the medium. For a suitably ionized plasma, this combination of high charge state ions with the electron density produced by the multiphoton coupling appears capable of producing a new mode of radiative channeling.

Indeed, preliminary analysis [7] supports the presence of the following mechanism. For a sufficiently short pulse (~ 100 fs), the massive ions remain spatially fixed while the relatively mobile electrons are expelled by the ponderomotive force from the high intensity zone. Thereby, a state of equilibrium can be established between the ponderomotive and the electrostatic force densities owing to the charge displacement. Since the electrons, which embody a negative contribution to the index, are expelled, an on–axis region of relatively high refractive index is formed which supports the channeling. In a limiting case, it appears that the behavior approaches that characteristic of a metallic waveguide. Interestingly, a focusing mechanism of this type is not describable in terms of the conventional [8] nonlinear index parameter n_2. A further unusual aspect of this process, since there is a strong tendency to locally reduce the plasma frequency ω_p in the region where the intensity is high, is that it may enable propagation for appreciable distances in plasmas that would normally be considered as overdense.

The essence of the idea can be understood in the following manner. The steady–state force balance between the radially outward ponderomotive force and the oppositely directed electron–ion attraction is represented, in cylindrical symmetry for a completely ionized tenuous ($\omega >> \omega_p$) plasma, by

$$\frac{2\pi e^2}{m\omega^2 c}\,\nabla I(r) + e^2 n_e \int \frac{\rho(r)\,(r - r')}{|r - r'|^3}\,d^3r' = 0. \quad (1)$$

For a cylindrical gaussian intensity distribution $I(r)$, the total charge density $\rho(r)$ can be written in exact form as

$$\rho(r) = 2B\,(1 - r^2/r_0^2)\,\exp(-r^2/r_0^2) \quad (2)$$

in which $B = I_0(m\omega^2 c n_e r_0^2)^{-1}$ and m, c, n_e, and

r_e denote the electron mass, speed of light, quiescent plasma density, and radius (HWHM) of the assumed gaussian intensity profile, respectively. The form of this solution is shown in Fig. (1) for a value of B = 0.4. The expulsion of the electrons from the central region is apparent.

A charge distribution of this nature can lead to channeled propagation. An estimate of the condition necessary can now be made by describing the charge displacement by two regions, such that $\rho(r < r_e\sqrt{2}) = \rho(0)$ and $\rho(r \geq r_e\sqrt{2}) = \rho(r_e\sqrt{2})$, and equating the angle of total internal reflection to the angle corresponding to the first minimum of diffraction. This procedure yields a critical intensity

$$I_C = \frac{\pi \cdot m\omega^2 c}{64(1 + e^{-2})r_e} = (4.3 \times 10^{-2}) \frac{m\omega^2 c}{r_e}, \quad (3)$$

in which r_e denotes the classical electron radius. Significantly, this intensity is independent of the electron density n_e and contrasts with the power threshold [8] normally arising from induced index charges in transparent dielectrics. Analytic approximations extending to high electron density show a significant dependence of I_C on n_e only quite near the critical density. Furthermore, it is easily demonstrated that I_C normalized to the Compton intensity [9] is a constant (0.54) independent of frequency, a finding which shows that the charge-displacement mechanism is associated with relativistic conditions. For a wavelength of 248 nm, $I_C = 2.4 \times 10^{19}$ W/cm^2. Finally, a striking aspect of the analysis [7] is the extremely strong frequency dependence favoring the use of ultraviolet wavelengths to establish the conditions for channeling. Scaling laws are derived [7] indicating variations as rapid as ω^6.

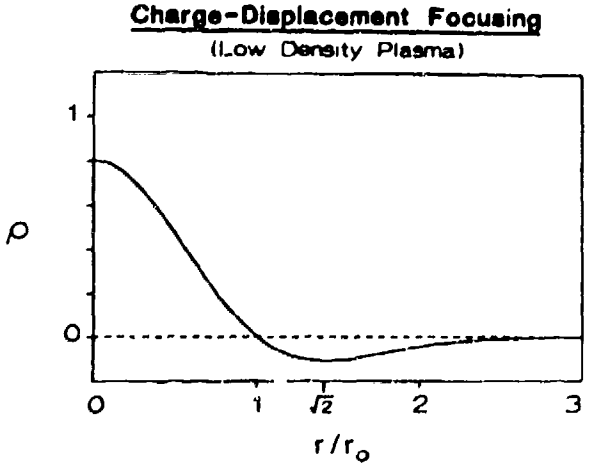

Figure 1. Illustration of the total charge density ρ as a function of normalized radial distance r/r_e for B = 0.4.

Controlled Energy Concentration – Summary

In terms of the basic question of the controlled deposition of energy at high specific powers, the answer that emerges from these considerations involves three separate components. They are (1) a new ultraviolet pulsed power technology, [10] (2) an energy deposition mechanism based on highly nonlinear coupling, [11] and (3) a condition for channeled propagation. [7] It can be seen that these three elements, which appear capable of producing conditions comparable to, or possibly exceeding those of a thermonuclear environment, [10] fit together in a remarkably congenial way. Figure (2) illustrates these relationships. A principal finding is that the radiative conditions needed for the strong multiphoton coupling governing the energy transfer rate [11] are essentially identical to those required for the channeled propagation [7] and that the laser technology [10] can readily produce the regime of irradiation necessary. The compatibility of these three factors is a key feature of this method for the attainment of very high energy density states of matter.

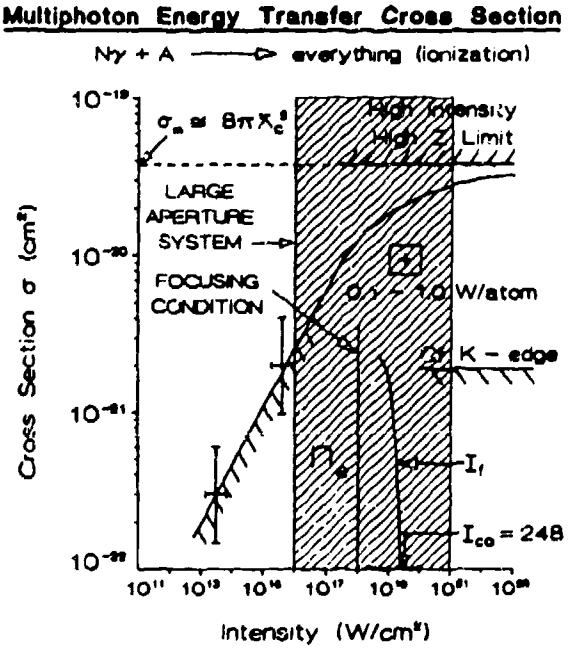

Figure 2. Illustration of how (1) the energy transfer cross section σ, (2) the channeling condition, and (3) the pulse power technology all fit together. The significant fact is that the conditions needed for the strong multiphoton coupling governing the energy transfer ($I \simeq I_{CO} \simeq 10^{19}$ W/cm^2) are identical to those required for the channeled propagation ($I_f \simeq I_{CO} \simeq 10^{19}$ W/cm^2), and that the developing large aperture ultraviolet laser technology moves us into the desired range.

Acknowledgements

This work was supported by AFOSR, LLNL, ONR, and SDI.

† permanent address: Theoretical Division, MS–B210, Los Alamos National Laboratory, Los Alamos, NM 87545

References and Notes

1. A. V. Vinogradov and I. I. Sobel'man, "The Problem of Laser Radiation Sources in the Far Ultraviolet and X–Ray Region," Sov. Phys.–JETP 36, 1115 (1973).
2. C. K. Rhodes, "Physical Processes at High Field Strengths," Physica Scripta T17, 193 (1987).
3. C. K. Rhodes, "Multiphoton Ionization of Atoms," Science 229, 1345 (1985).
4. W. B. Mori, C. Joshi, J. M. Dawson, D. W. Forslund, and J. M. Kindel, "Evolution of Self–Focusing of Intense Electromagnetic Waves in Plasma," Phys. Rev. Lett. 60, 1298 (1988).
5. G.–Z. Sun, E. Ott, Y. C. Lee, P. Guzdar, "Self–Focusing of Short Intense Pulses in Plasmas," Phys. Fluids 20, 526 (1987).
6. Ya. L. Bogomolov, S. F. Lirin, V. E. Semenov, and A. M. Sergeev, "Ionization Self–Channeling of Extremely Intense Electromagnetic Waves in a Plasma," Pis'ma Zh. Eksp. Teor. Fiz. 45, 532 (1987) [Engl. transl.: Sov. Phys. – JETP Lett. 45, 680 (1987)].
7. J. C. Solem, T. S. Luk, K. Boyer, and C. K. Rhodes, "X–Ray Amplification with Charge–Displacement Self–Channeling," Phys. Rev. Lett., submitted.
8. P. L. Kelley, "Self–Focusing of Optical Beams," Phys. Rev. Lett. 15, 1005 (1965).
9. The Compton intensity is given by $I_{CO} = m\omega^2 c/4\pi\lambda\!\!\!^{-}_C\alpha$ with $\lambda\!\!\!^{-}_C$ the Compton wavelength of the electron and α the fine structure constant. The intensity is defined by the condition that the average nonrelativistically calculated quiver speed of the electron be equal to the speed of light.
10. K. Boyer, G. Gibson, H. Jara, T. S. Luk, I. A. McIntyre, A. McPherson, R. Rosman, J. C. Solem, and C. K. Rhodes, "Strong–Field Processes in the Ultraviolet Region," this volume.
11. K. Boyer, H. Jara, T. S. Luk, I. A. McIntyre, A. McPherson, R. Rosman, and C. K. Rhodes, "Limiting Cross Sections for Multiphoton Coupling," Revue Phys. Appl. 22, 1793 (1987).

Appendix B: Statement of Work

NRL
STATEMENT OF WORK
FOR
MCR TECHNOLOGY CORPORATION
PHASE II SBIR

1. Background

Advances in x-ray imaging technology and x-ray sources are such that a new technology enabling the microvisualization of condensed materials can be brought to commercialization. In order to accomplish this goal, further development of the computational technology of holographic image reconstruction and corresponding aspects of source technology, particularly concerning the spatial control of the energy deposition, are needed. This Phase II SBIR is directed at these objectives.

2. Scope

This is an SBIR Phase II contract, therefore it is anticipated that a commercially viable product will be developed under this contract.

3. Applicable Documents

None.

4. Requirements

Development of a high brightness x-ray source for directed energy and holographic imaging applications.

4.1.1A The contractor shall develop advanced algorithms for multidimensional holographic reconstruction from a holographic microscope operating in the visible, but able to simulate the parameters of an x-ray holographic microscope. This task to be performed in conjunction with a subcontract to Robotronix, Inc.

4.1.1B The contractor shall explore techniques for low resolution optical reconstruction of selected portions of the hologram as a means for rapid screening of data prior to numerical reconstruction.

4.1.1C The contractor shall begin the technological developments that will enable the performance of experimental studies to examine channeled propagation in capillaries with N_2 serving as the medium. In these studies, the contractor shall place emphasis on (1) the launching of the wave in the capillary and (2) determining the relationship governing the length of propagation that can be achieved and the density of the medium. This task to be performed on a subcontract basis with the University of Illinois at Chicago.

4.1.1D In conjunction with a subcontract to Robotronix, the contractor shall develop supporting theoretical capability for the analysis of the experiments being performed for in task 4.1.1C. The contractor shall place particular emphasis on (1) the dynamics of channel formation and (2) channel stability.

4.1.1 Deliverable products

Preprints of any articles submitted to Journals for Publication, which cover any of the work under this contract. A letter type or formal progress report.

4.1.2 **Schedule**
Tasks 4.1.1A -- 4.1.1D are to be completed twelve months after start of work.

4.2.1A The contractor shall design, build, test and operate a holographic microscope operating in the visible region suitable for simulation of the parameters governing the x-ray holographic application.

4.2.1B The contractor shall continue development of the algorithms of task 4.1.1A.

4.2.1C The contractor shall evaluate techniques for microfabrication of target systems for both visible wavelength simulation and x-ray exposures.

4.2.1D The contractor shall continue the development of the low resolution optical reconstruction techniques started in task 4.1.1B.

4.2.1E The contractor shall continue the experiments noted in task 4.1.1C.

4.2.1F The contractor shall experimentally explore the possibility of self channeling in N_2. The contractor shall evaluate the suitability of other materials, both atomic and molecular, for the generation of considerably shorter wavelengths. This task to be performed on a subcontract basis with the University of Illinois at Chicago.

4.2.1G The contractor shall continue the theoretical developments of 4.1.1D.

4.2.1H The contractor shall develop a prototype of the target conversion system based on the work of tasks 4.1.1C, 4.1.1D, 4.2.1E, and 4.2.1F.

4.2.1 **Deliverable products**
Preprints of any articles submitted to Journals for Publication, which cover any of the work under this contract. A final report containing designs, calculations, source code of and users guide for any software developed wholly under this contract, drawings, cost estimates, test plans and conclusions resulting wholly from tasks 4.1.1A – 4.1.1D and 4.2.1A – 4.2.1H.

4.2.2 **Schedule**
Task 4.2.1A – 4.2.1H to be completed twenty-four months after start of work.

5. **Progress reports**
The contractor shall submit a letter type or formal progress report at the end of twelve months and a final report by the end of twenty-four months, in addition, as directed by the COTR, the contractor shall submit viewgraphs and other material for use in program reviews.

STATEMENT OF WORK REVISIONS

Tasks 4.2.1B, 4.2.1D, 4.2.1E and 4.2.1G are revised to read as follows:

4.2.1B The contractor shall develop the algorithms of task 4.1.1A.

4.2.1D The contractor shall develop the low resolution optical reconstruction techniques started in task 4.1.1B.

4.2.1E The contractor shall do the experiments noted in task 4.1.1C.

4.2.1G The contractor shall do the theoretical developments of 4.1.1D.

APPENDIX C

FOURIER TRANSFORM HOLOGRAPHIC MICROSCOPE

Waleed S. Haddad, David Cullen, Johndale C. Solem, James W. Longworth,

Armon McPherson, Keith Boyer and Charles K. Rhodes

MCR Technology Corporation

P. O. Box 10084, Chicago, IL 60610–0084

ABSTRACT

We describe a holographic microscope with spatial resolution approaching the diffraction limit. The instrument uses a tiny drop of glycerol as a lens to create the spherically diverging reference illumination necessary for Fourier–transform holography. Measurement of the point–spread function, obtained by imaging a knife edge in dark–field illumination, indicates a transverse resolution of 1.4 μm with wavelength λ = 514.5 nm. Longitudinal resolution was obtained from the holograms by the numerical equivalent of optical sectioning. We describe the method of reconstruction and demonstrate the microscope's capability with selected biological specimens. The instrument offers two unique capabilities: (1) it can collect three–dimensional information in a single pulse of light, avoiding specimen damage and bleaching; and (2) it can record three–dimensional motion pictures from a series of light pulses. The conceptual design is applicable to a broad range of wavelengths and we discuss extension to the x–ray regime.

Key Words: Microholography, Fourier–Transform Microholography, Biological Samples, Glycerol Microdrop, Resolution, Numerical Reconstruction Reference Scatterer

---

* Submitted to Applied Optics, 22 April 1991, revised 21 January 1992

I. INTRODUCTION

Although Gabor invented holography[1] with microscopy applications in mind[†], the problem of recording medium resolution[2] was not solved until the introduction of the Fourier transform[3] technique. Shortly after the technique was proposed, Leith and Upatnieks[4] attempted Fourier–transform microholography and were able to resolve a bar pattern spaced at 7 – 10 μm using a 632.8 nm laser. Although their report is sketchy, VanLigten and Osterberg[5] claimed an optimum resolution of detectability of 12 μm and very serious difficulties in obtaining a resolution of ~ 5 μm. Their holographic microscope formed a hologram from a pre–magnified image rather than using the Fourier method. Apparently because initial results were disappointing, visible–light Fourier–transform microholography was generally abandoned. Most papers[6] of the 70's and 80's are concerned with its application to x–ray microscopy.

In the present work, we describe an instrument that is capable of resolution approaching the diffraction limit. The camera design discussed herein represents a new technology for three–dimensional visualization that is applicable to a spectral range spanning from visible (~ 700 nm) to x–ray (~ 0.6 nm) wavelengths. Descriptions of the Fourier–transform technique, biological target design and related numerical reconstruction simulations have been given in previous work.[7] The new camera system has been operated with visible radiation (λ = 514.5 nm) from an argon–ion laser. The experiments in the visible region have enabled the imaging properties of the camera to be studied and optimized as well as demonstrating that this camera design can be employed for applications in embryology where three–dimensional information is of particular value.

[†] The original concept was for lensless electron microscopy.

II. MICROHOLOGRAPHY WITH VISIBLE RADIATION

A. Camera Design

Figure (1) is a schematic of the microholographic camera. The target holder is positioned horizontally so gravity will hold the sample and a glycerol droplet in place. A side view schematic of the target design used for visible light exposures is shown in Fig. (2). The glycerol droplet proved to be a superb lens for generating the reference illumination. It can spread the illumination to the large angles necessary for good resolution and can be placed very close to the specimen. Furthermore, its size can be varied to match the reference intensity to the intensity of radiation scattered from the specimen.

The basic functions of the camera, such as shutter timing and triggering, are controlled by a personal computer (PC). The holograms are recorded electronically, digitized and stored by the PC. The holographic data are then transferred by an ethernet link to a Stardent GS 2000 supergraphic work station where the numerical image reconstruction is performed. The reconstructed image can then be manipulated, scaled, and checked for three–dimensional information and displayed on a high resolution graphics monitor.

The holograms were registered on a customized charge–coupled device (CCD) having a sensitive area of 18.43 mm x 18.43 mm containing 2048 x 2048 square pixels each with a dimension of 9 μm. To protect the CCD from the direct laser beam, we installed a cover glass with a central opaque square.

B. Liquid Microdrop Lenses

The drop of glycerol is placed on the microscope cover slide, close to the edge of the sample and nearest the region of interest in the sample, as shown in Fig. (2). The droplet acts as a lens intercepting a portion of the illuminating plane wave front and converting it into a diverging, nearly spherical wave. The

focal point of this lens acts as the point source of reference illumination. Glycerol is a particularly suitable liquid for the microdrops because of its low vapor pressure, high surface tension, and polarity. To improve the characteristics of the microdrops, it is often necessary to pre–coat the glass cover slide with a thin layer of silicone. Dricote, a standard anti–wetting agent for PH electrodes, proved to be adequate for this purpose. Both the reduced wetting and the surface tension help the glycerol to form a round lens with a relatively short focal length. This conveniently produces a system with a low f number. The microdrop of glycerol is positioned on top of the sample cover slide so that the illuminating beam first impinges on the object, then on the microdrop ~ 200 μm closer to the detector. Since the microdrop is a positive lens, the reference point source is formed even closer to the detector. The transverse and longitudinal resolution of the camera system is dependent on the angular aperture subtended by the hologram. Consequently, it is necessary that the cone angle of the diverging reference and object waves be large enough to produce interference over an aperture which is sufficient to give the desired resolution in the image. Hence, the f number of the microdrop lens determines the usable f number of the camera

The microdrops are formed using a glass micropipette which is mounted on an X–Y–Z micropositioner. The sample and micropipette tip are viewed through a dissecting microscope while manipulating the micropipette into position with the micropositioner. When the tip of the micropipette has been positioned properly, it is brought almost in contact with the glass slide. A slight pressure at the back of the pipette dispenses the desired quantity of glycerol. The tip is then slowly lifted away from the slide, allowing the droplet to form.

The droplet size is an important factor in the formation of a good hologram because it is primarily the diameter of the drop that determines the brightness of

the reference wave. The larger the diameter of the drop, the larger the portion of the illuminating wavefront which is intercepted, and consequently, the brighter the reference wave. In order to form a hologram with a good signal–to–noise ratio[6], it is necessary to have the reference wave brightness approximately equal to the object wave brightness. Depending on the type of object being imaged, we have used microdrops ranging between 20 and 200 μm in diameter.

C. Numerical Reconstruction

For the sake of clarity, it is necessary to define a series of parallel planes: (1) the hologram plane is the sensitive surface of the CCD; (2) the reference plane contains the focal point of the droplet; and (3) an object plane is any plane we wish to reconstruct, generally a plane intersecting the specimen.

The basic method of image reconstruction used for all results presented in this article is a fast Fourier transform (FFT). However, some pre–processing of the holographic data is performed in order to form the best image. Since the hologram contains three–dimensional data, a specific object plane must be chosen as the focal plane for the reconstructed image. If an FFT is performed on the raw holographic data, the object plane will be the same as the reference plane. Therefore, the hologram formed in the Fourier–transform geometry can be thought of as containing an implicit lens which causes it to form a focused image at the reference plane. If a different object plane is chosen, it is necessary to add a second lens to the hologram such that the combined action of the implicit lens and the additional lens cause the image to be in focus at the desired object plane. This second lens can be added numerically by multiplying the hologram by a phase factor ϕ given by

$$\phi\ (x,y) = \exp\left[i\pi\ \frac{x^2 + y^2}{\lambda f_a}\right], \qquad (1)$$

where x and y are coordinates in the hologram plane whose origin is at the center of the hologram and f_a is the desired focal length of the additional lens. The focal length a can be determined from knowledge of the position of the reference plane and the position of the desired object plane by[8]

$$f_a = \frac{bc}{b - c} \tag{2}$$

where b is the distance from the reference plane to the hologram plane and c is the distance from the object plane to the hologram plane.

The next preprocessing step is to numerically clip the corners of the hologram and remove the central region, thus converting the originally square hologram into an annulus. Removal of these portions of the data reduces noise in the reconstructed image and invcives a negligible loss of image quality. The holographic data are also scaled and converted to a floating point format prior to performing the FFT.

Post–processing of the reconstruction can also improve the quality of the image. First, the central portion of the image is eliminated, since it contains only a reconstruction of unwanted scattering sources on or near the reference point source and is overwhelmingly bright. Secondly, the image brightness can be rescaled. The best images are given by the power spectrum of the holographic data, namely, the natural log of the sum of squares of the real and imaginary parts of ... Fourier transform. The image data must then be converted from floating point to integer format for display.

D. Resolution

We measured the microholograph transverse resolution by direct observation of the spread in the image of a very fine line, i.e., the transverse point spread function. The line was produced by side illumination of a sharp edge, specifically, the edge of one of the figures in a microscope test reticle. The image of this

edge appears as a line because, for the camera geometry presented here, only light scattered by the object is collected to form an image (a form of dark–field illumination). The width of this line as observed at high magnification with the same sort of dark–field illumination in a compound microscope, was seen to be much less than 1 μm. The hologram of the line was recorded and reconstructed in the usual manner. An intensity distribution at a representative cross section perpendicular to the line was then generated at small spatial increments. This intensity distribution is shown in Fig. (3). Remarkably, the full width at half maximum is about 1.40 μm, less than three times the wavelength.

The standard expression for diffraction limited resolution of a microscope is:

$$\delta = \frac{1.22\ \lambda}{2n \sin \theta} \qquad (3)$$

where (n sin θ) is the numerical aperture (N.A.) of the imaging system. This expression is valid since, for the camera geometry described herein, the hologram fringe spacing is always greater than the pixel size of the detector, and hence, the image resolution is not limited by the detector pixel size. In this case, the refractive index is n = 1, and at f/2 the N.A. = 0.24. Thus, using Eq. (3), δ = 1.29 μm. This compares favorably with our measured value for the point spread function of 1.40 μm.

E. Image Reconstructions

Although we have examined a wide variety of specimens, we show here an image of a **Parascaris univalens** (Ascaris) larva because it demonstrates several of the capabilities of our microholograph simultaneously.

Figure (4) shows the reconstructed image from a hologram taken at f/2 of a section of the Ascaris larvae in its maturation stage. Since this sample is not a strong scatterer, the reference microdrop had to be only ~ 25 μm in diameter in

order to make the reference wave and object wave brightness comparable. Visible in the image is the cuticle of the Ascaris as well as individual cells. Cell walls are clearly visible and in some cells nuclear structure is evident.

A detailed section of the Ascaris containing 10^6 spatial resolution elements (10^2 x 10^2 x 10^2) in the volume is shown in Fig. (5) for four different positions in depth of the focal plane. The set of 100 slices was reconstructed from a single hologram. The spatial range covered by the full set of 100 slices (depth-wise) is 72 μm; consequently, each slice is separated by 0.72 μm. However, the actual thickness of the sample is ~ 15 – 16 μm as measured with a research-grade compound microscope. The two slices shown in Fig. (5b) and (5c) represent the lower and upper surfaces of the sample, respectively, and are separated by 16.56 μm. Figure (5a) and (5b) correspond to focal planes well below and above the boundaries of the object. For Fig. (5a) the focal plane is 24.48 μm below Fig. (5b), and for Fig. (5d) the focal plane is 24.48 μm above Fig. (5c). This is because longitudinal blurring of the image introduces ambiguities which can be partially alleviated by focusing well outside the sample volume. This quality of longitudinal resolution is comparable to what we observe with a compound microscope with an 0.25 N.A. (~ f/2) objective.

Blurring of the image is primarily due to two factors: (1) a longitudinal spatial resolution which is lower than that governing the transverse coordinates and (2) aberration from coma that is inherent in the use of a Fourier-transform for image reconstruction. The changing character of the image is clear. The central nuclear region is visible and the structure in the double wall can also be seen. These features vary with the frame shown, since they change with depth. We have found that a video representation assembled from the separate 100 slices, which shows the continuous variation of these images, is a more informative

method to demonstrate the three dimensional character of the microholographic camera.

Those familiar with the lore of holographic microscopy will note that our reconstructions are conspicuously devoid of speckle. Speckle is not a problem with dark-field illumination because the image is produced by scattered light.

III. CONCLUSION

A microholographic camera capable of three-dimensional imaging has been constructed, tested and applied to the imaging of biological materials. This system has recorded holograms of test patterns and biological specimens with transverse resolutions near the diffraction limit at f/2 with 514.5 nm light. The three dimensional character of the recorded images has also been demonstrated. This instrument can be directly applied to imaging in the x-ray range when suitable sources become available.

IV. ACKNOWLEDGEMENTS

This research was supported in part by the Department of Energy (DoE) under Grant #DE-FG02-86ER13610 and #DE-FG02-89ER60898, and by the National Cancer Institute (NCI) under grant number 1 R43 CA53917-01. Such support does not constitute an endorsement by DoE or NCI of the views expressed in this article. Additional support by the SDIO/IST and managed by NRL, under SBIR contract #N00014-89-C-2274 is acknowledged. Support by Eastman Kodak Company and Maxwell Laboratories is also acknowledged.

V. REFERENCES

1. D. Gabor, "A New Microscopic Principle", Nature 161, 777–778 (1948); D. Gabor, Proc. R. Soc. London Ser. A197, 454–487 (1949).

2. G. Stroke, "Attainment of High Resolutions in Image–Forming X–Ray Microscopy with 'lensless' Fourier–Transform Holograms and Correlative Source–Effect Compensation", **Optique des Rayons X et Microanalyse** (Hermann, Paris, 1966), p. 30–46.

3. J. Winthrop and C. Worthington, "X–Ray Microscopy by Successive Fourier Transformation," Phys. Lett. 15, 124–126 (1965); G. Stroke and R. Restrick, "Holography with Spatially Noncoherent Light", Appl. Phys. Lett. 7, 229–230 (1966); G. Stroke and D. Falconer, "Attainment of High Resolutions in Wavefront Reconstruction Imaging – II," J. Opt. Soc. Am. 55, 595 (1965).

4. E. Leith and J. Upatnieks, "Microscopy by Wavefront Reconstruction", J. Opt. Soc. Amer. 55, 569 (1965); E. Leith, J. Upatnieks, and A. Vander Lugt, "Hologram Microscopy and Lens Aberration Compensation by the Use of Holograms", J Opt. Soc. Amer. 55, 595 (1965).

5. R. VanLigten and H. Osterberg, "Holographic Microscopy", Nature 211, 282–283 (1966).

6. J. C. Solem, G. C. Baldwin, and G. F. Chapline, "Holography at X–Ray Wavelengths," in Proc. of Intl. Conference on Lasers 1981 (STS Press, McClean, VA. 1981) pp. 296–235; J. C. Solem and G. C. Baldwin, "Microholography of Living

Organisms," Science 218, 229–235 (1982); J. C. Solem and G. F. Chapline, "X-Ray Biomicroholography," Opt. Engineering 23, 193–203 (1984); I. McNulty, J. Kirz, C. Jacobsen, M. R. Howells, and E. H. Anderson, "First Results with a Fourier Transform Holographic Microscope," in X-Ray Microscopy III, A. G. Michette et al., eds. (Springer-Verlag, Berlin, 1991), to be published.

7. W. S. Haddad, D. Cullen, K. Boyer, C. K. Rhodes, J. C. Solem and R. S. Weinstein, "Design for a Fourier-Transform Holographic Microscope," in X-Ray Microscopy II, D. Sayre, M. Howells, J. Kirz and H. Rarback, eds. (Springer-Verlag, Berlin, 1988) pp. 284–287; W. S. Haddad, J. C. Solem, D. Cullen, K. Boyer, and C. K. Rhodes, "A Description of the Theory and Apparatus for Digital Reconstruction of Fourier Transform Holograms," in Electronics Imaging '87, Advanced Printing of Paper Summaries, Vol. II (Institute for Graphic Communication, Inc., Boston, 1987) pp. 683–688; W. S. Haddad, D Cullen, J. C. Solem, K. Boyer, and C. K. Rhodes, "X-Ray Fourier-Transform Holographic Microscope," in Short Wavelength Coherent Radiation: Generation and Applications, Vol. 2, R. W. Falcone and J. Kirz, eds. (Optical Society of America, Washington, D.C., 1988) pp. 284–289.

8. F. A. Jenkins and H. E. White, in Fundamentals of Optics, Fourth Edition (McGraw-Hill, New York, 1976) pp. 71–72.

FIGURE CAPTIONS

Fig. (1): Schematic of Fourier–transform microholographic camera configured for operation in the visible range.

Fig. (2): Side–view schematic of the target system prepared for visible microholography.

Fig. (3): Transverse point spread function (PSF) measured by imaging the edge of a microscope test reticle. The curve is comprised of 250 data points reconstructed with a transverse spacing of 10 nm.

Fig. (4): Reconstructed image of an Ascaris in maturation stage. Visible are the cuticle and individual cells. Cell diameter is ~ 40 μm. The nuclear region visible within some cells is ~ 20 μm in diameter.

Fig. (5): Local region of Ascaris image involving 10^6 resolution elements (10^2 x 10^2 x 10^2). The region is centered around one cell adjacent to the cuticle. Features arising from the depth resolution are visible as the focal plane is positioned at different depths (a) – (d). See text for discussion.

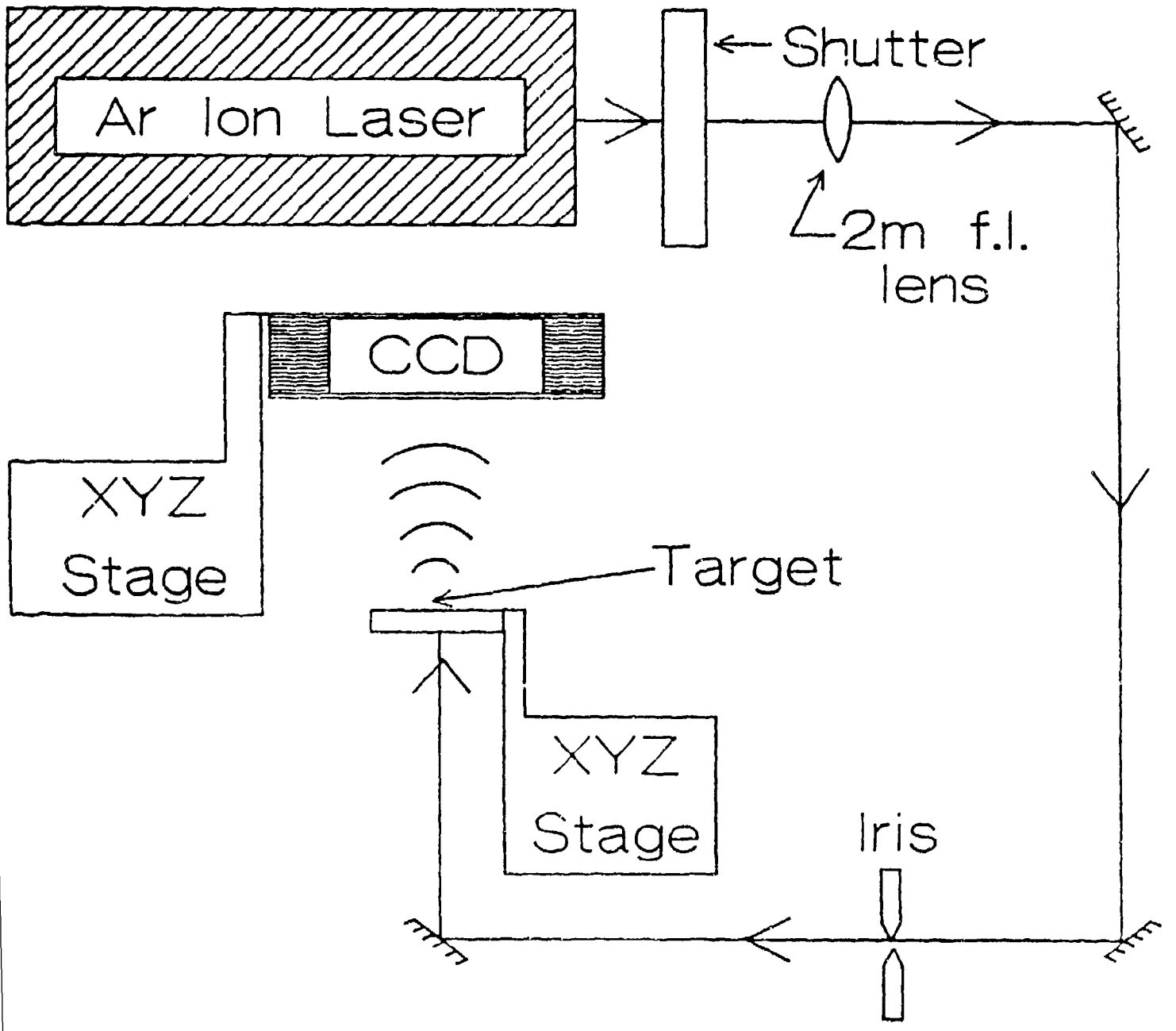
Ar Ion Laser
Shutter
2m f.l.
lens
CCD
XYZ
Stage
Target
XYZ
Stage
Iris

FIGURE (1)

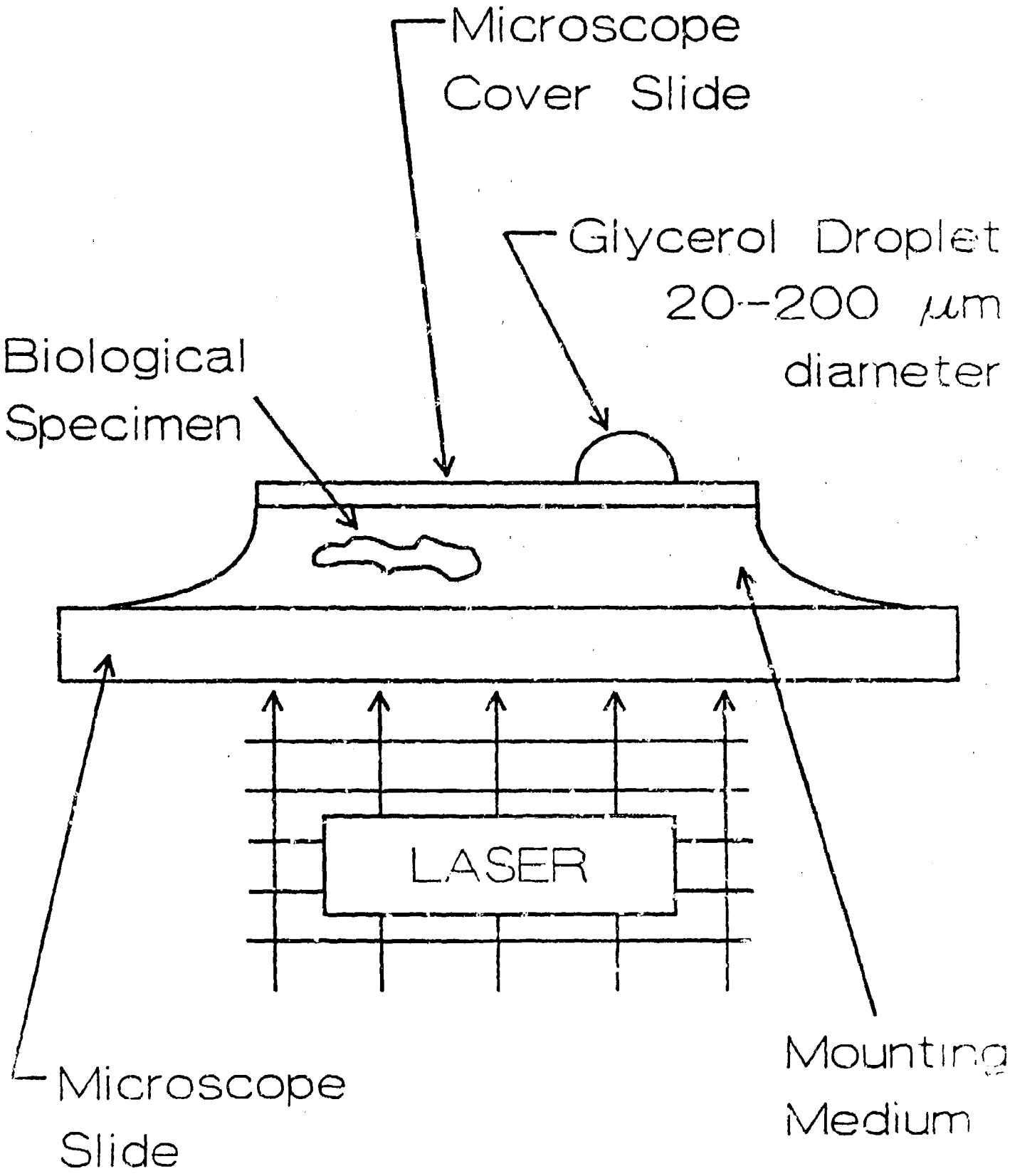
Microscope
Cover Slide
Glycerol Droplet
20--200 μm
diameter
Biological
Specimen
LASER
Microscope
Slide
Mounting
Medium

FIGURE (2)

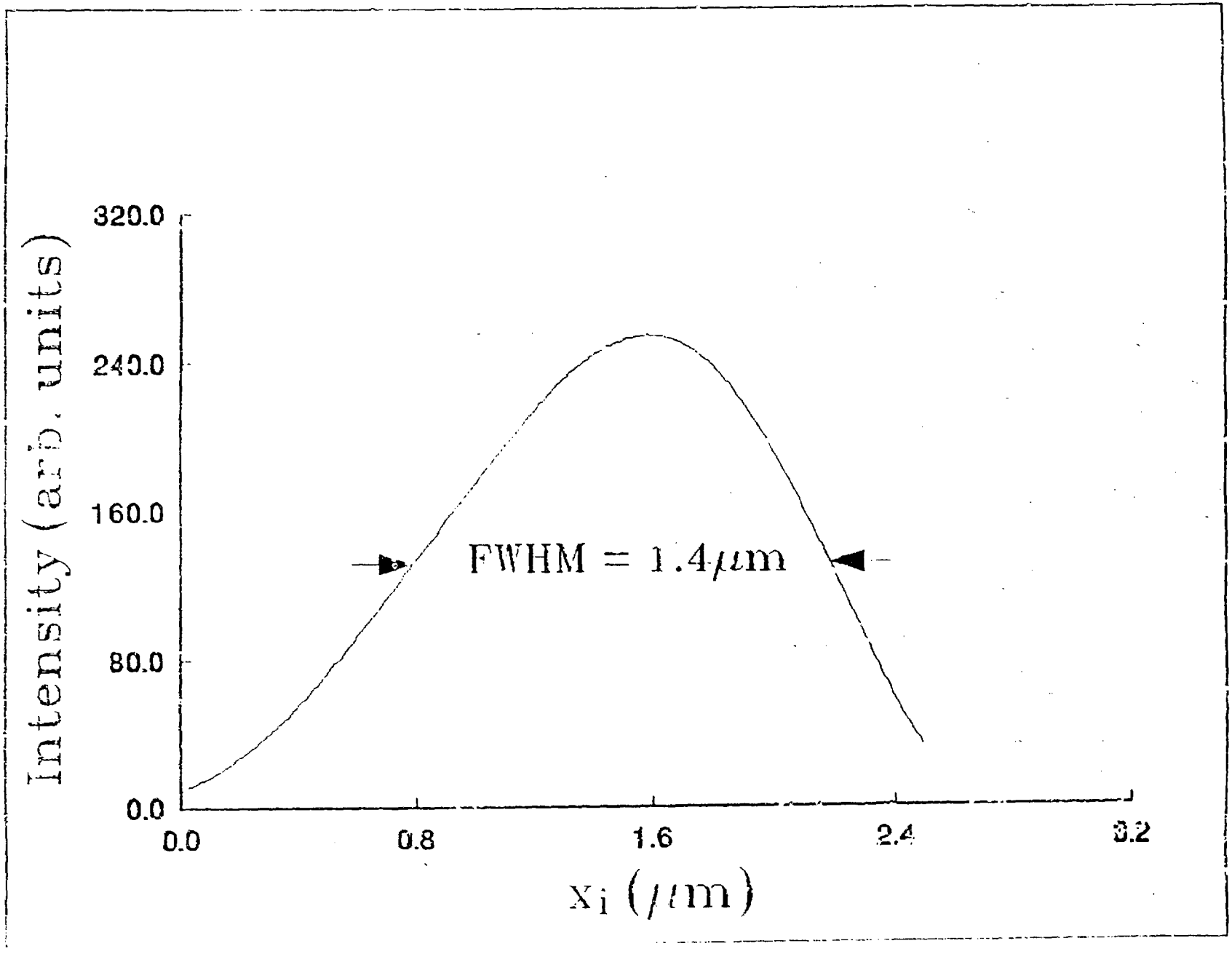
320.0
240.0
160.0
80.0
0.0
Intensity (arb. units)
FWHM = 1.4μm
0.0
0.8
1.6
2.4
3.2
x_i (μm)

FIGURE (3)

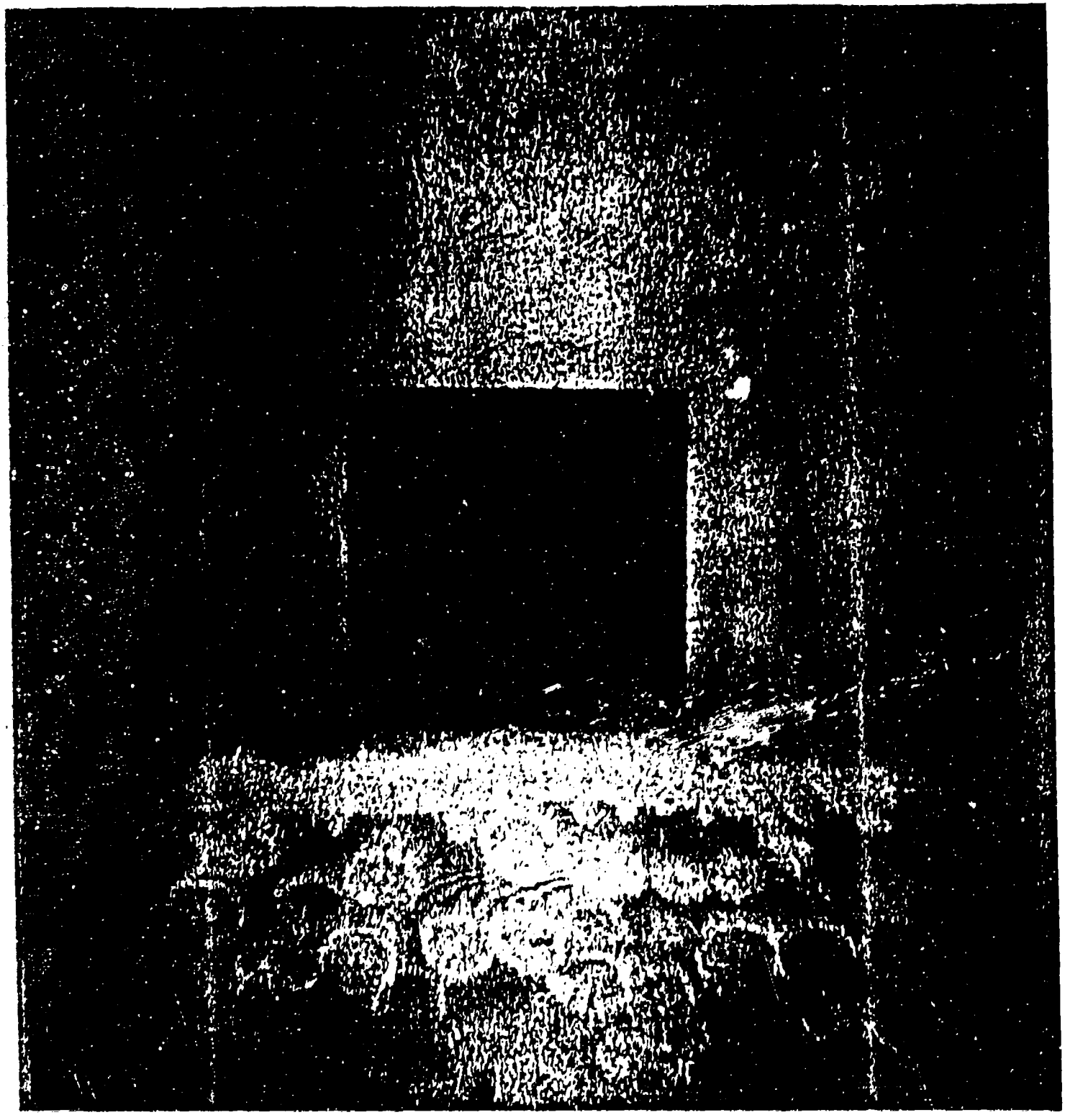

FIGURE (4)

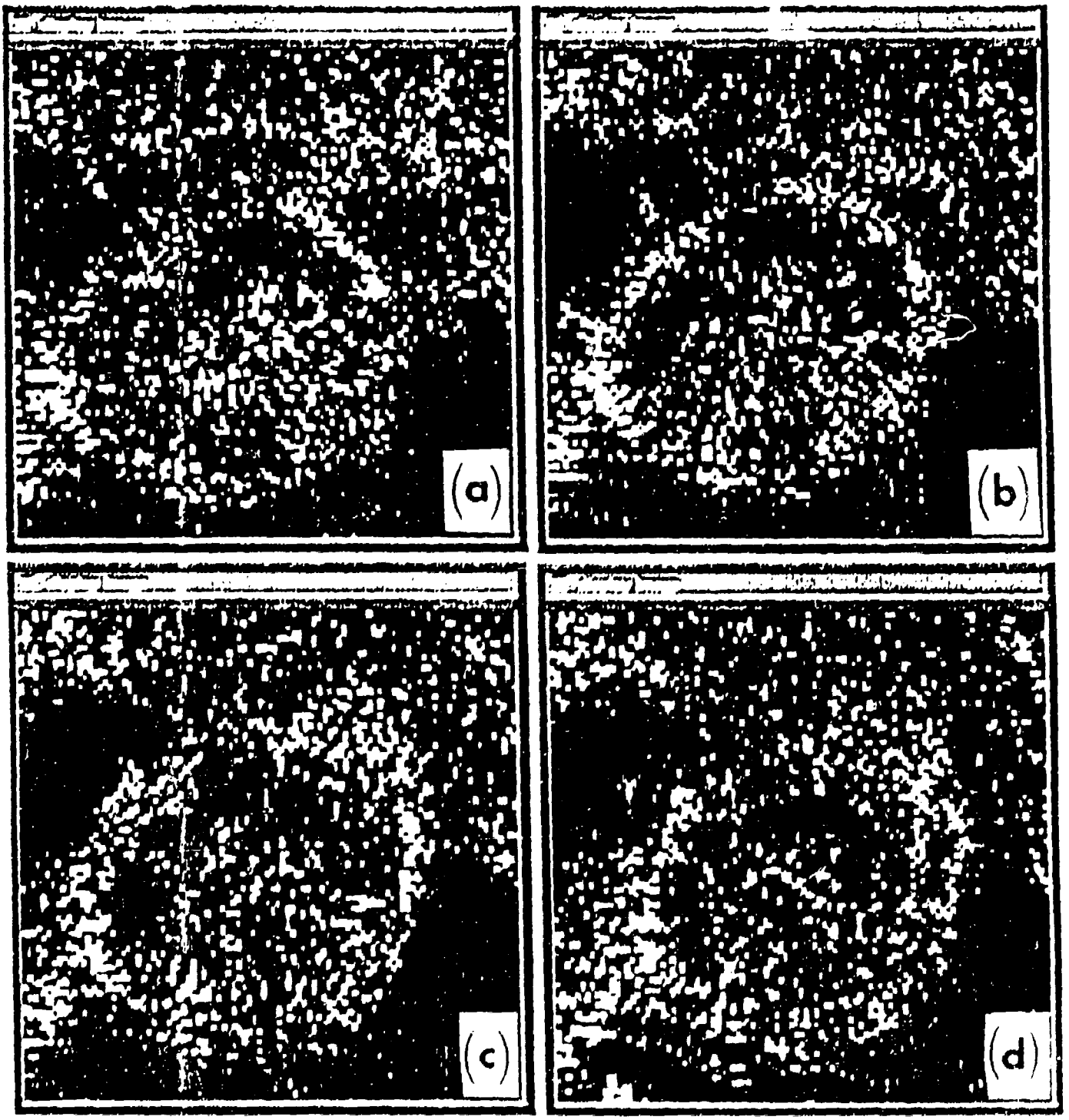

FIGURE (5)

APPENDIX D

Fourier-transform holographic microscope*

W.S. Haddad, D. Cullen, J.C. Solem, J. W. Longworth,
A. McPherson, K. Boyer, and C.K. Rhodes

MCR Technology Corporation
P.O. Box 10084, Chicago, IL 60610-0084

1. ABSTRACT

A camera system suitable for microholography has been constructed, tested, and applied to the imaging of biological materials. The design of this instrument is compatible with operation over a very wide spectral range spanning from visible to x-ray wavelengths. In order to evaluate its properties, visible light Fourier transform microholograms of biological samples and other test targets have been recorded and digitally reconstructed using a glycerol microdrop as a reference wave scatterer. Current results give a resolution of ~ 4 λ with λ = 514.5 nm.

2. INTRODUCTION

Advances in high speed computation and electronic detection have accelerated the development of practical instruments for microholography. The concept discussed herein promises a new technology for three-dimensional visualization of condensed matter that is applicable to a spectral range spanning from visible (~700 nm) to x-ray (~ 0.6 nm) wavelengths. Several important results in this area have already been achieved by Howells et al.[1], D. Joyeux and F. Polack[2], McNulty et al.[3], J. C. Solem et al.[4-6], and London et al.[7].

Descriptions of the Fourier-transform system, target design, and related numerical simulations have been given in previous work[8-10]. Tests of the operation of the system, which have enabled the details of its imaging properties to be studied, have been performed with visible radiation. The experiments in the visible region, in addition to allowing optimization of the instrument, have independently demonstrated that this is an attractive technique for visualizations in fields such as embryology where three-dimensional information is of particular interest.

3. VISIBLE LIGHT MICROHOLOGRAPHY

3.1. Apparatus

A schematic for the holographic microscope, configured for operation with visible radiation is shown in Fig. (1). The beam path through the target is vertical so that the target holder is horizontal and gravity can be used to hold the sample and reference wave scatterer in place. Several objects have been used as reference wave scatterers. These include GRIN rod lenses, glycerol microdrops, and reflecting microspheres. The microspheres represent the optimum choice for use with soft x-rays[4,6], and the corresponding x-ray target design is described elsewhere[10]. Glycerol microdrops have performed very well in experiments with visible light. A magnified side view schematic of the target used for visible light exposures is shown in Fig. (2).

The basic functions of the apparatus, such as shutter timing and triggering, are controlled by a P.C. The holograms are recorded electronically, digitized, and stored by the P.C. The data are then transferred by an ethernet link to a Stardent GS 2000 supergraphic workstation where the image reconstruction is performed numerically. The reconstructed image can then be manipulated, scaled, and displayed on a high resolution graphics monitor. A schematic of this computer system is shown in Fig. (3).

* manuscript submitted for the SPIE/SPSE's Symposium on Electronic Imaging: Science & Technology, 24 February - 1 March 1991, San Jose, CA, to be published in the Proceedings of the Symposium on Electronic Imaging: Science and Technology, SPIE, Bellingham, WA.

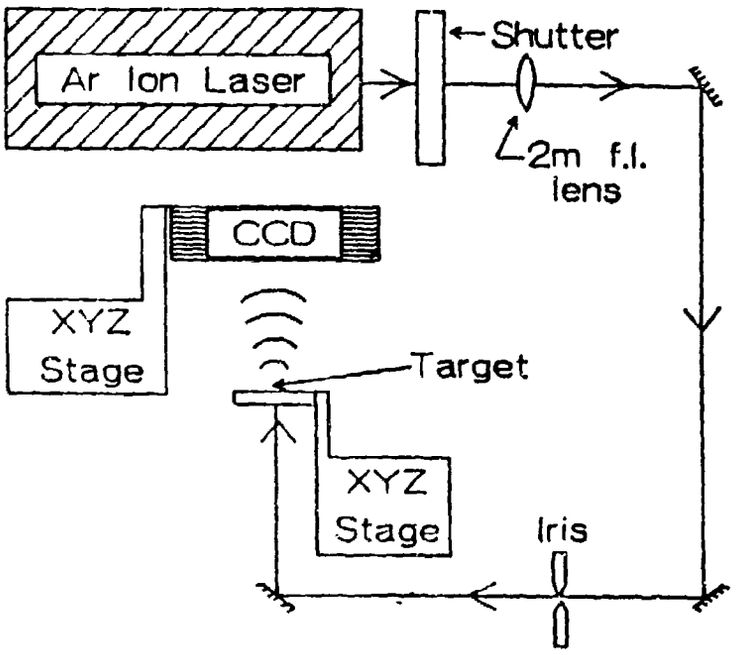

Fig. (1): Schematic of apparatus for visible/UV Fourier-transform microholographic microscope configured for operation in the visible range.

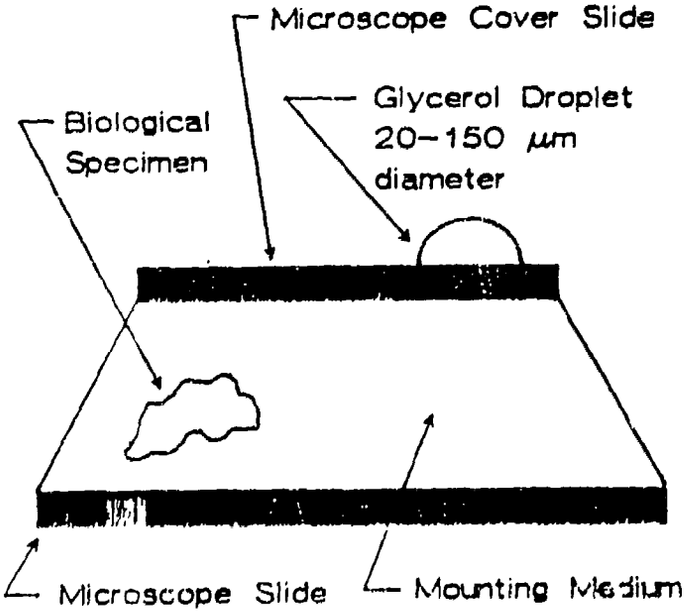

Fig. (2): Magnified side-view schematic of the target system prepared for visible microholography

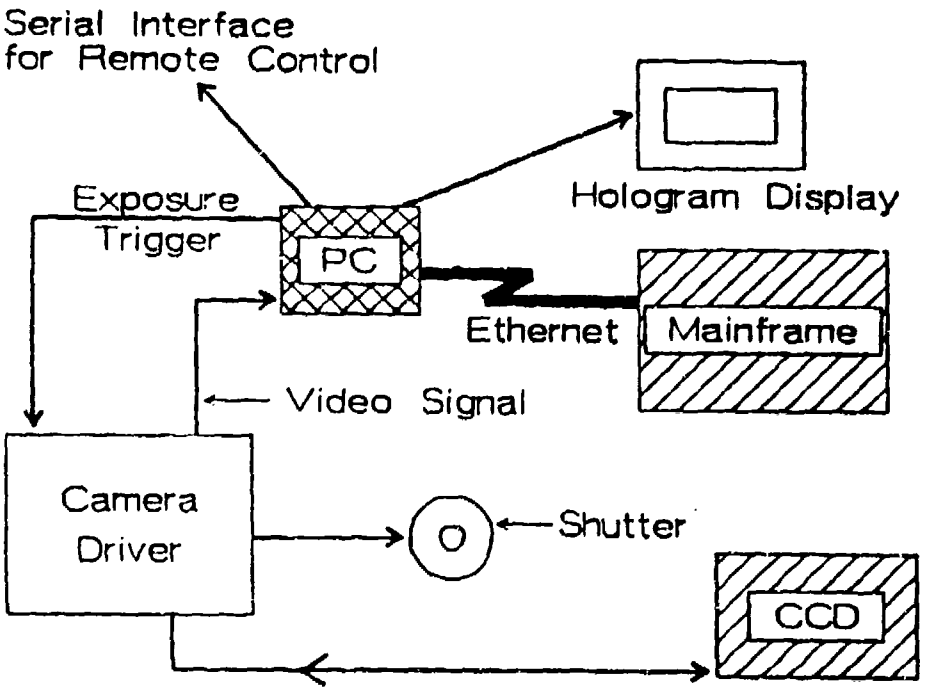

Fig. (3): Diagram of computer system and electronics for acquisition and reconstruction of microholograms.

3.2. Hologram detector

The holograms are recorded on a charge-coupled device (CCD). The chip has a sensitive area of 18 mm x 18 mm containing ~ 4 x 10^6 pixels (2048 x 2048). The pixels are square with a dimension of 9 μm. For these experiments, a protective window is placed over the CCD which carries a small central opaque square serving as a blocker for the unscattered incident beam. Specially modified drive electronics were designed for this system including a separate headboard which carries the CCD and allows for remote mounting of the detector. Access through the headboard to the back of the CCD also is available to permit cooling of the chip. The pixel clock rate (data readout rate) has also been reduced from ~ 20 MHz to 2 MHz to allow the system to function well when cooled to ~ -40° C. Such cooling would allow direct integration of photons on the chip for periods of up to about one hour without a significant accumulation of dark counts.

3.3. Liquid microdrop lenses

A liquid microdrop of glycerol has been found to serve well as a reference wave scatterer for visible radiation. The drop is placed on the glass slide, close to the edge of the sample and nearest the region of interest in the sample, as shown in Fig. (2). The droplet acts as a lens intercepting a portion of the illuminating plane wavefront and converting it into a diverging, nearly spherical wave. The focal point of this lens acts as the reference point source. The imaginary plane parallel to the detector plane (hologram plane), and containing the reference point source, will be referred to as the reference plane. The object can be divided up into a series of planes (object planes) which lie parallel to the hologram plane. In most cases, the reference plane is located a significant distance away from the object planes. The usual situation is that the microdrop is placed on top of the sample coverslide, so that the illuminating beam

first impinges on the object, then a short distance later (~ 200 μm closer to the detector), the microdrop. Since the microdrop is a positive lens, the reference point source is then formed even closer to the detector.

Glycerol is a suitable material for the microdrops because of its low vapor pressure, high surface tension, and polarity. To improve the characteristics of the microdrops, it is often necessary to pre-coat the glass coverslide with a thin layer of silicone. Dricote, a standard anti-wetting agent for PH electrodes, has been found useful for this purpose. The reduced wetting and the viscosity help the glycerol form a round lens with a relatively short focal length. This produces a system with a low F number.

The microdrops are formed by the use of a glass micropipette. The micropipette is mounted on an X-Y-Z micropositioner and the operator views the sample and micropipette tip through a dissecting microscope while manipulating the micropositioner. When the tip has been positioned properly, it is brought almost into contact with the glass slide, and a slight pressure is put at the back of the pipette, thus dispensing the desired amount of liquid. The tip is then slowly brought vertically away from the slide, allowing the drop to form.

The droplet size is an important factor in the formation of a good hologram. This is because it is primarily the diameter of the drop that determines the brightness of the reference wave. The larger the diameter of the drop, the larger the portion of the illuminating wavefront which is intercepted, and therefore, the brighter the reference wave. In order to form a hologram with a good signal-to-noise ratio, it is necessary to have the reference wave brightness approximately equal to the object wave brightness. Depending on the type of object, we have used microdrops ranging between 20 μm and 200 μm in diameter.

3.4. Reconstruction technique

The method of image reconstruction used for all results presented in this article is basically a fast Fourier transform (FFT). However, some pre-processing of the holographic data is performed in order to form the best image. A specific plane parallel to the hologram plane must be chosen as the focal plane for the reconstructed image. This plane will be referred to as the image plane. If an FFT is performed on the raw holographic data, the image plane will be the same as the reference plane. Therefore, the hologram formed in the Fourier transform geometry can be thought of as containing a lens which causes it to form a focused image at the reference plane. If a different image plane is chosen, it is then necessary to add a second lens to the hologram such that the combined action of the implicit lens and the additional lens cause the image to be in focus at the desired plane. To do this, the hologram must be multiplied by a phase factor $L(x_h, y_h)$ given by

$$L(x_h, y_h) = e^{i\alpha(x_h^2 + y_h^2)},$$

where x_h and y_h are coordinates in the hologram plane whose origin is at the center of the hologram.

The next preprocessing step is to clip the corners of the hologram and remove the dark region, thus converting the originally square hologram into an annulus. Removal of these portions of the data reduces noise in the reconstructed image without loss of image information. The holographic data are also scaled and converted to a floating point format prior to performing the FFT.

Post processing of the reconstruction can also improve the quality of the image. First, the central portion of the image is eliminated, since it contains only a reconstruction of the unscattered beam and would be overwhelmingly bright. Secondly, the image brightness can be

re-caled. The best images are given by the "power spectrum" of the holographic data, namely, the natural log of the sum of squares of the real and imaginary parts of the Fourier transform. The image data must then be converted from floating point to integer format for display.

3.5. Results of image reconstructions

3.5.1. Swordtail melanoma

All the holograms described below were produced with the use of 514.5 nm radiation from an argon ion laser. Figure (4) shows a hologram of swordtail (Xiphophorus maculatus x helleri) malignant melanoma and the reconstructed image. Also shown are images taken with a standard low power optical microscope with both white light and laser illumination. Clearly visible in Fig. (4a) is the ~ 130 μm glycerol droplet used to produce the reference wave. This sample was provided to us by R. B. Setlow of Brookhaven National Laboratory.

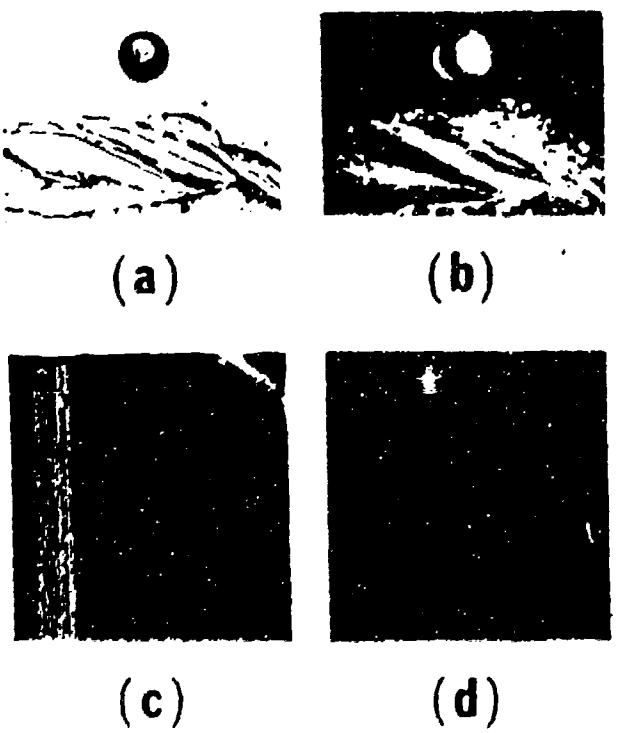

Fig. (4): Fish melanoma histological sample with glycerol microdrop reference wave source. (a) Image of the target taken with a standard optical microscope and white light illumination (b) Same as (a) except with Ar^+ (514.5 nm) laser illumination. (c) Digital recording of hologram. (d) Numerical reconstruction of the image; resolution ≈ 4 μm.

3.5.2. Air Force target

Figure (5) is a reconstructed image from a hologram of a U.S. Air Force resolution target. The full reconstruction is shown in Fig. (5a), and a zoomed image of the region containing the smallest features is shown in Fig. (5b). These slots have width equal to the slot spacing and for the smallest, this dimension is ~ 2 μm. Since the features of the target are holes in a metallic coating, they scatter the incident radiation by diffraction. Therefore, it is only the edges of the features that show up in the reconstruction. In principle, the information about the central regions of the target features is present at the center of the hologram, however this information would not be available because of the overwhelming brightness of the unscattered

laser beam. In Fig. (5b), it is possible to resolve the edges of both the vertical and horizontal sets of slots for the smallest group (~ 2 μm separation). Since λ = 514.5 nm, a conservative estimate for the resolution of this instrument is ~ 4λ. The theoretical resolution limit for such an imaging system operated at f/2 is ~ 1 λ, a value which compares favorably with our result.

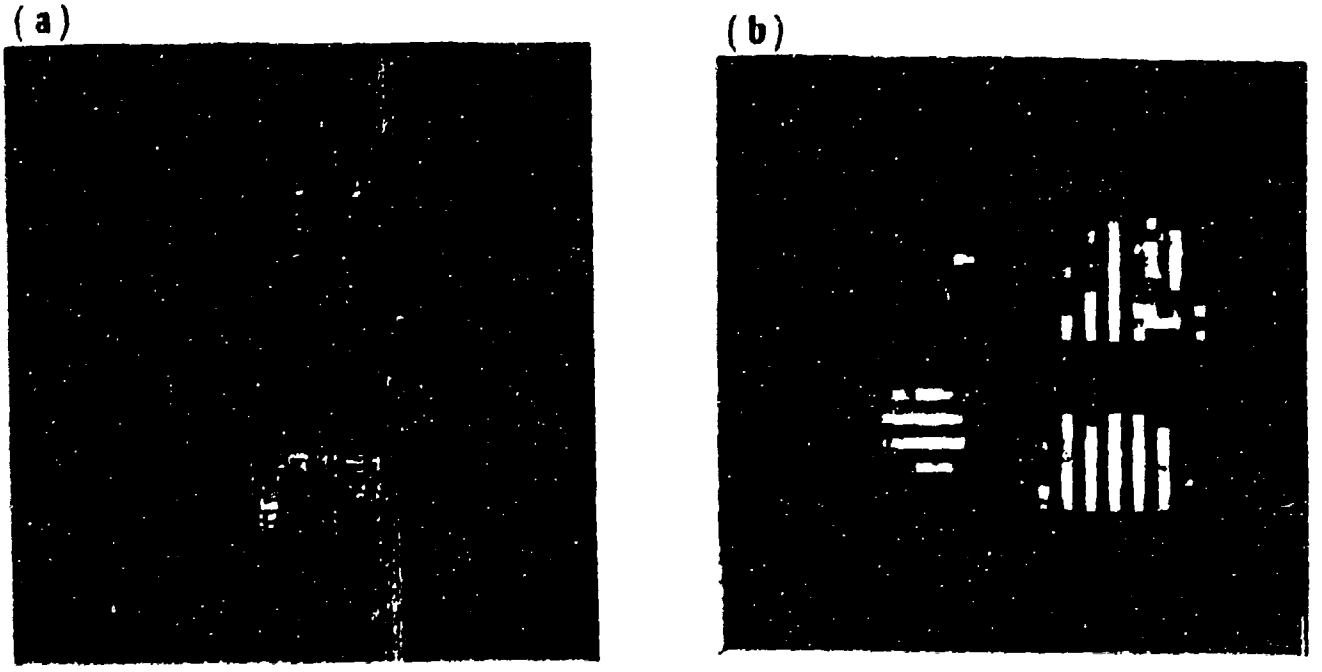

Fig. (5): Reconstructed image from a hologram of a U.S. Air Force resolution target taken at f/2 with 514.5 nm light. A glycerol microdrop was used as the reference wave scatterer. (a) Full-size reconstructed image. (b) 16x zoom from (a) of the smallest slots (2 μm separation between each edges).

3.5.3. Ascaris

Figure (6) shows the reconstructed image from a hologram taken of an Ascaris in its maturation stage, also at f/2. Since this sample is not a strong scatterer, the reference microdrop had to be only ~ 25 μm in diameter. Visible in the image is the cuticle of the Ascaris as well as individual cells. Cell walls are clearly visible and in some cells nuclear structure is evident.

4. CONCLUSIONS

A holographic microscope capable has been constructed, tested, and applied to the imaging of biological materials. This system has recorded holograms of test targets and biological specimens with resolutions in the range of ~ 4 λ with 514.5 nm light. This instrument can be directly applied to imaging in the x-ray range when suitable sources become available.

5. ACKNOWLEDGEMENTS

We are grateful to Dr. Richard B. Setlow of Brookhaven National Laboratory for providing samples of fish melanoma. This research was supported in part by the Department of Energy under Grant #DE-FG02-86ER13610 and #DE-FG02-89ER60898. Such support does not constitute an endorsement by DoE of the views expressed in this article. Additional support by the SDIO/IST and managed by NRL, under SBIR contract #N00014-89-C-2274 is acknowledged.

Support by Eastman Kodak Company and Maxwell Laboratories is also acknowledged.

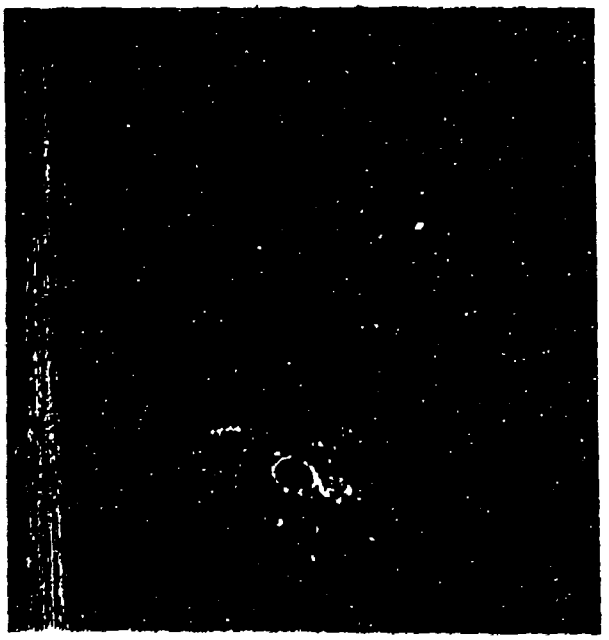

Fig. (6): Reconstructed image of an Ascaris in maturation stage. Visible is the cuticle and individual cells. Cell diameter is ~ 40 μm. Nuclear region visible within some cells is ~ 20 μm in diameter.

6. REFERENCES

1. M. Howells, C. Jacobsen, J. Kirz, R. Feder, D. Quaid, and S. Rothman, "X-Ray Holography at Improved Resolution: A Study of Zymogen Granules", Science, Vol. 238, pp. 514 (1987). C. Jacobsen, M. Howells, K. Quaid, and S. Rothman, "X-Ray Holographic Microscopy: Improved Images of Zymogen Granules", OSA Proceedings on Short Wavelength Coherent Radiation, Vol. 2, R. Falcone and J. Kirz, eds., Optical Society of America, Washington D.C., pp. 295, 1988.

2. D. Joyeaux and F. Polack, "Progress in Optical Reconstruction of Submicron X-Ray Holograms" OSA Proceedings on Short Wavelength Coherent Radiation, Vol. 2, R. Falcone and J. Kirz eds., Optical Society of America, Washington, D.C., pp. 295, 1988.

3. I. McNulty, J. Kirz, C. Jacobsen, M. R. Howells, and E. H. Anderson, "First Results with a Fourier Transform Holographic Microscope", X-Ray Microscopy III, edited by A. G. Michette et al., Springer-Verlag, Berlin, 1991, to be published.

4. J. C. Solem, G. C. Baldwin, and G. F. Chapline, "Holography at X-Ray Wavelengths" Proc. of Intl. Conference on Lasers 1981, STS Press, McClean, VA, pp. 296.

5. J. C. Solem and G. C. Baldwin, "Microholography of Living Organisms", Science Vol. 218, pp. 229, 1982.

6. J. C. Solem and G. F. Chapline, "X-Ray Biomicroholography", Opt. Engineering Vol. 23 pp. 193 1984.

7. R. London, "Radiation Damage and its Influence on Source Requirements for High Resolution X-Ray Holography", X-Ray Microimaging for the Life Sciences, Lawrence Berkeley Laboratory Report, LBL-27660, UC-600, CONF-8905192, p. 51, August, 1989; R. London, M. Rosen, and J. Trebes, "Wavelength Choice for Soft X-Ray Laser Holography of Biological Samples", Applied Optics, Vol. 28, p. 2297, 1989.

8. W. S. Haddad, D. Cullen, K. Boyer, C. K. Rhodes, J. C. Solem and R. S. Weinstein, "Design for a Fourier-Transform Holographic Microscope", X-Ray Microscopy II, edited by D. Sayre, M. Howells, J. Kirz and H. Rarback, Springer-Verlag, Berlin, 1988, pp. 284-287.

9. W. S. Haddad, J. C. Solem, D. Cullen, K. Boyer, and C. K. Rhodes, "A Description of the Theory and Apparatus for Digital Reconstruction of Fourier Transform Holograms", Electronics Imaging '87, Advanced Printing of Paper Summaries, Vol. 2, Institute for Graphic Communication, Inc., Boston, 1987 p. 693.

10. W. S. Haddad, D. Cullen, J. C. Solem, K. Boyer, and C. K. Rhodes, "X-Ray Fourier-Transform Holographic Microscope", Short Wavelength Coherent Radiation: Generation and Applications, Vol. 2, edited by R. W. Falcone and J. Kirz, Optical Society of America, Washington, D.C., 1988, p. 284.

APPENDIX E

Prospects for x-ray holography with free electron lasers

J.C. Solem*, K. Boyer, W. Haddad, and C. K. Rhodes

MCR Technology Corporation
P.O. Box 10084
Chicago, IL 60610-0084

1. ABSTRACT

We review the technical advantages offered by x-ray holographic microscopy for imaging the structure of living biological specimens. We discuss the wavelength, coherence, energy, and pulse-length requirements and conclude that these could be met by free-electron laser architectures of the near future. We also show that Fourier-transform holography using a reference scattering sphere is the best optical configuration for a practical instrument.

2. INTRODUCTION

X-ray microholography will ultimately allow three-dimensional imaging of living organisms with a spatial resolution far beyond the reach of optical microscopes. In the wavelength region between the K-edges of carbon and oxygen, we find a high contrast between protein and water that will allow imaging of the structural elements of cells without staining.[1] Because of the quantum nature of any probe on the < 100-Å level of resolution, the specimen will be severely damaged in the imaging process.[2] If the x-ray energy can be delivered in a very short pulse, however, a snapshot view of the specimen in the living state can be obtained, even though the specimen is obliterated in the process.[3] An ultrashort pulse x-ray laser could provide the illumination for such snapshot microholography. Another option is the free electron laser, if the coherence and energy requirements can be met.

3. WATER WINDOW

Figure 1 shows the absorption length (e-folding distance) in normal density protein and water.[4] Between the K-edges of carbon and oxygen, there is a region of high contrast; water is transparent and protein is opaque. This wavelength interval has become known as the **water window** and the maximum contrast appears at the K-edge of nitrogen. Most of the structural elements of a cell are made of protein. Therefore, within the water window, most biologically interesting features are visible without staining. This compelling fact has provided the principal impetus for the emergence of the field of x-ray microscopy.

Determining exposure requirements for x-ray microscopy from the data in Fig. (1) is fairly straightforward. For holography, however, the problem is a bit more subtle. About a decade ago one of the present authors[2,3] calculated the exposure requirements from the cold opacities alone. An approximation to the Mie scattering problem for a semitransparent sphere in a vacuum revealed that the scattering cross section could be estimated by the geometric cross section times the square of the beam extinction.[5] Since that time, quantum dispersion theory has been applied to the soft x-ray regime to give both real and imaginary atomic scattering factors and researchers have solved the Mie problem for protein sphere immersed in water, including both absorption and dispersion.[6] The results have revealed that the best wavelength for holography is not at the nitrogen K-edge, as in microscopy, but just below the carbon K-edge, a region actually below the threshold of the water window.

There appears to be no impediment to free-electron lasers producing coherent radiation within

---

* Consultant to MCR Technology Corporation

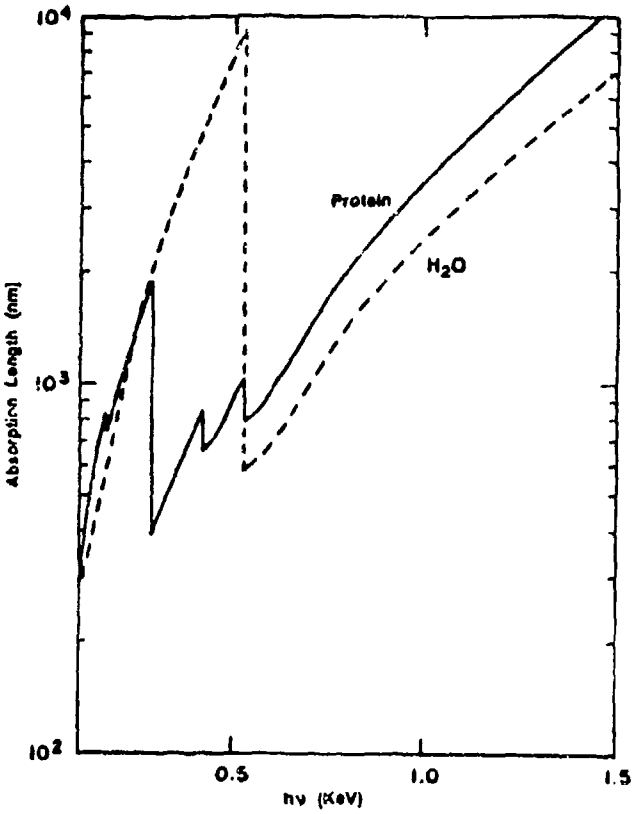

Fig. 1. X–Ray absorption lengths for protein and water at 1 gm·cm^{-3}.

the water window. The shortest wavelength achieved to date is 2,400 Å by the Soviet storage–ring FEL at Novosibirsk,[7] but many of the requisite technologies to permit extension below 100 Å using RF linear accelerators[8] are now in hand.[9] The foremost of these is the photoelectron injector.[8]

Projecting from current rf linac and x–ray optical technology,[8] either an FEL oscillator or a single–pass, self–amplified–spontaneous–emission amplifier may qualify.[8–11] Both conceptual designs could be operated at the third harmonic, for which high gain could be achieved with sufficiently large undulator parameter. In one speculative single–pass design,[12] tuning to 132 Å, and using the third harmonic, gives about three orders of magnitude more gain than tuning directly to 44 Å. An oscillator can produce the requisite power with higher emittance than required for a single–pass amplifier. For example, an FEL oscillator using a 750 period undulator (1.6 cm·period^{-1}) and 35%–reflectance multilayer mirrors could produce 44 Å radiation at 5 x 10^6 W in 2.5 x 10^{-12} s pulses with peak beam current of 400 A and normalized electron beam emittance of 10π mm·mr. A single–pass laser with the same characteristics would require an emittance of 4π mm·mr and an undulator twice as long.[11]

4. HOLOGRAPHY

Holography uses interference with a reference wave to record the amplitude and phase of the specimen–scattered wave. From the symmetry properties of Maxwell's equations it can be shown that, if the fields are known on a surface, they are also known in three–dimensional space. Thus, it is possible to reconstruct rather complete three–dimensional information about the geometric structure of the specimen from its scattered wave. Although the configurations of holographic apparatus are diverse and varied, all recording techniques divide into two basic

categories: Fresnel transform and Fourier transform.

4.1. Fresnel–transform holography

In Fresnel–transform holography,[10] the reference waves are planar. The specimen is illuminated by the same beam of radiation that supplies the reference waves: the specimen simply stands between the radiation source and the recording surface. The wider the angle from the specimen to the edge of the reference illuminated area on the recording surface, the better the resolution. The same cone–angle dependence applies to an optical microscope. The cone–angle dependence further implies that the resolution depends on the coherence of the radiation. Spatial coherence must be maintained over the extent of the reference illuminated area of the recording surface and the temporal coherence length must be larger than the difference between the perpendicular distance from the recording surface to the specimen and the distance from the edge of the reference illuminated area to the specimen.[11]

A more severe limitation derives from the intrinsic resolution of the recording medium. The resolution of a Fresnel transform holograph is limited to twice the grain size of the recording medium.[12] This limitation makes x-ray holography exceedingly difficult, even with the finest grain commercial films. The deus ex machina is photoresist. Developed for microlithography, photoresists are photosensitive etchable polymers with no significant grain structure.[13] X–rays will break cross links in these polymers making them more susceptible to etching in the regions of x–ray exposure. After etching, the resist resembles a relief map, with lowest elevations corresponding to greatest exposures. The spatial resolution of photoresists (more properly, x–ray resists) is dependent on the wavelength of the x–rays to which it is exposed. For long wavelengths, it is limited by diffraction within the resist itself. For short wavelengths, it is limited by the range of secondary electrons, which can also break cross links and thereby cause blurring. The optimum wavelength[14] is about 50 Å, serendipitously close to the lower edge of the water window. The best spatial resolution of resist at the optimum wavelength is 50 to 100 Å.

Two groups are presently making holograms of biological specimens using the Fresnel transform technique. An American group[15] working at the National Synchrotron Light Source of Brookhaven National Laboratory uses a specially equipped beamline with an undulator for high brightness in the water window. After exposing and etching the resist on which their hologram is recorded, they shadow the contours with gold. They then read out the hologram with a transmission electron microscope, digitize it, and reconstruct it with a computer. A French group[16] using a synchrotron at Orsay records their holograms on photoresist in a similar manner. They reconstruct the hologram by passing a He–Ne (6,328 Å) laser through the etched resist, whose contours produce locally differing phase shifts. This produces a magnified image of the specimen. They can accomplish the same phase shifting effect by aluminizing the surface of the resist and reflecting the laser beam.

4.2 Fourier transform holography

Fourier transform holography[17] does not suffer from the resolution limits of the recording medium that affect Fresnel transform holography. The Fourier technique uses curved rather than planar reference waves. In the far field using ideally spherical reference waves, the technique maps increments of distance in the specimen into spatial frequencies at the recording surface — thus the name "Fourier transform". In the far field, the spatial relationship among the fringes simply scales with distance from the specimen. Thus, the hologram can be faithfully registered by recording media of <u>any</u> resolution by simply adjusting the distance from the specimen to the recording surface. A charge–coupled device (CCD) array is particularly attractive in this application. CCDs can be made to work with high efficiency in the water window,[18] and their signal can be digitized directly for simplified computer reconstruction.

Curiously, small increments of distance (minute features of the specimen) are mapped into low spatial frequencies, while large increments of distance (gross features) are mapped into high spatial frequencies. This counterintuitive result can be reconciled with familiar optics by noting that the diffractive resolution limit of the holograph is again determined by the angle over which the hologram is recorded. A larger angle will allow a better measurement of lower spatial frequencies.

The Fourier–transform technique has less stringent coherence requirements than the Fresnel transform technique.[4] Spatial coherence is reduced because the coherent part of the wavefront need only span the specimen and the lens that is creating the reference wave, and these may be placed quite close together. Temporal coherence is reduced because the difference in pathlength from the reference source and the specimen is always small. Figure 2 compares the coherence requirements for the two techniques as a function of specimen mass over 11 orders of magnitude. A free–electron laser will have no difficulty meeting these coherence requirements, but the Fourier–transform technique is clearly less demanding.

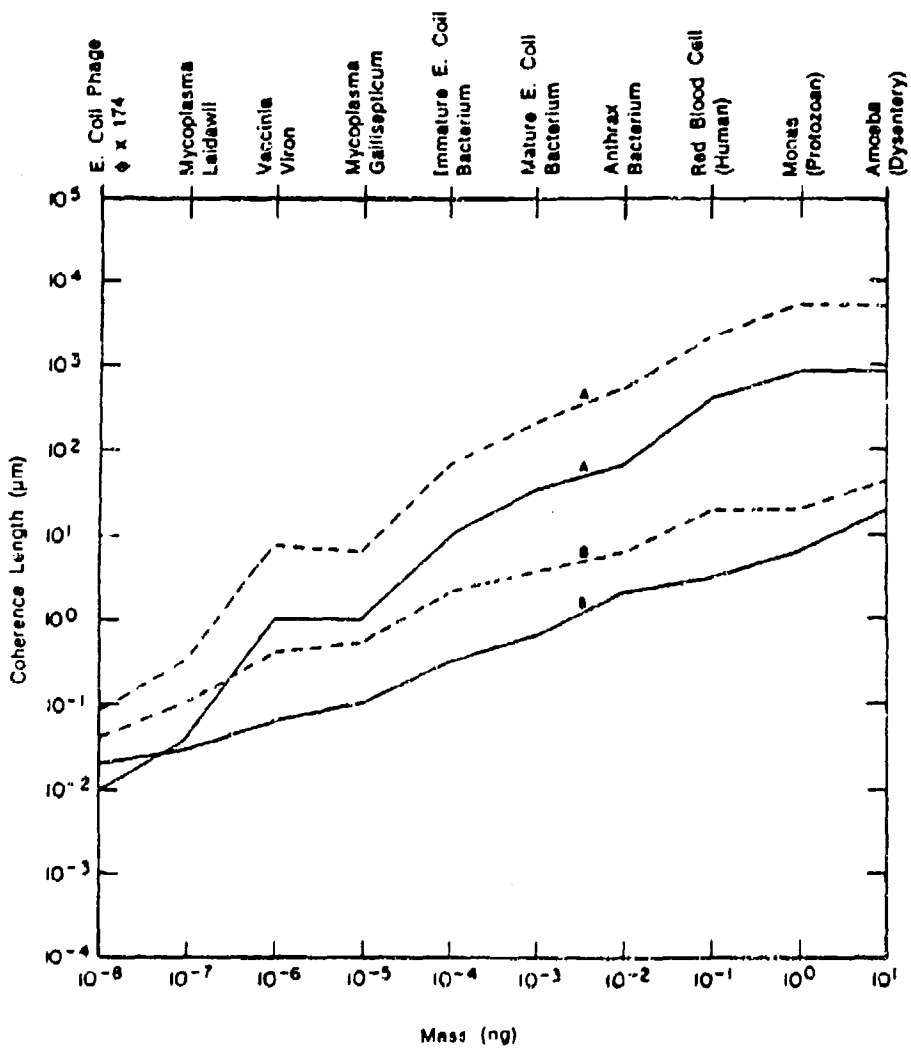

Fig. 2. Coherence requirements as a function of specimen mass: (A) Fresnel transform with high contrast; (B) Fourier transform. Solid lines and temporal coherence and dashed lines are spatial coherence. The specimens at the top were used as models.

A principal difficulty in Fourier transform holography is the generation of spherically diverging reference waves. A straightforward technique involves the use of a lens. The water window is too far from any strong resonances for a refractive lens to be used, so we must use a diffractive lens in the form of a Fresnel zone plate. It can be shown, however, that the resolution is then limited to the same order as the finest spacing of the zone plate. In other words, we need to be able to fabricate x-ray optics to the same precision as we wish to resolve the specimen. Present technology is limited to a few hundred angstroms.[19] If a pinhole with a diameter less than the finest zone spacing is placed at the focus, then the resolution is on the order of the pinhole diameter. It may be possible to fabricate pinholes with diameters somewhat smaller than the finest zone-plate spacing. The real solution to the reference wave dilemma is a reflecting sphere, which will be discussed in detail later.

Despite these difficulties, the Brookhaven group is now generating Fresnel transform x-ray holograms using a zone plate and a CCD as a recording surface.[20] The CCD output can be directly digitized for computer reconstruction.

5. EXPOSURE

Holography results from the symmetry properties of Maxwell's equations—classical electrodynamics. We know this is only an approximation to quantum theory. While the wavefunction is analytic and deterministic, any measurement is inherently statistical. We must count particles just as in nuclear physics experiments. Since the energy carried by a single photon in the water window is more than a hundred times the energy carried by an optical photon, the damage to the specimen is enormous. Furthermore, we are trying to resolve much finer features than in the optical range and each of these features must scatter a statistically significant number of photons. Thus for diffraction limited resolution, the damage is increasing very roughly as the fourth power of wavelength. For an electron microscope, the damage for the same resolution is even greater.[11,14]

Table I lists some specimens and the dosage required to image them to a resolution of 100 Å with signal-to-noise of 5, using x-rays at the nitrogen K-edge. Somewhat higher dosages are required for the virons because there is less contrast between DNA and protein.[11] Higher doses are required for the larger cells because of their physical thickness. For most cells, a few times 10^8 rad is the required dosage. Using the optimal wavelength just below the water window would reduce these exposures about an order of magnitude, but the enormity of the dose is very clear. To put this in perspective, 10^2 rad would make you very sick and 10^3 rad would be surely fatal. The sturdiest known living thing is the bacterium **Micrococcus radiodurans**, which has been alleged[21] to survive 3×10^6 rad. Surely no specimen can survive the exposure. The best we can do is try to record its true image when it was in the living state, and this is best accomplished by taking a snapshot.

6. SNAPSHOT HOLOGRAPHY

X-ray flash pictures or snapshots seem essential to imaging living specimens. The required dosages are so high that we can expect the specimen to explode owing to the sudden heating.[22] If the pulse is short enough, the image can be captured from the **plasma ghost** of the specimen before there is sufficient bulk motion to blur the features we are seeking to resolve.[1] Analytic expressions for hydrodynamic blurring owing to the explosion of semiopaque features are useful for estimating pulse length requirements. To achieve a resolution δ, a specified number of photons must be coherently scattered from a volume δ^3 during the exposure time Δt, and no dimension of the specimen can be allowed to change by more than δ during Δt. To examine a feature with resolution $\delta << d$, where d is the transverse dimension of that feature, the maximum exposure time is

Specimen	Mass(g)	Dosage(rad)	Specimen	Mass(g)	Dosage(rad)
Echerichia coli phase ϕx174	10^{-17}	2×10^{12}	Anthrax bacterium	10^{-11}	4×10^{9}
Herpes viron	10^{-16}	2×10^{12}	Red blood cell (human)	10^{-10}	5×10^{9}
Vaccinia viron	10^{-16}	6×10^{13}	White blood cell (human)	10^{-9}	4×10^{9}
Mycoplasma pneumoniae	10^{-14}	3×10^{9}	Amoeba (dysentery)	10^{-8}	2×10^{9}
Escherichia coli (immature)	10^{-13}	3×10^{9}	Smooth muscle cell	10^{-7}	4×10^{10}
Escherichia coli (mature)	10^{-12}	3×10^{9}	Paramecium (protozoan)	10^{-6}	2×10^{10}

Table I. Dosage to Obtain 100 Å Resolution with S/N = 5 at N K-Edge.

$$\Delta t \simeq \left[\frac{\delta^3 m}{F I \sigma_a} \right]^{1/3} \qquad (1)$$

where m is the mass of the feature being examined, σ_a is its absorption cross section, I is the x-ray intensity, and F is a dimensionless coefficient accounting for equation-of-state parameters and the rate at which transport processes remove energy from the exploding feature to the surrounding material. If $\delta >> d$ is acceptable, then Δt should be multiplied by δ/d after substituting a different dimensionless coefficient G.

The number of useful photons elastically scattered from a single resolution element is approximated by

$$N \simeq \frac{\epsilon \lambda}{\hbar m} \rho I \sigma_e \delta^2 \Delta t$$

where ρ is the density, σ_e is the elastic scattering cross section of the feature, λ is the wavelength, and ϵ is the quantum efficiency of the recording medium. This number must be statistically significant compared to photon noise. Combining Eqs. (1) and (2) gives the required intensity as a function of resolution.

$$I \simeq m \left[\left(\frac{N \hbar}{\sigma_e \rho \lambda \epsilon} \right)^3 \frac{\sigma_a}{\delta^{11}} \right]^{1/2} \begin{cases} F^{1/2} & , \delta < 3d/8 \\ G^{1/2} (d/\delta)^{3/2} & , \delta \geq 3d/8 \end{cases} \qquad (3)$$

Intensity increases very rapidly as better resolution is sought. For typical biological specimens, intensities on the order of 10^{12} W·cm^{-2} with pulse lengths on the order of [illegible]

are required for a resolution of 100 Å. The projected designs for free-electron lasers will have no difficulty meeting these requirements.

7. REFERENCE SCATTERING SPHERES

The resolution dilemma encountered with the Fresnel zone plate reference source in Fourier transform holography is solved by using a reference scattering sphere.[23] The zone-plate holograph is limited to a resolution about the same as the finest zone-plate spacing because the largest angle covered by the reference illumination is determined by that spacing. A tiny, highly reflective, smooth sphere, which can be used to replace the zone plate as the reference source, will not suffer this limitation.

Reference-sphere-Fourier-transform holography also offers a host of advantages when an x-ray laser is used: (1) the sphere can provide reference illumination over a sufficiently large angle to realize diffraction-limited resolution; (2) the sphere is appropriate to the narrow beam of a laser in that it is small and can be placed quite close to the specimen; (3) orientation of the sphere is unimportant; and (4) the sphere is rather inexpensive to fabricate in large quantities, so unlike the zone plate, it is unimportant whether the sphere is damaged or destroyed on each exposure. Figure 3 is a schematic of how the reference sphere might be used in practice. The most logical recording device is a CCD, the output of which can be digitized for direct computer analysis. The scattering sphere will not produce spherical reference waves, there will always be an angle-dependent phase shift. Thus it will not generate a true Fourier transform, even in the far field. However, any scattering shape can be used as long as we know exactly what it is and how it is oriented. A set of basis functions, analogous to the sinusoidal basis functions of Fourier reconstruction which incorporates the appropriate correction, can be generated by the computer and used to recover the image.[24] The image can also be reconstructed optically using a scaled reflecting sphere and a computer modified hologram that compensates for the angular dependence of reflectivity. The hologram might even be an array of liquid crystal optical gates for direct interfacing with the computer and "real-time" reconstruction.

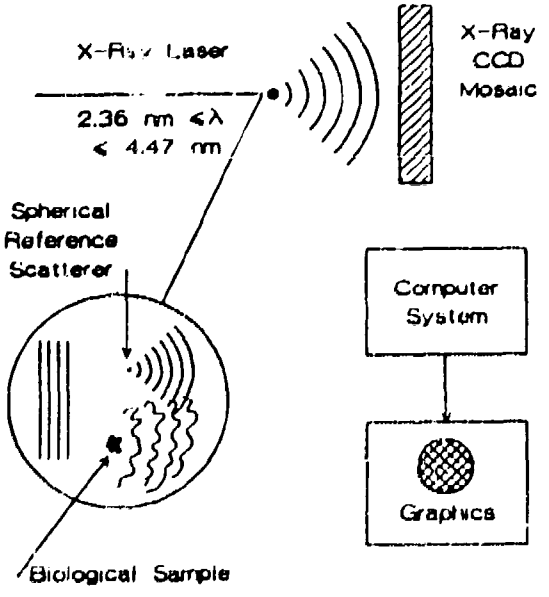

Fig. 3. Schematic of a reference-sphere-Fourier-transform holographic microscope.

That it is possible to manufacture a sphere with the requisite surface smoothness was not obvious in the beginning of our research program. We found that many of the spheres manufactured by laser ablation had rather crystalline surfaces resulting from slow cooling. However, in examining some hollow spheres that were manufactured as laser fusion targets, we found surfaces so smooth that no structure could be resolved with an electron microscope. The smoothness was attributed to rapid cooling of the thin layer, which left the metal in a glassy state rather than forming crystals.[23,25] Smooth spheres have also been manufactured in very small sizes at Lawrence Livermore Laboratory. Finally, if there is a problem with the metallic spheres, a clear alternative exists. For example, we can use readily available glass spheres, which will have the necessary smoothness, and then coat them by metal evaporation, a process which is known to produce amorphous layers with a smoothness better than 3 Å. Actually, recent work[26] on x-ray mirrors has demonstrated the ability to achieve a microroughness of ~ 2 Å. Processes to provide uniform coating have been developed. The spheres also turn out to be exceedingly round owing to rapid damping of multipole oscillations on the time scale of cooling. This removes completely the necessity for measuring departure from sphericity and for orientation of the sphere.

We surveyed the periodic table for elements of optimum specular reflectivity to serve as reference scatterers in the water window. Unless a compound can significantly enhance the density of an element, the pure element will be the best reflector. We used the tables of real and imaginary atomic scattering factors[25] calculated from quantum dispersion theory[27] to obtain the reflectivities shown in Fig. 4. Nickel is found to be the best reflector at the water window threshold (carbon K-edge). If we are able to precisely select our wavelength, it would behoove us to use the optimum wavelength just below the threshold, so nickel is the element of choice. Furthermore, osmium is only slightly superior to nickel and suffers from a variety of fabrication and handling difficulties. Figure 5 shows the reflectivity of nickel as a function of grazing angle at 44.7 Å. It provides adequately uniform reference illumination out to an angle of about 28°. This is sufficient to obtain good resolution in both the transverse and longitudinal directions. The transverse resolution is given by $\delta t \simeq \lambda/2\theta$, while the longitudinal resolution[28] is given by $\delta_\ell \simeq \lambda/4\theta^2$. Table II shows the resolutions that can be obtained at the carbon K-edge and the nitrogen K-edge.

Assuming an average specimen diameter and as compact a spacing as possible between the sphere and specimen, the laser beam would have to illuminate about an area of about 10^{-6} cm^2. This means the free-electron laser would have to supply about 10^{-8} J in a single pulse, which is quite reasonable.

	Nickel 44.7 Å	Osmium 31.6 Å
θ	30°	22°
δ_t	43 Å	41 Å
δ_ℓ	41 Å	53 Å

Table II. Spatial Resolution at carbon and nitrogen K-edges.

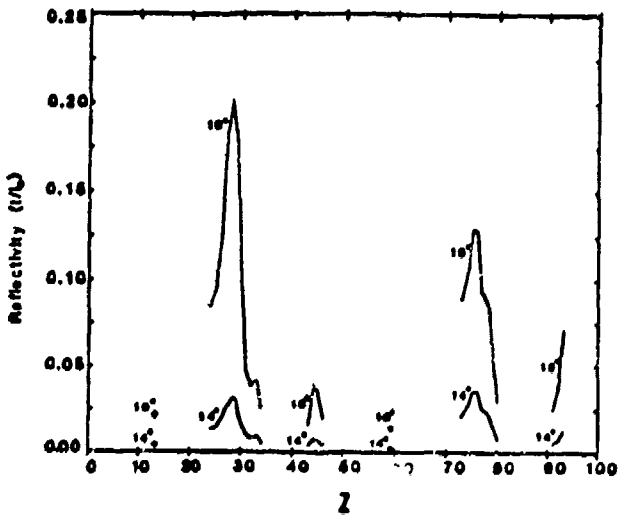

Fig. 4. Specular reflectivities of various elements at selected grazing angles.

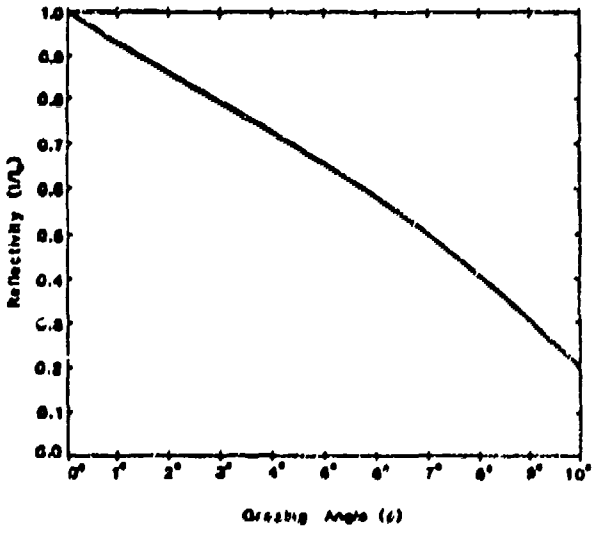

Fig. 5. Specular reflectivity of nickel as a function of grazing angle.

8. CONCLUSIONS

If the proposed design[7,9] can be reduced to practice, no impediment is seen to using a free electron laser to obtain water window, x-ray holographic images of biological specimens. The best arrangement is to use the Fourier transform technique with a nickel reference scattering sphere and a CCD to register and record the interference pattern.

9. ACKNOWLEDGEMENTS

This research was supported in part by the Department of Energy under Grant #DE-FG02-86ER13610 and #DE-FG02-89ER60898. Such support does not constitute an endorsement by DoE of the views expressed in this article. Additional support by the SDIO/IST and managed by NRL, under SBIR contract #N00014-89-C-2274 is acknowledged.

10. REFERENCES

1. J. Solem and G. Baldwin, "Microholography of Living Organisms", Science, Vol. 218, p. 229, 1982.
2. J. Solem, "High Intensity X-Ray Holography: An Approach to High-Resolution Imaging of Biological Specimens", Los Alamos National Laboratory Report LA-9508-MS, 1982.
3. J. Solem, G. Baldwin, and G. Chapline, "Holography at X-Ray Wavelengths", Proceedings of the International Conference on Lasers '81, STS Press, McLean, VA, p. 296, 1982.
4. J. Solem and G. Chapline, "X-Ray Biomicroholography", Optical Engineering, Vol. 23, p. 193, 1984.
5. R. Glauber, Lectures in Theoretical Physics, W. Brittin and A. Dunham, eds., Vol. 1, p. 315, Interscience, New York, 1959.
6. R. London, "Radiation Damage and its Influence on Source Requirements for High Resolution X-Ray Holography", X-Ray Microimaging for the Life Sciences, Lawrence Berkeley Laboratory Report, LBL-27660, UC-600, CONF-8905192, p. 51, August, 1989; also R. London, M. Rosen, and J. Trebes, "Wavelength Choice for Soft X-Ray Laser Holography of Biological Samples", Applied Optics, Vol. 28, p. 2297, 1989.
7. V. Litvenenko, "Results of the USSR Storage Ring FEL", Nucl. Instr. and Methods in Physics Research, to be published, 1990.
8. B. E. Newnam, "Projected Performance of RF-Linac-Driven Free-Electron Lasers in the Extreme-Ultraviolet Spectral Region", Nucl. Instr. and Methods in Physics Research, Vol. B40/41, p. 1053-1057, 1989.
9. J. Fraser and R. Sheffield, "High-Brightness Injectors for RF-Driven Free-Electron Lasers", IEEE Journal of Quantum Electronics, Vol. QE-23, p. 1489, 1987; and R. Sheffield, E. Gray and J. Fraser, "The Los Alamos Photoinjector Program", Nuclear Instruments and Methods in Physics Research, Vol. A272, p. 222, 1988.
10. J. C. Goldstein, T. F. Wang, B. E. Newnam, and B. D. McVey, "A Single-Pass Free-Electron Laser for Soft-X-Rays with Wavelengths ≤ 10 nm", in Proceedings of the 1987 IEEE Particle Accelerator Conference, E. R. Lindstrom and L. S. Taylor, eds., IEEE Cat. No. 87CH2387-9, pp. 202-204, 1987; Abstract in Bull. Am. Physical Soc., Vol. 32, p. 206, 1987; also, T. F Wang, J. C. Goldstein, B. E. Newnam, and B. D. McVey, "Generation of Coherent Soft X-Rays Using A Single-Pass Free-Electron Laser Amplifier", Intl. J. Electronics, Vol. 65, pp 589-595, 1988.
11. B. Newnam and J. Goldstein, "Free-Electron Lasers as Potential Sources for Soft X-Ray Holographic Microscopy of Biological Structures", Abstract for Microimaging for the Life Sciences, May 24-26, 1989, Lawrence Berkeley Laboratory, Berkeley, CA, LA-UR-89-1797
12. H. Shay, W. Barletta, S. Yu, E. Scharlemann, R. Schlueter, and G. Deis, "Short Wavelength FELs as High Brilliance Sources", X-Ray Microimaging for the Life Sciences, Lawrence Berkeley Laboratory Report, LBL-27660, UC-600, CONF-8905192, p. 176, August, 1989.
13. D. Gabor, "A New Microscope Principle", Nature, Vol. 161, p. 777, 1948; also D. Gabor Proceedings of the Royal Society, Series A, Vol.197, p. 454, 1949.
14. J. Solem, "X-Ray Imaging of Biological Specimens", Proceedings of the International Conference on Lasers '83, STS Press, McLean, VA, p. 635, 1984.
15. G. Stroke, Optique des Rayons X et Microanalyse, Herman, Paris, p. 3, 1966.
16. D. Sayre, J. Kirz, R. Feder, D. Kim, and E. Spiller, "Potential Operating Region for Ultrasoft X-Ray Microscopy of Biological Materials", Science, Vol. 196, p. 1339, 1977.
17. D. Sayre, J. Kirz, R. Feder, D. Kim, and E. Spiller, "Transmission Microscopy of Unmodified Biological Materials: Comparative Radiation Dosages with Electrons and Ultrasoft X-Ray Photons", Ultramicroscopy, Vol. 2, p. 337, 1977.
18. M. Howells, C. Jacobsen, J. Kirz, R. Feder, D. Quaid, and S. Rothman, "X-Ray Holography at Improved Resolution: A Study of Zymogen Granules", Science, Vol. 238, p. 514 (1987). and C. Jacobsen, M. Howells, K. Quaid, and S. Rothman, "X-Ray Holographic Microscopy Improved Images of Zymogen Granules", OSA Proceedings on Short Wavelength Coherent Radiation, Vol. 2, R. Falcone and J. Kirz, eds., Optical Society of America, Washington

D.C., p. 295, 1988.
19. D. Joyeaux and F. Polack, "Progress in Optical Reconstruction of Submicron X-Ray Holograms", OSA Proceedings on Short Wavelength Coherent Radiation, Vol. 2, R. Falcone and J. Kirz, eds., Optical Society of America, Washington, D.C., p. 295, 1988.
20. J. Winthrop and C. Worthington, "X-Ray Microscopy by Successive Fourier Transformation", Physics Letters, Vol. 15, p. 124, 1965; and G. Stroke and R. Restrick, "Holography with Spatially Noncoherent Light", Applied Physics Letters, Vol. 7, p. 229, 1966.
21. J. Janesick, "Potential of CCDs for UV and X-Ray Plasma Diagnostics", Reviews of Scientific Instruments, Vol. 56, p. 795, 1985; K. Marsh, "Nondispersive Spectroscopy and Imaging of Plasmas using a Charge-Coupled Device", Reviews of Scientific Instruments, Vol. 56, p. 837, 1985; and D. Lumb, G. Hopkinson, and A. Wells, Advances in Electronics and Electron Plasmas, Vol. 64B, p. 467, Academic Press, London, 1985.
22. Y. Vladimirsky, D. Kern, W. Meyer-Ilse, and D. Attwood, "X-Ray Imaging of Nanostructure Patterns", Applied Physics Letters, Vol. 54, p. 286, 1989.
23. I. McNulty, J. Kirz, C. Jacobsen, E. Anderson, M. Howells, and H. Raeback, "Soft X-Ray Microscope Using Fourier Transform Holography", to be published in the Proceedings of the 6th Synchrotron Radiation Instrumentation Conference, August, 1989.
24. 1990 Guinness Book of World Records, D. McFarlan and N. McWhirter, eds, Sterling Publishing Co., New York, p. 78, 1989.
25. J. Solem, "Imaging Biological Specimens with High-Intensity Soft X-Rays", Journal of the Optical Society of America B, Vol. 3, p. 1551, 1986.
26. W. Haddad, J. Solem, D. Cullen, K. Boyer, and C. K. Rhodes, "A Description of the Theory and Apparatus for Digital Reconstruction of Fourier Transform Holograms", Electronics Imaging '87, Advanced Printing of Paper Summaries, Vol. 2 (Institute for Graphic Communication, Inc., Boston, 1987) p. 693.
27. W. S. Haddad, D. Cullen, K. Boyer, C. K. Rhodes, and J. C. Solem, "Design for a Fourier-Transform Holographic Microscope", Proceedings of the International Symposium on X-Ray Microscopy, edited by D. Sayre, Springer-Verlag, Berlin, in press; W. S. Haddad, D. Cullen, J. C. Solem, K. Boyer, and C. K. Rhodes, "X-Ray Fourier-Transform Holographic Microscope", OSA Proceedings on Short Wavelength Coherent Radiation: Generation and Application, edited by R. W. Falcone and J. Kirz (Optical Society of America, Washington, D.C., 1988) p. 284.
28. B. Henke, P. Lee, T. Tanaka, R. Shimabukure, and B. Fujikawa, "Low-Energy X-Ray Interaction Coefficients: Photoabsorption, Scattering, and Reflection", Atomic Data and Nuclear Data Tables, Vol. 27, p. 1, 1982.
29. B. Aschenbach, "Design, Construction, and Performance of the ROSAT High-Resolution X-Ray Mirror Assembly", Applied Optics, Vol. 27, p. 1404, 1988.
30. A. Compton and S. Allison, X-Rays in Theory and Experiment, Van Nostrand, 1935; and U Fano and J. Cooper, "Spectral Distribution of Atomic Oscillator Strengths", Reviews of Modern Physics, Vol. 40, p. 441, 1968.
31. A. Kondratenko and A. Skrinsky, Optical Information Processing, Vol. 2, p. 1, Plenum Press, New York, 1978.

UIC
The University of Illinois at Chicago

Laboratory for Atomic, Molecular, and Radiation Physics (M/C 273)
Department of Physics
College of Liberal Arts and Sciences
Box 4348, Chicago, Illinois 60680
(312) 996-4868

Aug. 6, 1990.

MCR Technology Corporation
P. O. Box 10084
Chicago, IL 60610–0084

Dear Dr. Rhodes:

Enclosed please find the report for the "Propagation Studies for High Brightness X–Ray Sources" (subcontract 090189–SDI–1).

The main findings of this study are (1) capillary tubes are effective in enhancing harmonic conversion as well as parametric processes, (2) propagation properties of intensity laser beam are influenced by electrons produced from ionizations to the extend that the laser fluence inside the capillary tube falls off rapidly.

One of the aspects in this study, namely large fluctuation in the harmonic intensity, have not been studied in great detail. However, one can speculate that it is directly related to the focal intensity distribution of the pump beam. Recently, we have developed a method of examining the focal intensity distribution from any focussing system. From these investigation, although incomplete, reveals that unless the laser beam is properly aligned to the focussing optics, the focal intensity distribution can be distorted severely by astigmatism and spherical aberration. This immediately suggests that the performance of harmonic and parametric conversion can be expected to improve substantially when these optical distortions can be controlled judicially. Furthermore, availability of this diagnostic tool will allows us to perform better controlled experiments to investigate spectral stability issue of harmonic radiation in the future.

It has been a pleasure working on this contract. If there is any questions about the report, please feel free to contact me.

Sincerely yours,

Ting Shan Luk

UIC
The University of Illinois at Chicago

Laboratory for Atomic, Molecular, and Radiation Physics (M/C 273)
Department of Physics
College of Liberal Arts and Sciences
Box 4348, Chicago, Illinois 60680
(312) 996-4868

13 July 1990

FINAL TECHNICAL REPORT
"Propagation Studies for High Brightness X-Ray Sources
5 September 1989 – 5 February 1990
Subcontract No. 090189-SDI-1

Principal Investigator: Ting Shan Luk

Prepared for: Charles K. Rhodes, President
MCR Technology Corporation
P. O. Box 10084
Chicago, Illinois 60610-0084

Approved:

Ting Shan Luk

Abstract

The advent of subpicosecond laser systems capable of achieving focal intensities exceeding 10^{19} W/cm^2 allow consideration of a fundamentally new mode of electromagnetic propagation, namely channeled propagation, in which both relativistic electronic motions and electron expulsion from the region of high laser intensity produces a channel which could be useful as a high–aspect–ratio longitudinally pumped x–ray laser source. Two classes of experiments to investigate longitudinal pumping were performed. The first used small bore capillary tubes to investigate the propagation of the pump laser through an extended gas target and to examine the radiation emitted from this target. The second class of experiments investigated the laser beam propagation through a static gas by photographing the breakdown of the target gas in the laser focal region in order to determine the spatial location of the emitted radiation.

CONTENTS

Channeled Propagation Simulation in Capillary Tube Targets

I. Introduction

The interaction of high intensity subpicosecond laser systems with gaseous targets allow the production of plasmas that are characterized by a low temperature, perhaps as low as a few tens of electron–volts, and a density that may approach the critical value. A fundamentally new mode of electromagnetic propagation is theorized to arise in this species of plasma, namely, channeled propagation produced when the laser intensity exceeds a value approximately one half of the Compton intensity,[1] which for a KrF^* laser is 4.5×10^{19} W/cm^2. Because of charge displacement, the boundary of a channel can be associated with a sharp change of index of refraction of the target medium resulting from relativistic motions and the expulsion of electrons from the region of high laser intensity. If a channel is formed, a self–contained cylindrical region of target material would be created which could serve as a high–aspect–ratio source of stimulated radiation. Recent dynamical calculations[2] have indicated the existance of such a stable mode of propagation. The ability to propagate high intensity radiation via channeled propagation, and thus, longitudinally pump a target material is the main motivation for pursuing the investigations described below.

It has been established that atoms can be put into high charge states through a multiphoton absorption process when gaseous atomic targets are exposed to strong electromagnetic fields created by high intensity laser systems.[3,4] Experiments in this laboratory have demonstrated that the resulting ion can be left in an excited state, although whether the excitation is a direct consequence of the multiphoton process or is the result of collisional recombination processes is yet to be determined. What is certain is that, depending upon the target material, copious quantities of short wavelength radiation are produced from the small interaction volume of target gas produced from a pulsed gas jet and the focal volume of the

laser system, the lighter gases up through Ne being the noted exceptions.[5]

The following premise was proposed to investigate longitudinal pumping of a gaseous target medium. Assume that the observed radiation from a pulsed gas jet target is produced by either a direct multiphoton process or by collisional recombination processes. Further, assume that this radiation can be made to originate from an extended source rather than the typical focal volume of the laser. Can or will this extended emission region, which would be generated by confining the target gas inside a small bore capillary tube, exhibit amplification?

Longitudinal pumping is accomplished by utilizing a small bore capillary tube to extend the length of the target gas to a cylindrical volume. In the event that recombination is the primary method of producing excited state ions, the capillary tube walls will assist in rapidly cooling[6] the plasma produced. Small bore glass capillary tubes are used because the smooth interior wall has a high reflectivity at grazing incidence, a fact which allows for the reflection of the laser beam rather than its absorption, much like the anticipated refractive index boundary resulting from channeled propagation at high laser intensity in a gaseous target. Emission will then presumably occur along some fractional length of the capillary tube. Only radiation emitted in the direction parallel to the capillary bore, or parallel to the axis of propagation and not absorbed by residual gas, will be able to escape the capillary tube and be detected. Whether the detected radiation is the result of a direct multiphoton absorption process yielding an excited state, and therefore prompt, or if it is due to collisional recombination mechanisms, amplification parallel to the capillary tube bore should result if absorption from the ambient material is sufficiently low.

II. Capillary Transmission Studies

A. Low Power

Preliminary studies considered the transmission of a HeNe laser beam focused

into and through a small bore capillary tube. These studies established the methodology of focusing and aligning a laser through a small bore capillary tube. Essentially, the capillary tube was found to be correctly aligned when the transmitted beam produced a TM_{00} image on a screen positioned beyond the output side of the capillary tube. Figure 1 illustrates the initial setup for these studies. The capillary tube was positioned inside a small vacuum chamber equipped with CaF_2 input and output windows and pumped to a base pressure of a few millitorr. The exact base pressure was not important as long as it was much lower than the target gas pressure and sufficient not to affect the laser beam propagation, especially when the KrF^* laser was used. Alignment of the HeNe beam, and the KrF^*, was facilitated by placing the vacuum chamber with the enclosed capillary tube upon an X–Y–Z–θ–ϕ translation stage. A HeNe laser was focused into a 250 μm bore capillary tube which has a length of approximately 10 cm. The focusing optic was a 56 cm focal length lens. Since the HeNe laser beam was expanded and collimated to a 1.3 cm diameter beam, an effective f/42 focal system resulted. The transmission of the HeNe beam through this capillary tube was measured using an empty capillary tube as well as the capillary tube with N_2 flowing through it. Gas was supplied to the capillary tube by attaching another tube to a small hole which had been drilled into the side of and at the center of the capillary tube. A constant gas flow was maintained while measuring the transmission. The capillary tube was translated along the laser path to assure that the entrance of the capillary tube was positioned at the focal position of the laser beam. The target gas density was varied by changing the gas line pressure to the capillary tube from 10 psi up to 70 psi. The transmission of HeNe through the capillary tube for a target gas line pressure of 50 psi is plotted in Figure 2 and compared to a static air fill of 760 torr or less. Nearly 90% of the HeNe beam was transmitted through the empty capillary tube. However almost 97% was transmitted through the capillary tube

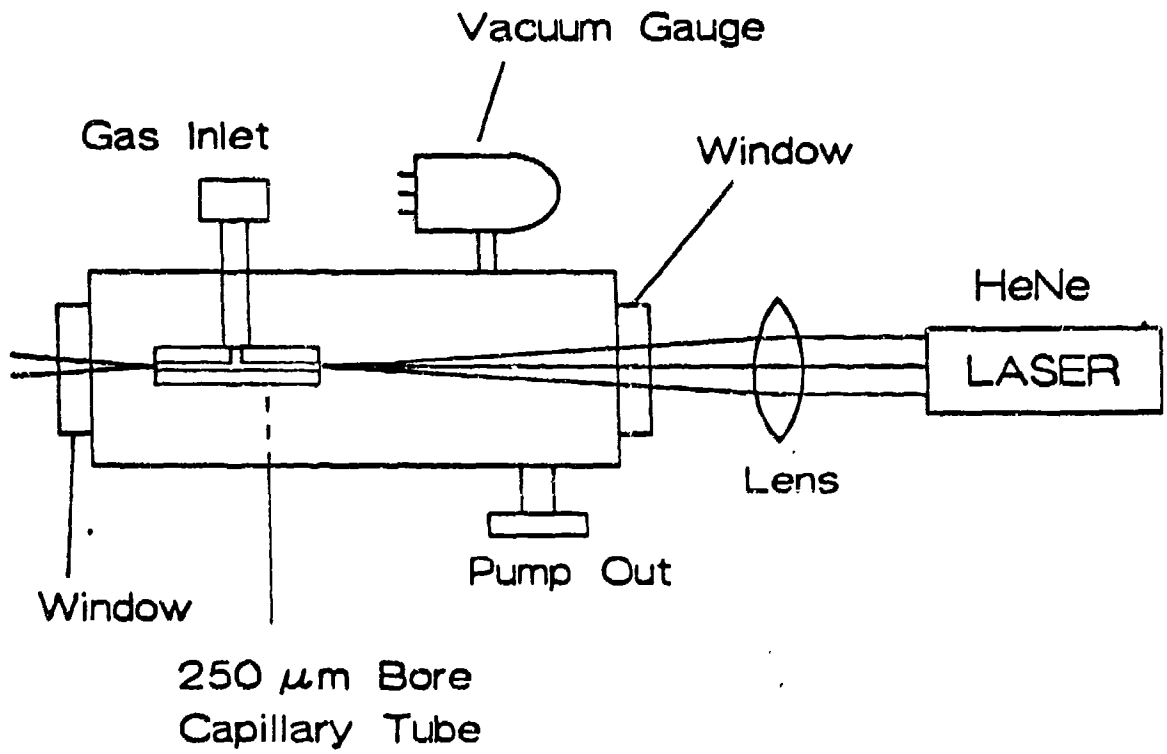

Figure 1. Initial experimental setup to measure the transmission of laser light through a small bore capillary tube.

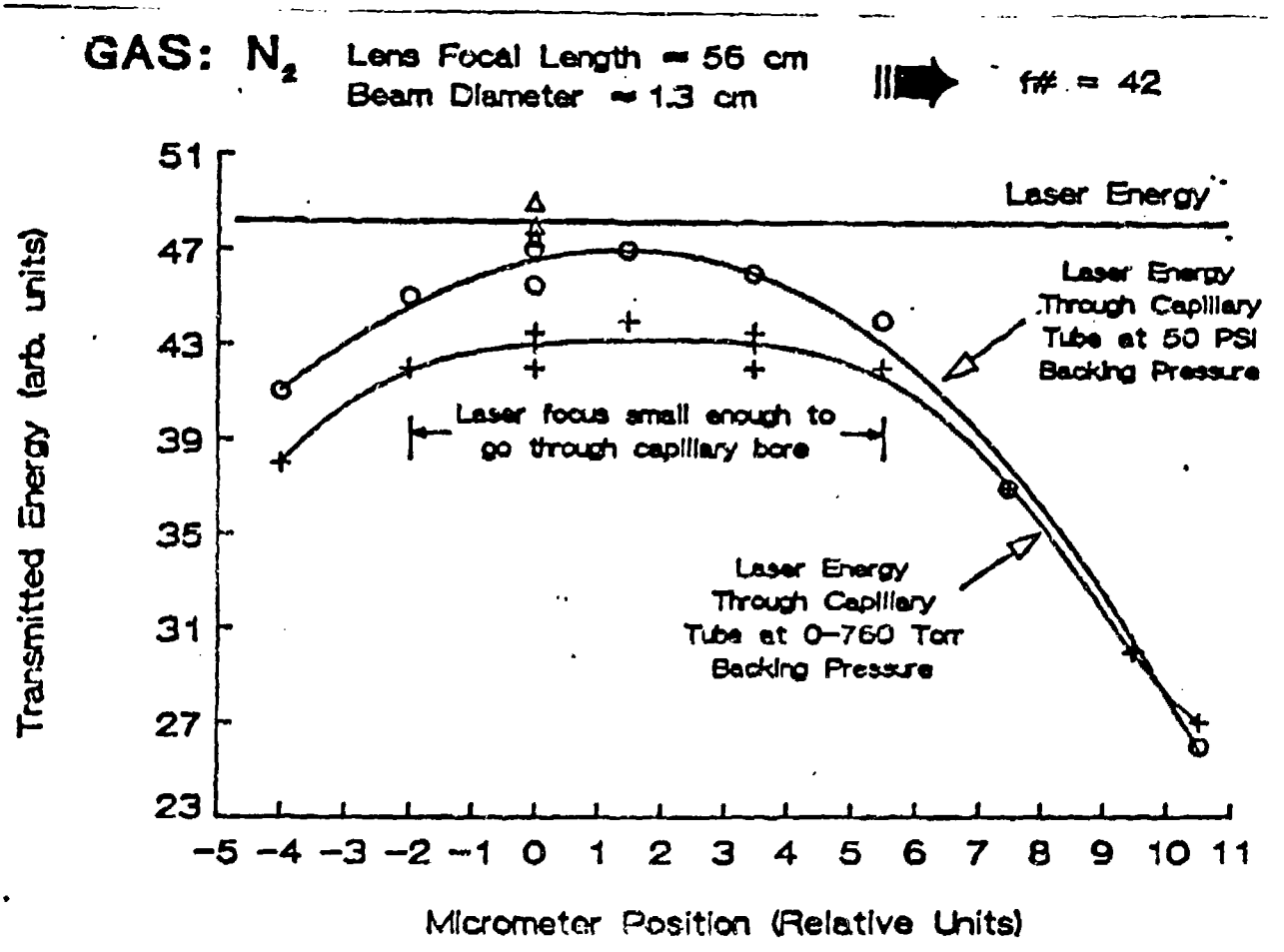

Figure 2. A relatively high percentage of HeNe laser light was transmitted through the 250 μm bore capillary tube. When gas was flowed through the tube, the transmission increased.

when N_2 was flowing through it and being pumped out of the encompassing vacuum chamber. This increase in transmission was attributed to a lensing effect of the gas jet escaping out the end of the capillary tube. The escaping gas served to favorably deflect the laser beam into the capillary bore. Increasing the gas flow above a characteristic maximum value, typically 40 psi, but which depended upon the diameter of the capillary bore, yielded no additional transmission due to this lensing effect. Changing the bore diameter of the capillary tube to 150 μm resulted in a reduced transmission, perhaps because of the focusability of the HeNe laser beam. However, the lensing effect became more pronounced as indicated in Figure 3 with the transmission increasing from 72% to 83%. Smaller bore capillaries were not considered because of an inability to remove all debris from the bore resulting from the side hole drilling process.

Having demonstrated that a HeNe laser beam could be transmitted through a small bore capillary tube of considerable length, propagation of the KrF^* beam through the capillary tube was considered. Initially, a KrF^* beam of approximately 100 μJ was focused into the capillary tube using the same setup as described in Figure 1. Alignment of the capillary tube bore with respect to the KrF^* laser beam was found to be critical as evident by the reduced quality of the TM_{00} mode. Data was taken after the best TM_{00} mode image was obtained. Transmission through an empty 10 cm long capillary tube with a 250 μm bore diameter was determined to be approximately 40% to 50%. The transmission dropped rapidly as the capillary tube was rotated away from the maximum transmission orientation.

B. High Power

After performing several experiments involving the acquisition of emission spectra, which are discussed below, the transmission of the small bore capillary tubes was tested using approximately 100 mJ of KrF^* energy from the amplifier Prometheus.[7] The focusing optic used was a 10 cm diameter lens with a focal

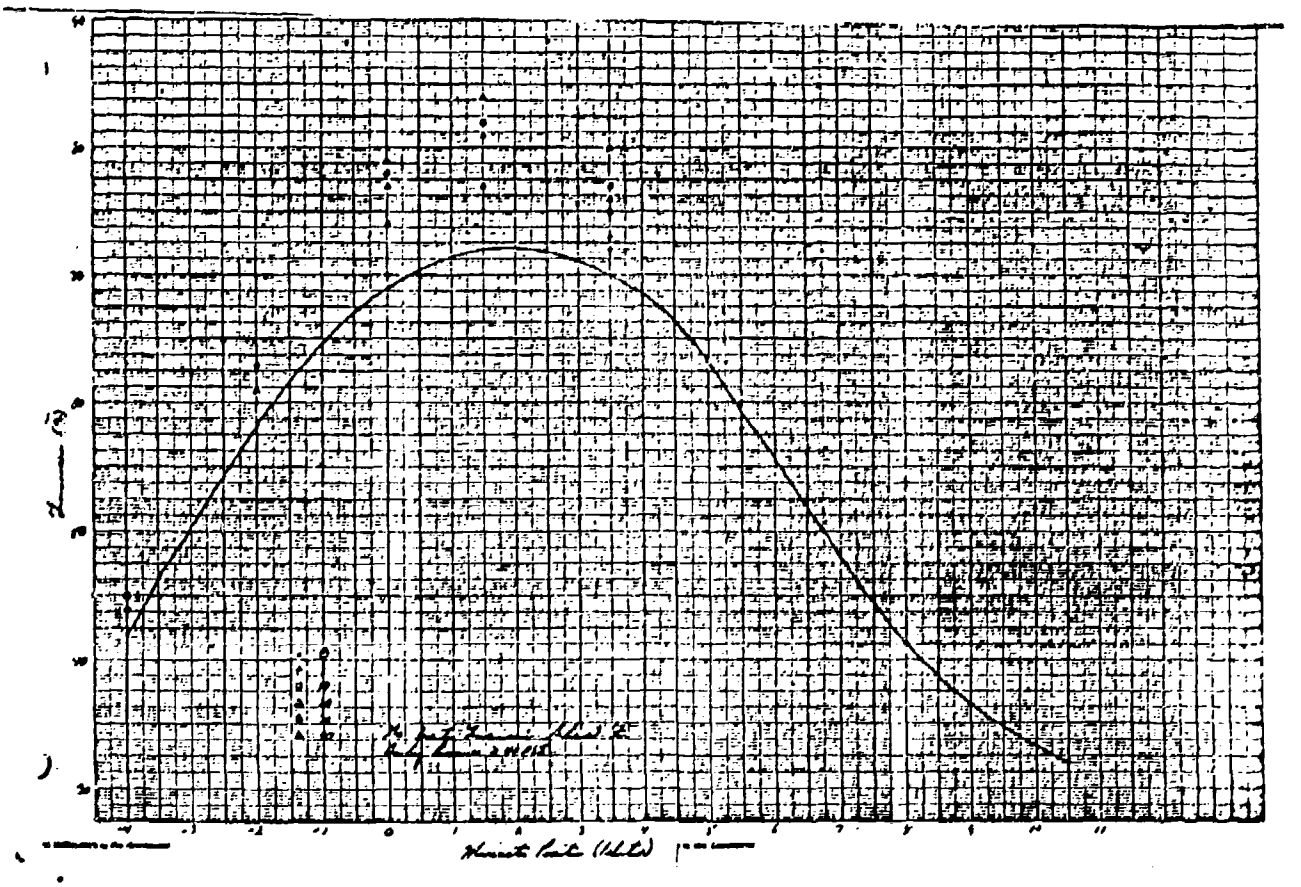

Figure 3. When the capillary bore was reduced to 150 µm, the transmitted HeNe energy was reduced. However, the effect of gas flowing through the tube was increased.

length of 100 cm. Since the KrF^* laser beam from Prometheus has a rectangular 2" by 4" shape, the focal system was f/10 to f/20. Two sizes of capillary tubes were used, 40 mm long with a 0.75 mm bore and 30 mm long with a 0.25 mm bore. Gas was admitted into the capillary tube through a pulsed valve gas jet assembly similar to that shown in Figure 4. Later modifications allowed capillary tube lengths from 2.5 cm up to 23 cm to be tested. Target density in the capillary tube could be varied in two ways. One could change the backing pressure to the pulsed valve or one could change the time delay between the laser fire signal and the pulsed valve open signal. The gas flow through the capillary tube was monitored and calibrated using a differential microphone. Typical responses for two capillary tube lengths and bores are illustrated in Figure 5.

For the transmission test using the Prometheus amplifier, the timing was set so that the capillary tube was completely filled with gas and the gas flow was nearly a maximum at the capillary tube exit. Figures 6–9 illustrate the results. As noted in Figures 6 and 7, some fraction of the KrF^* laser beam could be transmitted through <u>all</u> of the test gases even at high pulsed valve backing pressure when using a 750 μm bore 4 cm long capillary tube. However, when the capillary tube bore was reduced by a factor of 3, to 250 μm, and the length was decreased to 3 cm, the transmission of the KrF^* beam dramatically changed. Transmission through the empty capillary tube dropped. While transmission through He and Ne remained high, even at high pulse valve backing pressure, transmission through the heavier gases rapidly dropped to zero. This effect cannot be attributed only to a refractive effect due to the abundance of electrons occuring from ionizing Ar and Kr because H_2 behaved like Ar and Kr in attenuating the laser beam as illustrated in Figure 8. The transmission of the KrF^* beam through an empty 30 mm long capillary tube with a bore of 250 μm was measured to be approximately 60%, or roughly equal to the transmission through a much longer capillary tube using 100 μJ

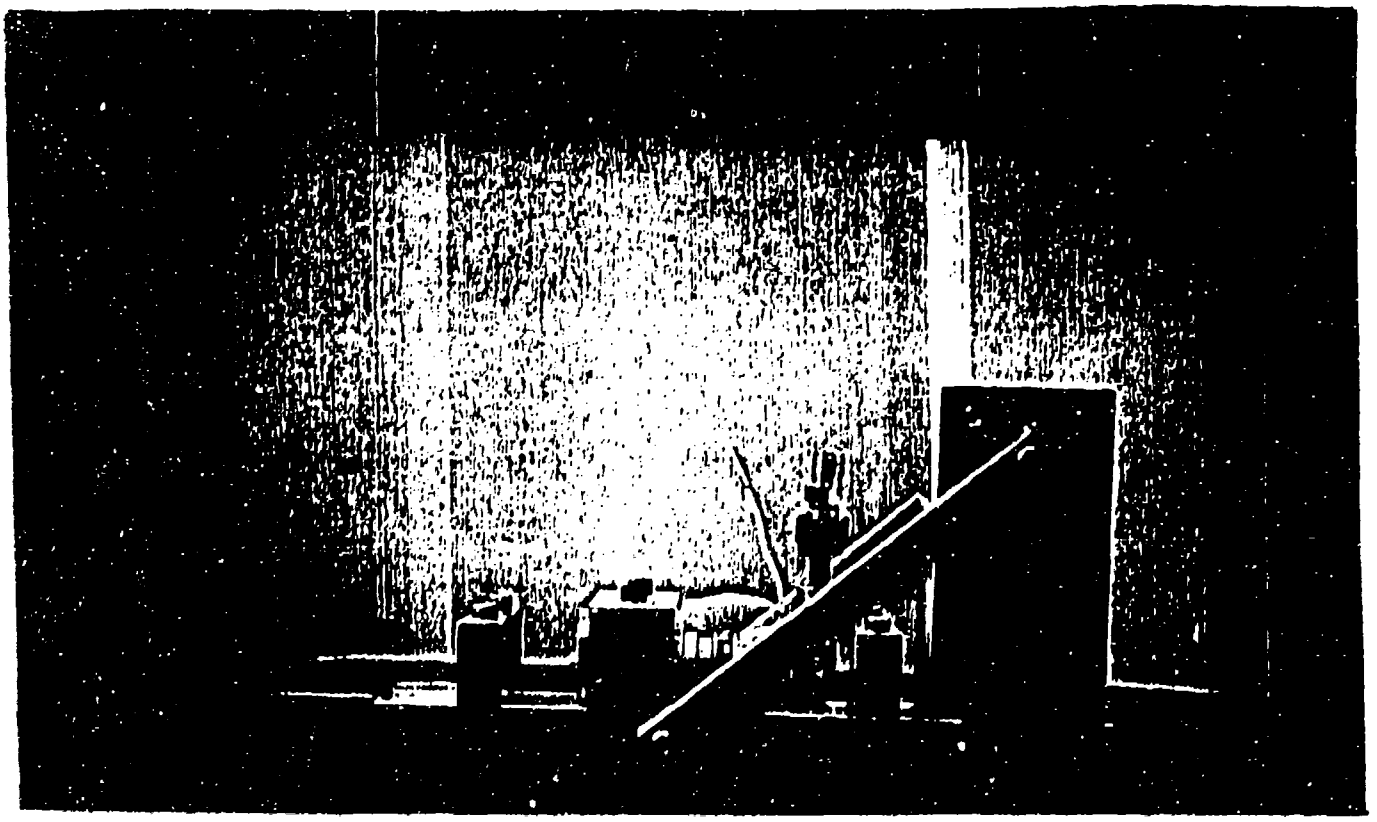

Figure 4. A pulsed valve assembly was constructed which allowed gas to be injected into capillary tubes of varying length.

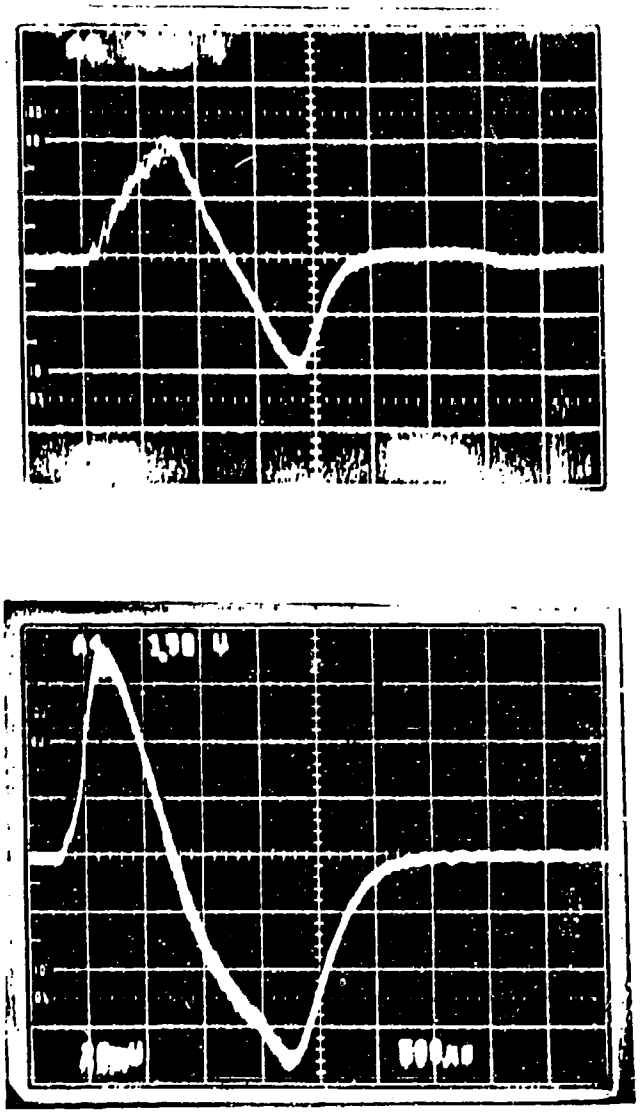

Figure 5. Using a microphone, the gas flow through the capillary tube could be monitored. A 750 µm bore 23 cm long capillary with 50 psi backing pressure was used in (a). A 250 µm bore 3 cm long capillary with 40 psi was used in (b). Maximum flow occures when the curve crosses the x-axis. The x-axis time scale is 500 µsec per division.

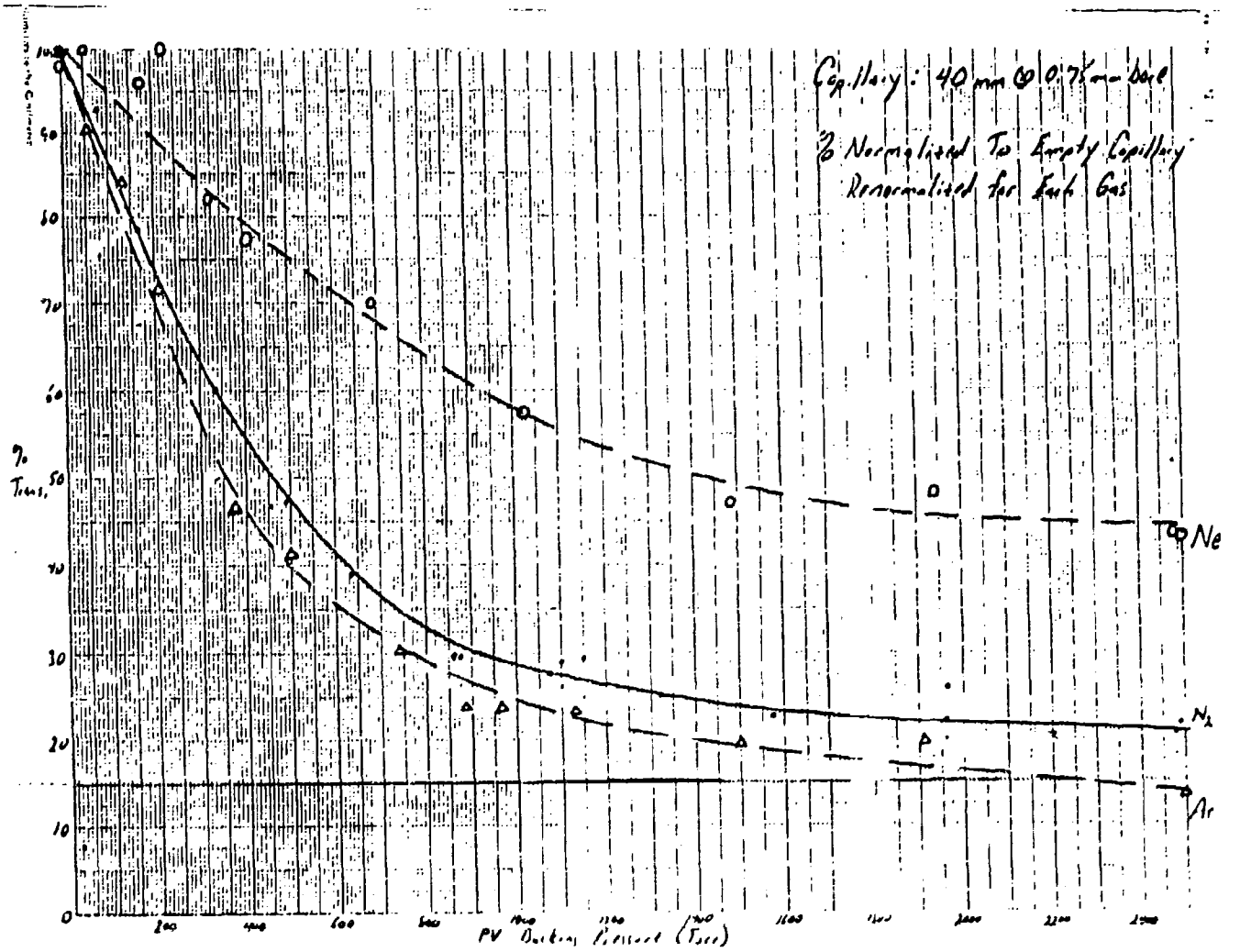

Figure 6. The KrF^* beam could be transmitted through a 750 μm bore 4 cm long capillary tube even at pulsed valve backing pressure of 2500 torr for Ne, N_2 and Ar. Note the high transmission for Ne.

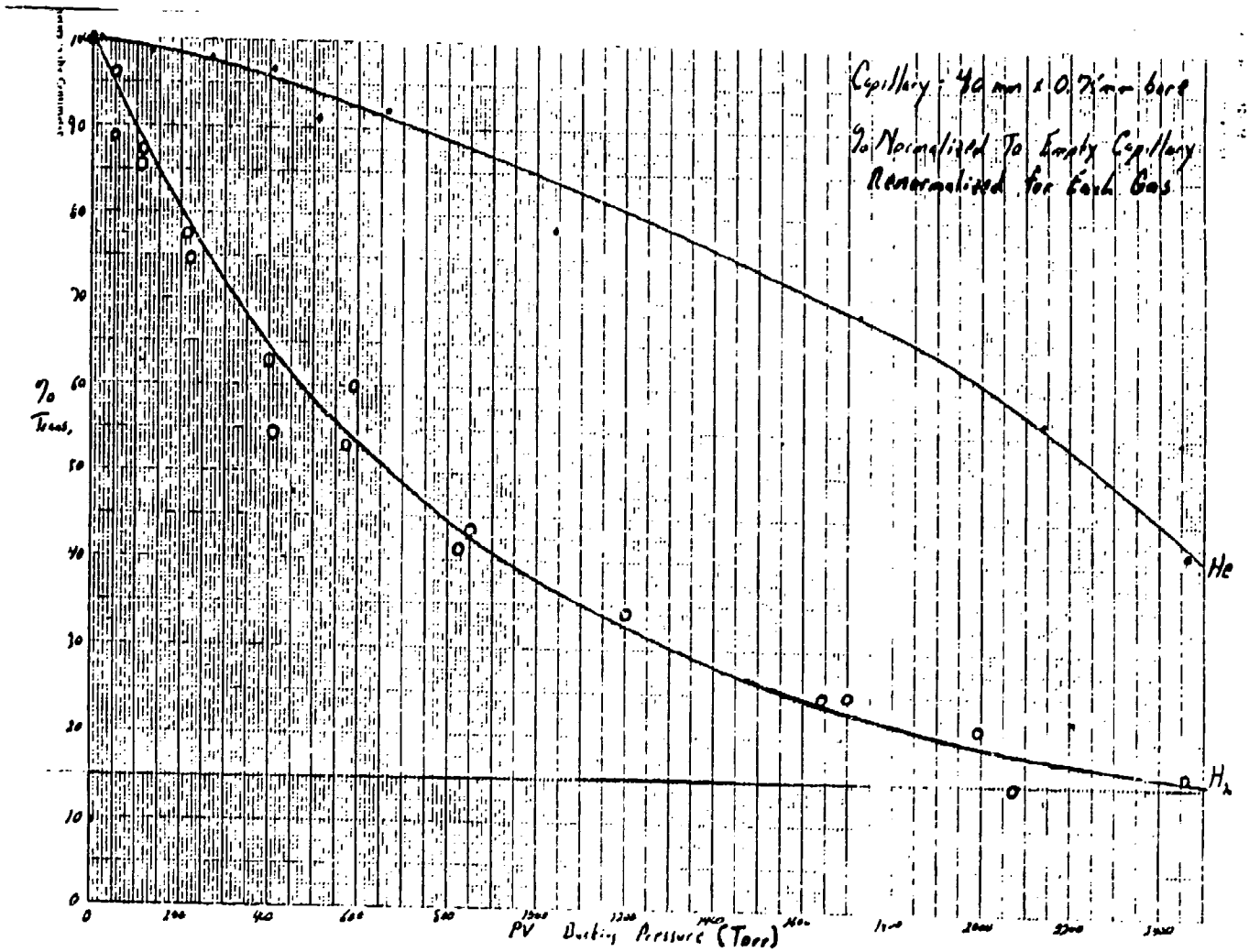

Figure 7. The KrF^* beam could be transmitted through a 750 μm bore 4 cm long capillary tube even at pulsed valve backing pressure of 2500 torr for He and H_2. Note the high transmission for He and that the transmission for H_2 is simular to that of Ar.

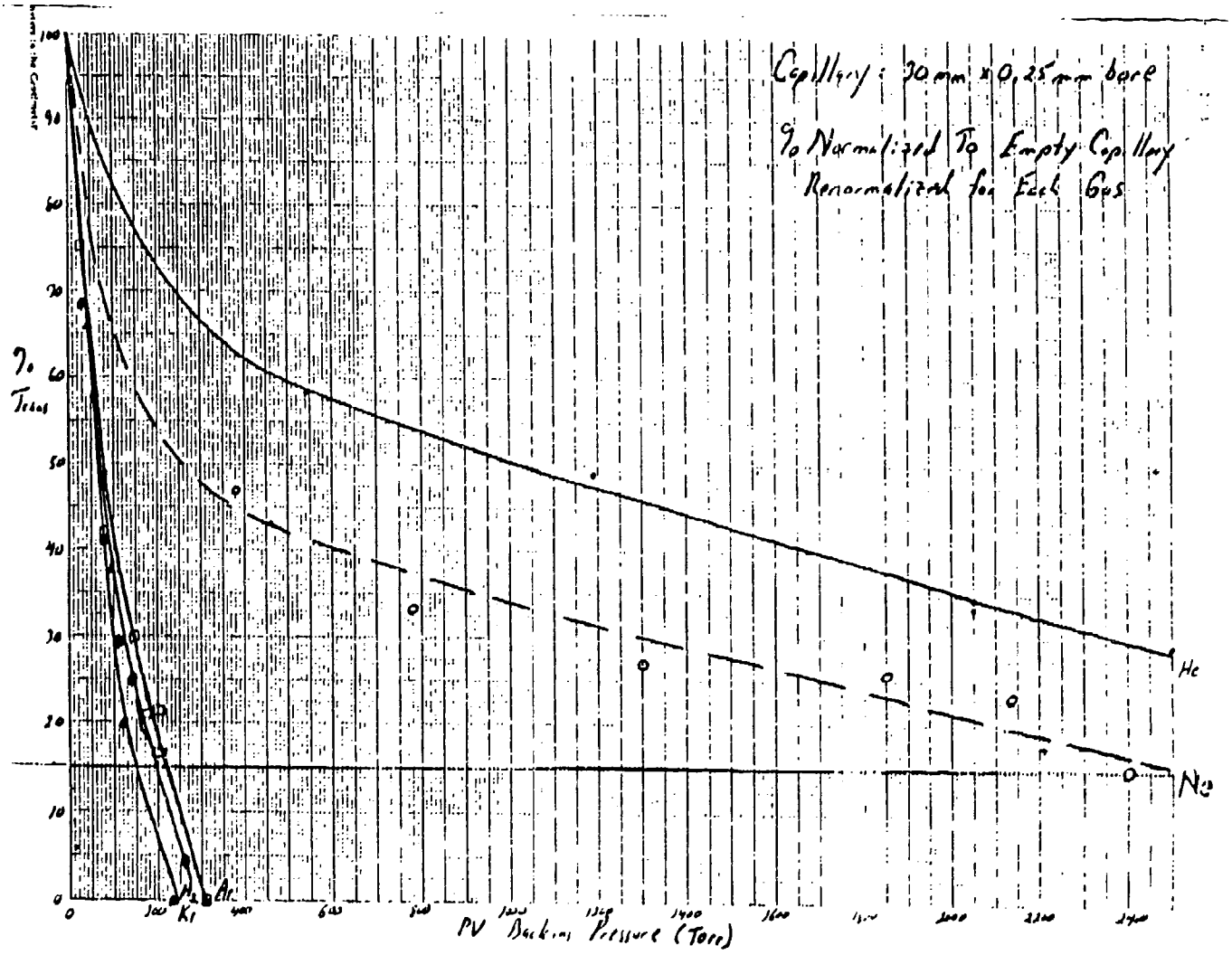

Figure 8. When the capillary tube bore was reduced to 250 μm and the length decreased to 3 cm, the KrF^* beam transmission was significantly reduced. While He and Ne still transmitted the beam H_2, Ar and Kr did not.

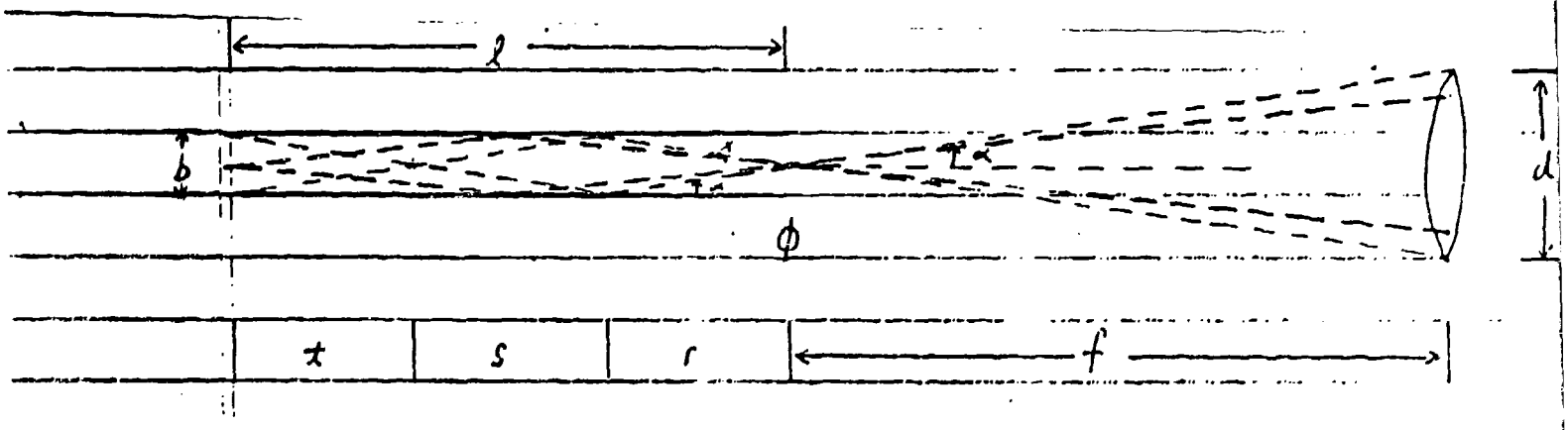

Figure 9. Schmatic illustrating the laser being focused into a capillary tube of length l and bore diameter b. The focusing optic has a diameter of d and a focal length f. The first reflection occurs at position r into the capillary tube.

of energy and a larger f–number focal system. Clearly, the KrF^* beam is being absorbed into the capillary tube walls at each reflection. Finally, note that addition of gas does not produce a lensing effect. Rather, the laser transmission through the capillary tube decreases, for all gases, as the gas flow through the capillary tube is increased. Only by increasing the capillary tube bore diameter to 750 μm does the laser beam transmission impove. A defocusing action due to the electron density could, at least in part, account for these observations.

C. Capillary Reflections

Internal reflections are important since the laser beam is partially absorbed at each reflection. Consider Figure 9 in which a lens is used to focus laser light [illegible] and at the bore of a capillary tube. Using light rays to define similar triang[illegible] the first reflection is found to occur at the position

$$r = bf/d$$

where b is the capillary bore diameter, d is the laser beam diameter and f is the focal length of the lens. Additional reflections will occur at (2n–1)r along the length of the capillary tube where n is an integer. The total number of reflections, N, in a capillary tube is found from

$$(2N - 1)r = l$$

where l is the total length of the capillary tube. In the two transmission exampies cited above, there will be 2 reflections for the 40 mm long capillary tube and 4 reflections for the 30 mm long capillary tube, the small bore capillary tube experiences more reflections. Following several light rays through the capillary tube indicates that beyond the point 2r, the laser beam establishes an average intensity over a diameter of approximately b/2. The angle of reflection is given by

$$\delta = \tan^{-1}(d/2f).$$

If the focusing optics result in an angle of incidence which is too large, absorption will be severe. Denote the absorption of the laser beam at a reflection as Υ. For

the examples of Figures 6–8, the laser beam traveling through the 250 μm bore capillary tube would experience considerably more absorption, γ^{-2}, than the laser beam traveling through the 750 μm bore capillary tube.

Since the gas flow through the capillary tube will be important, as indicated by the strong attenuation of the KrF^* beam when using H_2, Ar and Kr, as well as the need to know the target density, a model was established which assumes that the gas flow is viscous. The validity of this model was checked using an interferometer to measure the rate of gas flow in the capillary tube and found to be within 10% of the calculated value. For details of the interferometer measurement see Appendix A. Further testing of the gas flow was accomplished using a microphone to monitor the flow through the capillary tube as illustrated in Figure 5. From the model, the pressure at the end of a tube is related to the pressure at the input of the tube by

$$P' = -\alpha/2 + (\alpha^2 + 4P_o^2)^{1/2}$$

where

$$\alpha = 16\eta v_m L/a^2,$$

η is the viscosity of the gas, v_m is the molecular velocity of the gas, L is the length of the tube, and a is the bore radius. A worked example is presented in Appendix B indicating that target densities as large as 10^{19} cm^{-3} are encountered. With modest ionization of the target gas along the capillary tube, rather large electron densities could result.

III. Spectral Studies

A. Normal Incidence Spectrometer

Spectra from various gases were obtained using the capillary target geometry. Two seperate data acquisition systems were employed, a 1–meter normal incidence spectrometer (NIS) with a 1200 l/mm grating and a 1–meter grazing incidence spectrometer (GIS) with a 300 l/mm grating. Each spectrometer employed

a microchannel plate (MCP) detector mounted at the exit focal plane of the spectrometer. For the NIS, a charge coupled device (CCD) camera was coupled to the MCP allowing 21–nm regions of the spectrum to be simultaneously collected. For the GIS an optical multichannel analyser (OMA) was coupled to an MCP mounted tangentially to the Rowland Circle and allowed 6–nm regions of the spectrum to be collected. Spectral resolution on the NIS was 0.9 nm due to using the capillary tube bore as the spectrometer entrance slit. The GIS gave 0.2 nm resolution. Alignment of the capillary tube bore with the optical axis of the spectrometer was achieved using an X–Y–Z manipulator which allowed tilt motion.

The gases H_2, He, N_2, Ne, Ar, Kr and Xe were used as target materials. Spectra between 35 nm and 90 nm were obtained for all gases, with a few extending up to 130 nm. The gases Ar and N_2 will be discussed seperately with the remaining gases being summarized together for completeness. Three general areas of investigation were examined: (1) the spectrum as a function of capillary tube length and bore diameter; (2) the spectrum as a function of target density; and (3) the spectrum as a function of laser energy and confocal parameter. Most of the experimential effort is limited to the first two areas. Careful studies requiring changing the laser energy and the confocal parameter were not possible, only large changes were attempted to clearly determine if an effect was present.

The first experimential configuration utilized the NIS. A 23 cm long capillary tube with a 0.75 mm bore diameter was positioned at the image plane and served as the entrance aperture to the spectrometer. Argon was selected as the initial target material because of familiarity with the VUV spectrum.[5] Figure 10 illustrates the typical spectrum obtained. Two features are noted. First, the third, fifth and seventh harmonics are evident although the seventh is weak. These three lines can be used as an approximate wavelength calibration to compensate for errors introduced by using the capillary bore as the spectrometer entrance slit. Second,

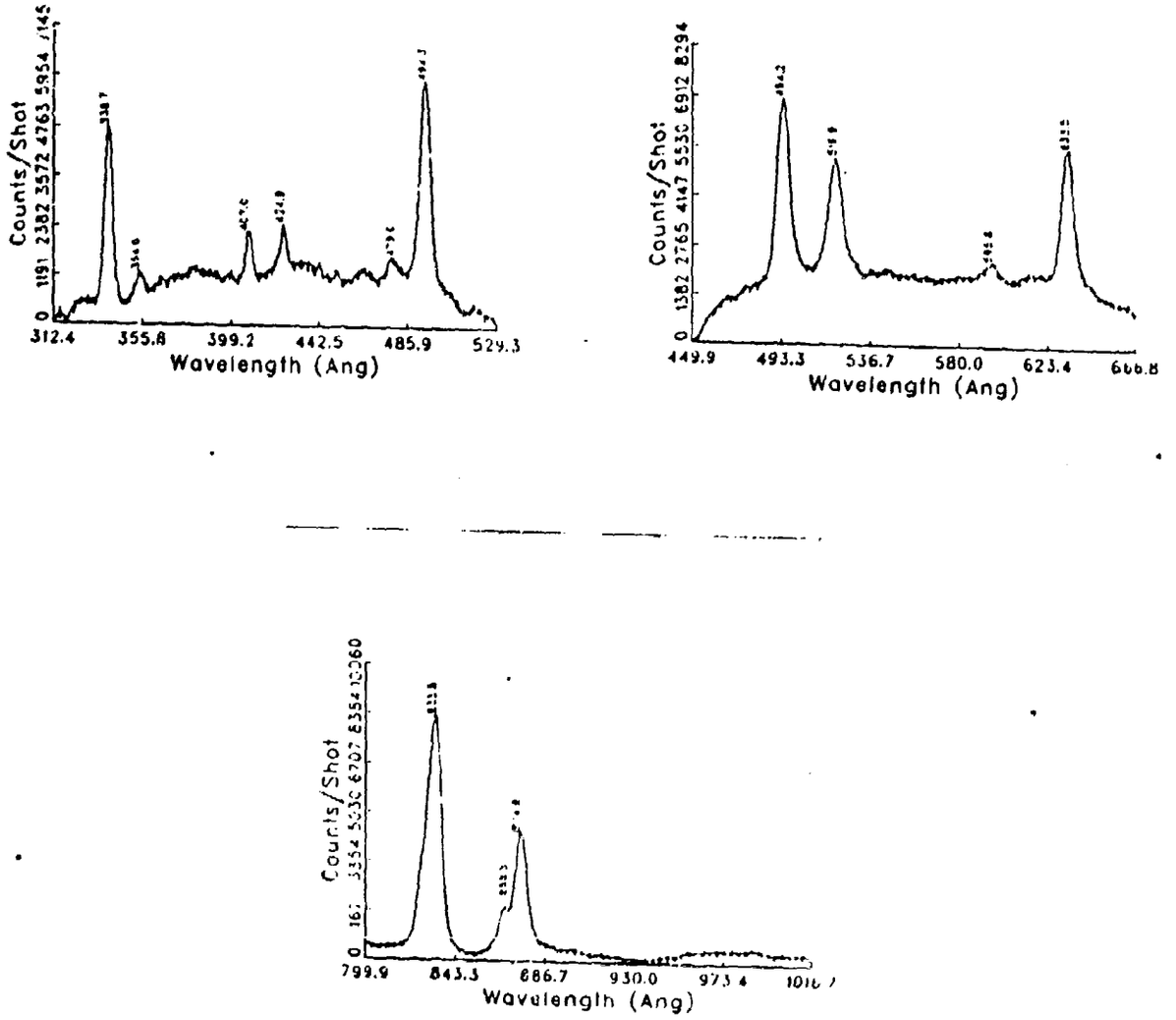

Figure 10. Argon spectrum obtained using a 23 cm long capillary tube with a 750 μm bore as the target geometry. The KrF* laser energy was approximately 10 mJ. Focusing was with an f/25 to f/10 optical system.

all of the remaining spectral lines are unidentified lines, and the spectrum is not nearly as rich as that obtained previously using only a gas jet target.[5] The strengths of the signals vary considerably with the third harmonic, at nearly 2000 times stronger than the fifth harmonic, being the strongest feature. No lines were observable below 33 nm because scattered light from zeroth order prevented observation below this region.

Argon was searched at longer wavelength. Figure 11 illustrates an interesting feature observed at ≈124 nm which is thought to be Ar_2^*. Since this transition has a natural line width of ≈ 10 nm, the signal in Figure 11a would represent a gain of ≈3.5 cm^{-1}, the strongest gain yet recorded for this excimer transition.[8–10] As should be expected, this line exhibited a strong dependence upon laser energy and confocal parameter as illustrated in Figures 11a–d.

Figure 12 illustrates the lines grouped around the third harmonic in the Ar spectrum as the target pressure is increased by increasing the backing pressure of the pulsed valve. Figure 13 plots the signal strength as a function of backing pressure as the pressure is increased and then decreased and illustrates that the effect is reproducible. Two features are evident. First, the third harmonic has a strong target density dependence as evidenced by the rapid increase in signal when the backing pressure is increased from 15 to 25 psi. Second, when the target density reached a critical value, the third harmonic signal drops rapidly and a new signal at 87 nm rises. The association between these two spectral signals will be discussed later.

As noted earlier, the target density within the capillary tube could be varied other than by changing the pulsed valve backing pressure. By changing the timing between the laser fire command and the pulse valve open command, the laser pulse could be made to arrive at any time during the gas flow. Figure 14 illustrates the change in signal which could be achieved by altering the target density in this

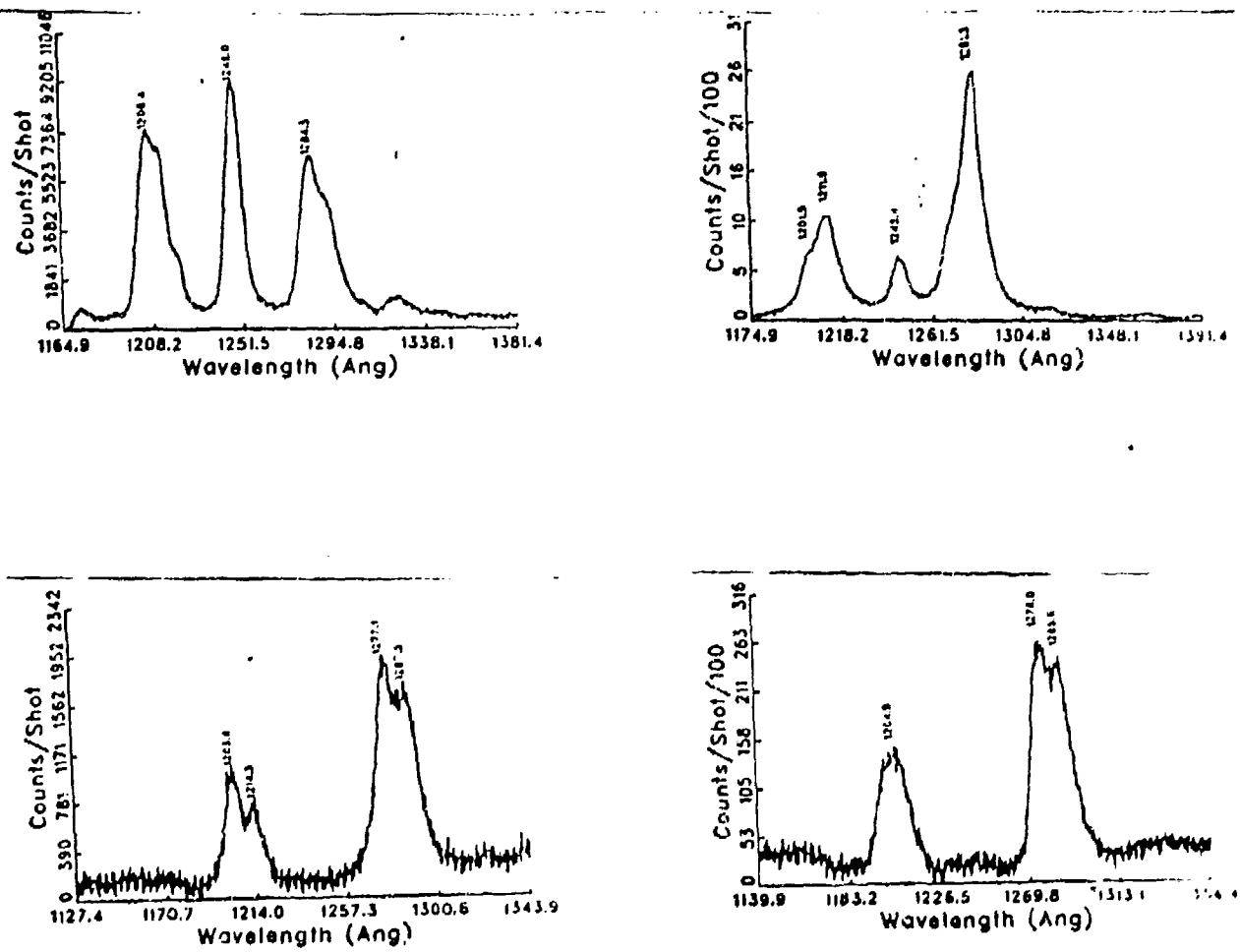

Figure 11. Argon spectrum illustrating the laser energy dependence and confocal parameter dependence of the Ar_2^* 124-nm line. (a). Laser energy < 25 mJ. Large confocal parameter achieved by aperaturing down the laser beam. (b). Laser energy = 25 mJ. Full laser beam aperature. (c). Laser energy = 100 mJ. Full laser beam aperature. (d). Laser energy = 140 mJ. Full laser beam aperature.

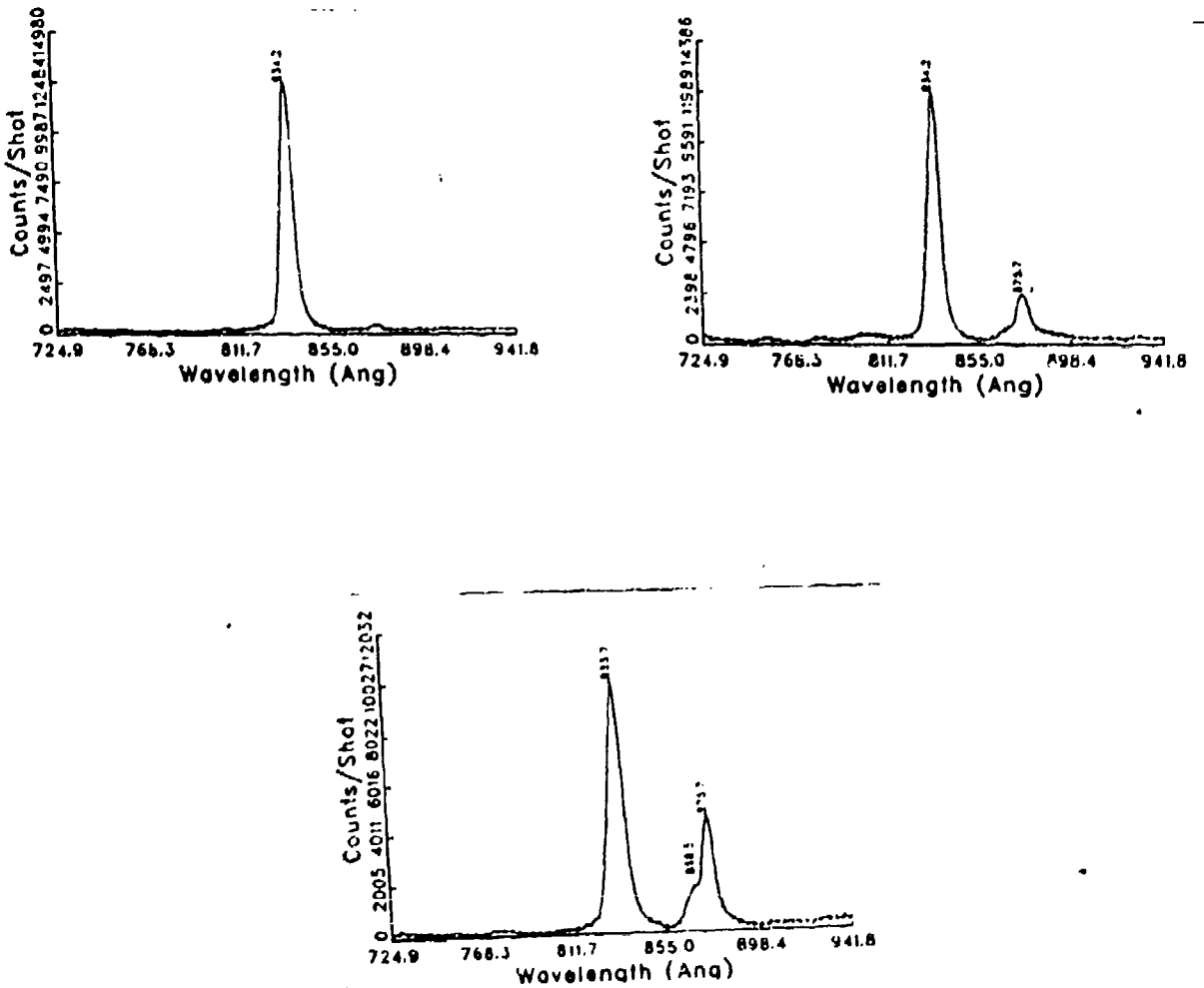

Figure 12. Argon spectrum illustrating the growth of lines near the third harmonic as the pulsed valve backing pressure is increased. (a). 20 psi. (b). 30 psi. (c). 40 psi. Note that as the 87–nm line grows, the third harmonic decreases.

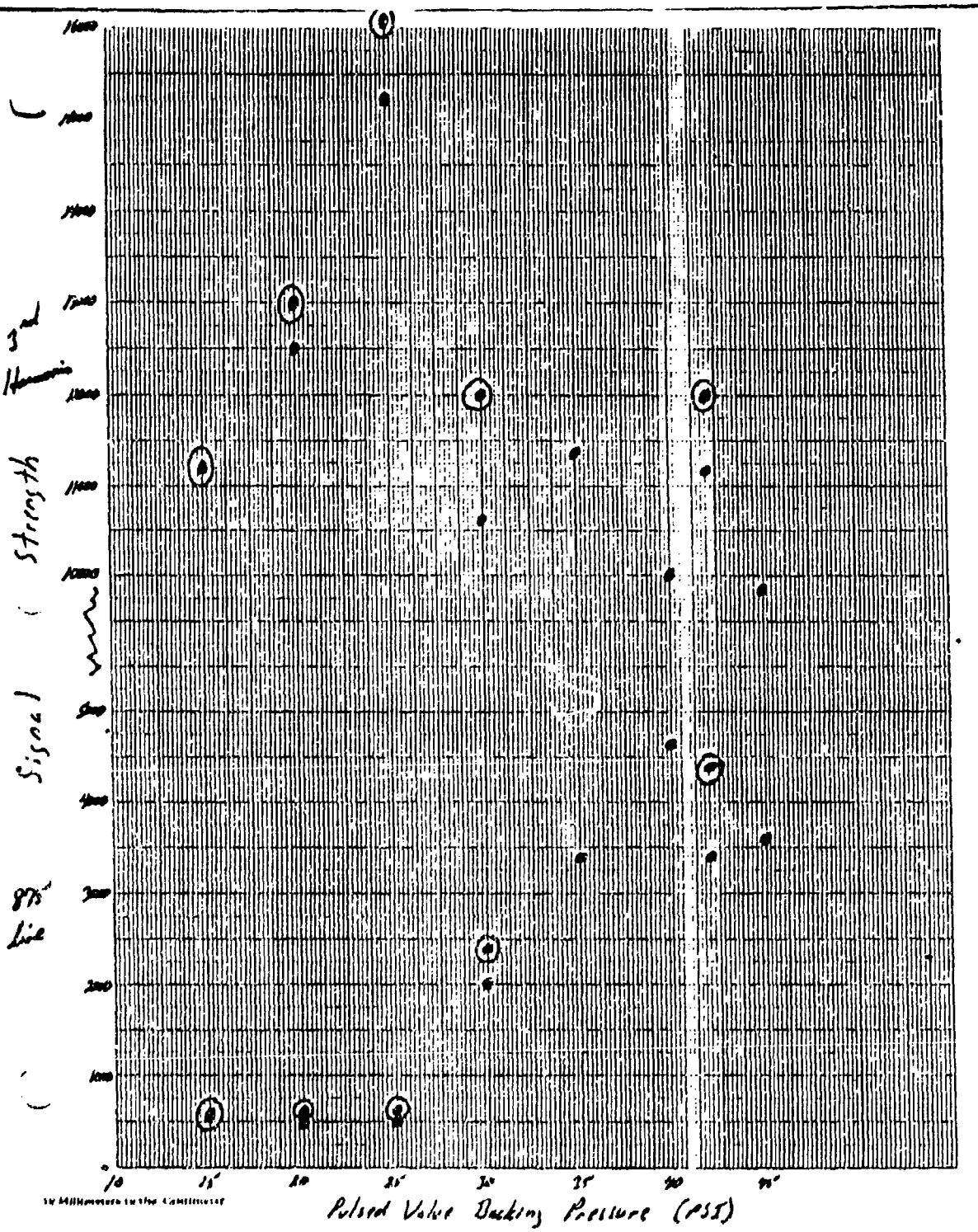

Figure 13. Plot of the signal strength vs pulsed valve backing pressure of the third harmonic and 87-nm line in argon. The backing pressure was increased (dots) and then decreased (circled dots) to demonstrate that the result was repeatable.

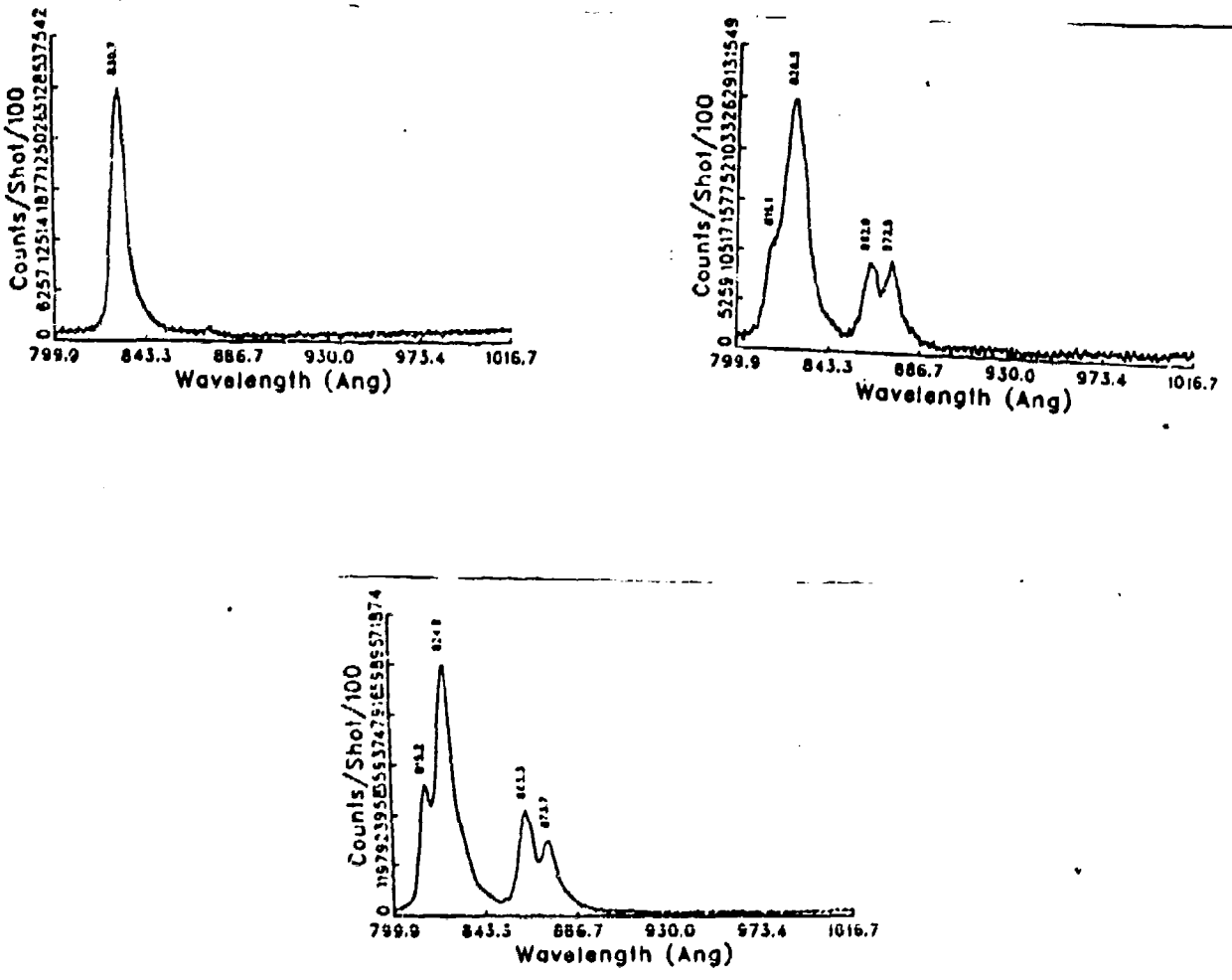

Figure 14. Using a 23 cm long capillary tube with a 750 μm bore, the region of Ar spectrum around the third harmonic changes as the target density is changed by varying the delay between the laser fire signal and the turn on of the pulsed valve. (a). 500 μsec. (b). 1000 μsec. (c). 1500 μsec.

fashion. Note the presence of the 87 nm feature as seen in Figure 12 and that the third harmonic has decreased significantly while lines at lower wavelength have appeared to replace it. Changing the timing was a more accurate and reproducible method of changing the target density than changing the pulsed valve backing pressure on the present setup.

When a 9 cm long capillary tube with a 0.75 mm bore was used with Ar as the target gas, the basic spectrum was not changed. However, the variation with target density did become more pronounced. Figure 15 illustrates the variation in the third harmonic region and the 87–nm region as the target density was changed. Note the sharp growth of the signal in the 87–nm region and its near equal intensity with the third harmonic region once it is established. More about this variation with target density will be discussed later in association with the observed change in the N_2 spectrum.

B. Grazing Incidence Spectrometer

The instrumentation was changed to the GIS to obtain better resolution of the observed spectrum. In order to reduce the absorption of emitted radiation along the capillary tube axis, a 40 mm long capillary with a 0.75 mm bore was used. Since no new spectral lines were seen, the region around the third harmonic was selected for a more detailed study. Figure 16 illustrates the results. The laser energy was ≈200 mJ or greater. The target gas density was changed by using a capacitance manometer to monitor the pulsed valve backing pressure. Accurate reproducable low backing pressures to the pulsed valve were achieveable by this method. The time delay between the laser fire signal and the pulsed valve open signal was held constant. It was selected so that the gas flow had reached the end of the capillary bore, but not yet reached a maximum value. Considerable structure was found in the region of the third harmonic as the target gas density was changed. None of the lines could be identified with the known spectrum of argon.

fashion. Note the presence of the 87–nm feature as seen in Figure 12 and that the third harmonic has decreased significantly while lines at lower wavelength have appeared to replace it. Changing the timing was a more accurate and reproducible method of changing the target density than changing the pulsed valve backing pressure on the present setup.

When a 9 cm long capillary tube with a 0.75 mm bore was used with Ar as the target gas, the basic spectrum was not changed. However, the variation with target density did become more pronounced. Figure 15 illustrates the variation in the third harmonic region and the 87–nm region as the target density was changed. Note the sharp growth of the signal in the 87–nm region and its near equal intensity with the third harmonic region once it is established. More about this variation with target density will be discussed later in association with the observed change in the N_2 spectrum.

B. Grazing Incidence Spectrometer

The instrumentation was changed to the GIS to obtain better resolution of the observed spectrum. In order to reduce the absorption of emitted radiation along the capillary tube axis, a 40 mm long capillary with a 0.75 mm bore was used. Since no new spectral lines were seen, the region around the third harmonic was selected for a more detailed study. Figure 16 illustrates the results. The laser energy was ≈200 mJ or greater. The target gas density was changed by using a capacitance manometer to monitor the pulsed valve backing pressure. Accurate reproducable low backing pressures to the pulsed valve were achieveable by this method. The time delay between the laser fire signal and the pulsed valve open signal was held constant. It was selected so that the gas flow had reached the end of the capillary bore, but not yet reached a maximum value. Considerable structure was found in the region of the third harmonic as the target gas density was changed. None of the lines could be identified with the known spectrum of argon.

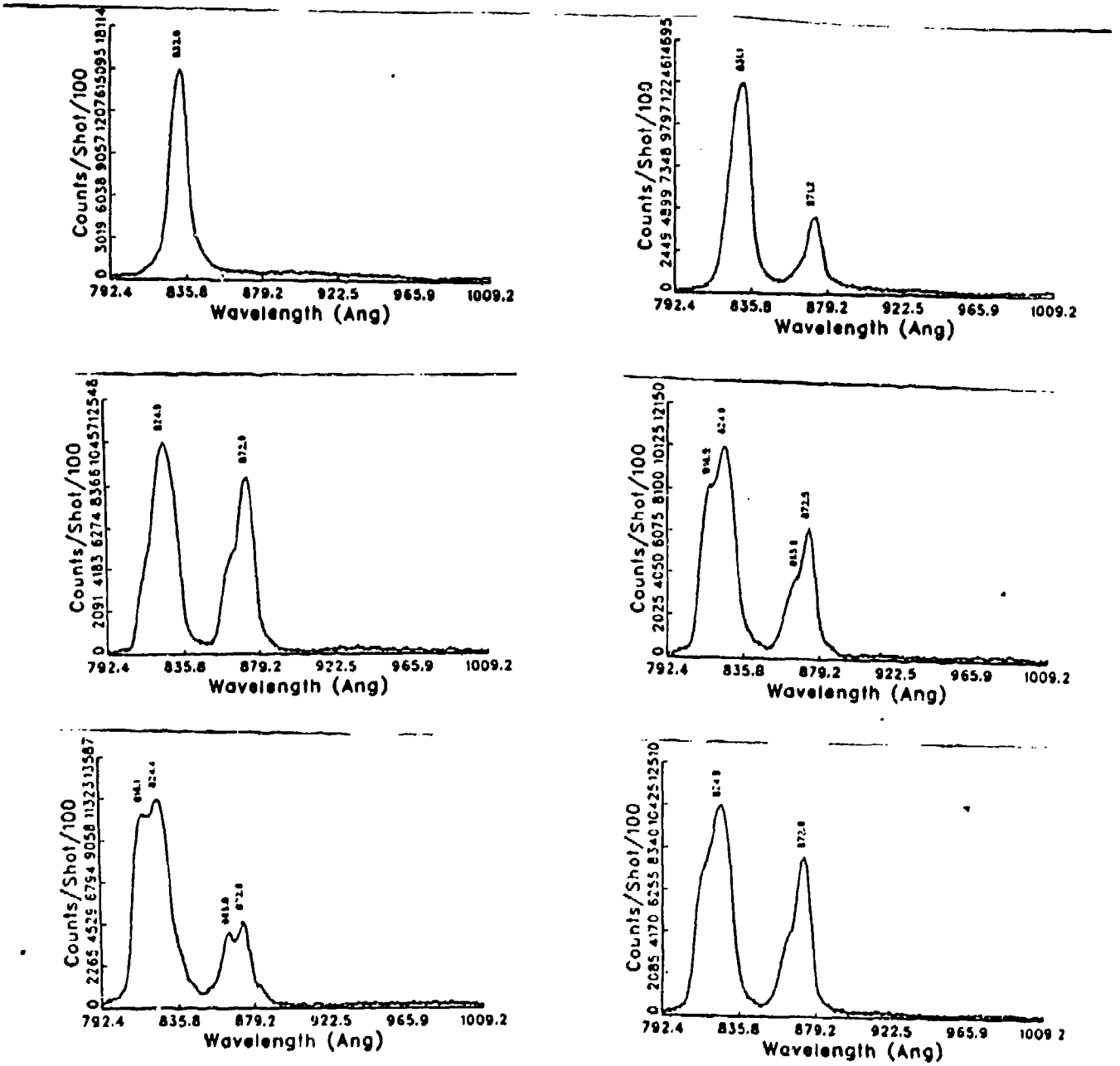

Figure 15. Using a 9 cm long capillary tube with a 750 μm bore, the region of Ar spectrum around the third harmonic exhibits simular structure as illustrated in Figure 14. (a). 250 μsec. (b). 500 μsec. (c). 750 μsec. (d). 1000 sec. (e). 1500 μsec. (f). 2000 μsec.

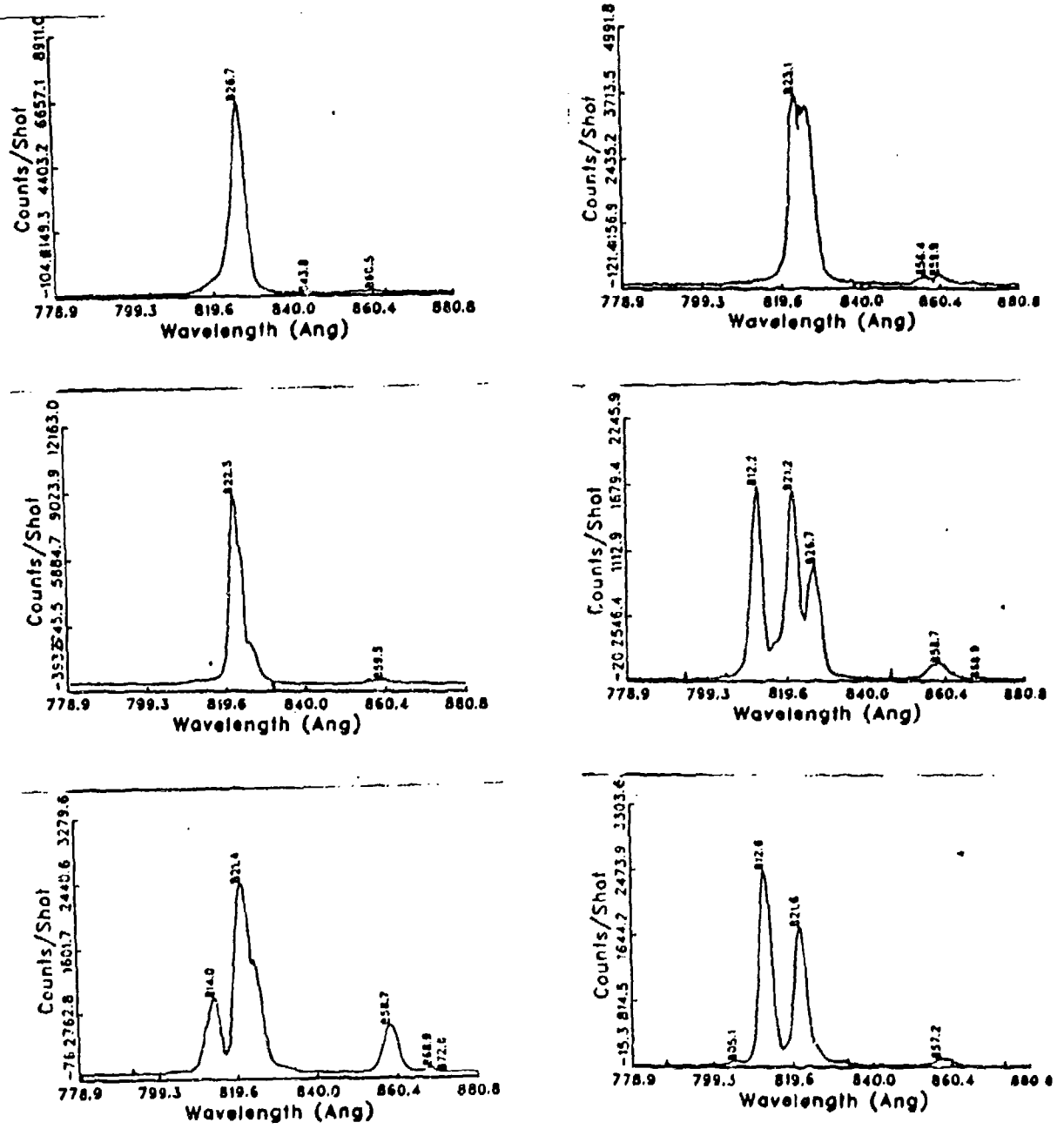

Figure 16. Using a 4 cm long capillary tube with a 750 μm bore, a more detailed Ar spectrum around the third harmonic is obtained with the GIS. The target density was now changed by varying the pulsed valve backing pressure. (a). 200 torr. (b). 325 torr. (c). 550 torr. (d). 760 torr (e). 1975 torr. (f). 2475 torr.

The capillary tube was changed to one which was 30 mm long and had a bore diameter of 0.25 mm. The results for the region around the third harmonic are illustrated in Figure 17. Again the structure around the third harmonic is distinct as the target gas pressure is increased. With the smaller bore capillary tube, the structure is more quickly achieved as the target gas density is increased and the structure extends over a greater wavelength range. Once the extended structure is established, the observed lines exhibit a strong dependence upon laser energy. Rarely do all of the lines appear together during a single laser shot, rather they jump in and out depending upon the laser energy. This is evident in Figures 17e and 17f in which the target gas density changes little, yet the spectrum changed noticeably.

The most unusual feature found in the Ar spectrum involves the 63–nm line, see Figure 10. This line was found to exhibit amplification! While the amplification is small, only $\approx 1.4\ cm^{-1}$, it did seem to lend creedance to the idea that this capillary target geometry could be longitudinally multiphoton pumped to produce lasing. Not only did this line exhibit gain, but it also exhibited line narrowing. Figure 18 illustrates the increase in signal and the decrease in line width as a function of pulse valve backing pressure.

The difficulty in understanding the 63–nm line in Ar is manifested by the discovery that many of the lines observed around the third harmonic and 87 nm could fit into a parametric process involving six wave mixing. For details, see Appendix C. Figure 19 illustrates the various six wave mixing processes identified. That six wave mixing had never been reported in Ar was not the problem. The 63–nm line playing a prominent role in the six wave mixing process does present a problem. If the 63–nm line is the result of six wave mixing, it can exhibit gain. However, it is not clear that such a parametric process would exhibit line narrowing. The measurement was repeated with the same results, a rapid increase

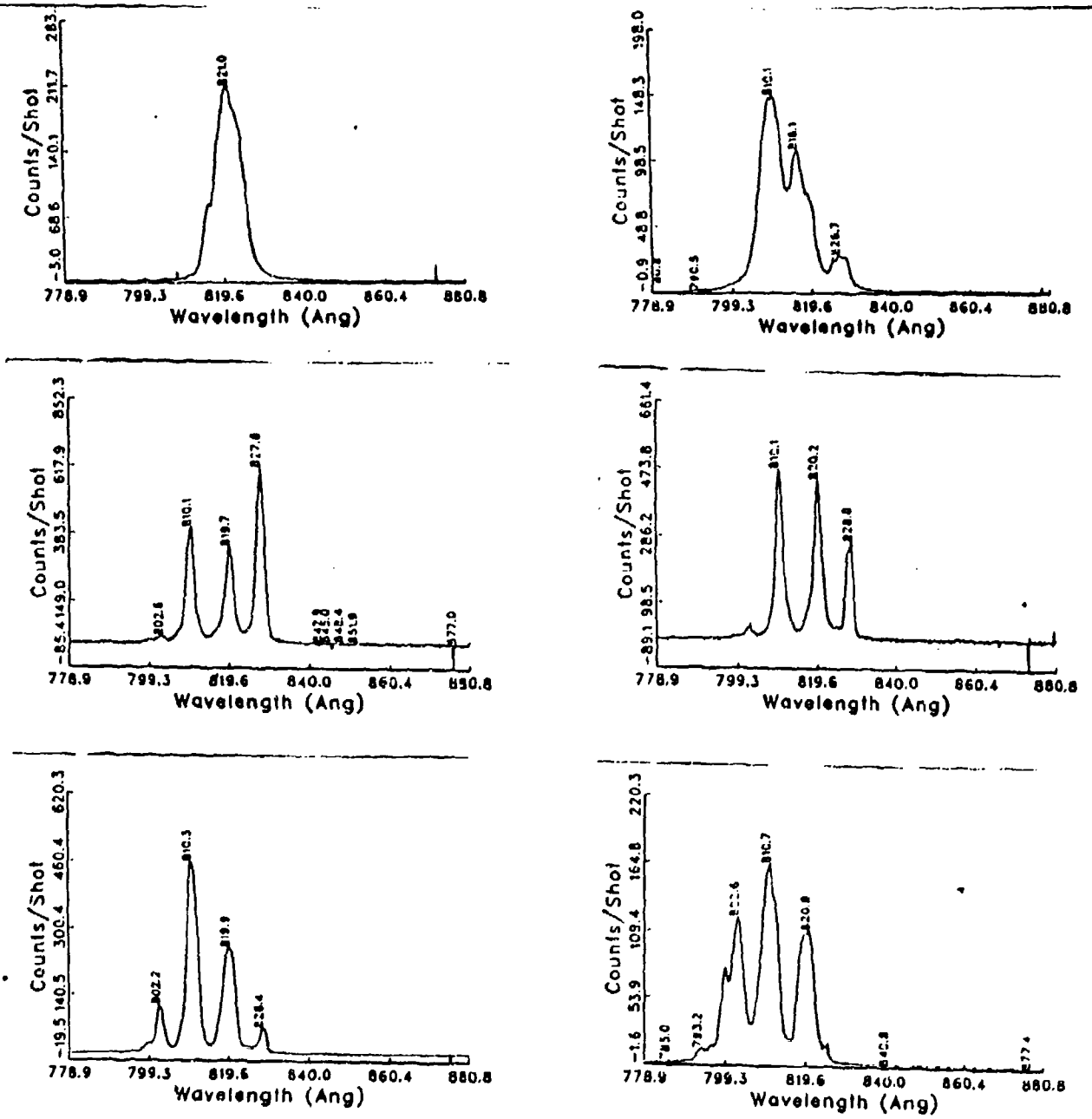

Figure 17. Argon spectrum around the third harmonic using a 3 cm long capillary tube with a 250 μm bore. Note the increase in structure compared to Figure 16. The pulse valve backing pressure is: (a) 50 torr; (b) 290 torr; (c) 620 torr; (d) 1040 torr; (e) 1950 torr; (f) 2000 torr.

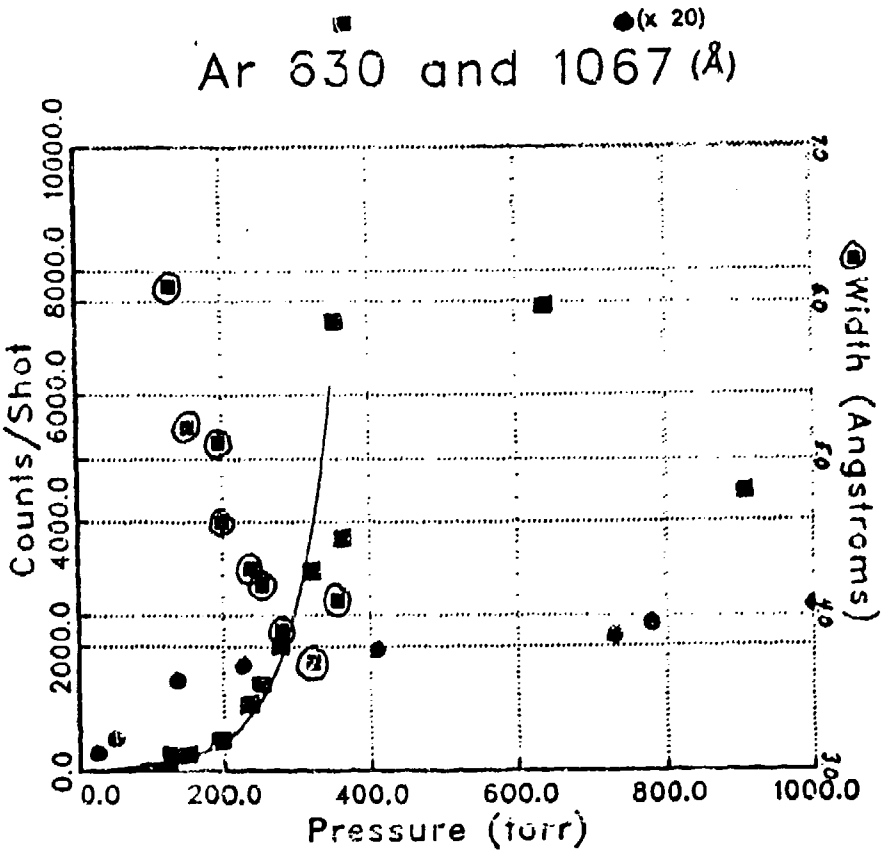

Figure 18. The appearent gain in the 63–nm argon line is compared to the known argon resonance line at 106.7 nm. During the increase in 63–nm signal, this line exhibited line narrowing.

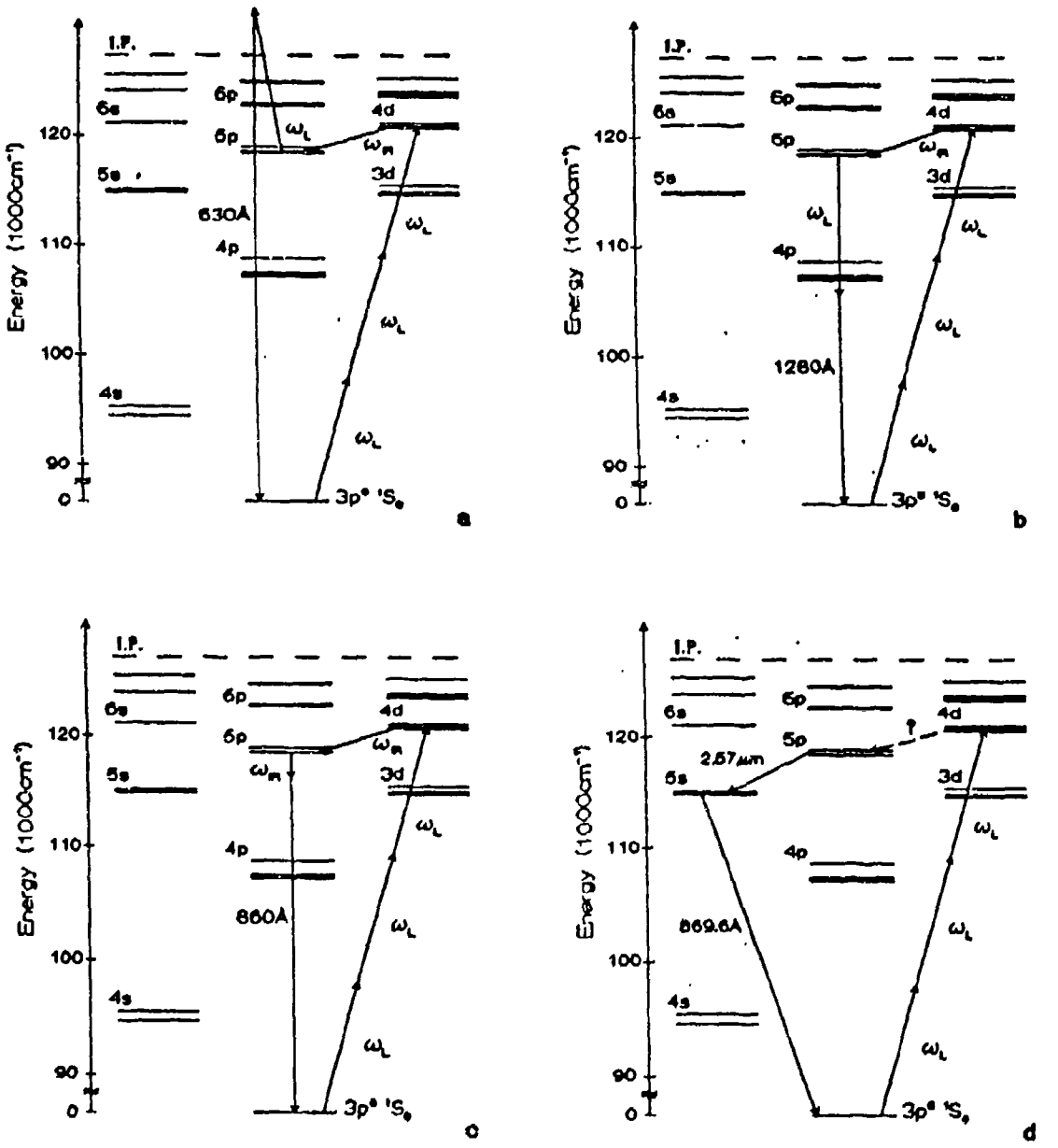

Figure 19. Four argon energy level diagrams illustrating six-wave mixing processes which could account for some of the observed radiation. The dotted arrow in (d) is a predicted but unconfirmed transition at 5.78 μm.

in signal to a saturation point as the target gas density is increased and a corresponding linewidth decrease. These aspects of the behavior remain to be completely understood.

Nitrogen was an important target gas to consider for these capillary tube target experiments because of the results obtained from multiphoton ionization experiments as well as the radiation experiment results obtained from using a gas jet target.[11–13] Previous measurements on molecules suggested that molecular species would exhibit interesting properties in regard to the production of excited states. Moreover, the previous N_2 work implied that more complicated molecular species containing high Z material symmetrically surrounded by lighter material could be better candidates for target gases.[14]

When N_2 was used as the target gas in a 23 cm long capillary tube with a 0.75 mm bore, qualitatively similar results were obtained. The spectrum illustrated in Figure 20 shows a strong third harmonic, a weak fifth harmonic and a few weak unidentified lines. Regions of the spectrum not illustrated were devoid of spectral lines. Figure 21a–b and 21c–e illustrate the rapid change in line intensity as the target density is changed by increasing the delay between the laser fire signal and the pulsed valve open signal. The results are the same as observed in Ar, especially as pertains to the region around the third harmonic.

Later a 9 cm long capillary tube with a 0.75 mm bore was used as the target geometry. The typical N_2 spectrum obtained is illustrated in Figure 22. Basically there is no change in the spectrum from using the much longer 23 cm capillary tube except for the few additional longer wavelengths. Using the shorter capillary tube did result in a significant change in the observed spectrum when the target density was changed by altering the time delay between the laser fire command and the pulse valve open command. Figures 23 and 24 illustrate the point. Figures 23a–b show a dramatic change in the third harmonic with it being completely replaced by

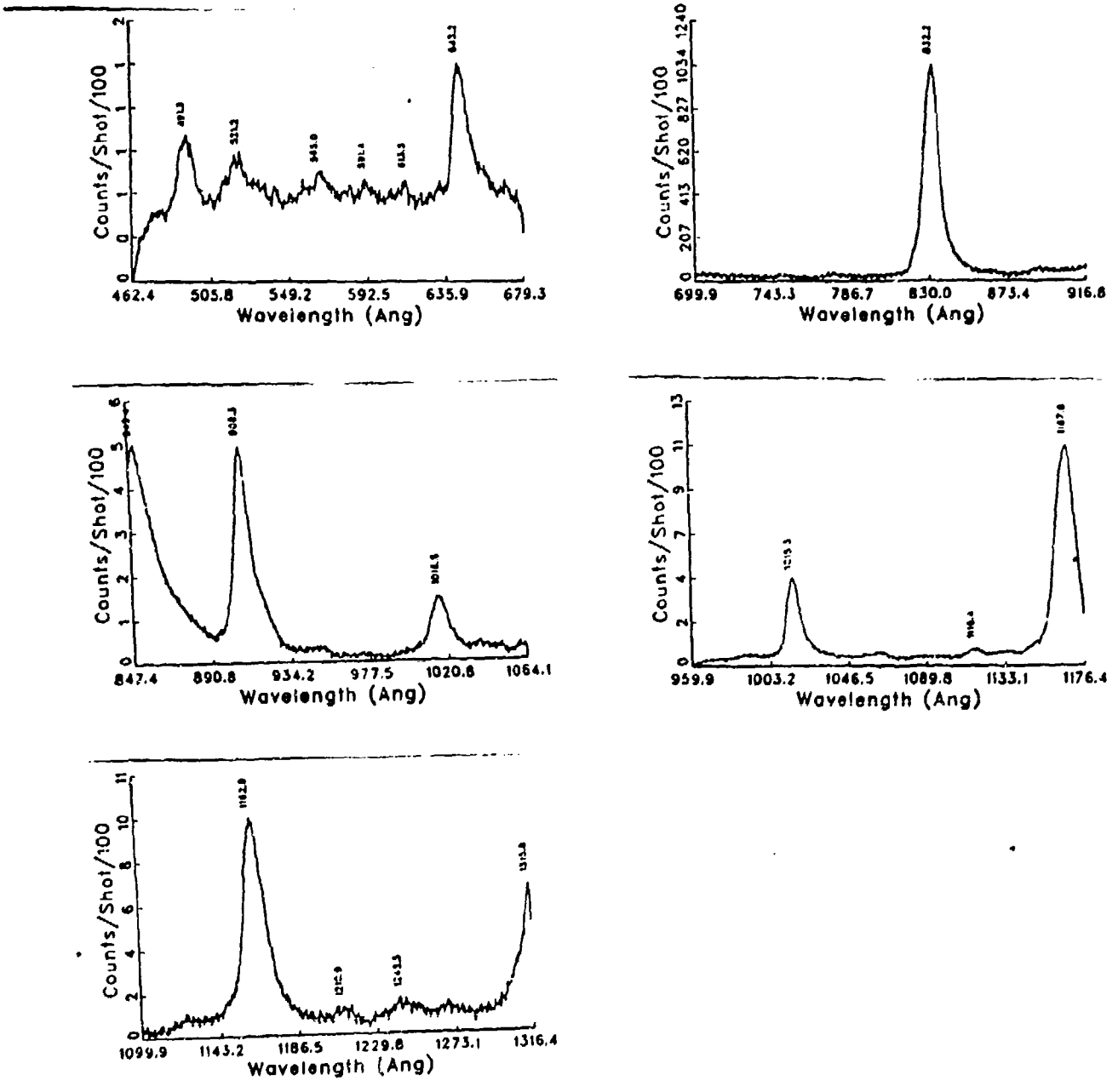

Figure 20. Nitrogen spectrum obtained using a 23 cm long capillary tube with a 750 μm bore.

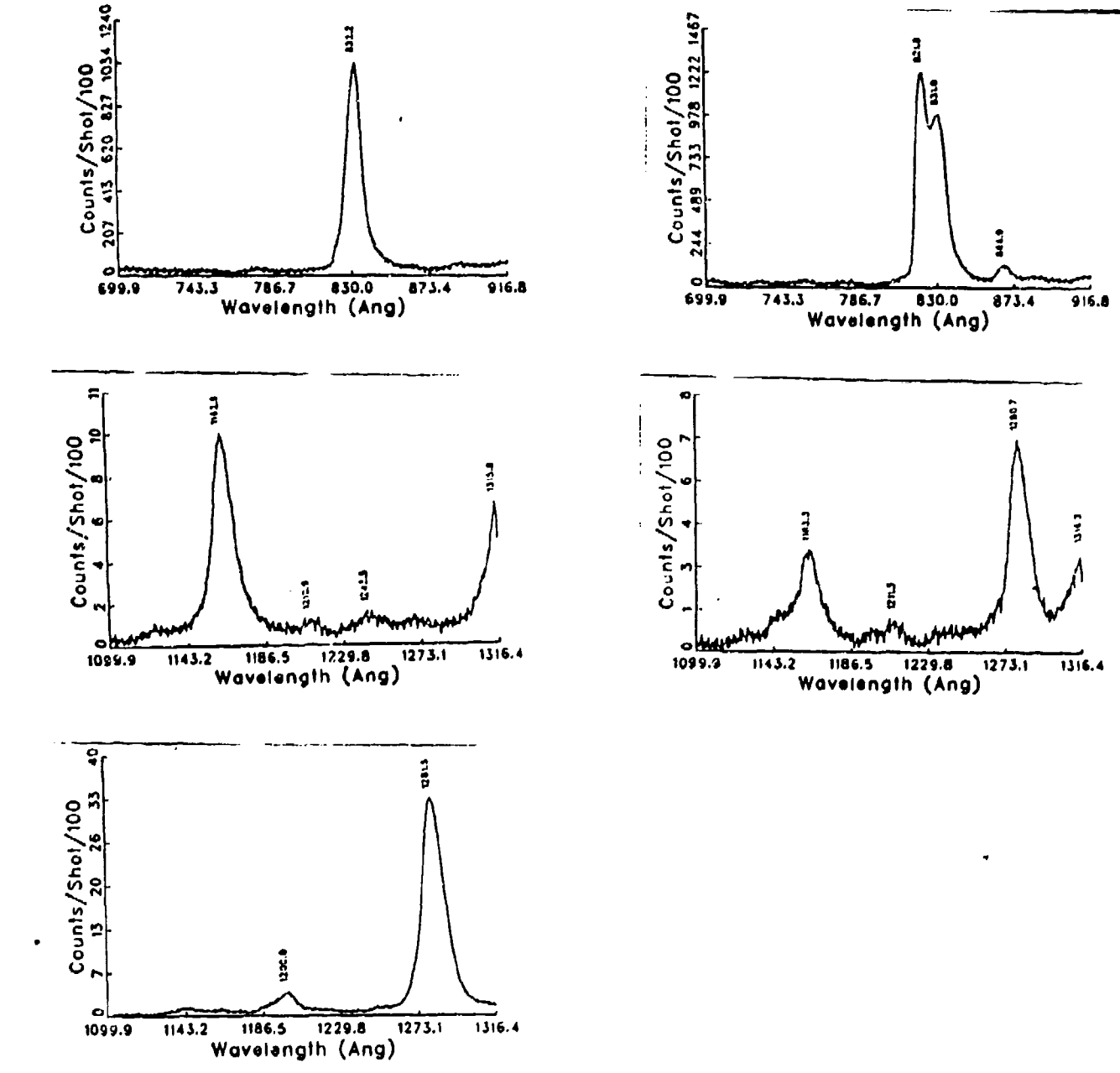

Figure 21. Nitrogen spectrum obtained using a 23 cm long capillary tube with a 750 µm bore. Note the rapid change in the line structure as the target density is changed by altering the time delay between the laser fire signal and the pulsed valve open signal. (a). 500 µsec. (b). 1500 µsec. (c). 500 µsec. (d). 750 µsec. (e). 1000 µsec.

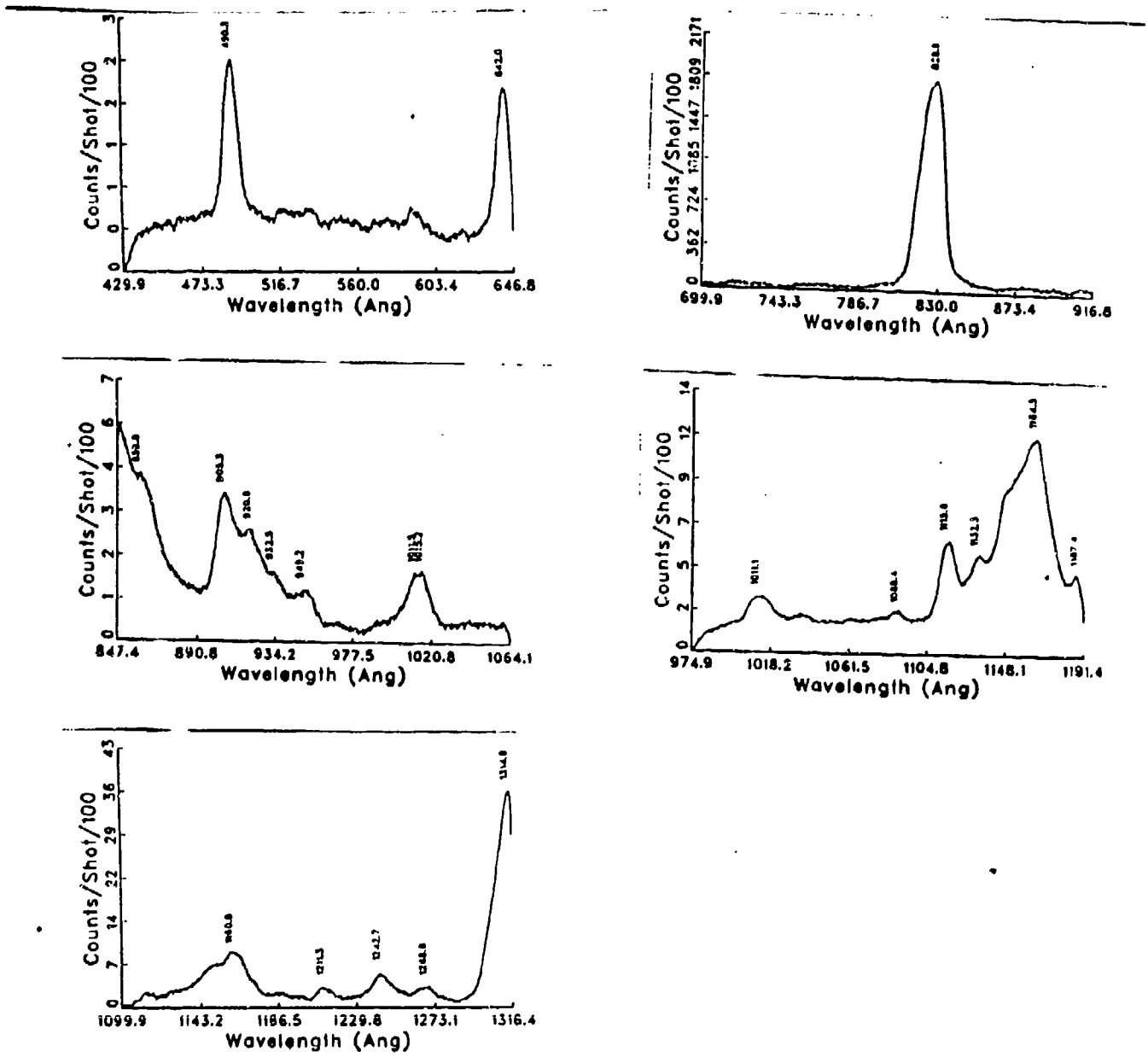

Figure 22. Nitrogen spectrum obtained using a 9 cm long capillary tube with a 750 µm bore. Note the longer wavelengths.

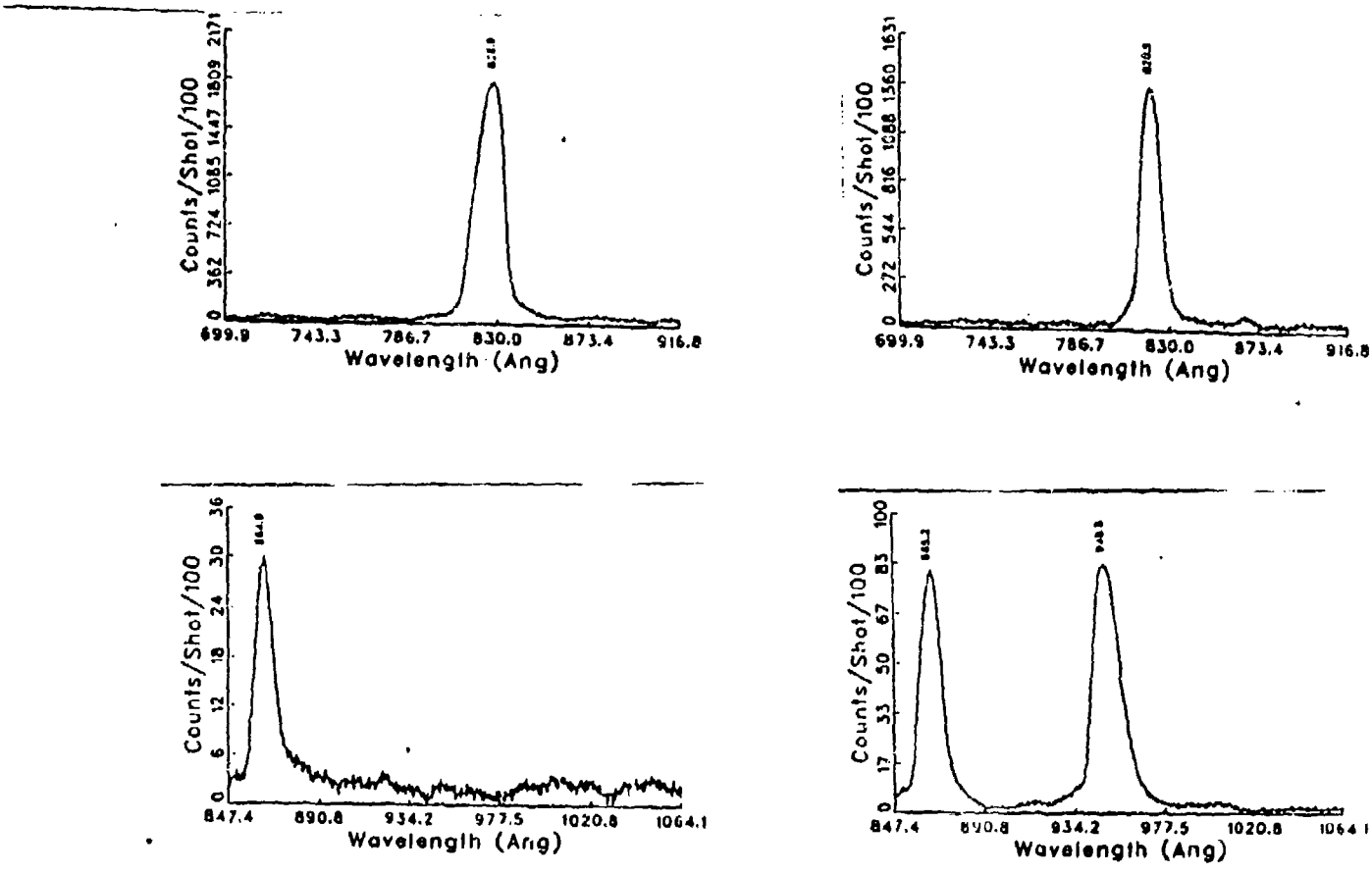

Figure 23. Changing the N_2 target density by varying the time delay significatly altered the spectrum. (a). 500 µsec. (b). 1500 µsec. (c). 750 µsec. (d). 1000 µsec.

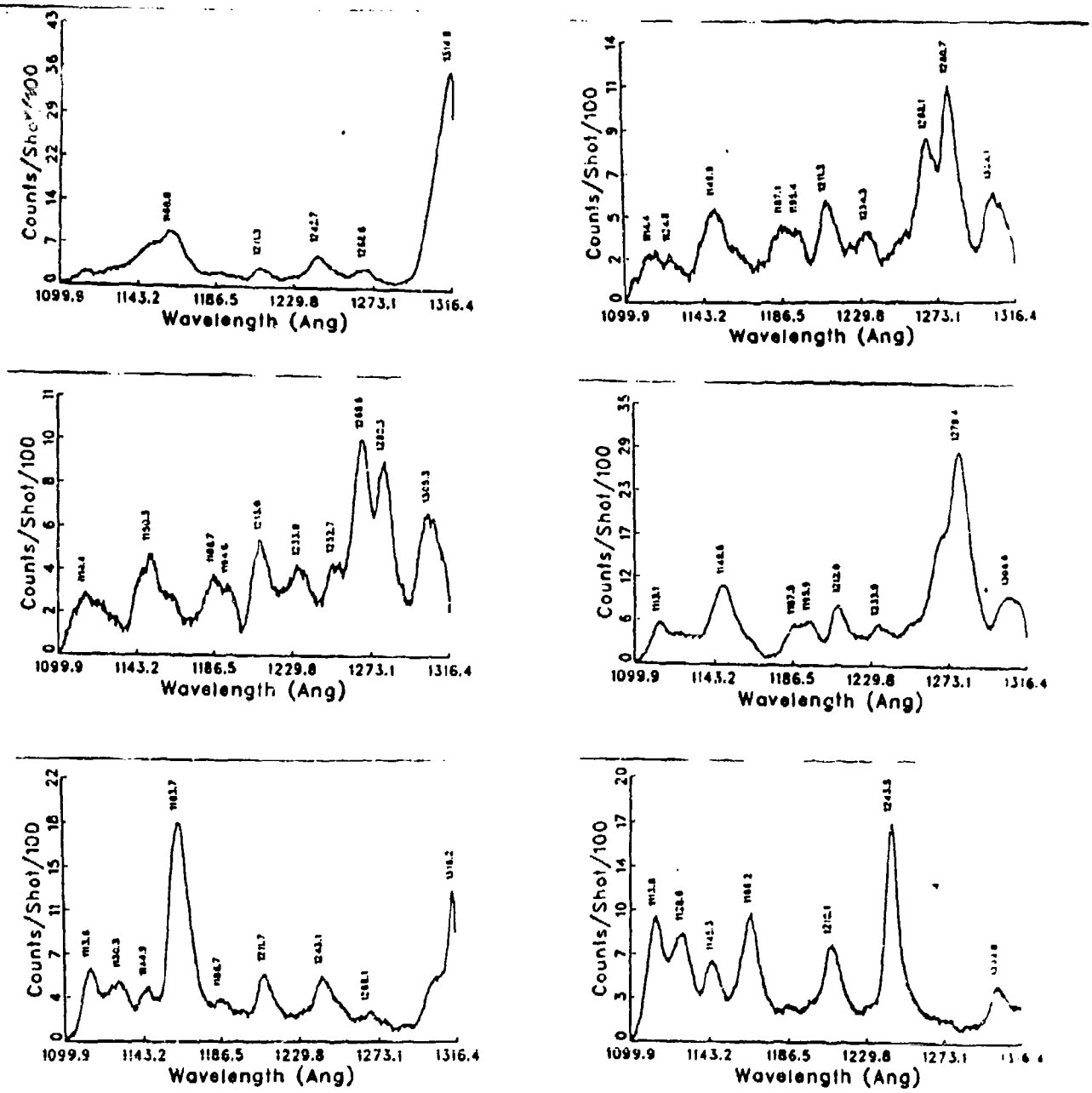

Figure 24. Changing the N_2 target density by varying the time delay significantly altered the spectrum. (a). 500 μsec. (b). 1000 μsec. (c). 1500 μsec. (d). 2000 μsec. (e). 3000 μsec. (f). 4000 μsec.

a new line of equal strength while Figures 23c–d show an equally dramatic variation concerning the line at ≈95 nm. The variation of the spectral line intensities observed in Figure 24 is difficult to explain on the basis of only a changing target density. The pulsed valve is turned on for approximately 250 μsec. During this time gas is flowing into the small reservoir seperating the pulsed valve body and the capillary bore. The pulsed valve closed before the gas reached the end of the capillary bore at approximately 500 μsec. Changes in the spectrum are expected to occur as the target gas density increases and the capillary tube is filling with gas. This change is clearly evident in Figures 24a–b. When the capillary tube was filled with gas and the gas density was maximized throughout this volume, the spectrum should exhibit little change for some range of timing change. This is clearly shown in Figures 24b–c. Beyond this time delay the target gas density is decreasing. As the time delay is increased, the resulting spectrum should reproduce the spectrum seen with a small time delay. Figures 24d–f show that this is clearly not happening. What are the differences in the target between Figures 24a and 24f which could account for this variation in observed spectrum? They are three. First the target gas density really is different. In Figure 24f the target gas density is the result of residual gas remaining in the capillary tube. In Figure 24a the gas is beginning to flow into the capillary tube but has not yet reached the end of the tube. Second, the resulting lengths of the target gas are different for the reason stated above. The target gas density integrated along the interaction length should be much less in Figure 24f than in Figure 24a, because of the much lower gas density. Third, the target gas density gradient in Figure 24f should be small, since the gas flow has ceased whereas in Figure 24a it should be large since the gas flow is just beginning, see Figure 5. This target gas density gradient is probably the dominating factor in the observed spectrum because the increased density gradient would have a strong effect upon the propagation of the laser

beam through the capillary tube.

Gas mixtures of N_2 and Ne were also tried. Neon was added because Ne is the best harmonic generator found to date for KrF^*.[5] Mixtures ranging from 10% Ne to 90% Ne were used. The resulting spectrum was either the same or the spectrum was weaker depending upon the spectral region. Variation in the shot to shot laser energy could have had an effect, but it was difficult to accurately monitor such behavior. The spectrum changed with each laser shot, but generally the time averaged spectrum exhibited little variation.

When the GIS was employed for greater resolution, emphasis was place upon the third harmonic region. Using a 30 mm long capillary tube with a 0.25 mm bore produced a spectrum strongly dependent upon target density, confocal parameter and shot to shot variation in laser energy. The results are summarized in Figure 25. Figures 25a–b illustrate the effect produced by increasing the confocal parameter and, hence, reducing the laser energy. Figure 25c–d illustrate the large variation in signal strength even when 10 laser shot averages were considered. Increasing the confocal parameter by aperturing down the laser beam had the effect of producing slightly shorter wavelengths when the target gas density was increased as illustrated in Figure 26.

A quick look was taken at the fifth harmonic. Similar structure was observed which varied over the accumalated 10 shot averages as illustrated in Figure 27.

The other target gases used, H_2, He, Ne, Kr, produced similar modulation of the third and fifth harmonic as a function of target gas density and laser energy. These results are summarized in Figures 28–31. A partial spectrum of Xe is included in Figure 32. Little was done with either Kr or Xe because of the ease in ionizing these gases. Ionization effectively prevents the laser beam propagation in the capillary tube as shown in Figure 9. The lines which were appearing in all of the gases around the harmonics were related to the fundamental or the harmonics

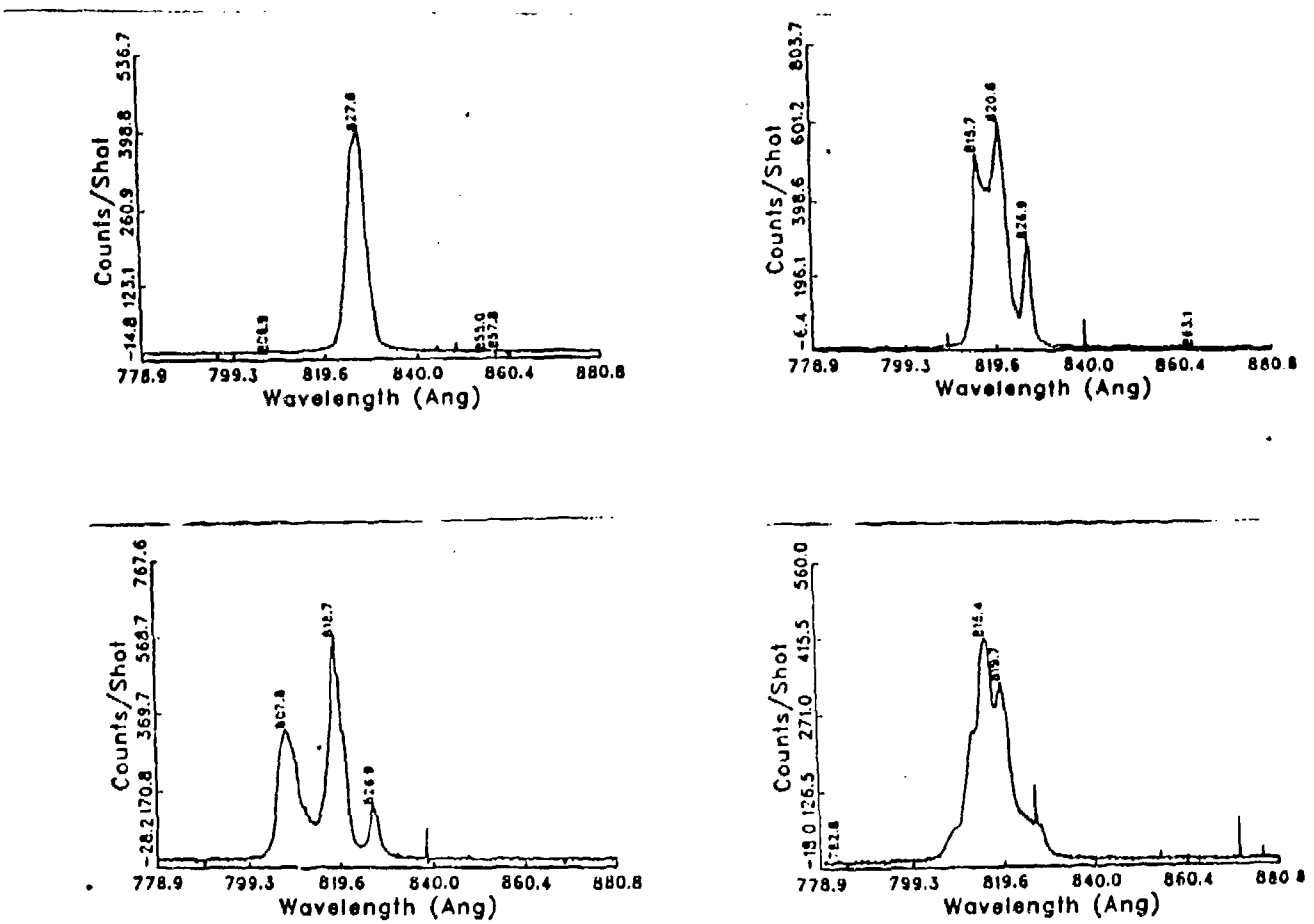

Figure 25. Nitrogen spectrum near the third harmonic using a 3 cm long capillary tube with a 250 μm bore. The spectrum changes with target density, confocal parameter as well as varied from shot to shot. (a). Pulsed valve backing pressure = 20 torr. Beam aperatured to 1" diameter. (b). Pulsed valve backing pressure = 50 torr. Full beam aperature. (c). Pulsed valve backing pressure = 100 torr. Full beam. (d). Pulsed valve backing pressure = 100 torr. Full beam.

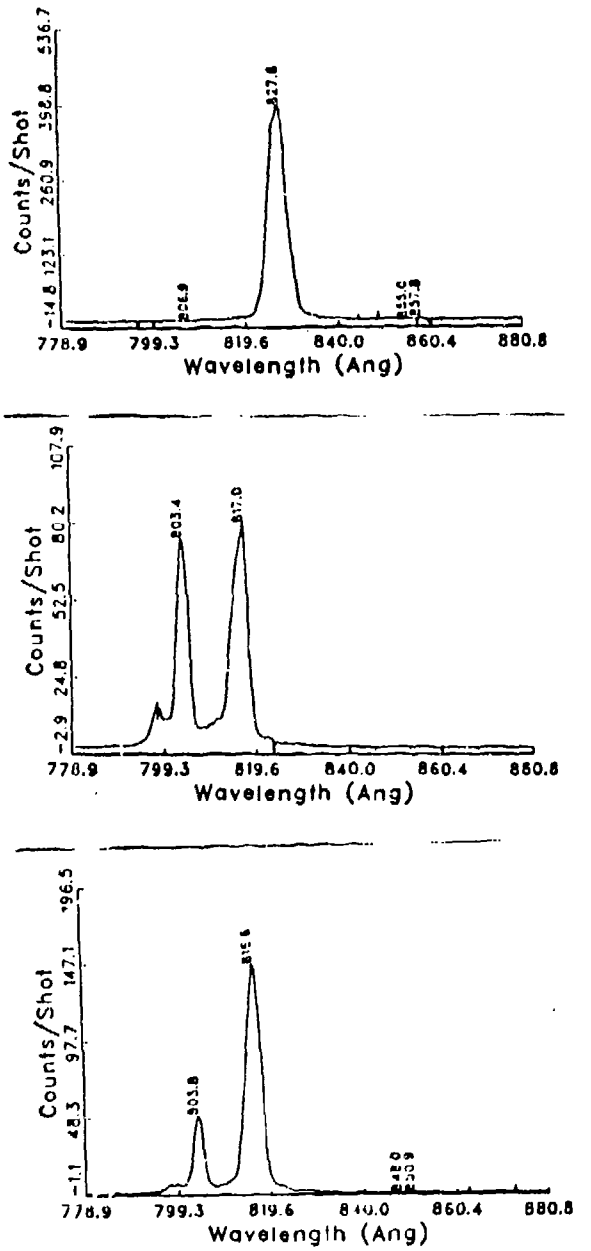

Figure 26. Nitrogen spectrum as in Figure 25 with the laser beam apertured to 1". The pulsed valve backing pressure was changed. (a). 20 torr. (b). 465 torr. (c). 700 torr.

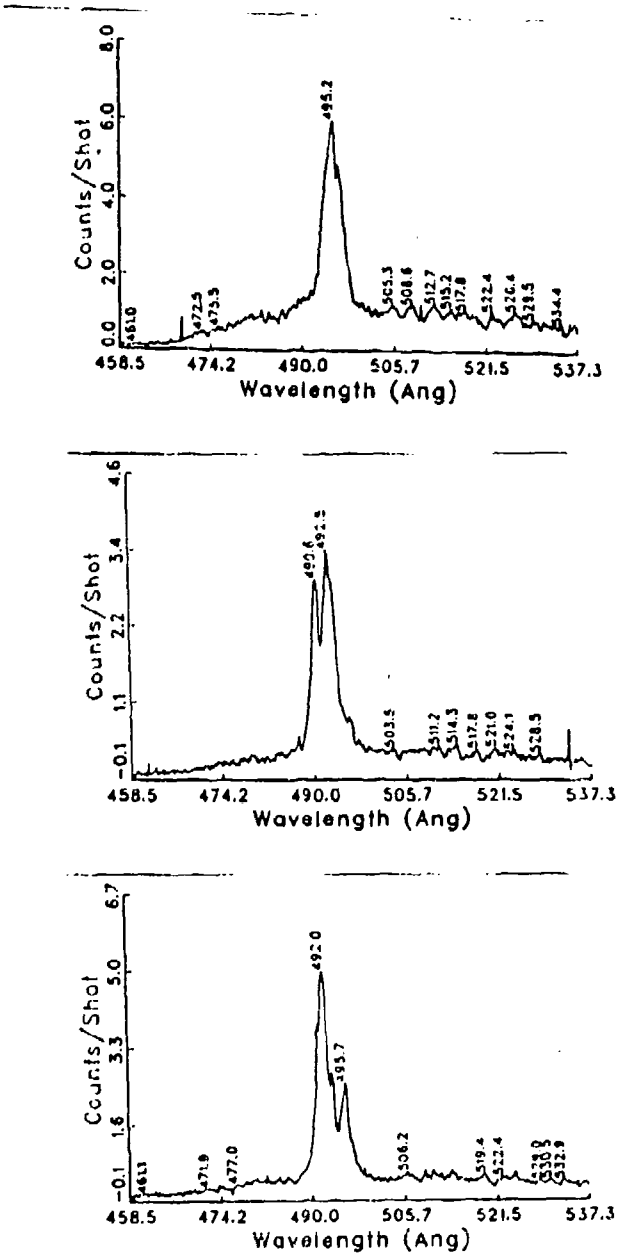

Figure 27. Nitrogen spectrum near the fifth harmonic showing that even here the spectrum changed as the target density was changed and that there varations over 10 shot averages. (a). 20 torr. (b). 50 torr. (c). 50 torr.

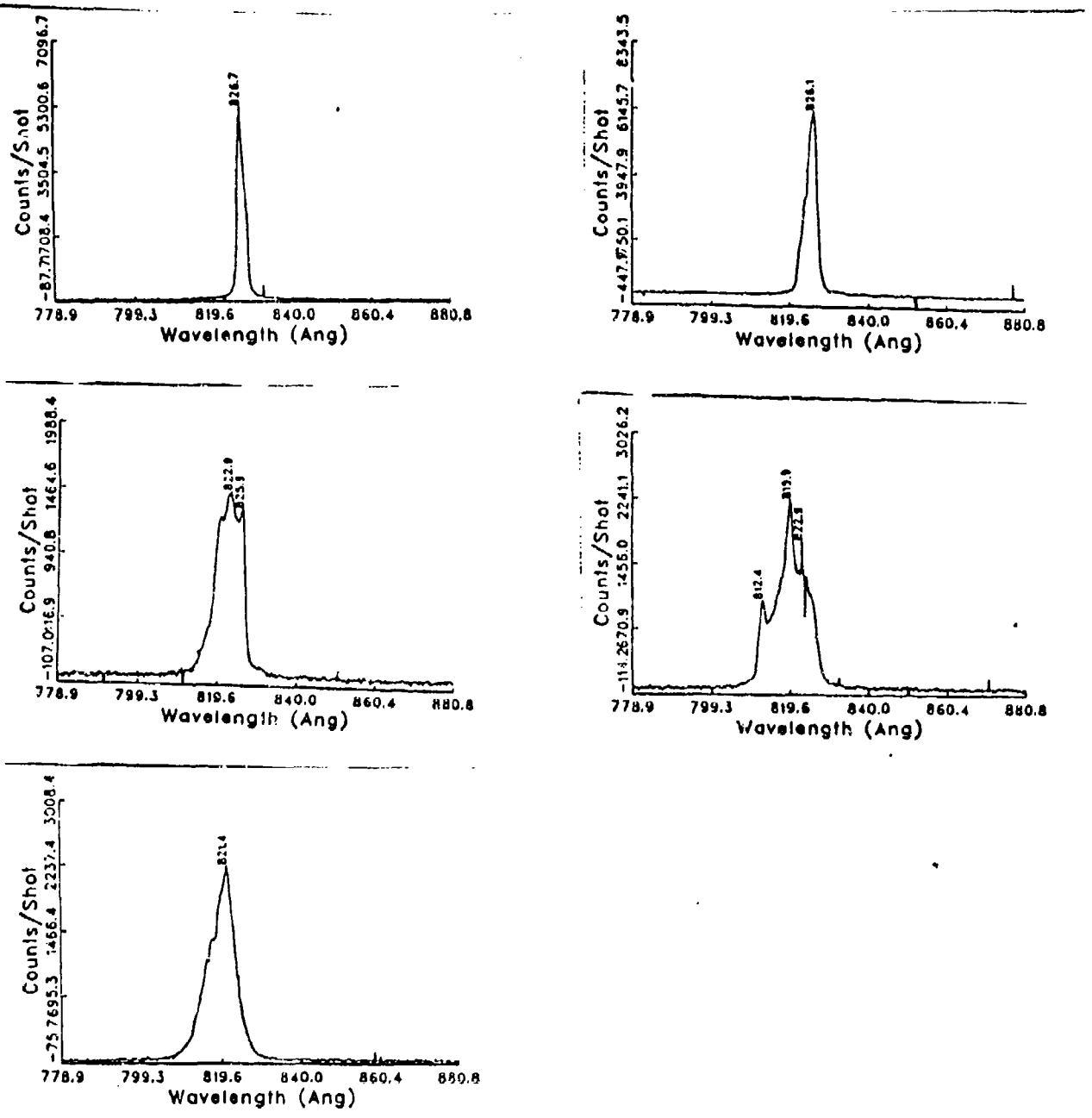

Figure 28. Hydrogen spectrum near the third harmonic showing the modulation obtained by varying the target density. Each spectrum is a ten shot average. (a). 30 torr. (b). 65 torr. (c). 105 torr. (d). 175 torr. (e). 250 torr.

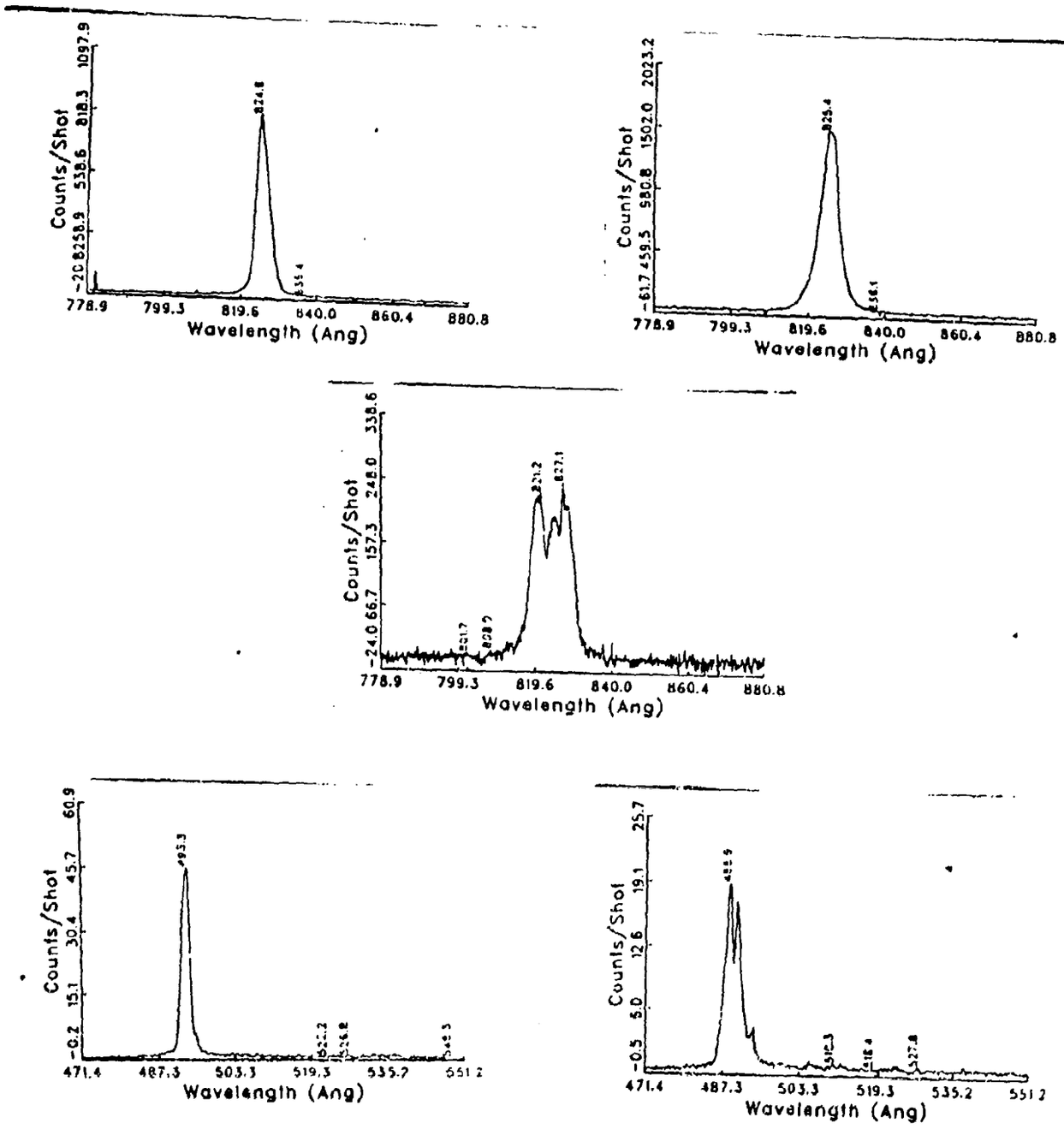

Figure 29. Helium spectrum near the third and fifth harmonic. Note the strong variation in the single shot plots. (a). 58 torr. 10 shots. (b). 750 torr. 10 shots. (c). 1400 torr. 1 shot. (d). 850 torr. 1 shot. (e). 850 torr. 1 shot.

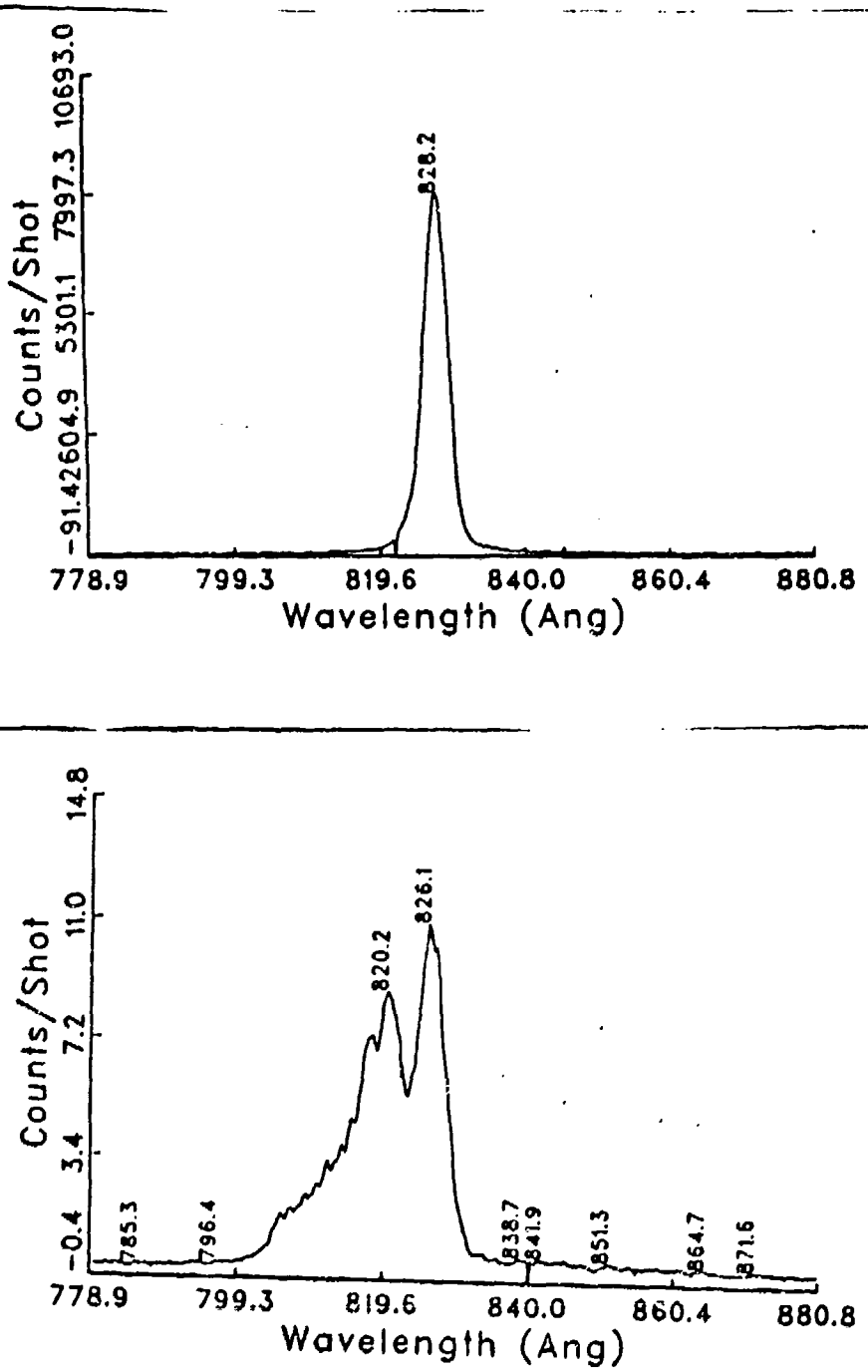

Figure 30. Neon spectrum near the third harmonic using 10 shot averages. (a). 105 torr. (b). 2050 torr.

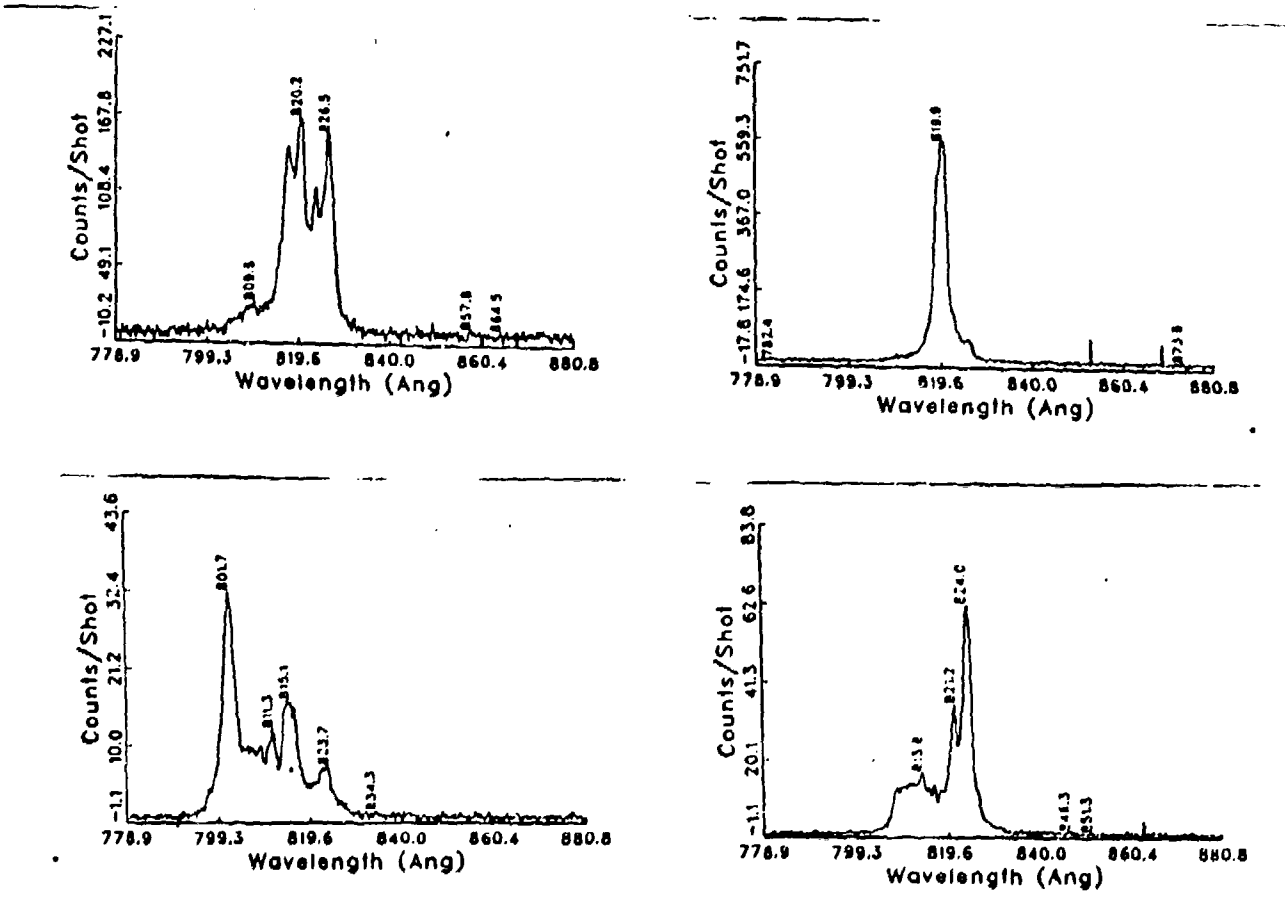

Figure 31. Krypton spectrum near the third harmonic. Single shot spectra. (a). 85 torr. Laser energy = 223 mJ. (b). 85 torr. Laser energy = 252 mJ. (c). 375 torr. Laser energy = 260 mJ. (d). 375 torr. Laser energy = 193 mJ.

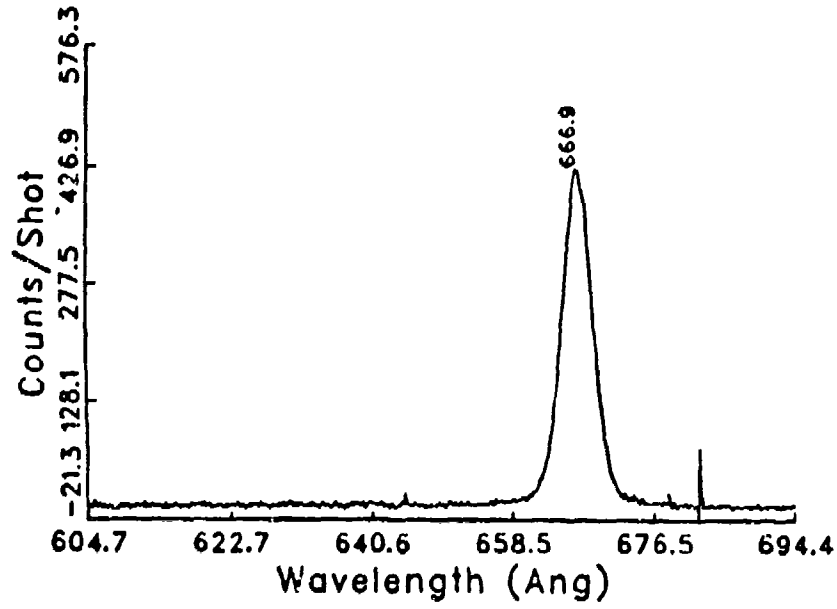

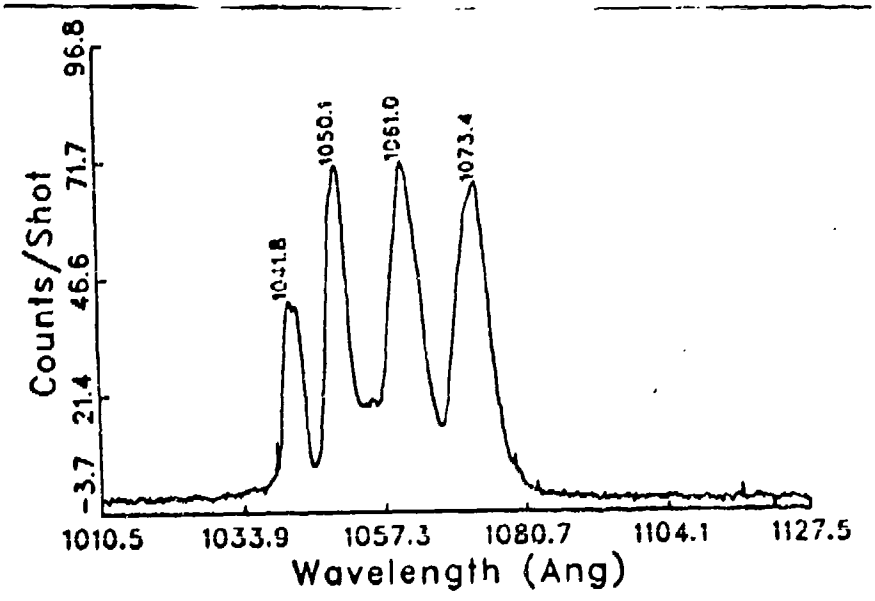

Figure 32. Partial xenon spectrum showing the strongest observed lines. (a). 297 torr. Laser energy = 99 mJ. (b). 628 torr. Laser energy = 77 mJ.

in some unknown way. It is not clear at present if they are due to a wave mixing process as discussed for the case of Ar, although a six-wave mixing scheme does exit in Xe.

IV. Photographic Study of Propagation in Static Gases

In addition to the longitudinal pumping studies using the capillary tube to obtain spectra, beam propagation was investigated by photographically recording the focal region in H_2, He and Air for different gas densities. Initially an f/10 lens system was used to focus ≈150 millijoules of energy in air. Figure 33 shows the typical results. The convergence of the incoming laser beam is observable as a blue glow due to excitation of the air. Once the laser intensity becomes sufficient to ionize the air, the observed emission becomes white. The resulting bright fireball at the focal zone of the lens system is the result of the explosion of the ionized gas. At this point the laser intensity is sufficient to significantly ionize N_2 and O_2 producing many free electrons. These electrons should change the refractive index of the surrounding space. Hence, the resulting plasma should have either absorbed the laser beam, deflected it or caused it to diverge. What the photograph clearly shows leaving the breakdown region is a beam with a cone angle less than that of the incoming laser beam. Either this emerging beam is the result of third harmonic excitation of the surrounding air, or some other process allowed the KrF^* beam to propagate through the breakdown region and emerge with a smaller divergence.

The results of focusing the laser beam in air lead to a more careful study of the laser beam propagation through static gas targets of various density. Now the KrF^* beam was focused using a 30 cm focal length aspheric mirror. With up to 200 mJ of energy available from the Prometheus amplifier, the maximum focal intensity is expected to reach 10^{19} W/cm^2. It is assumed that the laser beam was focusible to a spot size of 2 micrometers.[7]

Figures 34–38 illustrate some of the salient features of the laser beam

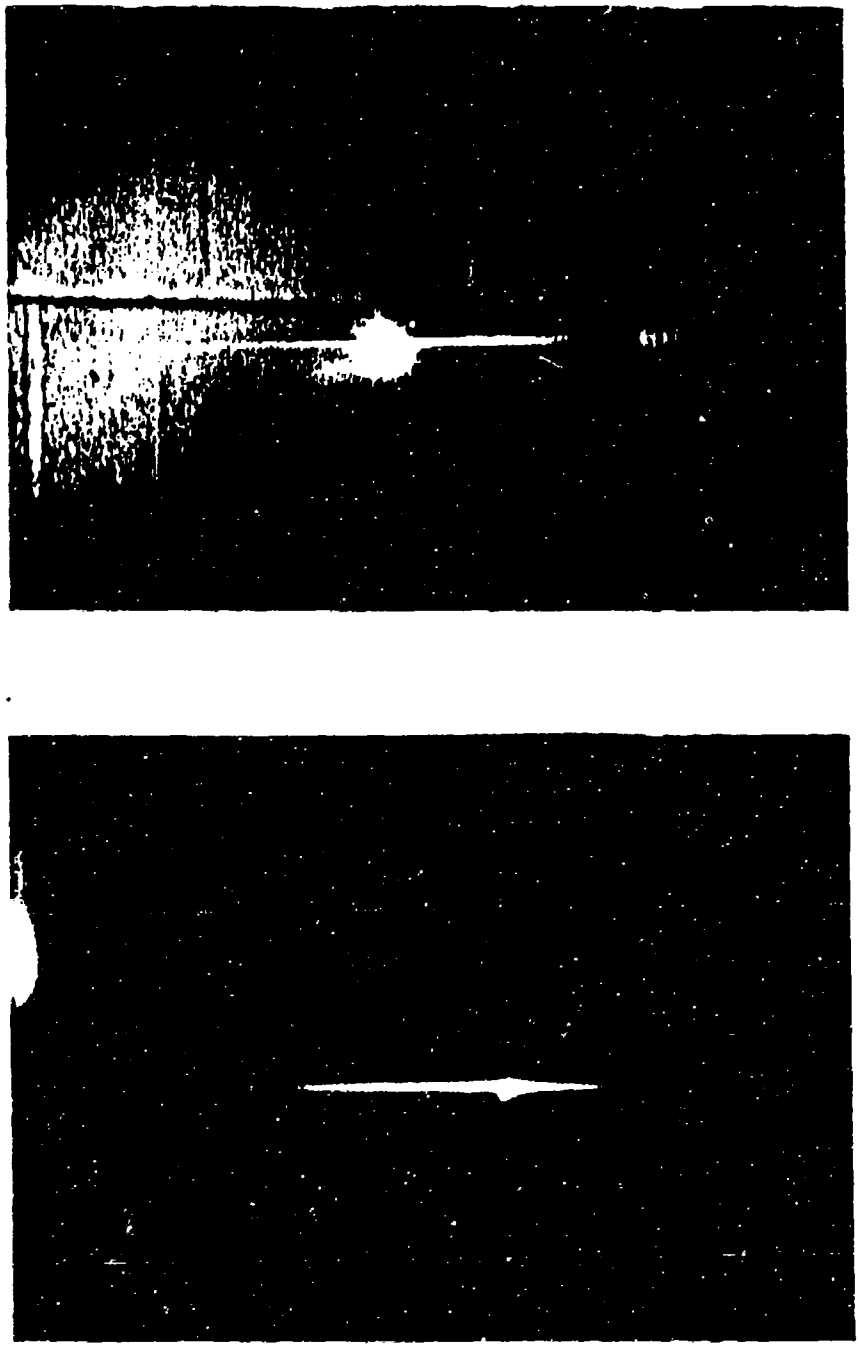

Figure 33. Laser beam focused in air using f/10 optics. In (a) note that the beam leaving the focal breakdown region has a smaller divergence than the incoming beam. In (b) note that the focus region has two lobes, the smaller one appearing just before the main breakdown.

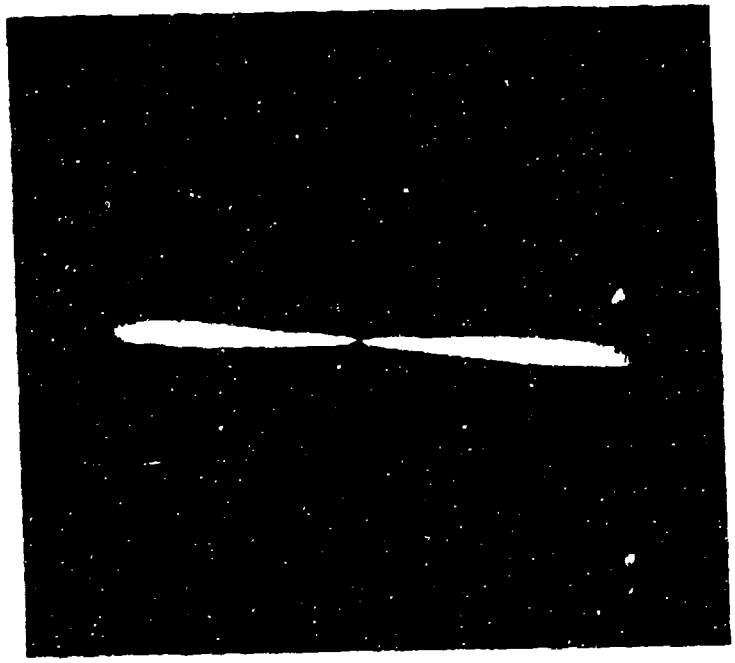

Figure 34. Laser beam focused into Xe at 0.59 torr pressure. Photo is single shot. Note the center dark region. This could be caused by either a lack of radiating target material in the focal volume or by the radiation in the focal volume being of higher energy.

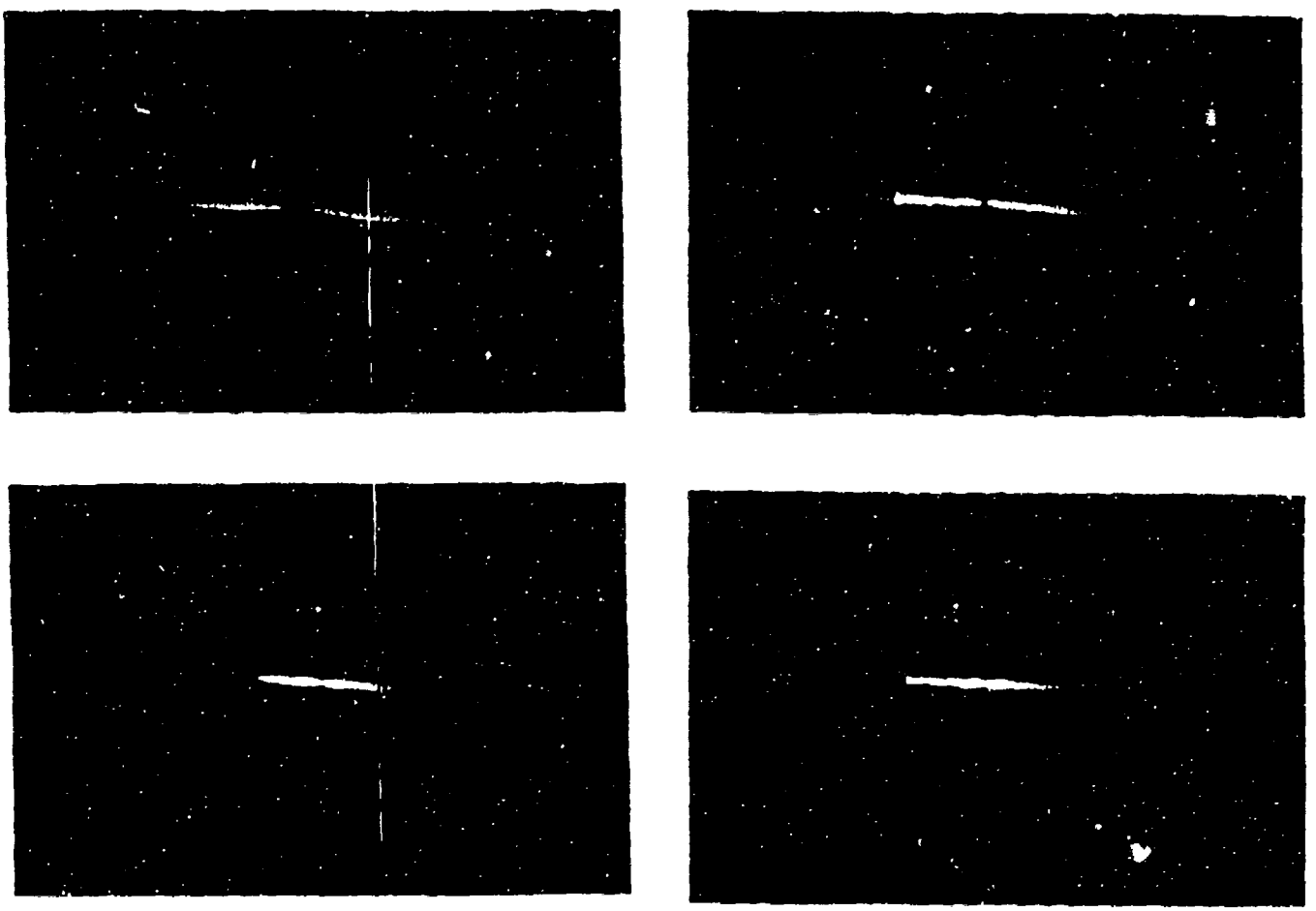

Figure 35. Laser beam focused into air at 0.15 torr, 0.35 torr, 1.23 torr and 3 torr. Photos are of 10 to 20 shots. The photos are generally of two colors, a blue or white center with long red tails along the laser beam direction. Note that as the target density increases the dark central region vanishes.

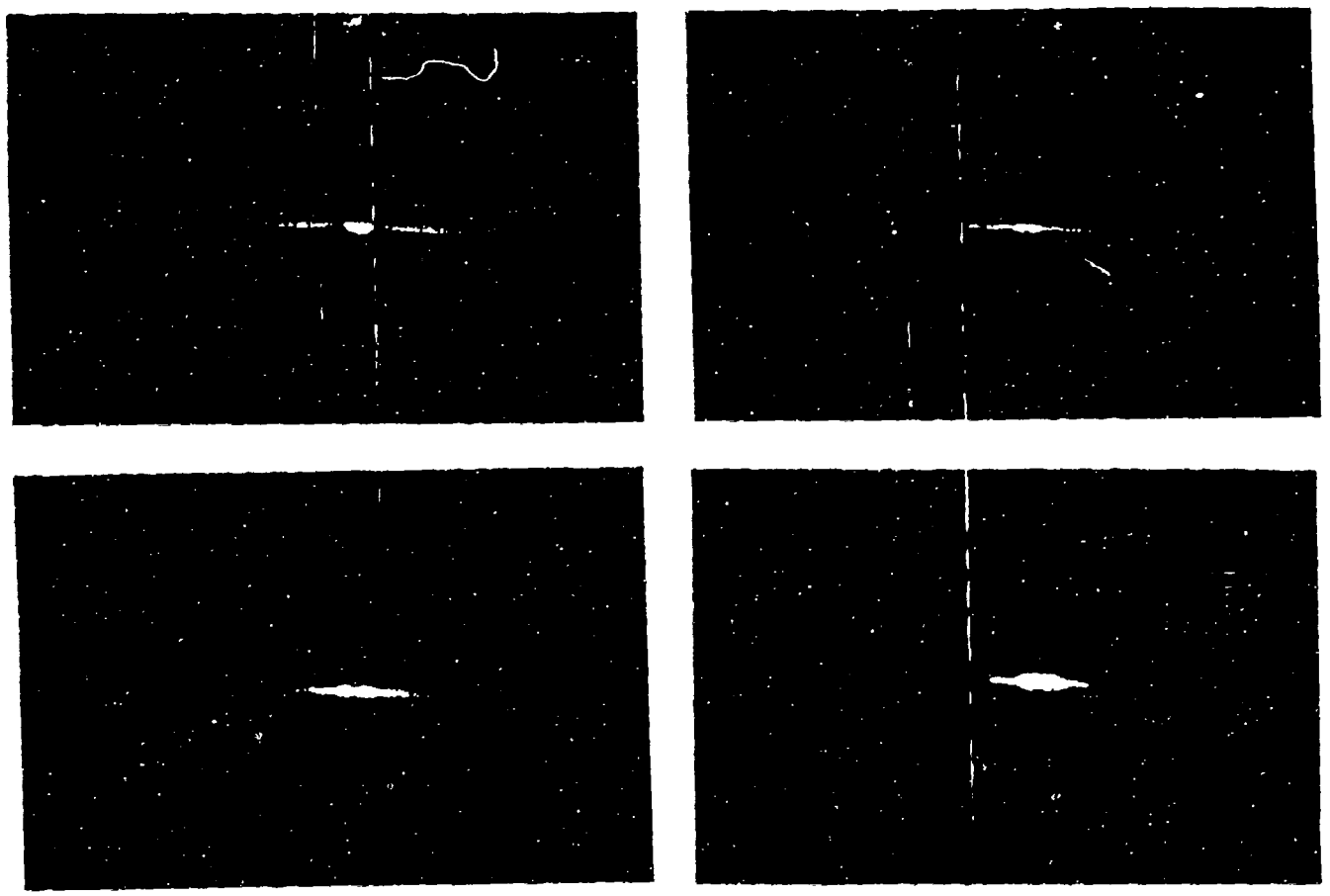

Figure 36. Laser beam focused into He at 0.4 torr, 1.2 torr, 3.3 torr and 10 torr. Photos are of 10 to 30 shots. Photos appear simular to those of air except at the lowest target density where now a bright central region appears.

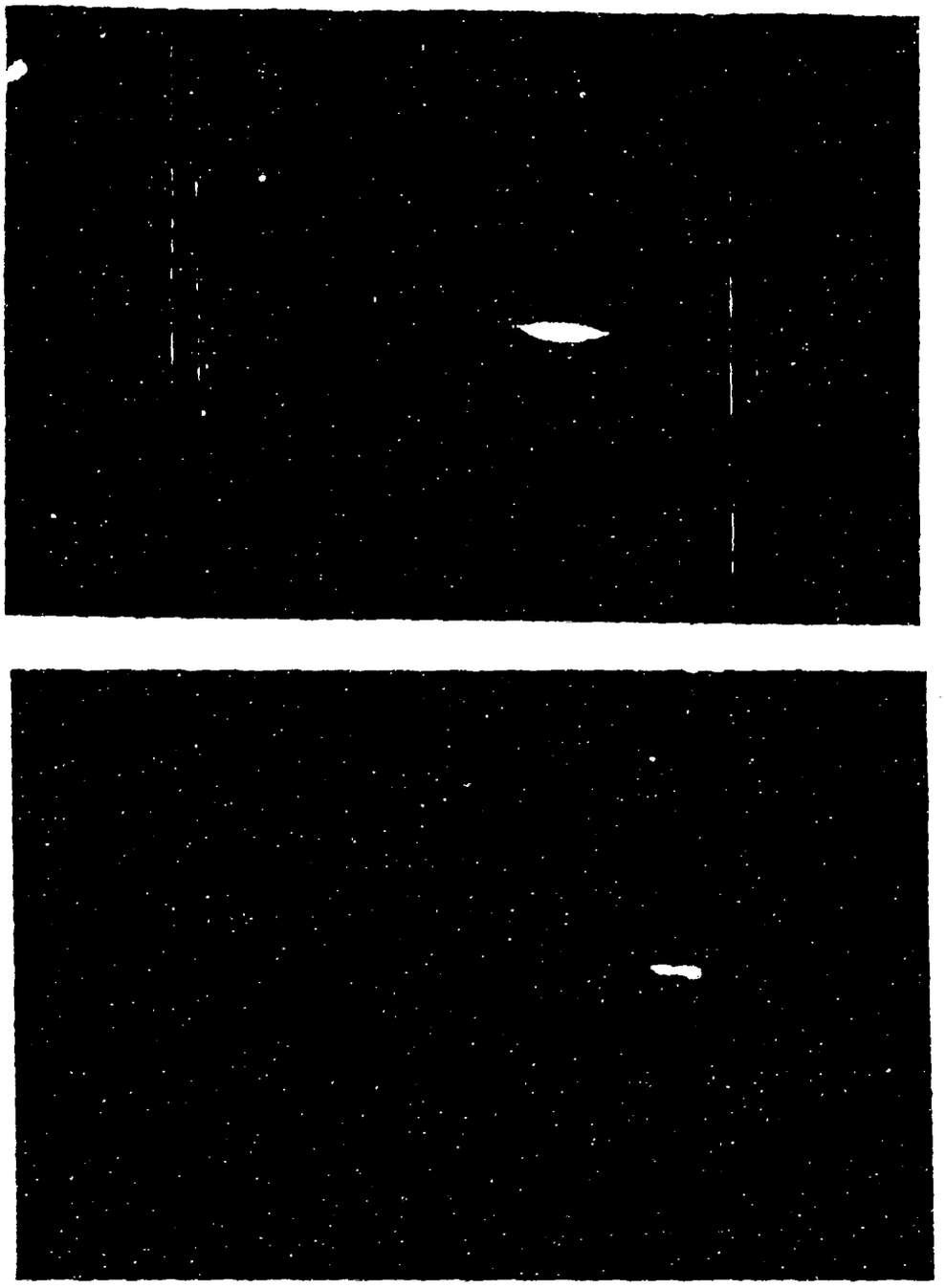

Figure 37. Laser beam focused into He at 100 torr pressure. Photos are single shots. (a). Basically a bright breakdown with small red tails. (b). Filter is used to block out the red. The focusing lobes are now clearly visible.

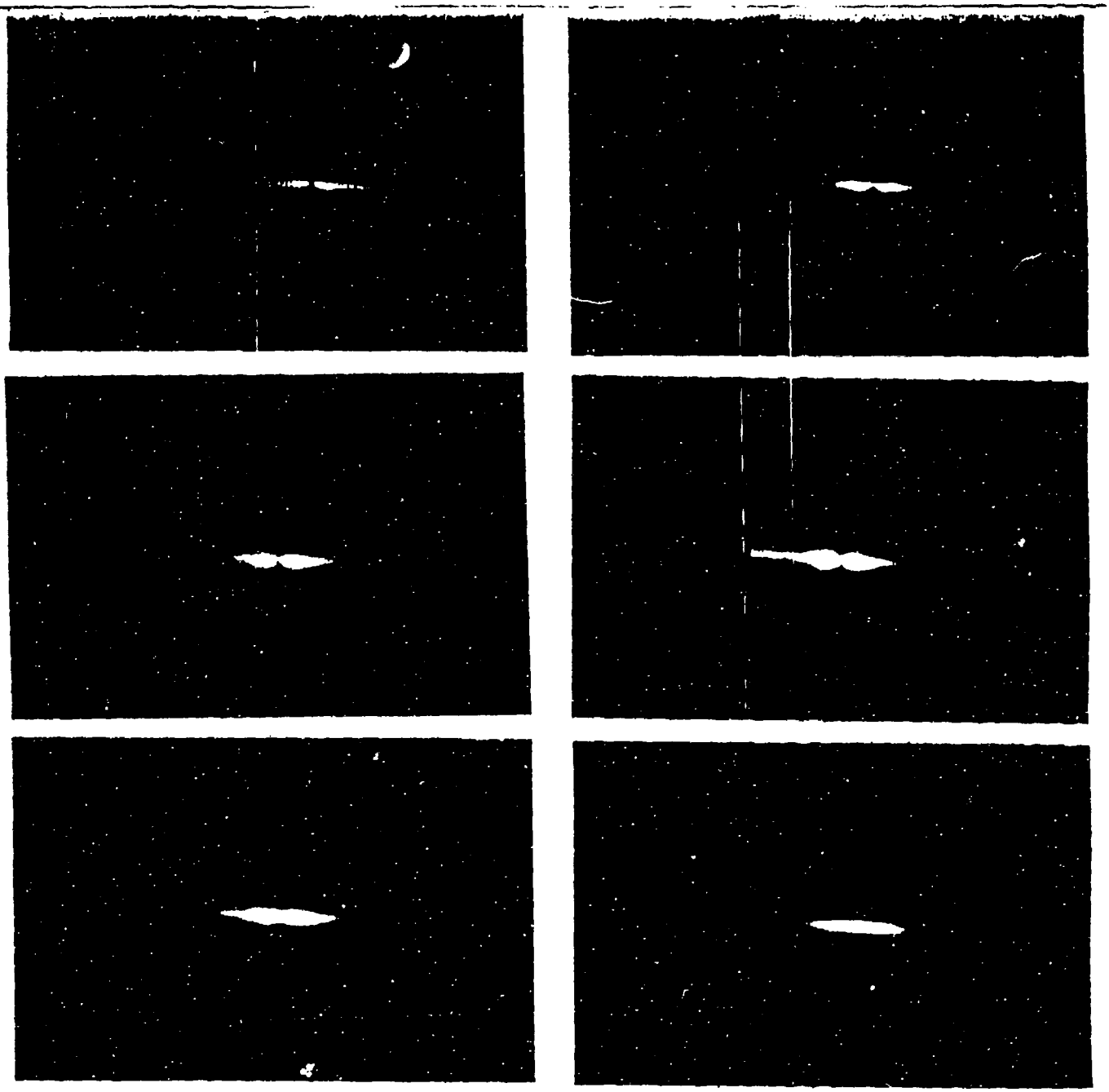

Figure 38. Laser beam focused into H_2 at 0.36 torr, 1.1 torr, 3 torr, 10 torr, 30 torr and 100 torr. Photos range from 40 shots at low pressure to 1 shot at high pressure. Note the formation of the bright focusing lobes in (a) to (e) and the collision of these lobes in (f) as evidenced by the small jets perpendicular to the laser beam direction.

propagation through the focal region observed in Xe, air, He, and H_2. All of them show basically the same phenomena, a breakdown symmetrical about the point of focus. This is in contrast to the asymmetric breakdown illustrated in Figure 34. In all cases, the laser beam intensity became sufficient to produce breakdown quite some distance before the focal region. The figures show that the width of the breakdown region increases as the target gas density increases.

Using He, the spatial extent of the observed blue and red radiation was mapped. The focal region was mapped onto the entrance slit of a 0.3 meter spectrometer using a Nikon 105 mm lens. The imaging experienced a reduction of approximately 1.7. Ion lines were seen to originate from the center of the focal region where the laser intensity would be greatest. The neutral lines are spread out over the entire breakdown region and experience a dip at the center where neutrals would tend to be more scarce.

There are perhaps many factors necessary to explain the propagation of a laser beam through the gaseous targets illustrated in Figures 33–38. But in each case it is clear that a large portion of the laser energy is deposited into the region leading up to the focal area as evidenced by the observed breakdown. This must have some effect upon beam propagation because the abundance of free electrons changes the refractive index of the medium. Figure 33 clearly indicates that breakdown can become so catasrophic that the laser beam propagation is strongly affected. The results of Figures 6–9 give an indication when this occurs for the different gases.

V. Conclusions

Three main conclusions are drawn from the experiments described above. First, the laser beam propagation is strongly affected by ionization of the target gas and by any density gradient in the target gas that the laser beam has to pass through in order to reach the focal point. Second, as evidenced by the spectrum obtained from the various target gases, the lengths of the capillary tubes used in

these studies were probably too long for longitudinal pumping of the target gases because a) once breakdown occurs in the capillary tube the capillary tube wall absorbs the laser energy, presumably in a nonlinear process, rather than reflecting it back into the target gas, and b) the resulting laser intensity along the capillary tube was too low to produce sufficient ionization for the surrounding gas to be transparent to the short wavelength radiation produced. A somewhat greater intensity is required. Third, longitudinal pumping of the target gas in the capillary tube generates a very strong third harmonic at 82.8 nm. This signal could have enough power to be experimentally quite useful. For example, using Ne as the target gas could yield a third harmonic with as much as 1% energy conversion. This would be a sufficient conversion to serve many important application, such as holography.

VI. References

1. Johndale C. Solem, Ting Shan Luk, Keith Boyer and Charles Kirkham Rhodes, IEEE Journal of Quantum Electronics, V25, December 1989, pp 2423–2430.

2. A. B. Borisov, A. V. Borovskiy, V. V. Korobkin, A. M. Prokhorov, C. K. Rhodes, O. B. Shiryaev, submitted to Physical Review Letters.

3. T. S. Luk, U. Johann, H Egger, H. Pummer, and C. K. Rhodes, Physical Review A, V32, July 1985, pp 214–224.

4. Charles K. Rhodes, Science, V229, 27 September 1985, pp 1345–1351.

5. A. McPherson, G. Gibson, H. Jara, U. Johann, T. S. Luk, I. A. McIntyre, K. Boyer, and C. K. Rhodes, Journal of Optical Society Society of America B, V4, April 1987, pp 595–601.

6. W. T. Silfvast, L. H. Szeto, and O. R. Wood, II, Applied Physics Letters, V36, 1 April 1980, pp 500–502.

7. T. S. Luk, A. McPherson, G. Gibson, K. Boyer, and C. K. Rhodes, Optics Letters, V14, 15 October 1989, pp 1113–1115.

8. John Shannon and Robert Hunter, Applied Physics Letters, V24, 15 May 1974, pp 488–490.

9. W. –G. Wrobel, H. Rohr, K. –H. Stever, Applied Physics Letters, V36, 15 January 1980, pp 113–115.

10. T. Efthimiopoulos, B. P. Stoicheff, and R. I. Thompson, Optics Letters, V14 15 June 1989. pp 624–626.

11. K. Boyer, T. S. Luk, J. C. Solem, and C. K. Rhodes, Physical Review A, V39, 1 February 1989, pp 1186–1192.

12. T. S. Luk, A. McPherson, G. Gibson, K. Boyer, and C. K. Rhodes, Nuclear Instruments and Methods in Physics Research, V43, 1989, pp 468–470.

13. G. Gibson, T. S. Luk, A. McPherson, K. Boyer, and C. K. Rhodes, Physical Review A, V40, 1 September 1989, pp 2378–2384.

14. G. Gibson, T. S. Luk, A. McPherson, K. Boyer, and C. K. Rhodes, Submitted to Applied Physics B.

VII. Appendices

Appendix A

Measurement of the gas target pressure in the capillary tube is determined using a HeNe laser interferometer. The experimental setup is illustrated in Figure A1. The index of air at a pressure of 760 torr is given by

$$n - 1 = 0.000293. \qquad \text{A1}$$

Since the optical path in the capillary tube is given by

$$O_p = (n - 1)\, d\, P/760 \qquad \text{A2}$$

where d is the length in the capillary tube and P is the average gas pressure in torr inside the capillary tube, the number of fringes for the HeNe laser is given by

$$f = (n - 1)\, d\, P/760\lambda = 0.00609 \qquad \text{A3}$$

where f is in units of fringes per cm–torr. The average pressure in the capillary tube is given by combining Equations A2 and A3.

As an example, the flow through a 10 cm long capillary tube with a 150 μm bore was measured by placing it inside a vacuum chamber as illustrated in Figure A1b. Port B was opened to vacuum and the entire chamber was pulled to less than 1 mTorr pressure. Using 1 atm backing pressure at port A, gas flow was established through the capillary tube with port B open to vacuum. When port A was closed, 29 fringes were counted. Likewise, when port A was reopened, 29 fringes were counted. When the capillary tube was not in position, so that air leaked into the vacuum chamber through port A, the fringe shift was approximately 1/2. From equations A2 and A3 this gives the average pressure in the capillary tube as

$$P_a = 28.5 \text{ fringes–cm–torr}/(10 \text{ cm} \times 0.00609 \text{ fringes})$$

$$P_a = 468 \text{ torr.}$$

The rate of flow through the capillary tube can be found by closing port B and opening port A to atmosphere. When this is done, 32 fringes per 30 seconds is

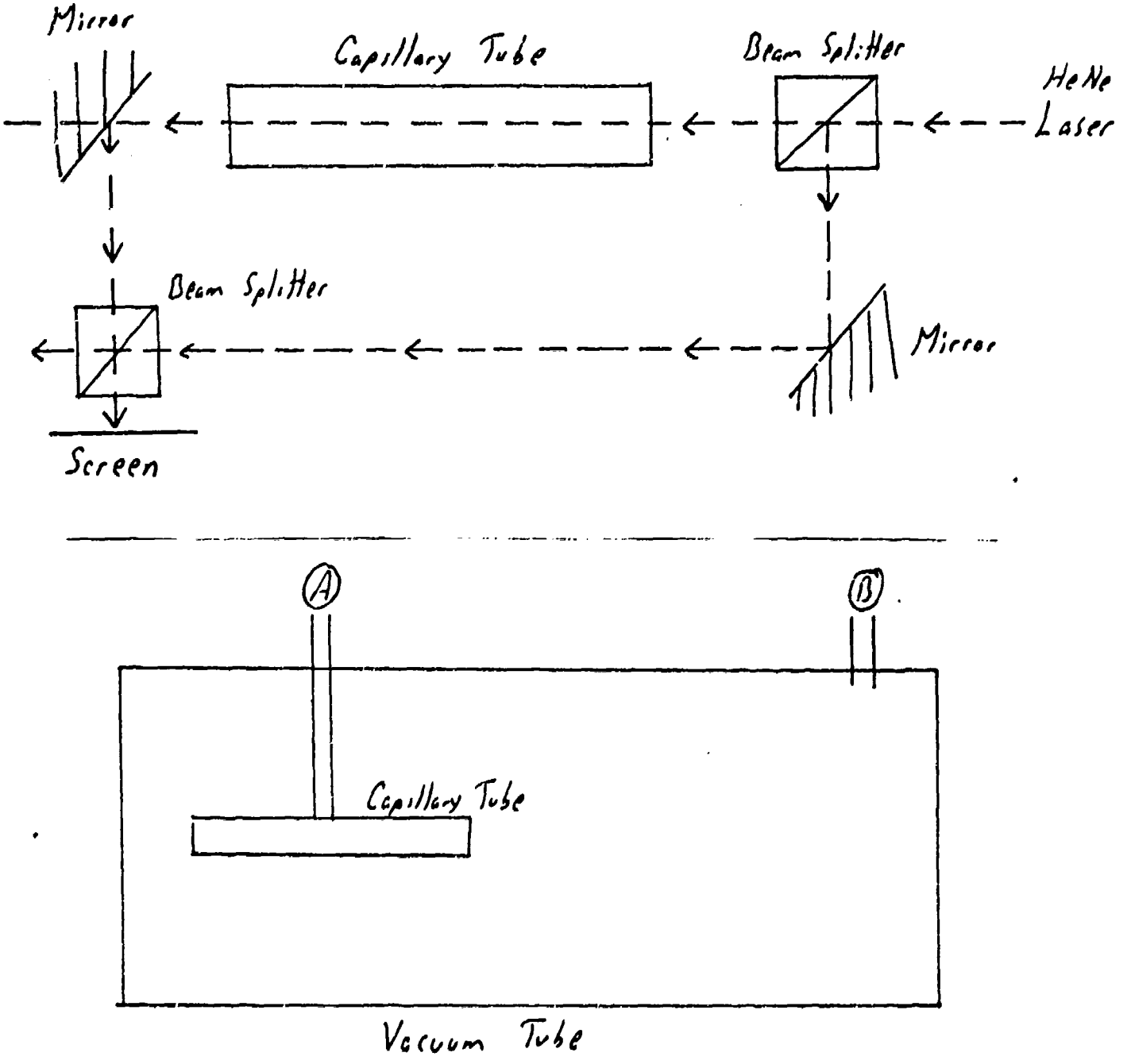

Figure A1. The target gas pressure is determined by interferometric means as illustrated in (a). The capillary tube was positioned inside a vacuum chamber as illustrated in (b) and gas flowed in and out of ports A and B producing a change in the fringe pattern observed on the screen.

recorded. Since the volume of the vacuum chamber is 1.7 liters, the flow rate is found to be

$$Q = \frac{32 \text{ fringes}}{30 \text{ sec}} \times \frac{760 \text{ torr}}{296 \text{ frng}} \times 1.7 \text{ liters}$$

$$Q = 4.65 \text{ torr–liter/sec.}$$

Appendix B

Assume viscous flow through a capillary tube of length l and bore radius a. The conductance, Q, through the capillary tube at each point x along the tube is given by

$$\frac{Q}{8\eta} = \frac{\pi a^4}{dx} P \frac{dP} \qquad \text{B1}$$

where P is the pressure along the tube and η is the viscosity of the gas. The gas flow through the capillary is subject to several assumptions. First, the flow speed is equal to the speed of sound, or the molecular speed, v_m. Second, steady state flow is assumed so that

$$Q = \pi a^2 P' v_m = \text{constant} \qquad \text{B2}$$

where P' is the pressure at the output end of the capillary tube. The boundary condition is

$$P|_{x=l} = P'. \qquad \text{B3}$$

Putting these conditions together gives

$$P^2 = -16\eta P' v_m x/a^2 + P_o^2 \qquad \text{B4}$$

where P_o is the pressure at the input end of the capillary tube. Applying the boundary condition again results in a quadratic equation for the output pressure in terms of the input pressure as

$$2P' = -\alpha + (\alpha^2 + 4P_o^2)^{1/2} \qquad \text{B5}$$

where

$$\alpha = 16\eta v_m L/a^2. \qquad \text{B6}$$

Both equations B5 and B6 are in units of μbars. The average pressure in the capillary tube can be obtained by integrating Equation B4 to give

$$P_a = (1/l) \int_0^l [P_o^2 - P'\alpha x/l]^{1/2} dx$$

$$= (2/3P'\alpha)[P_o^3 - P'^3] \qquad \text{B7}$$

where ι is the length from port A to the end of the capillary tube.

Consider Figure B1. The basis structure of the gas flow path is laid out with the respective length and dimensions indicated. For a given input pressure of P_o = 760 torr, what is the output pressure P_2 when the gas is argon? The molecular velocity is given by

$$v_m = (2kT/3m)^{1/2} \qquad B8$$

where k in Boltzman's constant, T is the gas temperature and m is the molecular mass. For argon at room temperature, 300 °K, the molecular velocity is 3.4×10^4 cm/sec. The viscosity is 1.8×10^{-4} dyne–sec/cm^2. For an effective length between P_o and P_1 of 1.55 cm and between P_1 and P_2 of 5 cm, equations B5 and B6 give

$$\alpha_1 = 74.5 \text{ torr}$$

$$P_1 = 723.7 \text{ torr}$$

$$\alpha_2 = 6840.3 \text{ torr}$$

$$P_2 = 75.7 \text{ torr.}$$

The average pressure in the capillary tube can be calculated from Equation B7. It is 487.4 torr. This is to be compaired to the experimental value found in Appendix A of 468 torr. From the difference of only 4%, it would appear that the viscous flow model of Appendix A is sufficient to describe the average flow through the capillary tube. With this average output pressure in a 0.15 mm bore capillary tube, the average target density would be 1.7×10^{19} cm^{-3}.

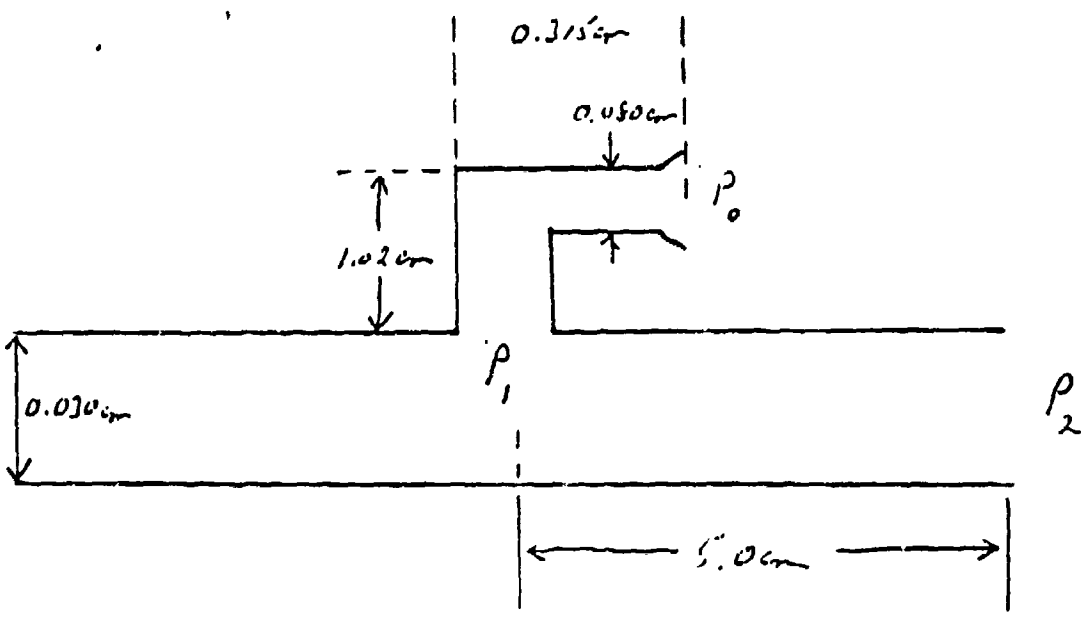

Figure B1. Typical schmatic of the gas flow path in the pulsed valve capillary tube assembly.

IEEE JOURNAL OF QUANTUM ELECTRONICS, VOL. 25, NO. 12, DECEMBER 1989

Prospects for X-Ray Amplification with Charge-Displacement Self-Channeling

JOHNDALE C. SOLEM, TING SHAN LUK, KEITH BOYER, AND CHARLES KIRKHAM RHODES, FELLOW, IEEE

(Invited Paper)

***Abstract*—We develop an analytic theory of charge-displacement self-channeling: a mechanism that can dynamically trap a short intense pulse of light. We focus our attention on the case of most interest for X-ray amplification: the strongly saturated channel, for which all free electrons are expelled from the channel core and the channel walls are overdense. Some curious results are: 1) the intensity at the channel walls is independent of the total laser power, 2) the radius of the channel increases very slowly with laser power, asymptotically as the fourth root, and 3) the power in the channel wall is a constant. The channel is energetically stable in the sense that a bifurcation will cause a net increase in the electrostatic potential energy, but is only marginally stable against relativistic filamentation in the walls. We also find that the channel is an effective waveguide for all secondary radiation. Scaling studies show a substantial advantage exists by using the highest frequency driving laser available. Since very large energy-deposition rates from multiphoton coupling are expected, the channel is ideal for generating coherent short-wavelength radiation, perhaps well into the X-ray range.**

I. Introduction

AMPLIFICATION in the X-ray region requires prodigious energy deposition rates [1] spatially organized in a high-aspect-ratio volume of material. We will show that the use of extremely intense, short-pulse radiation may be able to produce these conditions by combining the energy deposition [2], [3] arising from high-order multiphoton processes with a mode of channeled propagation involving the complete expulsion of free electrons from the central region of the channel. It is significant that the conditions needed for the strong multiphoton coupling are *identical* to those found required for the confined propagation. Previous work [2] discusses the energy deposition rates. Recent work suggests a paradigm for state-selective excitation by the observation of inner-orbital molecular transitions produced by multiphoton coupling [4]. The present discussion concentrates on the propagation.

When a very intense pulse of radiation enters a cold medium, multiphoton ionization produces a local plasma, which leads to the following qualitative behavior. The conversion of electrons from bound to free states by the ionization induces a strong reduction in the refractive response of the atomic material. The resulting plasma exhibits a further decrease in index from the free-electron component collaterally produced. If the ambient electron density n_0 is such that the plasma frequency $\omega_p = \sqrt{4\pi n_0 e^2/m}$ is below the frequency of the radiation ω, an interesting mode of channeled propagation could develop. For a sufficiently short pulse (~ 100 fs), the ions remain spatially fixed while the relatively mobile electrons are expelled by the ponderomotive potential from the high-intensity region of the beam. A state of equilibrium can then be established between the ponderomotive and the electrostatic force densities owing to the net charge displacement. Since the electrons, which embody a negative contribution to the index, are expelled, an on-axis region of relatively high refractive index is formed which can support channeling of the laser beam.

For the optimum condition conducive to laser action, we would like the density of excited states to be as high as possible, and consequently, a high atom density is desired. However, we may not have $\omega < \omega_p$ or the laser beam may not initially propagate to form the channel. While this constraint may be somewhat mitigated in the relativistic regime, in general it will be most propitious to set the atom density such that at the anticipated ionization level, the plasma frequency is just below the laser frequency.

In this paper, 1) we review self-channeling in a low-density plasma and present some simple physical models for calculating the critical intensity for channeling, the channel radius, and the power at which all electrons are expelled; 2) we discuss the ionization state achieved in initially cold material, and show that it is a good approximation to assume a common ionization state for all atoms involved in the channel; 3) we show that the index of refraction is dominated by the free-electron component; 4) we develop an analytic solution for the strongly saturated channel with overdense walls, which is the case of greatest interest for X-ray amplification; 5) we show that the motionless-ion approximation is valid in the regime of interest; 6) we demonstrate energetic stability of the channel, although it is only marginally stable against relativistic filamentation; 7) we discuss channeling of secondary

Manuscript received June 27, 1989, revised July 25, 1989. This work was supported by the Department of Energy, the Air Force Office of Scientific Research, the Office of Naval Research, and the SDIO.

J. C. Solem is with the Theoretical Division, Los Alamos National Laboratory, Los Alamos, NM 87545.

T. S. Luk, K. Boyer, and C. K. Rhodes are with the Laboratory for Atomic, Molecular, and Radiation Physics, Department of Physics, University of Illinois, Chicago, IL 60680.

IEEE Log Number 8931083.

0018-9197/89/1200-2423$01.00 © 1989 IEEE

radiation and energy deposition rates; and 8) we derive scaling relationships that show a substantial advantage with the use of high-frequency driving lasers.

II. Review of Self-Channeling in Low-Density Plasma: Simple Analytic Models

Some aspects of the self-channeling behavior have been calculated numerically in the regime of low-plasma density [5]. To get our arms around the problem, we review those results and show how they can be obtained from simple analytic models. We then proceed to the case of an initially cold material subjected to exceedingly high intensities.

The steady-state force balance between the radially outward ponderomotive force and the oppositely directed electron–ion attraction for a completely ionized tenuous ($\omega >> \omega_p$) plasma is given by

$$\frac{2\pi e^2}{m\omega^2 c}\nabla I(\vec{r}) = e^2 \int \frac{[n_0 - n(\vec{r})][\vec{r} - \vec{r}']}{|\vec{r} - \vec{r}'|^3} d^3r'. \quad (1)$$

For a cylindrically symmetric Gaussian intensity distribution $I(r)$, the electron density $n(r)$ is

$$n(r) = n_0 - \frac{2I(0)}{m\omega^2 c r_0^2}\left[1 - \left(\frac{r}{r_0}\right)^2\right]\exp\left[-\left(\frac{r}{r_0}\right)^2\right] \quad (2)$$

in which r_0 is the Gaussian radius. We can estimate the condition necessary for self-focusing by describing the charge displacement by two regions such that $n(r < r_0\sqrt{2}) = n(0)$ and $n(r \geq r_0\sqrt{2}) = n(r_0\sqrt{2})$ and equating the angle of total internal reflection to the angle corresponding to the first minimum of diffraction. This yields a critical intensity

$$I_c = \frac{\pi m\omega^2 c}{64(1 + e^{-2})r_e} \simeq 4.3 \times 10^{-9}\frac{m\omega^2 c}{r_e}\ \mathrm{W \cdot cm^{-2}}, \quad (3)$$

where $r_e = e^2/mc^2$ denotes the classical electron radius. Significantly, this intensity is *independent* of the ambient electron density n_0 and contrasts with the power threshold [7] normally arising from induced index changes in transparent dielectrics. We note that if the critical intensity is not achieved, ionization will generally result in a refractive index profile that will defocus the beam [7]. The ability to focus and form a self-trapped beam will also depend on the initial intensity distribution and the rise time.

If the intensity exceeds I_c, the beam will tend to form a channel, but the intensity range over which (2) is a good description of the electron distribution is quite narrow. The more common and more interesting situation is described by $I(0) > \frac{1}{2}m\omega^2 c n_0 r_0^2$. Under such conditions, all free electrons are expelled from the core of the channel, which is said to be *saturated* or *cavitating*. The radius of the channel will not necessarily be the same as the laser focal spot, and will, in general, depend on the electron density.

Here is a very simple and intuitive model. We estimate of the radius r_w of the saturated region [$n(r < r_w) = 0$] by treating the channel as a dielectric waveguide. We assume that the expelled electrons form a cylindrical sheath around the saturated region with a thickness comparable to r_w so that $n(r_w < r < 2r_w) = \frac{4}{3}n_0$ and $n(r > 2r_w) = n_0$. Consequently, the charge density $n(r)$ changes from n_0 to $\frac{4}{3}n_0$ at the interface. The cutoff frequency ω_c of the dielectric waveguide [8] can be written as

$$\omega_c \simeq \frac{x_{01}\omega c}{r_w e}\sqrt{\frac{m}{4\pi[n(r > r_w) - n(r < r_w)]}}, \quad (4)$$

where $x_{01} = 2.405$ is the first root of the Bessel function $J_0(x)$, i.e., $J_0(x_{01}) = 0$. We ignore the effect of the region $r > 2r_w$. The threshold for propagation occurs at $\omega = \omega_c$, for which we find $r_w \simeq (x_{01}c\sqrt{3/4})/\omega_p \simeq 2c/\omega_p$. This agrees with numerical calculations [5], which also show $r_w \simeq 2c/\omega_p$ for the unsaturated case and that (2) is a good description of the charge distribution with $r_0 = r_w$. The power P_s for the onset of saturation can be found from the condition $I(0) = \frac{1}{2}m\omega^2 c n_0 r_0^2$, which gives

$$P_s = \frac{2mc^3}{r_e}\left(\frac{\omega}{\omega_p}\right)^2 = 1.74 \times 10^{10}\left(\frac{\omega}{\omega_p}\right)^2 \mathrm{W}, \quad (5)$$

which is also in good agreement with numerical calculations [5].

III. Ionization State and Refractive Properties

The state of ionization and its radial profile are important aspects of the analysis. For these estimates, we use the formulation of Keldysh [9] corresponding to the situation in which tunneling dominates [10], [11], and have included a correction for the effect of the Coulomb field in the final state [11]. The influence of atomic shell structure is accounted for through the use of computed ionization potentials for multiply-charged ions [12]. An example involving holmium illustrates the outcome of this procedure. It is found that for a pulse of 100 fs duration, nickel-like holmium (Ho^{39+}) will be produced for intensities spanning the $1.3\text{-}4.8 \times 10^{20}$ W · cm^{-2} range. Therefore, if the spatial beam profile were a Gaussian with a radius r_0 and a peak intensity $I_0 = 4.8 \times 10^{20}$ W · cm^{-2}, the nickel state would exist from $r = 0$ to $r = 1.3r_0$, nearly the entire region of interest.

The radial dependence of the refractive index $N(r)$ governs the condition for channeling. Since the ions are inertially confined for the short time (~ 100 fs) considered, the expulsion of the free electrons from the channel results in a reduced plasma frequency or, equivalently, an increase of the refractive index in the central region.

The contribution to the index from the ions under the strong-field condition involves two opposing effects. They are: 1) the nonlinear contribution proportional to N_2, which is enhanced at more elevated field strengths, and 2) the tendency to produce high charge states, corresponding to low polarizabilities and depressed values of

N_2. The resulting ionic component of the index, however, is overwhelmed by the free-electron contribution. This fact is demonstrated by another example involving Ho at an intensity of 3.7×10^{19} W · cm^{-2}, the value at which Ho becomes krypton-like (Ho^{31+}). The refractive index, through the first nonlinear term, is $N = 1 + N_0 + N_2 E^2$ where $N_0 = 2\pi N_a \alpha_0$ and $N_2 = (\pi/3) N_a \alpha_2$, with N_a representing the ion density. We can relate these susceptibilities for Ho^{31+} to known values [13] for neutral Kr, namely, $\alpha_0 = 24.8 \times 10^{-25}$ esu and $\alpha_2 = 137.7 \times 10^{-38}$ esu. Since Ho^{31+} has a radius of ~ 0.032 that of Kr, hydrogenic scaling yields $\alpha_0 \simeq 10^{-28}$ esu and $\alpha_2 \simeq 10^{-46}$ esu for Ho^{31+}. At the given intensity, the ionic contribution then is $(N - 1)_{at} \simeq 10^{-28} N_a$. For a collisionless ($Ho^{31+}$) plasma with an electron density of $31N_a$, we obtain the free-electron contribution to the index at 248 nm as $(N - 1)_e \simeq -(\omega_p^2/2\omega^2) = -8.5 \times 10^{-22} N_a$ so that $(N - 1)_e/(N - 1)_{at} \simeq -10^7$. The free-electron contribution is far larger than the ionic contribution. Therefore, the ionic contribution can be safely neglected.

IV. The Strongly Saturated Channel with Overdense Walls

We now turn to the case of greatest interest for X-ray amplification: the strongly saturated channel. In Section II, we reviewed the case of a tenuous plasma ($\omega >> \omega_p$). Here, no such restriction applies, but we assume a density that allows enough initial propagation for the channel to form. We are seeking the steady-state conditions of propagation: the electrons are completely expelled out to a radius r_w and the channel is bounded by overdense walls with a very rapid rise in electron density. Our objective is to obtain an analytic approximation.

To this end, we make the following assumptions: 1) all electrons are expelled from the center of the channel out to a radius r_w; 2) beyond r_w, the electron density rises to a overdense value n_{0w} in a radial distance that is very small compared to r_w; 3) the density remains at n_{0w} for a radial distance δ representing one e folding of the high-frequency field and then drops to the ambient value $n_0 << n_{0w}$; and 4) the relativistic shift of the plasma frequency is determined by the high-frequency field at r_w.

A. Analytic Solution

Within the cylinder $r < r_w$, the fields for circularly polarized light are described by the equation [6]

$$\nabla_\perp^2 \psi + q\psi = 0, \tag{6}$$

where ψ is defined so the intensity $I = \psi^2$ and q is an eigenvalue established by the boundary conditions. The amplitude of the high-frequency field will drop off exponentially [14] in the overdense channel wall with a penetration depth given by

$$\delta = \frac{c}{\sqrt{\omega_{pw}^2 - \omega^2}} \simeq \frac{c}{\omega_{pw}}, \tag{7}$$

where ω_{pw} is the relativistically corrected [15] plasma frequency,

$$\omega_{pw} = \frac{\omega_{pw0}}{\sqrt{1 + \dfrac{e^2 E_0^2}{m^2 c^2 \omega^2}}}, \tag{8}$$

and $\omega_{pw0} = \sqrt{4\pi n_{0w} e^2/m}$ is the nonrelativistic plasma frequency in the channel wall. We assume the same ionization state throughout the channel wall as was justified in Section III. The amplitude of the high-frequency field for $r > r_w$ is given by

$$\psi(r) = \psi(r_w)\, e^{(r_w - r)/\delta}. \tag{9}$$

Assuming that all the electrons from the saturated region are moved to a thin cylindrical shell with inner radius r_w and outer radius $r_w + \delta$ where $\delta << r_w$ because $n_{0w} >> n_0$, by using (7) and (8) we can approximate

$$\delta \simeq \frac{\sqrt{1 + 2\beta\psi^2(r_w)}}{2\pi n_0 r_e r_w}, \tag{10}$$

where $\beta \equiv 4\pi r_e/m\omega^2 c$.

The solution to (6), which represents the saturated region $r < r_w$, is

$$\psi(r) = \psi(0)\, J_0(qr), \tag{11}$$

an expression we want to join to (9) at $r = r_w$. We note that this treatment is substantially different from the treatment used by Barnes *et al.* [16] which assumed a Gaussian solution near the beam axis.

The boundary conditions are continuity of ψ and $d\psi/dr$, which give

$$\psi(0)\, J_0(qr_w) = \psi(r_w) \tag{12}$$

$$-q\psi(0)\, J_1(qr_w) = -\frac{2\pi n_0 r_e r_w}{\sqrt{1 + 2\beta\psi^2(r_w)}}\, \psi(r_w), \tag{13}$$

or

$$\frac{q}{r_w} = \frac{J_0(qr_w)}{J_1(qr_w)} \frac{2\pi n_0 r_e}{\sqrt{1 + 2\beta\psi^2(r_w)}}. \tag{14}$$

We now use local force balance to obtain the wall radius. The radial ponderomotive force on an electron at r_w is

$$F_p(r_w) = \frac{2\pi e^2}{m\omega^2 c} \frac{d}{dr} \psi^2(r_w)$$

$$= -\frac{4\pi e^2}{m\omega^2 c}\, \psi^2(0)\, q\, J_0(qr_w)\, J_1(qr_w). \tag{15}$$

Equation (15) is nonrelativistic. As the intensity approaches the relativistic regime, the quiver motion of the electrons changes from a linear displacement in the electric-field direction to a *figure 8* pattern [17] extending in the direction of propagation. Under extremely relativistic conditions, the ponderomotive force will be mainly in the propagation direction, although the radial gradient of in

tensity will still contribute. We use (15) as an approximation to the force and we shall show that the intensity at r_w is independent of the total laser power. Thus, the use of (15) is equally good for all laser powers.

From Gauss' law, we obtain the electrostatic force

$$F_e(r_w) = e^2 n_0 \frac{4\pi}{r_w} \int_0^{r_w} \rho d\rho$$

$$= 2\pi e^2 n_0 r_w. \tag{16}$$

Balancing the forces $F_p(r_w) = -F_e(r_w)$ gives

$$\frac{r_w}{q} = \frac{2}{n_0 m \omega^2 c} \psi^2(0) J_0(qr_w) J_1(qr_w). \tag{17}$$

Combining (14) and (17), we obtain directly

$$\beta\psi^2(0) J_0(qr_w) = \frac{\sqrt{1 + 2\beta\psi^2(r_w)}}{J_0(qr_w)}, \tag{18}$$

and, using (12), we find

$$\beta\psi^2(r_w) = \sqrt{1 + 2\beta\psi^2(r_w)}. \tag{19}$$

The solution to (19) is then simply

$$\psi^2(r_w) = \frac{1 + \sqrt{2}}{\beta}. \tag{20}$$

The intensity at the channel wall is *independent* of laser power. Furthermore,

$$\omega_{pw} = \frac{\omega_{pw0}}{1 + \sqrt{2}} \simeq 0.414\omega_{pw0}, \tag{21}$$

always holds. From (12) and (20), we have

$$qr_w = J_0^{\text{inv}}\left(\frac{\sqrt{1 + \sqrt{2}}}{\psi(0)\sqrt{\beta}}\right), \tag{22}$$

where $J_0^{\text{inv}}[J_0(x)] = J_0[J_0^{\text{inv}}(x)] = x$ and we have restricted the functions to principal values. Fig. 1 shows qr_w as a function of the channel center intensity $I(0)$, as given by (22). Notice that $qr_w \to 0$ as $I(0) \to (1 + \sqrt{2})/\beta$ and $qr_w \to x_{01}$ as $I(0) \to \infty$. From (17) and (22), we have the result

$$r_w^2 = \frac{\sqrt{1 + \sqrt{2}}}{2\pi n_0 r_e} \psi(0)\sqrt{\beta} J_0^{\text{inv}}\left(\frac{\sqrt{1 + \sqrt{2}}}{\psi(0)\sqrt{\beta}}\right)$$

$$\cdot J_1\left[J_0^{\text{inv}}\left(\frac{\sqrt{1 + \sqrt{2}}}{\psi(0)\sqrt{\beta}}\right)\right]. \tag{23}$$

Fig. 2 shows the channel wall radius r_w as a function of the channel center intensity $I(0)$, as given by (23). Notice that $r_w \to 0$ as $I(0) \to (1 + \sqrt{2})/\beta$, as expected, and r_w increases indefinitely with $I(0)$.

B. Summary

To summarize results so far, we have derived a solution to an *approximate* model for the z-independent propagation of a laser beam through a charge-displaced channel. The channel walls are overdense. The treatment is relativistic and appropriate for very high intensity. The radial dependence of the laser intensity is

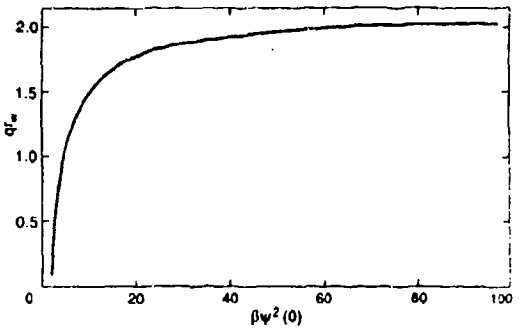

Fig. 1. The Bessel function parameter at the channel wall as a function of central intensity.

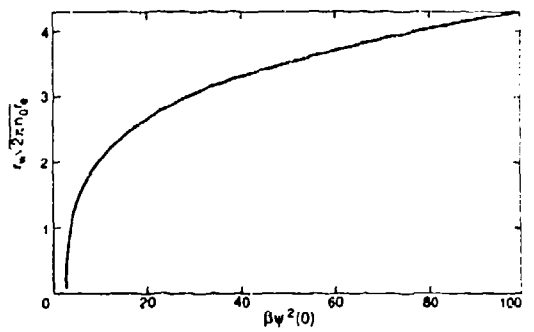

Fig. 2. The channel radius as a function of central intensity.

$$I(r) = \begin{cases} I(0) J_0^2(qr), & r \le r_w, \\ [(1 + \sqrt{2})/\beta] \exp[2(r_w - r)/\delta], & r > r_w. \end{cases} \tag{24}$$

and the radial dependence of the electron density is

$$n(r) = \begin{cases} 0, & r \le r_w; \\ n_0 r_w/2\delta, & r_w < r < r_w + \delta; \\ n_0, & r \ge r_w + \delta; \end{cases} \tag{25}$$

where $\delta = (1 + \sqrt{2})/(2\pi n_0 r_e r_w)$, as can be seen by substituting (20) into (10). Fig. 3 shows the intensity as a function of radius as given by (24) for some representative values of the intensity. Fig. 4 shows electron density distributions as given by (25) together with the corresponding intensity distributions.

C. Asymptotic Forms

A Taylor expansion at x_{01} gives $J_0(x) \simeq J_1(x_{01})(x_{01} - x)$, which can be used to find the asymptotic behavior of (22) as $I(0) \to \infty$.

$$qr_w \to x_{01} - \frac{\sqrt{1 + \sqrt{2}}}{J_1(x_{01})\sqrt{\beta I(0)}} \simeq x_{01} - \frac{3}{\sqrt{\beta I(0)}} \tag{26}$$

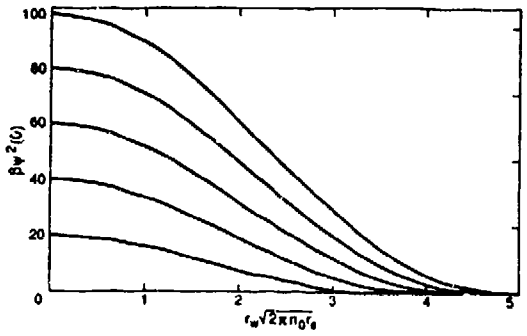

Fig. 3. The radial distribution of intensity for various values of the central intensity.

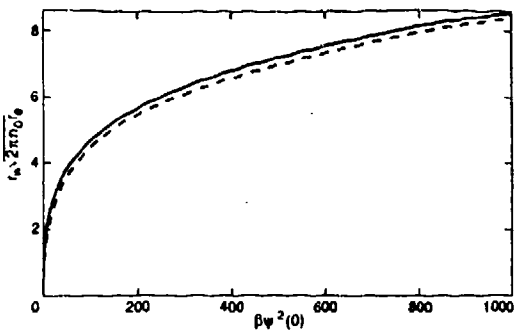

Fig. 5. Comparison of the asymptotic solution obtained by Taylor expansion, (27), to the exact solution, (23), for the channel radius as a function of central intensity. Dashed curve is the asymptotic solution.

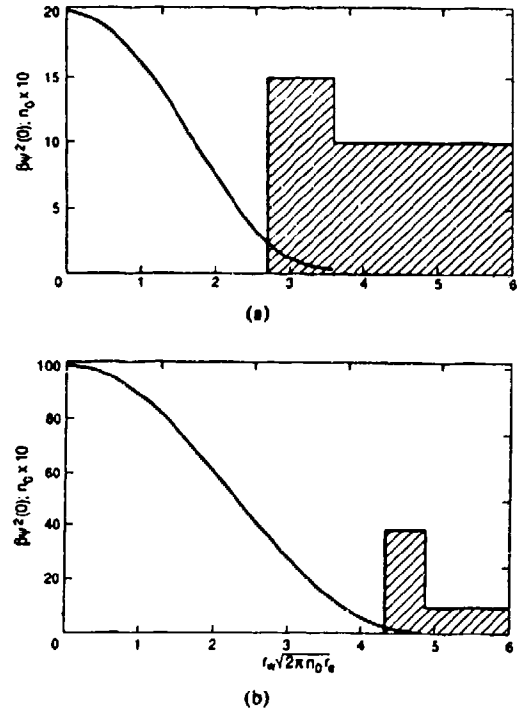

Fig. 4. The electron density distribution superimposed on the density distribution for various values of central intensity. (a) $\beta\psi^2(0) = 20$. (b) $\beta\psi^2(0) = 100$.

A Taylor expansion also gives $J_0(x)\,J_1(x) \simeq J_1^2(x_{01})\,(x_{01} - x)$, which can be combined with (26) to find the asymptotic behavior of (23), specifically,

$$r_w^2 \to \frac{x_{01}J_1(x_{01})\sqrt{(1+\sqrt{2})\,\beta I(0)} - 1 - \sqrt{2}}{2\pi n_0 r_e}$$

$$\simeq \frac{1.94\sqrt{\beta I(0)} - 2.41}{2\pi n_0 r_e}. \qquad (27)$$

Fig. 5 compares the asymptotic solution given in (27) to the exact solution given in (23). Remarkably, the asymptotic solution agrees with the exact solution within a few percent over the entire domain of definition: it is an excellent approximation. Equation (27) shows that in the limit of very high power, the channel radius increases as the fourth root of intensity at the channel center or about as the fourth root of total laser power.

V. Validity of the Motionless-Ion Approximation

The motionless-ion approximation is quite good over the intensity and pulse-length regime of interest. The ponderomotive force on an ion is proportional to its charge ζ and inversely proportional to its mass M. For Ho at $I_0 \simeq 4.8 \times 10^{20}\ \mathrm{W \cdot cm^{-2}}$, the ponderomotive force moves an ion a distance $\sim 4 \times 10^{-10}$ times that of the electron, which is completely negligible. A far larger force on the ions results from the charge displacement itself since the ions' mutual electrostatic repulsion will expel them from the beam. However, the ion motion due to this force is also small for a sufficiently short pulse. Assume that the saturated channel has been formed at $t = 0$. With the electrostatic force on an ion at radius $r < r_w$ given as $F = 2\pi r\,(\zeta e)^2 n_a$ by Gauss' law, an ion with initial position r_0 has its motion described by $r = r_0 \exp(y^2)$ where

$$\int_0^y \exp(y'^2)\,dy' = \sqrt{\frac{\pi\zeta^2 r_e c^2 n_a m}{M}}\,t, \qquad (28)$$

which leads to the approximate result for small displacements:

$$\frac{r - r_0}{r_0} \simeq \frac{\pi\zeta^2 r_e c^2 n_a m}{M}\,t^2. \qquad (29)$$

At $I_0 = 4.8 \times 10^{20}\ \mathrm{W \cdot cm^{-2}}$, the ion migration gives a relative change in its position of about 9 percent after 100 fs.

VI. Energy Loss Mechanisms

The two principal mechanisms leading to energy loss in the channel are: 1) ionization, and 2) the field energy associated with the charge displacement.

A. Ionization

The energy lost to ionization can be found by summing the ionization potentials [12] of electrons successively stripped from the atom up to the ionization level produced by the field. For the Ho^{39+} case, with $n_a = 2.3 \times 10^{18}$

cm^{-3} and a channel radius $r_w \simeq 2c/\omega_p = 1.1\ \mu m$, ionization produces a loss of $\sim 4.3\ mJ \cdot cm^{-1}$.

B. Charge Displacement

The radially directed electric field is given by

$$E(r) = 2\pi e n_0 \begin{cases} r, & r \le r_w; \\ r_w + r_w(r_w - r)/\delta, & r_w < r < r_w + \delta; \\ 0, & r \ge r_w + \delta \end{cases} \quad (30)$$

where we have corrected for the approximation in (25). By direct integration, the charge-displacement field energy per unit length of the channel is given by

$$\frac{d\epsilon_c}{dx} = \frac{1}{4}\int_0^\infty E^2(r)\, r\, dr = \frac{\pi^2 e^2 n_0^2 r_w^2 (r_w + \delta)(3r_w + \delta)}{12}$$
$$\simeq \frac{\pi^2 e^2 n_0^2 r_w^4}{4} \simeq \frac{mc^2}{16 r_e} \cdot \left[x_{01} J_1(x_{01}) \sqrt{(1+\sqrt{2})\,\beta I(0)} - 1 - \sqrt{2}\right]^2. \quad (31)$$

For the example above, this would be $\sim 44\ \mu J \cdot cm^{-1}$.

VII. Stability of the Channel

Two questions concerning the stability of such channels have been examined. The first involves energetic stability associated with the splitting of a single channel into two or more channels, each having a fraction of the total electrostatic energy. The second considers stability against relativistic self-focusing in the walls of the channel, a mode observed in numerical simulations [18].

A. Energetic Stability

For appraisal of the case based on energetics, using the approximation

$$\int_0^x J_0^2(x')\, x'\, dx' \simeq x_{01}^2 J_1^2(x_{01}) \left[1 - \left(1 - \frac{x}{x_{01}}\right)^{2.3}\right]^2, \quad (32)$$

which is accurate to within 10 percent over the $0 < x \le x_{01}$ range, for a total power $P = P_0 + P_1$, we find that inside the saturated region

$$P_0 = 2\pi I(0) \int_0^{r_w} J_0^2(qr)\, r\, dr$$
$$\simeq \left\{\frac{J_1^4(x_{01})\,\beta I^2(0)\sqrt{1+\sqrt{2}}}{2n_0 r_e \left[x_{01} J_1(x_{01})\sqrt{\beta I(0)} - \sqrt{1+\sqrt{2}}\right]}\right\} \cdot \left\{1 - \left[\frac{\sqrt{1+\sqrt{2}}}{x_{01} J_1(x_{01})\sqrt{\beta I(0)}}\right]^{2.3}\right\}^2, \quad (33)$$

while in the region outside

$$P_1 = \frac{2\pi(1+\sqrt{2})}{\beta}\int_{r_w}^\infty \exp\left[2(r_w - r)/\delta\right] r\, dr$$
$$= \frac{2\pi(1+\sqrt{2})}{\beta}\left[\frac{r_w\delta}{2} + \frac{\delta^2}{4}\right]$$
$$= \frac{m\omega^2 c(1+\sqrt{2})^2(1+\sqrt{2}+4\pi n_0 r_e r_w^2)}{32\pi^2 n_0^2 r_e^3 r_w^2}$$
$$\simeq \frac{m\omega^2 c}{8\pi n_0 r_e^2}(1+\sqrt{2})^2. \quad (34)$$

Combining (31) and (33) and taking the limit $I(0) \to \infty$, we find further

$$\frac{\epsilon_c}{l} = \frac{1}{4}\left[\frac{(1+\sqrt{2})\,\pi x_{01}^4 \sqrt{m r_e}\, c^2 n_0 P}{\omega^2}\right]^{2/3}, \quad (35)$$

a result which shows that the electrostatic energy ϵ_c per unit length l scales as (laser power)$^{2/3}$. Therefore, this energy would be *increased* by splitting into two channels, each of which contained half the laser power. Further inspection of (31) and (33) shows that an even more stable situation exists for powers less than the asymptotic limit.

B. Stability Against Relativistic Filamentation

The total power propagating in the channel walls is given by (34). The power threshold for relativistic self-focusing [19], [20] is

$$P_r = \frac{Km\omega^2}{4\pi n_0 e^2}, \quad (36)$$

in which $K = 1.5 \times 10^{10}$ W, so that the condition $P_r > P_1$ barring relativistic self-focusing in the walls is

$$K > \frac{mc^3}{2r_e}(1+\sqrt{2})^2 \simeq 2.6 \times 10^{10}\ \text{W}. \quad (37)$$

Although this stability criterion is not met, it is only slightly surpassed. The assumption that the relativistic shift of the plasma frequency is given by the intensity at the channel wall slightly overestimates the total power flowing in the walls. Thus, we can only conclude that the stability against relativistic filamentation is marginal.

Furthermore, although the power in the wall of the strongly saturated channel is always the same, the time (or distance) for the instability to develop fully depends on the geometry of the channel. A thick annulus will filament more quickly than a thin annulus. The more power flowing down the channel, the longer it will take for the instability to develop. The question of relativistic filamentation can be addressed by detailed numerical simulations, but ultimately only by experiment [21]. Both are beyond the scope of this paper.

C. Linear Stability

If the channel is to be used as the excited volume for an X-ray laser, it is desirable to have the channel propa

gate in a straight line. Linearity of the channel can be ensured by laying down a track of higher refractive index that the pulse will follow. For a gas, this might be done with a laser prepulse. In a solid, microfabrication techniques might be used.

VIII. Toward X-Ray Amplification

Several additional considerations pertain to the use of a charge-displaced channel for obtaining X-ray amplification.

A. Channeling of Secondary Radiation

Using the dielectric waveguide as a model for the channel reveals an interesting aspect of this mode of propagation. We see that if the frequency ω exceeds the cutoff in (4), a condition essential for the channel to form, then all higher frequencies will also be guided. This occurs because the index is dominated by the free electrons or, equivalently, the angle of total internal reflection is proportional to the angle of the first minimum of diffraction. Since all of the radiation which falls within the acceptance angle of the waveguide will propagate as a guided mode, these channels can serve naturally as bright directed sources of energetic radiation.

We note that linear stability is only a practical requirement: we need to know which way the laser is pointing. The channel acts as an optical fiber for all secondary radiation.

B. Deposition Rates

Energy deposition rates associated with such channels are expected to be extremely high. Extrapolation [2] of experimental energy-transfer rates suggests that the multiphoton absorption cross section will limit to a frequency-independent value of $\sim 10^{-20}$ cm^2 for heavy elements at intensities above 10^{19} W $\cdot$ cm^{-2}, a value near the Compton intensity in the ultraviolet. For the holmium case cited above, with an electron density $n_0 \sim 8.9 \times 10^{19}$ cm^{-3}, the rate is in excess of 10^{19} W $\cdot$ cm^{-3}, a value far above that needed for amplification of radiation in the kilovolt region [1].

C. Population of Active Atoms

From (27), we find that the number of atoms per unit length in the saturated core of the channel is

$$n_{act} \simeq \frac{x_{01} J_1(x_{01}) \sqrt{(1+\sqrt{2})\,\beta I(0)} - 1 - \sqrt{2}}{2\zeta r_e}, \quad (38)$$

where ζ is the degree of ionization. Using 248 nm radiation at 4.8×10^{20} W $\cdot$ cm^{-2}, we find $n_{act}\zeta \simeq 7 \times 10^{12}$ cm^{-1} or, recalling the example of holmium, $n_{act} \simeq 1.8 \times 10^{11}$ cm^{-1}. This is a rather small linear density, although volume density is quite high. It will be necessary to use the atoms very efficiently. Perhaps inner-shell multiphoton ionization is the best mechanism.

D. Scaling with Driving-Laser Frequency

The deposition rate has a strong dependence on primary laser frequency, which gives a substantial advantage to the use of higher frequencies.

When a tenuous-plasma channel is unsaturated or only slightly saturated, its radius is $\sim 2c/\omega_p$. The power propagating down the channel is roughly proportional to its central intensity times its square of the radius [5]. To compare the effectiveness of different driving lasers for creating channels that might become lasers themselves, it is appropriate to compare systems with the same values of ω/ω_p. So for a given central intensity, the driving-laser power scales as ω^{-2}.

For the strongly saturated channel, which is the main subject of this paper, driving-laser power scales even more rapidly with frequency. From (33), we obtain

$$P \simeq P_0 = \frac{J_1^3(x_{01}) \sqrt{\beta I^3(0)\,(1+\sqrt{2})}}{2 n_0 r_e x_{01}} = \frac{4 J_1^3(x_{01})}{x_{01}\omega\omega_p^2} \sqrt{\frac{\pi^3 c^3 r_e I^3(0)\,(1+\sqrt{2})}{m}} \quad (39)$$

in the high-power limit. For channels with the same ω/ω_p, the driving-laser power scales as ω^{-3}. Furthermore, higher frequencies generally allow shorter transform-limited pulse lengths, enabling the ions to remain motionless at higher driving-laser power. The ion migration scales approximately as the square of the pulse length. If pulse length then scales as ω^{-1}, the migration scales as ω^{-2}. Finally, the charge-displacement energy given in (31) becomes

$$\frac{d\epsilon_c}{dx} \simeq \frac{x_{01}^2 J_1^2(x_{01})\,(1+\sqrt{2})\,\beta I(0)\, mc^2}{16 r_e} = \frac{\pi x_{01}^2 J_1^2(x_{01})\,(1+\sqrt{2})\,\beta I(0)\, c}{4\omega^2} \quad (40)$$

in the high-power limit. So the charge-displacement energy scales as ω^{-2}, while the corresponding ionization energy goes as ω^{-3}.

IX. Conclusions

The analysis we have presented shows that nonlinear absorption and channeled propagation combine cooperatively in producing conditions favorable to the use of intense short-pulse high-frequency radiation for the production of X-ray amplification. Numerical calculations will be required to obtain a detailed description of the dynamics of channel formation and stability; however, the present technology is close to being able to answer many questions in the laboratory [21]. The ability to channel both the energy deposition and resulting emission can enormously increase the high-frequency gain and provide a natural mechanism for generating low-divergence high brightness X-ray sources.

ACKNOWLEDGMENT

The authors gratefully acknowledge the valuable discussions with G. Gibson and A. McPherson.

REFERENCES

[1] A. V. Vinogradov and I. I. Sobel'man, "The problem of laser radiation sources in the far ultraviolet and X-ray regions," *Sov. Phys.—JETP*, vol. 36, p. 1115, 1973.

[2] K. Boyer, H. Jara, T. S. Luk, I. A. McIntyre, A. McPherson, R. Rosman, and C. K. Rhodes, "Limiting cross sections for multiphoton couplings," *Rev. Phys. Appl.*, vol. 22, p. 1793, 1987.

[3] J. Cobble, G. Kyrala, A. Hauer, A. Taylor, C. Gomez, N. Delameter, and G. Schappert, "Kilovolt X-ray spectroscopy of a subpicosecond laser excited source," LA-UR-88-1181.

[4] G. Gibson, T. S. Luk, A. McPherson, K. Boyer, and C. K. Rhodes, "Observation of a new inner-orbital molecular transition at 55.8 nm in N_2^+ produced by multiphoton coupling," *Phys. Rev. A*, to be published.

[5] G. Z. Sun, E. Ott, Y. C. Lee, and P. Guzdar, "Self-focusing of short intense pulses in plasmas," *Phys. Fluids*, vol. 20, p. 526, 1987.

[6] P. L. Kelley, "Self-focusing of optical beams," *Phys. Rev. Lett.*, vol. 15, p. 1005, 1965.

[7] P. B. Corkum and C. Rolland, "Atomic and molecular processes with short intense laser pulses," in *NATO ASI Series B: Physics*, vol. 171, A. D. Bandrauk, Ed. New York: Plenum, 1987, p. 157.

[8] J. D. Jackson, *Classical Electrodynamics*. New York: Wiley, 1962, p. 259.

[9] L. V. Keldysh, "Ionization in the field of a strong electromagnetic wave," *Sov. Phys.—JETP*, vol. 20, p. 1307, 1965.

[10] S. Stenholm, "Laser-induced multiphoton transitions," *Contemp. Phys.*, vol. 20, p. 37, 1979; P. Lambropoulous, *Advances in Atomic and Molecular Physics, Vol. 12*, D. R. Bates and B. Pederson, Ed. New York: Academic, 1976, p. 86; H. B. Delone, "Multiphoton ionization of atoms," *Sov. Phys.—Usp.*, vol. 18, p. 169, 1975; T. P. Hughes, *Plasma and Laser Light*. London: Adam-Hilger, 1975, p. 142; C. Grey Morgan, "Laser-induced breakdown of gases," *Rep. Prog. Phys.*, vol. 38, p. 621, 1975.

[11] K. G. H. Baldwin and B. W. Boreham, "Investigation of tunneling process in laser-induced ionization of argon," *J. Appl. Phys.* vol. 52, p. 2627, 1981.

[12] T. A. Carlson, C. W. Nestor, Jr., N. Wasserman, and J. D. McDowell, "Calculated ionization potentials for multiply charged ions," *Atomic Data*, vol. 2, p. 63, 1970.

[13] M. P. Bogaard and B. J. Orr, "Electric dipole polarizabilities of atoms and molecules," *Int. Rev. Sci.; Phys. Chem. Ser. 2, Vol. 2*, A. D. Buckingham, Ed. London: Butterworths, 1975, p. 149.

[14] J. D. Jackson, *Classical Electrodynamics*. New York: Wiley, 1962, p. 227.

[15] P. Kaw and J. Dawson, "Relativistic nonlinear propagation of laser beams in cold overdense plasmas," *Phys. Fluids*, vol. 13, p. 474, 1970.

[16] D. C. Barnes, T. Kurki-Suonio, and T. Tajima, *IEEE Trans. Plasma Sci.*, vol. PS-15, p. 154, 1987.

[17] E. S. Sarachik and G. Schappert, "Classical theory of scattering of intense laser radiation by free-electrons," *Phys. Rev. D*, vol. 1, p. 2738, 1970.

[18] W. B. Mori, C. Joshi, J. M. Dawson, D. W. Forslund, and J. M. Kindel, "Evolution of self-focusing of intense electromagnetic waves in plasma," *Phys. Rev. Lett.*, vol. 60, p. 1298, 1988.

[19] H. Hora, "Nonlinear confining and deconfining forces associated with interaction of laser radiation with plasma," *Phys. Fluids*, vol. 12, p. 182, 1969; —, *Physics of Laser Driven Plasmas*. New York: Wiley, 1981, pp. 72-153.

[20] C. E. Max, J. Arons, and A. B. Langdon, "Self-modulation and self-focusing of electromagnetic waves in plasmas," *Phys. Rev. Lett.*, vol. 33, p. 209, 1974; P. Sprangle, C. M. Tang, and E. Esarey, "Relativistic self-focusing of short pulse radiation beams in plasmas," *IEEE Trans. Plasma Sci.*, vol. PS-15, p. 2, 1987.

[21] T. S. Luk, A. McPherson, G. Gibson, K. Boyer, and C. K. Rhodes, "Ultrahigh intensity KrF* laser system," *Opt. Lett.*, to be published.

Johndale C. Solem was born in Chicago, IL, in 1941. He received the B.S., M.S., M.Phil., and Ph.D. degrees all from Yale University, New Haven, CT, in 1963, 1965, 1967, and 1968, respectively.

After a brief tenure as a Research Associate at Yale, he joined the Theoretical Division, Los Alamos National Laboratory, Los Alamos, NM, 1969. His research activities have included both theory and experiment. Some career highlights include the areas of magnetism, transport theory, plasma physics, nuclear physics, equations of state, artificial intelligence and robotics, computational science, X-ray microholography, and laser theory, particularly as it applies to conceptual designs for the x-ray laser. In addition to his research, he has held several management posts. Group Leader of Thermonuclear Weapons Physics, Group Leader of Neutron Physics, Group Leader of High-Energy-Density Physics, Deputy Division Leader of Physics, and Associate Division Leader of Theory. He has served on the Air Force Scientific Advisory Board and numerous Department of Defense and Department of Energy panels. His current research interests include: X-ray lasers, quantum mechanics, and nuclear effects in metals.

Ting Shan Luk was born in Hong Kong in 1953. He received the B.Sc. degree in physics from the University of Hawaii, Manoa, and the Ph.D. degree, also in physics, from the State University of New York at Stony Brook in 1975 and 1981, respectively.

At present, he is a Research Associate Professor and Research Assistant Director of the Laboratory for Atomic, Molecular, and Radiation Physics at the University of Illinois at Chicago. The research projects being conducted involve two main disciplines working towards the development of a laboratory scale X-ray laser. These two areas are 1) the development of high-power laser source in the terawatt range, and with intensity greater than 10^{18} W/cm^2, and 2) the investigation of some basic aspects of atomic and molecular interaction with intense laser field exceeding typical atomic field strength, as well as laser plasma interaction.

Keith Boyer was born in 1915. He received the B.S. degree in electrical engineering from the University of Utah, Salt Lake City, and the Ph.D. degree in physics from the Massachusetts Institute of Technology, Cambridge, in 1942 and 1949, respectively.

At present he holds the rank of Research Professor with the Department of Physics, University of Illinois at Chicago, is a Senior Scientist at MCR Technology Corporation, and actively serves as a consultant to the Los Alamos National Laboratory. His past responsibilities included the original leadership of the Laser Division at the Los Alamos National Laboratory and the position of Assistant Director for Advanced Technologies. His professional publications number approximately 105 and cover an extraordinary range of scientific areas, including short wavelength generation. From his long period of service at Los Alamos in a number of important posts, he has extensive experience in defense and energy issues.

Dr. Boyer was the recipient of an Atomic Energy Commission Citation in 1979.

Charles Kirkham Rhodes (SM'79-F'89) received his undergraduate training at Cornell University, Ithaca, NY, and the Ph.D. degree in physics from the Massachusetts Institute of Technology, Cambridge, in 1969.

He is presently the Albert A. Michelson Professor of Physics at the University of Illinois at Chicago.

Dr. Rhodes is a Fellow of the American Physical Society, the Optical Society of America, and the American Association for the Advancement of Science.

VOLUME 65, NUMBER 14 PHYSICAL REVIEW LETTERS 1 OCTOBER 1990

Stabilization of Relativistic Self-Focusing of Intense Subpicosecond Ultraviolet Pulses in Plasmas

A. B. Borisov,[1] A. V. Borovskiy,[2] V. V. Korobkin,[2] A. M. Prokhorov,[2] C. K. Rhodes,[3] and O. B. Shiryaev[1]

[1]*Laboratory for Computer Simulation, Research Computer Center, Moscow State University, Moscow 119899, U.S.S.R.*
[2]*Coherent and Non-linear Optics Department, General Physics Institute, Academy of Science, U.S.S.R., Moscow 117942, U.S.S.R.*
[3]*Department of Physics, University of Illinois at Chicago, Chicago, Illinois 60680*

(Received 21 March 1990)

The characteristics of relativistic propagation in plasmas of subpicosecond ultraviolet (248 nm) radiation are studied for both spatially homogeneous plasmas and plasma columns. It is established for the first time that the defocusing properties of the interaction can represent a dynamical mechanism stabilizing the mode of propagation against radial oscillations. The dependence of both quasistabilized modes and pulsing waveguide regimes on the initial transverse intensity distribution is examined and, for the latter, the locus of the first focus produced in a homogeneous plasma is calculated.

PACS numbers: 52.40.Db, 42.10.−s, 42.65.Jx

The dynamics of propagation of extremely intense subpicosecond pulses of radiation in self-generated plasmas is a rapidly developing area of study. In this Letter certain aspects of this question are treated theoretically for the following ranges of physical parameters: peak intensity $I \cong 10^{18}$–10^{21} W/cm^2, pulse duration $\tau \cong 0.5$–1.0 ps, initial radial aperture $r_0 \cong 1$–3 μm, wavelength $\lambda = 248$ nm, and plasma electron density $\sim 10^{20}$–10^{21} cm^{-3}. A key finding of these calculations is insight into the physical processes enabling the formation at a quasistable mode of propagation of such high-intensity radiation in plasmas.

For pulses having a peak intensity in the 10^{18}–10^{21}-W/cm^2 range, rapid ($\Delta\tau \cong 1$ fs) processes of multiphoton ionization[1,2] occurring on the leading edge ($I \geq 10^{16}$ W/cm^2) of the wave form will remove several (~6–10) atomic electrons. Thereby, for a focused beam with a given radial aperture r_0, a plasma column is rapidly formed in which the central temporal zone of the pulse propagates. The spatial and temporal dynamics governing the resulting propagation are determined by the competitive interaction of diffraction, defocusing, and self-focusing. We note that in the early portion of the pulse, some defocusing is expected to occur while the ionization is commencing, since the contribution to the refractive index from the free electrons tends to locally reduce its value in the central high-intensity region. In addition, as shown below, the process of defocusing can give rise to a previously unknown mechanism of stabilized propagation.

For subpicosecond pulses and the radial dimensions considered, gross plasma motion involving the ions is negligible.[3] Similarly, for full ionization, noninertial Kerr self-focusing[4] is insignificant. In the present case, both the relativistic increase in the electron mass arising from induced oscillations in the intense field[5,6] and the charge displacement resulting from expulsion of free electrons from the ionized column by the ponderomotive force[3,7,8] can produce strong self-focusing action.

We now describe the specific equations governing the propagation and present calculated solutions illustrating the development of self-focusing and channeled propagation. The origin of the stability exhibited by the propagating radiation is of primary importance. In considering the central temporal region of the pulse, we neglect the energy losses associated with further ionization and spatial broadening of the plasma column, since these effects can be quite small.[9] With this condition, the space-time behavior of the radiation field in the column, including relativistic-charge-displacement self-focusing, diffraction, and defocusing, is governed by the nonlinear Schrödinger equation

$$\left(\frac{1}{c_1}\frac{\partial}{\partial t}+\frac{\partial}{\partial z}\right)E+\frac{i}{2k_0}\Delta_\perp E+\frac{ik_0}{2\varepsilon_{R_0}}\delta\varepsilon_R E+\frac{k_0}{2\varepsilon_{R_0}}\alpha_1 E=0, \tag{1}$$

where $E(t,z,r)$ is the slowly varying (t,z) complex amplitude of the wave, r is the transverse coordinate, $\Delta_\perp=(\partial/r\partial r)r\,\partial/\partial r$, $k_0=2\pi/\lambda$, $c_1=c\varepsilon_{R_0}^{1/2}$ is the group velocity in the plasma, and c is the vacuum speed of light.

The nonlinear term $\delta\varepsilon_R(r,|E|^2)$ describing the combined relativistic-charge-displacement self-focusing and defocusing of the pulse is expressed as

$$\delta\varepsilon_R=\varepsilon_R-\varepsilon_{R_0},\quad \varepsilon_R=1-\omega_p^2/(\omega^2+\nu^2),\quad \varepsilon_{R_0}=1-\omega_{p_0}^2/(\omega^2+\nu_0^2),$$

$$\omega_p^2=\{4\pi e^2N_e[I]/[m_e(1+3I/I_r)^{1/2}]\},\quad \omega_{p_0}^2=4\pi e^2N_{e,0}/m_e,$$

$$I_r=3m_e^2\omega^2c^3/4\pi e^2,\quad I=(c/2\pi)|E|^2.$$

In these expressions, ω_p is the relativistically shifted plasma frequency, ω is the laser angular frequency, ν is the electron-ion collisional frequency, I_r is the relativistic intensity,[2,5] and $N_e[I]$ is the electron density arising from the quasistatic balance of the ponderomotive and the electrostatic forces densities.[3] We assume that $N_i(r,z)=N_{i,0}f(r,z)$ is the static ion density, in which $N_{i,0}$ is a constant denoting the maximal ion density and $f(r,z)$ describes the spatial distribution of the ions. Hence, $f(r,z)\geq 0$, $\max f(r)=1$ [$f(r,z)\equiv 1$ for homogeneous plasma]. For quasineutrality, this gives $N_{e,0}f(r,z)$ as the initial electron density with $N_{e,0}=ZN_{i,0}$ and Z the ionic charge.

The expression for $N_e[I]$, which describes the perturbation of the plasma from local neutrality by both the ponderomotive and relativistic mechanism, is given by

$$N_e[I]=N_{e,0}\max\left\{0,f(r,z)+\kappa\,\mathrm{div}\left[\frac{\mathrm{grad}\,I}{(1+3I/I_r)^{1/2}}\right]\right\}, \quad (2)$$

where

$$\kappa=(2c\omega^2 m_e N_{e,0})^{-1}, \quad (3)$$

and m_e denotes the electron mass. In deriving Eq. (2), the electronic pressure has been neglected, since it is small for the beam and plasma parameters examined here. The expression $\max\{0,-\}$ simply provides for $N_e[I]\geq 0$.

Calculations of the propagation have been performed corresponding to the following parameters for the radiation field and the plasma: $\lambda=248$ nm, $I_r=1.34\times10^{20}$ W/cm^2, $I_0=\frac{1}{2}I_r\cong 3.0\times10^{19}$ W/cm^2, $r_0=3$ μm, $N_{i,0}=7.5\times10^{19}$ cm^{-3}, and $Z=10$.

Normalization of r and I by the initial beam radius r_0 and the maximal value of the initial intensity I_0, respectively, gives $\kappa_1=\kappa I_0 r_0^{-2}\cong 1.4\times10^{-3}$, the dimensionless analog of the coefficient κ defined by Eq. (3). Therefore, for this set of conditions, the charge displacement[3] is expected to be relatively small so that its influence is confined to the structure of the focal regions which arise from the relativistic mechanism. Because of this, we will utilize the approximation that $\kappa=0$ in the current work. It is important to note, however, that other choices of the parameters can lead to a generally strong role for the charge-displacement process and future study is being directed to that case.

The collisional absorption of light in plasma is given by $\varepsilon_I=-(\omega_p^2/\omega^2)\nu=-\mu^-/k_0$, where μ^- is the absorption coefficient. Estimates[3] of μ^-, for the values of the parameters used in this work, show that the collisional absorption is extremely weak and does not influence the numerically obtained solutions. Therefore, the results presented below have been calculated with $\mu^-=0$.

The nonlinear Schrödinger equation stated in Eq. (1) is only applicable to the description of the dynamics of the field in a small focal zone, if its longitudinal scale l satisfies the condition $l\gg\lambda$. The numerical experiments showed, for the range of parameters studied, that $l>50\lambda$. In this connection, we note that the spatial limitations on the minimal dimensions of the focal zones, and consequently the bounds on the intensities developed in those regions, arise from saturation of the nonlinearity expressed by $\delta\varepsilon_R(r,|E|^2)$.

The dynamics of propagation with relativistic self-focusing have been examined using model pulses $I(z,r,t)$ having spatial and temporal Gaussian or hyper-Gaussian incident beam profiles given by

$$I(0,r,t)\equiv I_0(r,t)=I_m\exp\{-(t/\tau)^{N_1}-(r/r_0)^{N_2}\}, \quad (4)$$

$$N_1\geq 2,\quad N_2\geq 2$$

for $I_m\sim I_r\gg I^*=10^{16}$ W/cm^2, the latter being the threshold intensity above which rapid multiphoton ionization occurs to the particles in the medium. Furthermore, we have concentrated on the central temporal zone of the pulse, $|t|\leq t_0$, where t_0 satisfies the expression

$$I_0(t_0)=I_0(0,t_0)=I_m\exp\{-(t_0/\tau)^{N_1}\}\gg I^*. \quad (5)$$

The transverse profile of the plasma column created by the front of the pulse is simulated by the hyper-Gaussian function

$$f(r)=\exp\{-(r/r_*)^{N_3}\},\quad N_3\geq 2, \quad (6)$$

with the aperture of the plasma column r_* defined by

$$I_0(r_*,t_0)\equiv I_0(t_0)\exp\{-(r_*/r_0)^{N_2}\}=I^*. \quad (7)$$

For a Gaussian transverse intensity distribution ($N_2=2$), an aperture defined with $I^*=10^{16}$ W/cm^2, and taking $I_0(t_0)=(0.1)I_r$, we find $r_*\cong 2.68r_0$. Consequently, the homogeneous plasma approximation $f(r)\equiv 1$ is valid.

The beam profiles of the solutions exhibit several salient features. Among them are the production of multiple foci and, under appropriate conditions, the development of a quasistable confined mode of propagation leading the generation of sharply focused regions. Importantly for the latter, the calculations reveal the nature of the mechanism leading to the stabilization. The results of computations presented in this work are given in the frame (s,z,r), $s=t-(z/c_1)$, connected with the wave front of the beam. The data in the figures below illustrate the propagation of the radiation along the z axis for $s=$const.

Figure 1(a) illustrates the propagation that develops for the physical parameters stated above corresponding to a pulse with an entrance intensity $I_0(t)=\frac{1}{2}I_r$ having a transverse distribution given by $N_2=8$. In accord with an earlier study,[9] as the nonlinearity $\delta\varepsilon_R(|E|^2)$ is saturated at a sufficiently low level, the behavior of pulses propagating in a homogeneous plasma without absorption can generate a mode similar to a pulsing waveguide.[9,10] The result shown in Fig. 1(a) illustrates the formation of such a regime. Interestingly, the pulsing waveguide represents an alternation of ring struc-

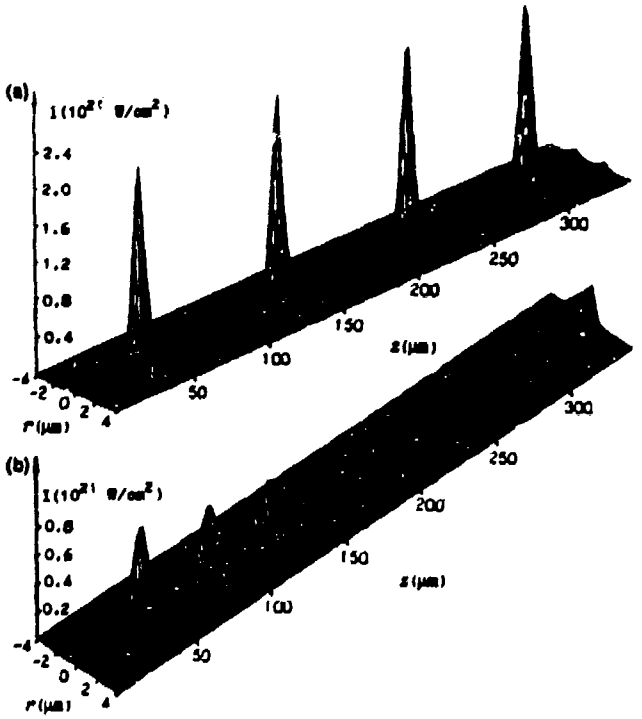

FIG. 1. The (r,z) distributions for relativistic self-focusing of the propagating intensity for a peak initial intensity $I_0=\frac{1}{2}I_r$ having a transverse distribution given by $N_2=8$ in Eq. (4) for the beam and plasma parameters defined in the text. (a) Spatially homogeneous fully stripped plasma. (b) Axially symmetric plasma column with $r_e=r_0$ whose transverse profile corresponds to $N_3=8$ in Eq. (6).

tures and focal regions along the axis of propagation. Significantly, the power trapped in it corresponds to approximately 90% of the total initial power of the beam.

From Eq. (7), it follows that, for plateaulike initial intensity distributions, the aperture r_e of the plasma column becomes comparable with the beam aperture r_0. For example, in the case treated above, we have $r_e \cong 1.28 r_0$. As the apertures of the laser beam and the plasma column tend toward coincidence, however, defocusing becomes relatively more significant. Therefore, this aspect of the propagation must be carefully taken into account when the evolution of pulses having plateaulike initial intensity distributions was studied.

Figure 1(b) shows the propagation of a pulse in a plasma column for $N_2=8$ corresponding to the same physical parameters as those pertaining to the illustration in Fig. 1(a). In this case, the transverse profile of the electron density in the plasma column is described by $f(r)$ in Eq. (6) for $N_3=8$ and $r_e=r_0$. The comparison of Figs. 1(a) and 1(b) demonstrates the strong effect of defocusing on the spatial dynamics of propagation when the column has a radial dimension close to that of the beam. Defocusing causes a fraction of the beam to spread away from the column while the remaining energy adjusts to balance the relativistic self-focusing, defocusing, and

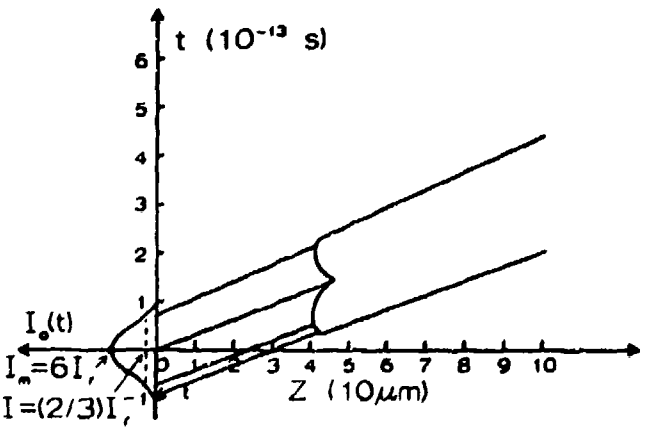

FIG. 2. The locus (t,z) of the first focal zone for a pulse with a Gaussian initial spatial and temporal intensity distribution for the parameters defined in the text. The solution pertains to relativistic self-focusing in a spatially homogeneous fully stripped plasma.

diffraction. In this way, the dynamics of the interaction tend toward the formation of a spatially stable mode of propagation. In addition, as evident from Fig. 1(b), a substantial fraction, nominally 25% of total initial beam power, can be confined in such a mode. Importantly, the further study of such cases has also indicated that such stable patterns can be maintained for a length of at least twenty normal diffraction lengths.

The solutions of Eq. (1), with the initial conditions given by Eq. (4), satisfy important similarity laws. Specifically, the results shown in Figs. 1(a) and 1(b) are valid for any other set of physical parameters satisfying the relationships $a_1 \equiv [(k_0 r_0)^2/8R_0]\omega_{pe}^2/\omega^2 = 2.486\times10^2$ and $a_2 \equiv I_0/I_r = 2/9$. Furthermore, if full account of both the relativistic and charge-displacement mechanisms ($\kappa_1 \neq 0$) is made, these similarity statements are preserved and $\kappa_1 = a_2/4a_1$.

Following earlier studies[10,11] we have analyzed the evolution of plane waves having small perturbations in order to determine the dependence of the self-focusing length on the initial pulse parameters. The results of this analysis showed that the largest growth rate of the perturbations and, consequently, the minimum self-focusing length occur at an entrance intensity on the beam axis of $I_0(t) = \frac{1}{2}I_r$. Specifically, the computations have shown that this inference remains true for the relativistic self-focusing of pulses with Gaussian initial intensity distributions.

The dynamic motion of the foci illustrated in Fig. 2 exhibits important characteristics. For example, the calculations show that the locus of the first focus in the (t,z) plane,[4] for the initial condition determined by Eq. (4) with $N_1=2$, $N_2=2$, $I_m=6I_r \cong 8.04\times10^{20}$ W/cm^2, $\tau=500$ fs, and $r_0=3$ μm, reaches the minimal z for $I_0(t)=\frac{1}{2}I_r$. If the extreme intensity on the beam axis is $I_m \gtrsim I_r$, this locus has three reversal points. Two of

them, corresponding to the same z, are due to $I_0(t) = \frac{1}{3} I_r$. The third and central one, corresponding to a greater z, occurs at $I_0(t) = I_m$. In principle, this feature establishes a clear diagnostic signature for relativistic self-focusing that enables it to be distinguished from the Kerr nonlinearity[4] which produces a locus with a single point of reversal.

The spatial character of propagation of sufficiently intense subpicosecond ultraviolet pulses in self-generated plasmas is significantly influenced by a relativistic-charge-displacement mechanism and two important classes of propagation have been distinguished. In a spatially homogeneous plasma, the interaction can produce self-focusing in the form of a pulsing waveguide involving a structure of alternating rings and focal zones. The location, formation, and nature of the focal regions, including the maximal intensities occurring in them, depend essentially on the properties of the initial transverse intensity distribution. The locus of the first focus in the (t,z) plane for pulses with Gaussian initial intensity distributions and maximum intensities $I_m \gtrsim I_r$ has three reversal points. For this class of pulses, the relativistic self-focusing length is minimal, if the intensity of the initial pulse on the axis equals $\frac{1}{3} I_r$.

A mechanism leading to a spatially stabilized mode of propagation is also revealed. In this case, the defocusing that occurs when the plasma column has a radius close to that of the beam is particularly significant. The effective action of the defocusing, which serves as a spatially distributed nonuniform energy loss, causes the rapid formation of intensity profiles that become quasistabilized along the beam axis. Therefore, it is accurate to state that the process of defocusing contributes directly to the dynamical development of stabilization. Further computational results using the procedures described above are available.[12]

One of the authors (C.K.R.) acknowledges fruitful conversations with J. C. Solem, T. S. Luk, K. Boyer, and A. McPherson. Support for this research was partially provided under Contracts No. AFOSR-89-0159, No. N00014-87-K-0558, and No. N00014-86-C-2354.

[1]L. V. Keldysh, Zh. Eksp. Teor. Fiz. 47, 1945 (1964) [Sov. Phys. JETP 20, 1307 (1965)].

[2]T. S. Luk, U. Johann, H. Egger, H. Pummer, and C. K. Rhodes, Phys. Rev. A 32, 214 (1985).

[3]J. C. Solem, T. S. Luk, K. Boyer, and C. K. Rhodes, IEEE J. Quantum Electron. 25, 2423 (1989).

[4]V. I. Ludgovoi and A. M. Prokhorov, Usp. Fiz. Nauk 111, 203 (1973) [Sov. Phys. Usp. 16, 658 (1974)].

[5]H. Hora, *Physics of Laser Driven Plasmas* (Wiley, New York, 1981).

[6]P. Sprangle, E. Esarey, and A. Ting, Phys. Rev. Lett. 64, 2011 (1990); Phys. Rev. A 41, 4463 (1990); P. Sprangle, C. M. Tang, and E. Esarey, IEEE Trans. Plasma Sci. 15, 145 (1987).

[7]G.-Z. Sun. E. Ott, Y. C. Lee, and P. Guzdar, Phys. Fluids 30, 526 (1987).

[8]T. Kurki-Suonio, P. J. Morrison, and T. Tajima, Phys. Rev. A 40, 3230 (1989).

[9]V. E. Zakharov, V. V. Sobolev, and V. S. Synakh, Zh. Eksp. Teor. Fiz. 60, 136 (1971) [Sov. Phys. JETP 33, 77 (1971)].

[10]V. I. Bespalov and V. I. Talanov, Pis'ma Zh. Eksp. Teor. Fiz. 3, 471 (1966) [Sov. Phys. JETP 3, 26 (1966)].

[11]T. B. Benjamin and J. E. Feir, J. Fluid Mech. 27, 417 (1967).

[12]A. B. Borisov *et al.*, Institute of General Physics, U.S.S.R. Academy of Science, Moscow, Report No. 4, 1990 (unpublished).

APPENDIX I

STABLE CHANNELED PROPAGATION OF INTENSE RADIATION IN PLASMAS ARISING FROM RELATIVISTIC AND CHARGE-DISPLACEMENT MECHANISMS

A. B. Borisov[†], A. V. Borovskiy[*], V. V. Korobkin[*], A. M. Prokhorov[*], O. B. Shiryaev[†], J. S. Solem[^], K. Boyer[††], and C. K. Rhodes[††]

[†] Laboratory for Computer Simulation, Research Computer Center, Moscow State University, Moscow, 119899, USSR

[*] General Physics Institute, Academy of Sciences USSR, Moscow, 117942, USSR.

[††] Department of Physics, University of Illinois at Chicago, Chicago, IL 60680, USA.

[^] Theoretical Division, Los Alamos National Laboratory, Los Alamos, NM 87545, USA.

ABSTRACT

Calculations of the dynamics of propagation in plasma of intense axisymmetric laser pulses incorporating both relativistic and charge-displacement mechanisms are presented. It is shown that the combined action of these two processes can lead to stabilized confined modes of propagation whose asymptotic properties correspond well to the lowest z-independent eigenmodes of the governing nonlinear Schrödinger equation. The effect of the charge-displacement is large and cavitation of the electron distribution is a general feature of the solutions for the range of parameters studied. The results of a specific example show that approximately one half of the incident power (~ 4 TW) can be trapped in the channels which, for a wavelength of 248 nm, an electronic plasma density of ~ 7.5×10^{20} cm^{-3}, and an initial beam radius of ~ 3 μm, develop propagating intensities of ~ 10^{21} W/cm^2.

The dynamics of propagation of intense subpicosecond laser pulses in plasmas in the strongly relativistic regime is currently undergoing vigorous theoretical analysis[1–6]. Of primary significance is the possible formation of quasistable self-channeled modes of propagation. Separately, the analyses of both relativistic[6–9] and charge-displacement[3] mechanisms give indications that confined modes of propagation can exist. In this Letter we examine theoretically the consequences of the combined action of these two mechanisms with particular attention to the development and character of highly stable confined modes of propagation. For radiation with a wavelength of 248 nm, the range of intensity of interest is $I > 10^{19}$ W/cm^2, since both relativistic[6] and charge-displacement[3] mechanisms are significant in that region.

The basic formalism and procedures describing these calculations have been described previously[6]. Assuming collisionless and lossless propagation[8] ($\mu = \nu = \nu_o = 0$), as in the earlier analysis, the complex field amplitude $E(t,z,r)$ is governed by the nonlinear Schrödinger equation

$$\left(\frac{1}{c_1}\frac{\partial}{\partial t} + \frac{\partial}{\partial z}\right)E + \frac{i}{2k_o}\Delta_\perp E + \frac{ik_o}{2\varepsilon_{R_o}}\delta\varepsilon_R E = 0, \tag{1}$$

where r is the transverse coordinate, $\Delta_\perp = \partial^2/\partial r^2 + r^{-1}\partial/\partial r$, $k_o = 2\pi/\lambda$, $c_1 = c\varepsilon_{R_o}^{1/2}$ is the group velocity in the plasma, and c is the vacuum speed of light. The nonlinear term $\delta\varepsilon_R(r,|E|^2)$ of key significance, which describes the combined action of the relativistic and charge-displacement mechanisms, is given by

$$\delta\varepsilon_R = \left(\frac{\omega_{p_o}^2}{\omega^2}\right)\left\{1 - (1 + 3I/I_r)^{-1/2}\max\left[0,\ f(r) + (c^2/\omega_{p_o}^2)\Delta_\perp(1 + 3I/I_r)^{1/2}\right]\right\} \tag{2}$$

in which $I_r = 3m_e^2\omega^2c^3/4\pi e^2$ is the relativistic intensity[3,8], ω_{p_o} is the plasma frequency, ω is the laser angular frequency, and $f(r)$ denotes the spatial distribution of the initially unperturbed electron density. The last term in the inner brackets of Eq. (2), $(c^2/\omega_{p_o}^2)\Delta_\perp(1 + 3I/I_r)^{1/2}$, describes the charge-displacement process and was

neglected in the earlier studies[6] of purely relativistic propagation. The form of Eq. (2) assumes that the propagating radiation is circularly polarized, since the relativistic Υ-factor can be written as $(1 + 3I/I_r)^{1/2}$ in that case. Futhermore, the structure of the terms in Eq. (2) clearly reveals that the relativistic and charge-displacement processes are fundamentally connected and cannot be considered as truly separate and independent mechanisms.

In consideration of the charge-displacement, the motion of the heavy ions is neglected, in accord with previous treatments[3], since the time scale of the laser pulse is assumed to be sufficiently short (~ 100 fs). In this picture, it is known that the electronic component of the plasma can be substantially perturbed by the ponderomotive potential generated by the propagating radiation[1,3]. For the present calculation, the electron distribution is determined by the force balance between the radially outward ponderomotive force and the oppositely directed electron-ion attraction[3]. This ponderomotively driven process is capable of completely expelling electrons from certain spatial regions, a condition described as "electronic cavitation"[1]. The calculations show that the charge-displacement plays a strong role in determining the spatial character of the propagating energy and, particularly, in stabilizing the confined high-intensity modes.

The essential finding of these calculations is insight into the formation and stabilization of spatially confined modes of propagation arising from the coöperative action of the relativistic and charge-displacement processes. The numerical simulations were performed with model pulses I(z,r,t) having spatial and temporal Gaussian or hyper-Gaussian incident beam profiles and initial homogeneous or hyper-Gaussian unperturbed electron densities, in accord with the procedures described previously[6]. Using that earlier notation[6], the relevant parameters are λ = 248 nm, I_r = 1.34 x 10^{20} W/cm^2, I_o = 3 x 10^{19} W/cm^2, r_o = 3 μm, $N_{e,o}$ = 7.5 x

10^{20} cm^{-3}, N_2 = 2, and f(r) = 1 (spatially uniform plasma). Moreover, the results described below are valid[6] for any other set of physical parameters satisfying the relationships $a_1 = \left(\frac{r_0\omega_{p_0}}{c}\right)^2 = 2.486 \times 10^2$ and $a_2 = I_0/I_r = 2/9$. The results of computations presented in this work are given in the frame (q,z,r), $q = t - (z/c_1)$, connected with the wave front of the beam. The graphical data represented below illustrate the propagation of the radiation along the z axis for q = constant.

The solutions for the spatial profiles of the electromagnetic energy and the corresponding electron density exhibit several important characteristics which are shown in Fig. (1) and Fig. (2), respectively. Among them are (1) the generation of intense focal regions, (2) the development of a stable confined channel of propagation, (3) the trapping of a substantial fraction of the incident power in the channel, and (4) strong cavitation in the electron density.

Figure (1a) illustrates the overall behavior of the normalized intensity distribution $I(r,z)/I_0$ and Fig. (1b) magnifies the region between the first two peaks appearing in Fig. (1a). The corresponding normalized electron density $N(r,z)/N_0$ is shown in Fig. (2a). Initially, although a small amount of energy can be seen diffracting away, a large fraction of the incident radiation collapses to form both an axial focal zone (~45%) and a high-intensity annular region. This early stage of evolution involves very little charge-displacement and resembles rather closely the dynamics seen in the purely relativistic case[6]. However, in the present situation, the development of these high-intensity zones leads rapidly to strong perturbations in the electron distribution and the formation of two regions of cavitation. This modified charge distribution, the cross section of which is shown in Fig. (2b) for the axial position z = 95.4 μm, clearly illustrates simultaneous cavitation along the axis ($r \lesssim 0.25$ μm) and in a relatively narrow annular region located at r ~ 1.7 μm. Subsequently, as energy is exchanged between these two structures, the annulus transfers some of its energy to the axial region and a smooth stable confined

mode of propagation on the z–axis containing ~ 46% of the incident power develops ($z \gtrsim 600$ μm). The electron density evolves in a corresponding manner and a single cavitated zone on the axis is formed ($z \gtrsim 600$ μm). The peak intensity associated with the channeled propagation is exceptionally high, reaching values of ~ 10^{21} W/cm^2 in this example.

The relativistic influence on the electron mass and the ponderomotively driven displacement of charge both encourage the formation of channeled propagation. On the basis of the dynamical picture revealed above, the combined effect of these two mechanisms can be, in reasonable approximation, summarized in the following simple way. The relativistic effect leads to the initial concentration of the radiation and the resulting displacement of electronic charge reinforces this tendency and stabilizes the confinement. The coöperative nature of this action appears to lead to highly stable conditions of propagation.

The behavior of the computed solutions for large z can be compared with the z–independent eigenmodes[1,10] of the nonlinear Schrödinger equation (1). In this comparison, it has been shown that the field amplitude tends asymptotically to the lowest eigenmode $V_s(r)$ of this equation. $V_s(r)$ is a real–valued positive monotonic function of r, carries a real dimensionless index s, vanishes as $r \longrightarrow \infty$, and is related to the electric field amplitude by the relation

$$E(r,z) = V_s(r) \exp[-iz(1 - s)\omega_{p_0}^2/2k_0c^2]. \qquad (3)$$

The computations have shown, for the case studied, that the field distribution for large z tends to the amplitude $V_s(r)$ for the index $s \cong 0.554$. The appropriate intensity distribution is then given by $I_s(r) \equiv V_s^2(r)$. Figure (2c) exhibits the normalized asymptotic field amplitude $(I_s(r)/I_0)^{1/2}$ and the corresponding asymptotic electron density distribution $N_s(r)/N_0$. Significantly, these asymptotic profiles, when compared to the corresponding distributions arising from the numerical dynamical

calculation of the propagation for $z \cong 900$ μm, differ by less than one percent. Therefore, the limiting behavior of the dynamically derived propagating solutions seems well described by the simpler z–independent analysis.

Earlier work[3] concerning the charge–displacement mechanism with a steady–state picture showed that the electrostatic energy per unit length associated with a channel arising from the charge–displacement scaled as $P^{2/3}$, with P denoting the laser power. Consequently, for a fixed total power, this electrostatic energy will necessarily be a minimum for a single channel. Therefore, the collapse of the annular structure shown in Fig. (1) is consistent with the system dynamically seeking to minimize this electrostatic energy. Indeed, for the electron density distributions shown in Fig. (2), direct calculation shows that the electrostatic energy per unit length of the large z solution (asymptotic) is approximately one half that associated with the region containing the cavitated annulus [Fig. (2b)]. In addition, it should be noted that the electrostatic energy per unit length in this example is far less (< 0.2%) than the corresponding energy per unit length in the radiation field.

The results of the dynamical calculations shown in Fig. (1) and Fig. (2) can be directly compared in three ways to the simple analytical picture previously used to estimate the properties of the propagation arising solely from the mechanism of charge–displacement[3]. (1) The analytical treatment found that the intensity at the wall I_w was independent of laser power and equal to $I_w = (1 + \sqrt{2})m\omega^2c/4\pi r_e \cong 1.1 \times 10^{20}$ W/cm^2. The dynamical result presently calculated gives good agreement with $I_w \sim 1.2 \times 10^{20}$ W/cm^2. (2) The peak intensity developed at the center of the channel in the asymptotic regime is also found to agree within ~ 10%. (3) Finally, the channel radius shown in Fig. (2c) is ~ 0.4 μm, while the analytic treatment[3] gives a corresponding value of ~ 0.7 μm. This difference is at least partially understood by the fact that the analytic theory[3] did not take into account the relativistic increase in electron mass in the equation for the force

balance. The use of a higher mass would naturally reduce the effective ponderomotive force, a correction that would translate into a reduced channel radius as indicated by the relativistic calculation. Overall, however, we can state that the full numerical treatment of the dynamics and the approximate analytical theory produce results that are in rather close agreement for these important properties of the asymptotic behavior.

Several other cases have also been considered. In particular, calculations examining the dynamics of propagation have been studied for initial intensity distributions other than Gaussian[6] (e.g. $N_2 = 8$) for both homogeneous plasmas [$f(r) \equiv 1$] and simulated plasma columns [$f(r) = \exp[-(r/r_0)^8]$]. The behavior was found to be qualitatively the same as that shown in Fig. (1) with asymptotically trapped fractions of the initial laser power ranging from 34% to 77%.

The dynamical behavior of channeled propagation arising from both relativistic and charge–displacement mechanisms has been studied theoretically. Two principal findings have been established. (1) These two processes can coöperatively reinforce one another and lead to stable confined high–intensity modes of propagation in plasmas which are capable of trapping a substantial fraction (~ 50%) of the incident power. (2) The spatial profiles of both the intensities and electron distributions tend asymptotically to those derived as lowest eigenmodes of a z–independent analysis.

The authors acknowledge fruitful conversations with A. R. Hinds, R. R. Goldstein, T. S. Luk, and A. McPherson. Support for this research was partially provided under Contracts No. AFOSR–89–0159, No. N00014–87–K–0558, No. N00014–86–C–2354, No. DE–FG02–91ER12108, and N00014–89–C–2274.

REFERENCES

1. Gou-Zheng Sun, E. Ott, Y. C. Lee, and P. Guzdar, Phys. Fluids **30**, 526 (1987).
2. P. Sprangle, E. Esarey, and A. Ting, Phys. Rev. Lett. **64**, 2011 (1990); P. Sprangle, C. M. Tang, and E. Esarey, Phys. Rev. A **41**, 4663 (1990).
3. J. C. Solem, T. S. Luk, K. Boyer, and C. K. Rhodes, IEEE J. Quant. Electron. **25**, 2423 (1989).
4. T. Kurki-Suonio, P. J. Morrison, and T. Tajima, Phys. Rev. A **40**, 3230 (1989).
5. J. N. Bardsley, B. M. Penetrante, and M. A. Mittleman, Phys. Rev. A **40**, 3823 (1989).
6. A. B. Borisov, A. V. Borovskiy, V. V. Korobkin, A. M. Prokhorov, C. K. Rhodes and O. B. Shiryaev, Phys. Rev. Lett. **65**, 1753 (1990).
7. G. Schmidt and W. Horton, Comments Plasma Phys. Controlled Fusion **9**, 85 (1985).
8. H. Hora, Physics of Laser-Driven Plasmas (Wiley, New York, 1981).
9. S. V. Bulanov, V. I. Kirsanov, A. S. Sakharov, Fizika Plasmi **16**, 935 (1990).
10. A. B. Borisov, A. V. Borovskiy, V. V. Korobkin, C. K. Rhodes, and O. B. Shiryaev, Trudi IOFAN **4** (1991), in press.

FIGURE CAPTIONS

Fig. (1): (a) The normalized intensity distribution $I(r,z)/I_o$ calculated for an initially homogeneous plasma [$f(r) \equiv 1$]. $I_o = 3 \times 10^{19}$ W/cm^2, $r_o = 3$ μm, $\lambda = 248$ nm, and $N_{e,O} = 7.5 \times 10^{20}$ W/cm^2. (b) Enlargement of the transition zone between the first two peaks shown in Fig. (1a).

Fig. (2): (a) The normalized electron density distribution $N(r,z)/N_o$ calculated for an initially homogeneous plasma [$f(r) \equiv 1$] and corresponding to the data shown in Fig. (1). $N_o \equiv N_{e,O} = 7.5 \times 10^{20}$ cm^{-3}. (b) Radial cross section of the normalized electron density shown in Fig. (2a) for axial distance $z = 95.4$ μm. Cavitation is present along the central axis ($r \lesssim 0.25$ μm) and in an annulus located at $r \sim 1.7$ μm. (c) Radial dependence of the asymptotic solutions for the normalized amplitude $[I_s(r)/I_o]^{1/2}$ and the normalized electron density $N_s(r)/N_o$ for the index $s = 0.554$.

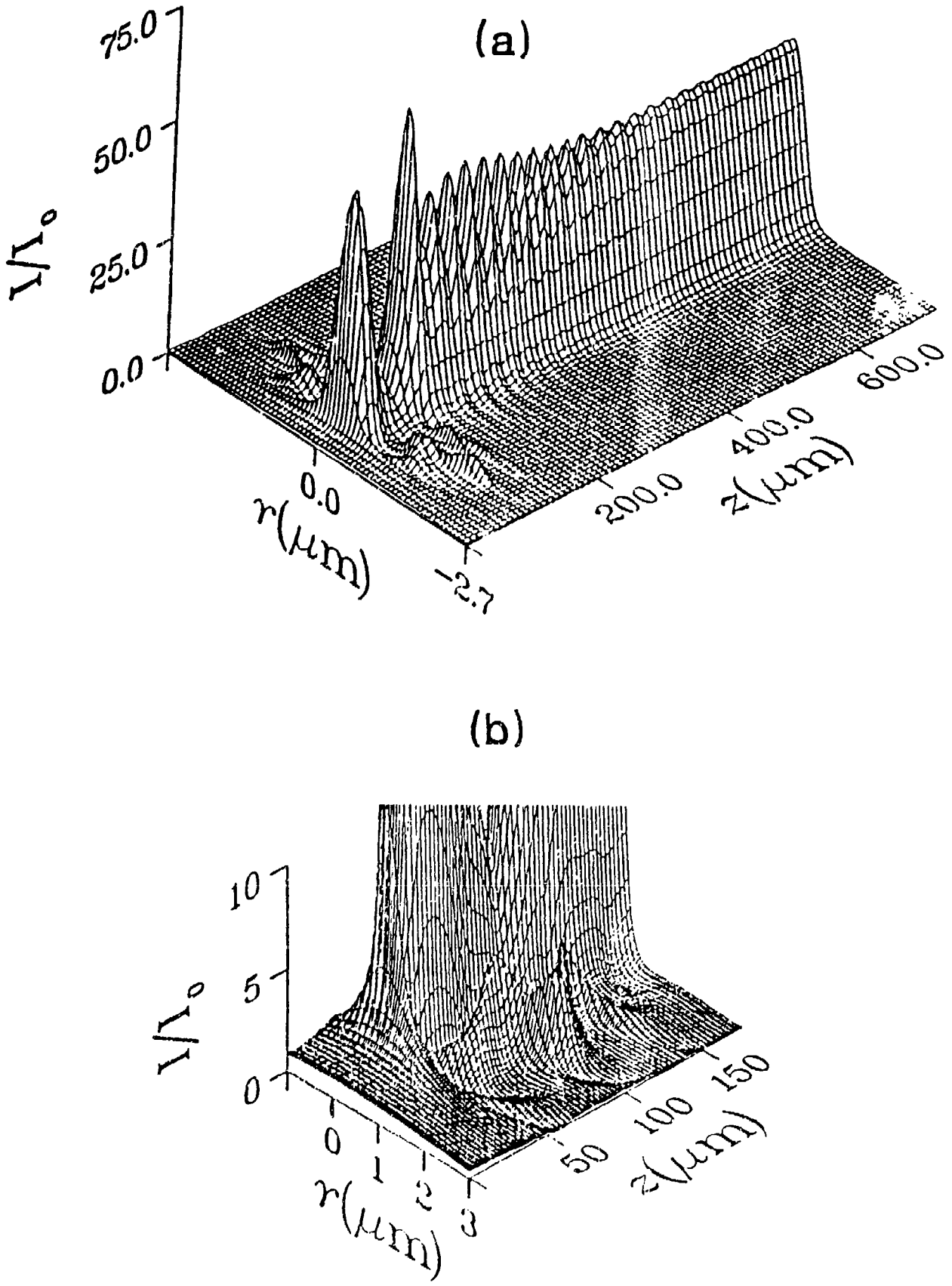
(a)
75.0
50.0
25.0
0.0
I/I°
0.0
r(μm)
-2.7
200.0
400.0
600.0
z(μm)
(b)
10
5
0
I/I°
0
1
2
3
r(μm)
50
100
150
z(μm)

FIGURE (1)

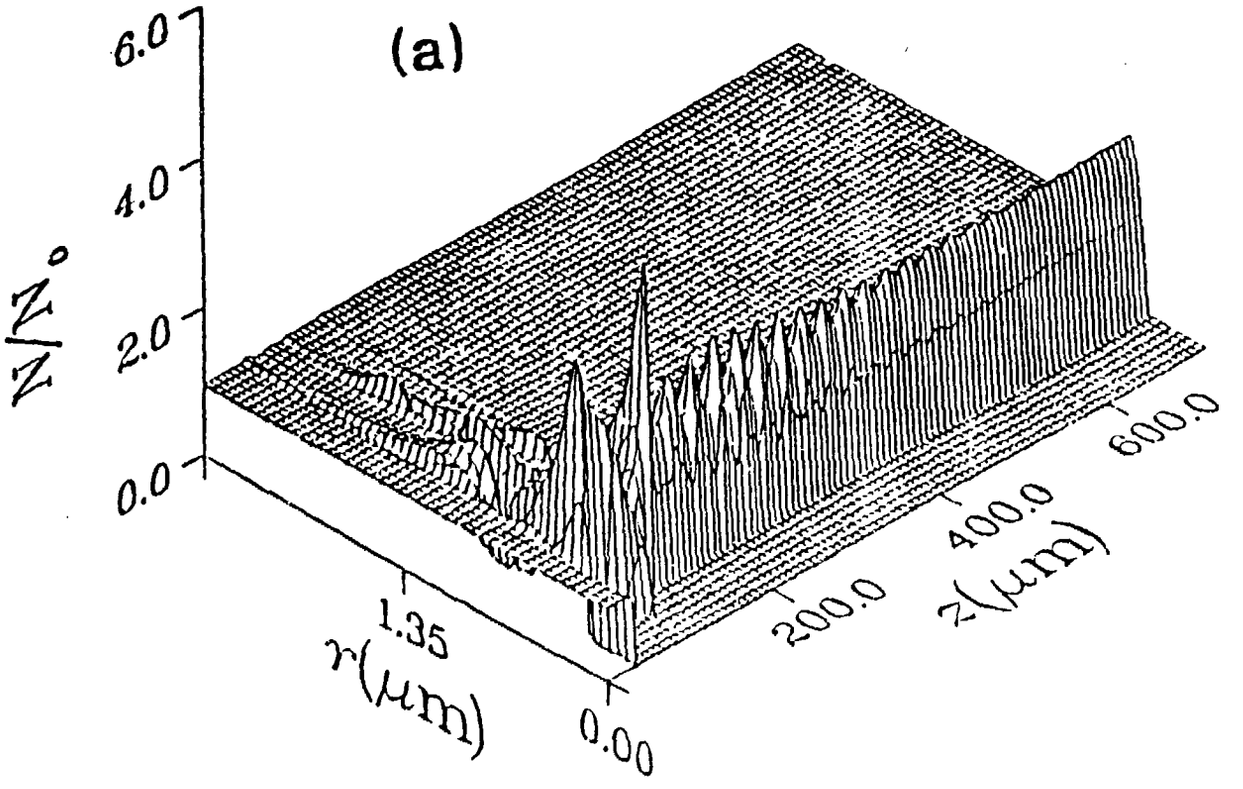
(a)
6.0
4.0
2.0
0.0
N/N°
1.35
r(μm)
0.00
200.0
400.0
600.0
z(μm)

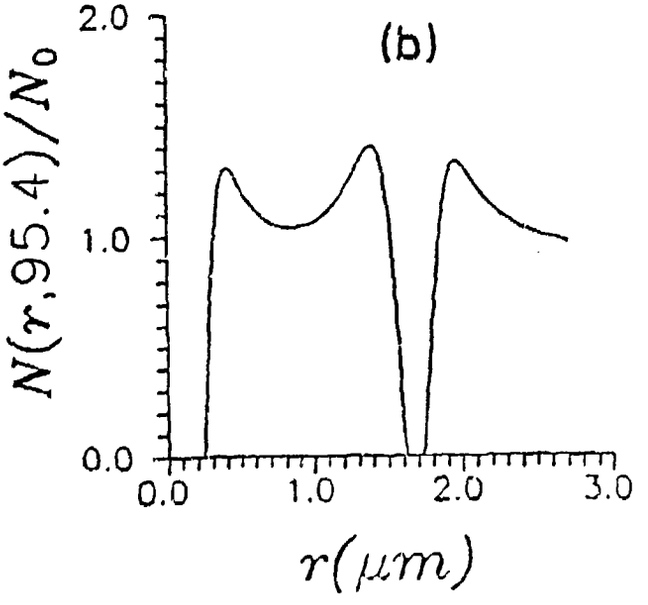
(b)
2.0
1.0
0.0
N(r,95.4)/N0
0.0
1.0
2.0
3.0
r(μm)

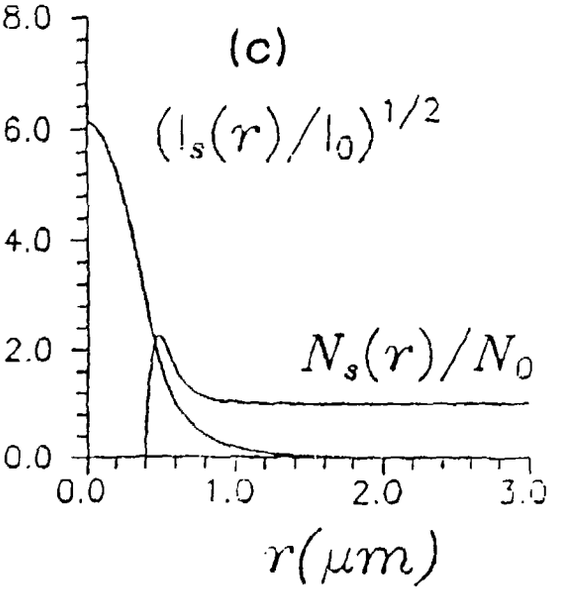
(c)
8.0
6.0
4.0
2.0
0.0
(Is(r)/I0)1/2
Ns(r)/N0
0.0
1.0
2.0
3.0
r(μm)

FIGURE (2)

APPENDIX J

Observation of Relativistic/Charge-Displacement Self-Channeling of Intense Subpicosecond Ultraviolet (248 nm) Radiation in Plasmas

A. B. Borisov[†], A. V. Borovskiy[*], V. V. Korobkin[*], A. M. Prokhorov[*], O. B. Shiryaev[†], X. M. Shi[††], T. S. Luk[††], A. McPherson[††], J. C. Solem[**], K. Boyer[††], and C. K. Rhodes[††]

[†] Laboratory for Computer Simulation, Research Computer Center, Moscow State University, Moscow, 119899, Russia

[*] General Physics Institute, Academy of Sciences of Russia, Moscow, 117942, Russia.

[††] Department of Physics, University of Illinois at Chicago, Chicago, IL 60680, USA.

[**] Theoretical Division, Los Alamos National Laboratory, Los Alamos, NM 87545, USA.

ABSTRACT

Experimental studies examining a new relativistic regime of high-intensity short-pulse propagation in plasmas have been performed which present evidence for the formation of a stable mode of spatially confined (channeled) propagation. For an electron density of ~ 1.35 x 10^{21} cm^{-3} and a power of ~ 3 x 10^{11} W, the results indicate a channel radius < 1 μm and a peak intensity ~ 10^{19} W/cm^2. Comparison of these findings with a dynamical theory yield agreement for both the longitudinal structure and the radial extent of the propagation observed.

A fundamentally new regime of electromagnetic propagation is expected to arise in plasmas for short-pulse radiation at sufficiently high intensity. Calculations of the propagation in plasmas, incorporating both relativistic[1,2] and charge-displacement mechanisms,[3-7] indicate that the combined action of these processes can lead to a new stable form of spatially confined (channeled) propagation. This Letter reports (1) the results of the first experimental study probing the physical regime relevant to the observation of relativistic/charge-displacement self-channeling and (2) presents the initial comparison of these experimental findings with matching theoretical calculations performed with the computational procedures described in Ref. 7.

The experimental arrangement used in these studies is illustrated in Fig. 1(a). The source of radiation was a subpicosecond KrF^* (λ = 248 nm) laser that has been described elsewhere.[8] It delivered a linearly polarized power of ~ 3 x 10^{11} W (~ 150 mJ, pulse duration ~ 500 fs) in a beam with a diameter of ~ 42 mm. When this radiation was focused into the chamber with lens L1 (f/7), a focal radius r_o ~ 3.5 μm was measured, giving a maximum intensity I_o ~ 8.6 x 10^{17} W/cm^2. The medium was provided by filling the chamber statically with gas [He, Ne, Ar, Kr, Xe, N_2, CO_2, or a mixture of Xe (4%) and N_2 (96%)] up to a maximum density of ~ 1.89 x 10^{20} cm^{-3}.

The diffracted 248 nm radiation was measured as a function of the angle (Θ) with respect to the direction of the incident radiation. The incident laser beam was blocked by a metal disk on the output window of the chamber and lens L2 imaged the region near the focal zone on a fluorescent screen S. The diaphragm D in front of lens L2 restricted the collection of the diffracted light to a solid angle of ~ 5° while simultaneously increasing the depth of field. The angle between the axis of the lens L2 and the axis of the incoming laser radiation

could be readily varied up to a maximum angle of $\Theta \sim 15^{\circ}$. Two flat mirrors coated for high reflection (~ 99%) at 248 nm, both having a spectral bandwidth of ~ 10 nm, served in reflection as spectral filters (F) for the diffracted laser radiation so that only the scattered 248 nm radiation could illuminate the screen. An attenuator A was employed to adjust the intensity on the screen and the images formed were recorded through the visible fluorescence produced with a microscope and a CCD camera.

The characteristic behavior observed is well illustrated by the data recorded with N_2. The measured result, shown in Fig. (1b), corresponds to a density $\rho_{N_2} \sim 1.35 \times 10^{20}$ cm^{-3}. To the left, in the photographic inset, a relatively large cone of light Rayleigh scattered from the plasma is visible at all angles as the energy propagates toward the focal point of the lens, while, in the region to the right of the conical apex, a narrow filament developed. The diameter of this filament is not greater than 10 μm, the measured spatial resolution of the imaging system The distribution of intensity observed along the filament exhibited several bright features attributed to diffraction because they could not be seen for $\Theta > 20^{\circ}$ Since the axis of the imaging lens corresponded to an angle $\Theta = 7.5^{\circ}$, the scale along the abscissa of the photographic data is reduced by ~ 8-fold, giving the maximum length of the filament as ~ 1 mm. The graph in Fig. (1b) represents a one-dimensional axial profile, taken along the direction of propagation (z), of the observed intensity pattern (inset). Three peaks (α, β, γ) are visible with a spatial separation of $\delta = 200 \pm 20$ μm. The normal Rayleigh range for the focal geometry used was ~ 200 μm.

The diameter of the filamentary channel is an important dynamical variable which we estimated by measuring the maximum angular deviation of the diffracted light. The experimental value ϕ of this diffracted cone was $\phi \sim 20^{\circ}$, a magnitude

indicating a radius r_ϕ ~ 0.9 μm though the relation $\phi = 1.22\ \lambda/r_\phi$. Filaments of this general nature were observed at densities above ~ 1.35×10^{20} cm^{-3} in N_2, Ne, Ar, Kr, CO_2 and a mixture of Xe (4%) and N_2 (96%), but not in He and Xe, two materials discussed further below.

Two mechanisms exist that could modify the refractive index of the medium and lead to the observed behavior. They are (1) the Kerr–effect stemming from the ions and (2) the relativistic/charge–displacement process.[7] Since the pulse duration is very short (~ 500 fs), the motion of the ions is negligible,[3] and no contribution can arise from expulsion of the plasma from the high–intensity zone. An implication of the estimate of the channel radius (r_ϕ ~ 0.9 μm) is that the observed propagation is associated with intensities in the 10^{18}–10^{19} W/cm^2 range. Under these conditions, available experimental evidence[9,10] on multiphoton ionization indicates that He should be fully ionized and the C, N, and O atoms constituting the molecular materials would retain, at most, only 1s electrons.

Consider explicitly the case of N_2, which has estimated[9,10] threshold intensities for the production of N^{5+}, N^{6+}, and N^{7+} of 1.6×10^{16} W/cm^2, 6.4×10^{18} W/cm^2, and 1.3×10^{19} W/cm^2, respectively. Hence, the volume of the channel would be largely ionized to N^{5+}, with certain localized high–intensity regions contributing some N^{6+}. Two consequences of this pattern of ionization follow, namely, (α) the Kerr–effect arising from the ions is small, since the polarizabilities of the remaining 1s electrons are low, and (β) the electron density (n_e) initially produced in the focal region is nearly uniform. Therefore, $n_e = 1.35 \times 10^{21}$ cm^{-3} for the data on N_2 shown in Fig. 1(b).

A critical power P_{cr} for self–channeling, arising from the relativistic/charge–displacement mechanism, can be defined[11] as

$$P_{cr} = (m_e^2 c^5/e^2) \int_0^\infty g_0^2(r) r dr \, (\omega/\omega_{p,0})^2 = 1.62 \times 10^{10} \left(\frac{n_{cr}}{n_e}\right) W, \quad (1)$$

where m_e, e, and c have their customary identifications, ω is the laser angular frequency, $\omega_{p,0}$ is the plasma frequency for the uniform unperturbed plasma with electron density n_e, n_{cr} is the critical electron density (for λ = 248 nm, n_{cr} = 1.82 x 10^{22} cm^{-3}), and $g_0(r)$ is the Townes mode.[12]

The critical powers associated with the experimental conditions, for He and N_2 at a medium density ρ = 1.35 x 10^{20} cm^{-3}, are 1.08 x 10^{12} W and 2.19 x 10^{11} W, respectively. Therefore, since the incident power was P $\simeq$ 3 x 10^{11} W, no filament was expected in He, a prediction conforming with the observation of none. Moreover, the diffracted cone of radiation was also absent with He. In contrast, $P/P_{cr} \simeq 1.37$ for N_2, a condition that held generally ($P/P_{cr} > 1$) for all materials which exhibited evidence for channel formation. We note, however, that some contribution from the Kerr–effect may be present, even for the light materials (Ne, N_2, and CO_2), in the early stage of channel formation prior to the development of a substantial level of ionization, and that the heavier gases, (Ar, Kr, and Xe) may involve a more significant influence from the Kerr process. A specific estimate of the nonlinear index change arising from both N^{5+} and N^{6+} at an intensity of ~ 10^{19} W/cm^2 indicates that their contribution is less than 10^{-3} that of the free electrons, hence the ionic contribution can be neglected in N_2 for the conditions studied.

A direct comparison will now be made between the theoretical analysis, fully described in Ref. (7), and the experimental findings for N_2. This comparison can be accomplished for both the longitudinal intensity profile and the radial extent of the channel. Figure 2(a) illustrates the intensity profile $I(r,z)/I_0$ calculated

with physical parameters corresponding to those of the experiment (i.e. $P \simeq 3 \times 10^{11}$ W, $r_o = 3.5$ μm, $n_e = 1.35 \times 10^{21}$ cm^{-3}, and $P/P_{cr} = 1.37$). Importantly, all of these parameters are based on independent measurements of (1) the laser pulse involving determinations of the energy and power (P), (2) the focal radius (r_o) of the incident radiation, and (3) the characteristics of the multiphoton ionization[10] generating the electron density (n_e). Therefore, this comparison does not involve a fit to a free parameter. The normalized electron density calculated is presented in Fig. 2(b) from which it is seen that electronic cavitation occurs only near the positions of the maxima in the intensity profile [Fig. 2(a)]. Curve (A) in Fig. 2(c) represents the one–dimensional axial intensity profile $I(0,z)/I_o$ corresponding to the calculated distribution shown in Fig. 2(a). The spacing (δ) of the maxima is seen to be $\delta \sim 185$ μm, a value in close agreement with the experimental figure ($\delta = 200 \pm 20$ μm) illustrated in Fig. 1(b). Furthermore, analysis has shown that the spacing δ is quite sensitive to the power P_o and electron density n_e, particularly in the region close to the threshold [see Eq. (1)]. With respect to the results illustrated in Fig. 2(c), an increase in n_e by less than 5 percent causes a reduction in the spacing δ by approximately 25 percent. Therefore, substantial changes in the physical parameters would grossly alter the comparison of the experimental and theoretical results.

Theoretical studies[3–7,11] indicate that the charge–displacement plays a very important dynamical role. In order to test this hypothesis, identical calculations were made for N_2 for the purely relativistic case[2] which explicitly neglects the charge–displacement term, namely, elimination of the term $[c^2/(\omega_{p,o}^2 r_o^2)]\ \Delta_\perp(1 + I/I_r)^{1/2}$ in Eq. (24) of Ref. (7). Significantly, the resulting axial profile [Curve B in Fig 2(c)] exhibits only a single relatively weak maximum, for $0 \leq z \leq 600$ μm, an outcome sharply at variance with both the full theoretical analysis and the experimental

observation. Although the expected charge–displacement is highly localized [Fig. 2(b)], this comparison reveals the strong influence it has on the propagation.[3,7,11] At a greater incident power ($P/P_{cr} \sim 10$), a continuous channel in the electron distribution is expected to develop.[7]

The measurements indicated an approximate value of $r_\phi \simeq 0.9$ μm for the radial extent of the channel, a result that can be compared with the corresponding theoretical figure. Figure 2(d) illustrates five radial intensity profiles $I(r,z_i)/I_o$ of the distribution pictured in Fig. 2(a). Since the measurement of this angularly scattered radiation did not correspond to a known longitudinal position, this comparison can only be qualitative, but the radial distributions shown indicate that the expected value lies in the interval $0.5 \leq r \leq 1.0$ μm, a range that comfortably includes the experimental value r_ϕ.

The results observed with Xe deserve additional discussion, since those experiments did not give evidence for the formation of a channel. In significant contrast to the case involving N_2, the electron density n_e produced by the multiphoton ionization[10] in Xe is expected to be very nonuniform spatially. For intensities spanning $10^{16} - 10^{18}$ W/cm^2, the corresponding density n_e would vary by over a factor of two. Since this nonuniformity would tend to reduce the refractive index locally in the central high–intensity region, a significant defocusing action is expected which could suppress the channel formation.

Finally, we note (1) that the intensity distribution is not expected to depend strongly on the state of polarization[13,14] and (2) that losses to the plasma may be significant, particularly at electron densities close to n_{cr}.

The first experiments examining a new relativistic regime of high–intensity pulse propagation in plasmas have been performed and the findings indicate the formation of a channeled mode of propagation over a length considerably greater

than the Rayleigh range. Specific comparisons of the experimental observations with a dynamical theory, which explicitly includes both the influence of the relativistic mass shift and the displacement of the electronic component of the plasma, produce excellent agreement for both the longitudinal structure of the intensity profile and the radial extent of the channel. While the present channel contains several foci, a continuous channel is predicted to develop at higher power. Finally, the intrinsically very high concentration of power associated with this mechanism of channeled propagation provides an efficient and general method for the production of conditions necessary for x–ray amplification.[15]

The authors acknowledge the expert technical assistance of J. Wright and P. Noel in addition to fruitful conversations with A. R. Hinds, R. R. Goldstein, and B. Bouma. Support for this research was partially provided under contracts AFOSR–89–0159, (ONR) N00014–91–J–1106, (SDI/NRL) N00014–91–K–2013, (ARO) DAAL 3–91–G–0174, (DoE) DE–FG02–91ER12108, and (NSF) PHY–9021265.

REFERENCES

1. C. Max, J. Arons, and A. B. Langdon, Phys. Rev. Lett. 33, 209 (1974).
2. A. B. Borisov, A. B. Borovskiy, V. V. Korobkin, A. M. Prokhorov, C. K. Rhodes, and O. B. Shiryaev, Phys. Rev. Lett. 65, 1753 (1990).
3. J. C. Solem, T. S. Luk, K. Boyer, and C. K. Rhodes, IEEE J. Quantum Electron. QE-25, 2423 (1989).
4. P. Sprangle, E. Esarey, and A. Ting, Phys. Rev. Lett. 64, 2011 (1990); P. Sprangle, C. M. Tang, and E. Esarey, Phys. Rev. A 41, 4463 (1990); A. Ting, E. Esarey, and P. Sprangle, Phys. Fluids B 2, 1390 (1990).
5. G. Z. Sun, E. Ott, Y. C. Lee, and P. Guzdar, Phys. Fluids 20, 526 (1987).
6. T. Kurki-Suonio, P. J. Morrison, and T. Tajima, Phys. Phys. Rev. A 40, 3230 (1989).
7. A. B. Borisov, A. V. Borovskiy, O. B. Shiryaev, V. V. Korobkin, A. M. Prokhorov, J. C. Solem, T. S. Luk, K. Boyer, and C. K. Rhodes, Phys. Rev. A 45, xxxx (in press, 15 April 1992).
8. T. S. Luk, A. McPherson, G. Gibson, K. Boyer, and C. K. Rhodes, Opt. Lett. 14, 1113 (1989).
9. S. Augst, D. Strickland, P. D. Meyerhofer, S. L. Chin, and J. H. Eberly, Phys. Rev. Lett. 63, 2212 (1989).
10. G. Gibson, T. S. Luk, and C. K. Rhodes, Phys. A 41, 5049 (1990).
11. A. B. Borisov, A. V. Borovskiy, V. V. Korobkin, A. M. Prokhorov, O. B. Shiryaev, and C. K. Rhodes, J. Laser Phys. 1, 103 (1991).
12. R. Y. Chiao, E. Garmire, and C. H Townes, Phys. Rev. Lett. 13, 479 (1964).
13. P. Avan, C. Cohen-Tannoudji, J. Dupont-Roc, and C. Fabre, J. de Phys. 37, 993 (1976).

14. S. V. Bulanov, V. I. Kirsanov, and A. S. Sakharov, Fiz. Plasmy 16, 935 (1990) [Sov. J. Plasma Phys. 16, 543 (1990)].

15. K. Boyer, A. B. Borisov, A. V. Borovskiy, O. B. Shiryaev, D. A. Tate, B. E. Bouma, X. M. Shi, A. McPherson, T. S. Luk, and C. K. Rhodes, "Method of Concentration of Power in Materials for X-Ray Amplification," Appl. Opt., in press.

Figure Captions

Fig. 1: (a) Experimental apparatus use in studies of propagation. See text for description. (b) Data concerning the pattern of propagation observed with a single pulse in N_2 at a density of ~ 1.35 x 10^{20} cm^{-3}. The maximum intensity is half the detector (CCD) saturation. The radiation is incident from the left. The inset shows the photographic data with a vertical spatial resolution of ~ 10 μm. The graph illustrates the one–dimensional axial profile taken along the direction of propagation (z) of the photographic data (inset). A spacing of the maxima $\delta \simeq 200 \pm 20$ μm is indicated.

Fig. 2: Calculations for N_2 with P = 3 x 10^{11} W, r_0 = 3.5 μm, n_e = 1.35 x 10^{21} cm^{-3}, and I_0 = 8.6 x 10^{17} W/cm^2; (a) Normalized intensity $I(r,z)/I_0$. (b) Normalized electron density $N(r,z)/N_0$ for N_2 with $N_0 = n_e$. (c) Normalized one–dimensional axial intensity profiles $I(0,z)/I_0$. (A) Full theory for data in panel (a), δ = 185 μm. (B) Calculation with charge–displacement term neglected. (d) Normalized radial intensity profiles $I(r,z_i)/I_0$ corresponding to panel (a). Longitudinal positions z_1 = 172 μm, z_2 = 245 μm, z_3 = 358 μm, z_4 = 441 μm, and z_5 = 559 μm and r_ϕ = 0.9 μm.

(a)
KrF Laser
150 mJ
500 fs
L1 F/7
Gas Cell
D
L2
AFS
Microscope
θ
CCD
camera

Figure 1(a)

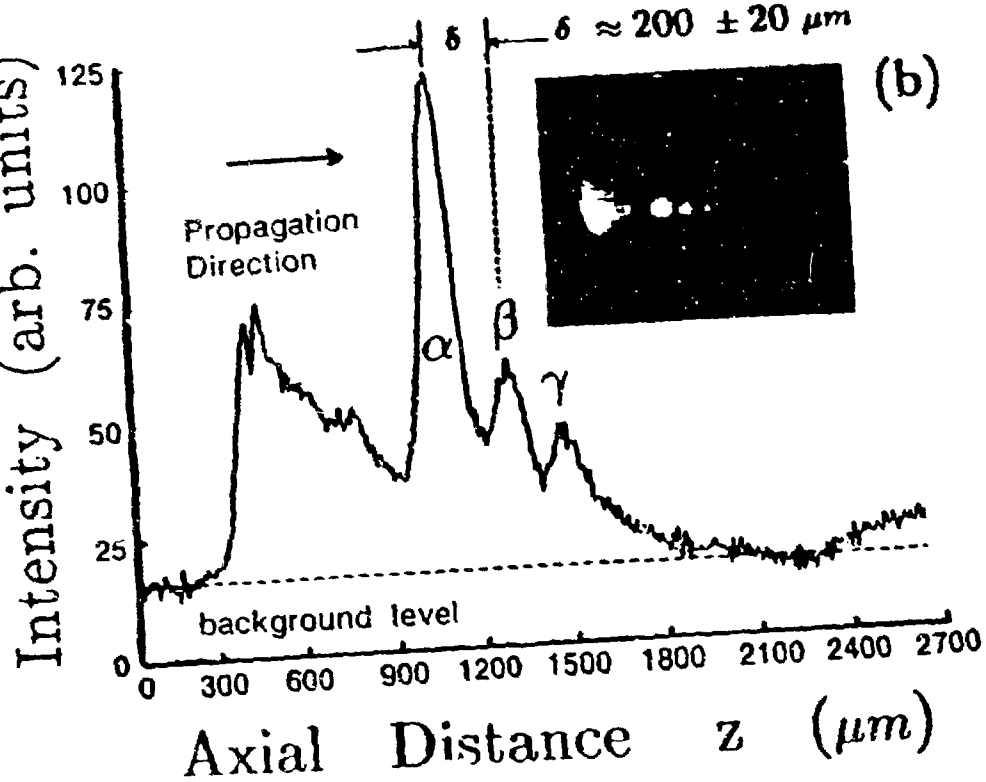
δ
δ ≈ 200 ± 20 μm
(b)
Intensity (arb. units)
125
100
75
50
25
0
Propagation Direction
α
β
γ
background level
0 300 600 900 1200 1500 1800 2100 2400 2700
Axial Distance z (μm)

Figure 1(b)

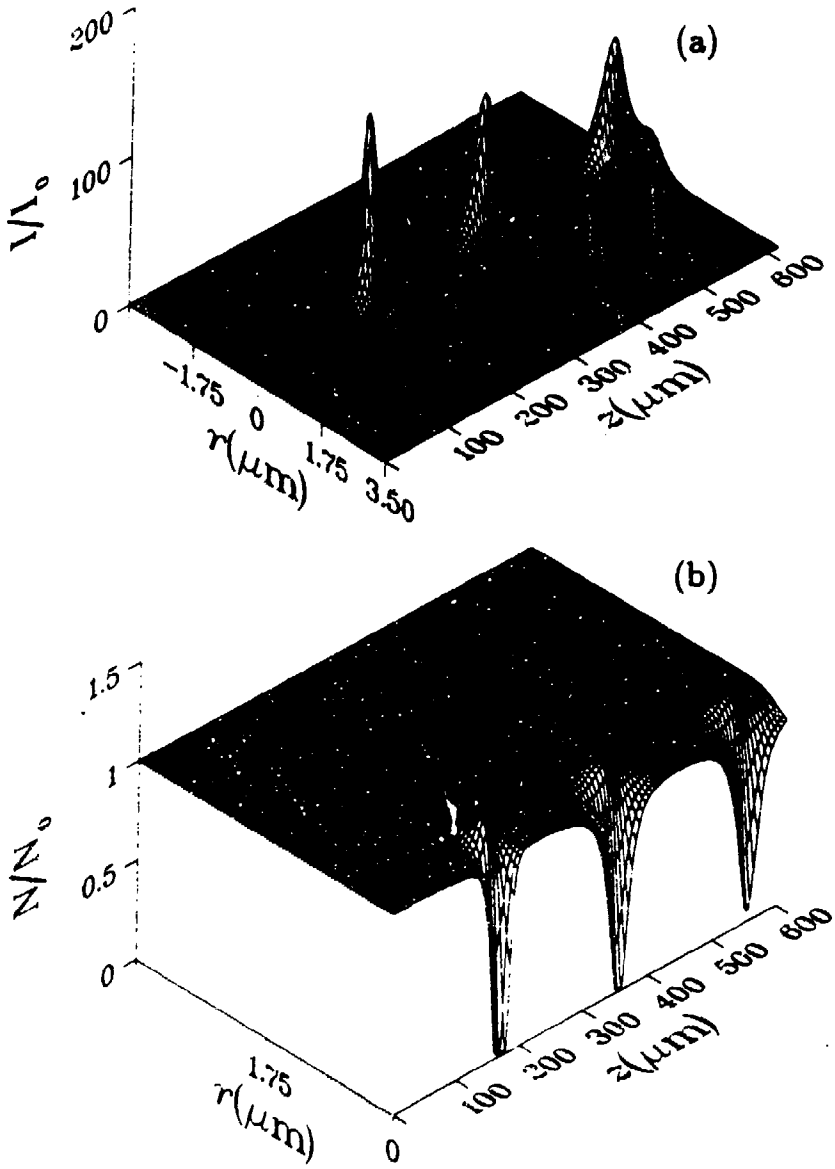
(a)
200
100
0
I/I°
-1.75
0
1.75
3.50
r(μm)
100
200
300
400
500
600
z(μm)

(b)
1.5
1
0.5
0
N/N°
1.75
0
r(μm)
100
200
300
400
500
600
z(μm)

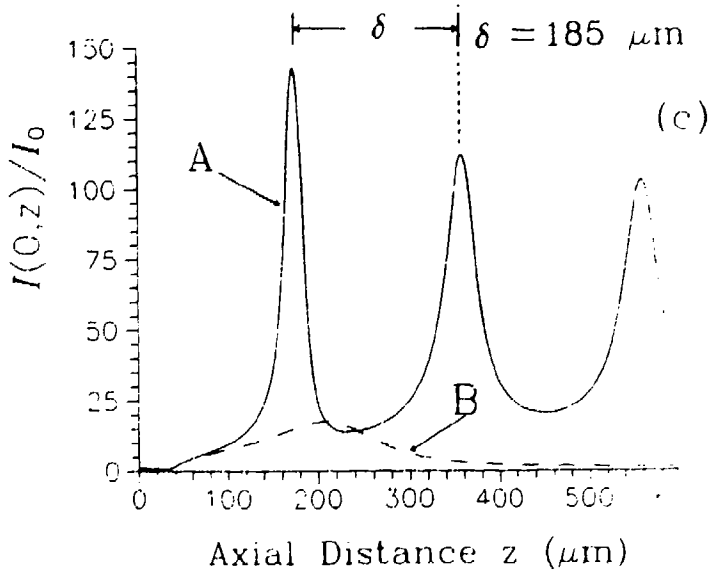
δ
δ = 185 μm
(c)
150
125
100
75
50
25
0
I(0,z)/I₀
A
B
0
100
200
300
400
500
Axial Distance z (μm)

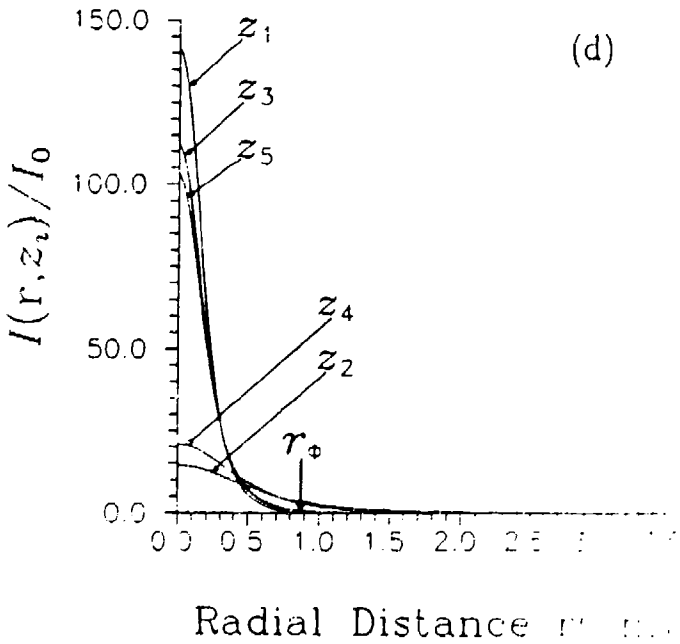
(d)
150.0
100.0
50.0
0.0
I(r,zᵢ)/I₀
z₁
z₃
z₅
z₄
z₂
r_Φ
0.0
0.5
1.0
1.5
2.0
Radial Distance

Figure 2